COHERENT OPTICAL MANIPULATION OF ELECTRON SPIN IN CHARGED SEMICONDUCTOR QUANTUM DOTS

by

M. V. Gurudev Dutt

A dissertation submitted in partial fulfillment
of the requirements for the degree of
Doctor of Philosophy
(Physics)
in The University of Michigan
2004

Doctoral Commitee:

Professor Duncan G. Steel, Chair
Professor Paul R. Berman
Professor Roberto D. Merlin
Professor Theodore B. Norris
Assistant Professor Cagliyan Kurdak

ACKNOWLEDGEMENTS

This thesis could not be possible without all the help I received along the way from many sources. Right at the beginning, I would like to thank my advisor, Professor Duncan Steel. He is a man of many talents, and many demands on his time including the management of two different laboratories, but he always found the time to listen and advise me as to my difficulties, both in my work and in my personal life. He has shown me how to look critically at data and how to always ground ones theoretical ideas in experimental reality, something I didn't imbibe in all my previous education. His desire to mentor others and his concern for both their professional and personal well-being is truly something I would like to emulate. Among my committee members, I would like to acknowledge Prof. Roberto Merlin for teaching me a lot about semiconductors and for his relentless pursuit of the physics, and Prof. Paul Berman for theoretical help and explaining the subtleties of the quantized field approach for deriving the spontaneously generated coherence. Some of the best classes I took at this university were the optics courses taught by Prof. Ted Norris and the semiconductor physics course by Prof. Cagliyan Kurdak. I would also like to thank Dr. Dan Gammon and Dr. Allan Bracker at the Naval Research Laboratory for their hospitality during my stay in Washington, DC and never tiring of answering my barrage of questions on the physics of trions and quantum dots.

During my time at Michigan, I have interacted with a number of other students, but I would first like to thank Dr. Anthony Lenihan for teaching me about the Mira laser, and the techniques of nonlinear spectroscopy in the laboratory. On the days when nothing seemed to work, Dr. Liz Batteh managed to keep things in perspective for me by reminding me that it wasn't the end of the world. I would also like to thank her for unselfishly sharing her knowledge and time on the CW lasers. Dr. Elaine Li showed me that to succeed in the laboratory, it required painstaking attention to even the seemingly unimportant details

and hard thinking about every aspect of the experiment. The fun discussions I had on the finer points of Michigan football with Drs. Gang Chen and Jeff Guest were definitely key to taking some of the stress out of my graduate life.

Among my current colleagues in the laboratory, I have learnt a great deal more from Jun Cheng and Yanwen Wu than I think I taught them. I would especially like to acknowledge Jun, Yanwen and Xiaodong Xu for their help with setting up, taking and analyzing the experimental data for the coherent control experiments in Chapter 6, and Jun for helping with the CW spectroscopy data on single QD trions. All the other students in the laboratory have contributed in innumerable ways to the experiments, but I would especially like to thank Bo Li, Wencan He and Qiong Huang for helping to run the experimental apparatus. I will fondly remember the tea sessions, playing volleyball and ultimate frisbee, and the potluck lunches in the office. A special thanks to Jun Cheng and Yanwen Wu for proof-reading this thesis. Any mistakes or oversights in this thesis are definitely due to my shortcomings, but there would have been many more if not for their efforts. I am confident that with their able stewardship, the laboratory will go on to achieve greater heights.

Finally, I would like to thank my family and friends for their support during my graduate career. Most of all, though, I would like to thank my wife and best friend Arthi, who has unflaggingly encouraged me when things seemed bleak. Her ability to keep my chin up and make me laugh during those times made all the difference in the world.

TABLE OF CONTENTS

LIST OF FIGURES

LIST OF APPENDICES

LIST OF ABBREVIATIONS

2DEG	Two-dimensional electron gas
AOM	Acousto-optic modulator
BAP	Bir-Aronov-Pikus
BIA	Bulk inversion asymmetry
CCD	Charge-coupled device
CI	Classical interferogram
CM	Center of mass
CNOS	Coherent nonlinear optical signal
CP	Circularly polarized
CQD	Charged quantum dot
CW	Continuous-wave
DP	D'yakonov-Perel
DT	Differential Transmission
EFA	Envelope function approximation
EPR	Einstein-Podolsky-Rosen
ESR	Electron spin resonance
EY	Elliot-Yafet
FR	Faraday rotation
FWHM	Full width at half maximum
FWM	Four wave mixing
GMR	Giant magneto-resistance
HH	Heavy hole
IFQD	Interface fluctuation quantum dot
LH	Light hole
LP	Linearly polarized
LT	Longitudinal-transverse
MBE	Molecular beam epitaxy
ML	Monolayer
MOCVD	Metal organic chemical vapour deposition
MODFET	Modulation doped field effect transistors
MOSFET	Metal oxide silicon field effect transistor
NMR	Nuclear magnetic resonance
NSOM	Near-field scanning optical microscopy
OCP	Orthogonal circular polarization
PL	Photoluminescence
PLE	Photoluminescence excitation
PZT	Piezoelectric transducer
QC	Quantum computing

QD	Quantum dot
QDQC	Quantum dot quantum computing
QI	Quantum interferogram
QW	Quantum well
RF	Radio-frequency
RWA	Rotating wave approximation
SAQD	Self-assembled quantum dot
SCP	Same circular polarization
SEC	Spontaneous emission cancellation
SGC	Spontaneously generated coherence
SHG-FROG	Second harmonic generation frequency resolved optical gating
SIA	Structural inversion asymmetry
SO	Split-off
SRP	Stimulated Raman process
SRS	Stimulated Raman scattering
STIRAP	Stimulated Raman adiabatic passage
SVEA	Slowly varying envelope approximation

CHAPTER 1

Introduction

Spin is fundamentally a quantum mechanical effect, and the prediction and discovery of electron spin by Goudschmidt and Uhlenbeck constituted a resounding affirmation of the quantum mechanical view of Nature. The methods developed for spin resonance in nuclei [2,3] and electrons [11,13] and the amazing discovery of the spin echo [4] showed that it was possible to generate, detect and manipulate the quantum state of the spin polarization by applying radio-frequency (RF) or microwave radiation. However, while the technology of nuclear and electron spin detection is applied routinely in chemical laboratories for analysis of compounds and in medical magnetic resonance imaging by doctors all around the world, it was only in the late 1980s that spin polarization was exploited for purposes of information storage. The discovery of the giant magnetoresistance (GMR) effect, wherein the state of the magnetization is used to change the resistance of a device, provided an impetus to the field of spintronics. The current generation of computer technology, which uses the charge of the electron to perform logical operations and to carry information, is commonly labeled as electronics (or "charge"tronics). For the last several years, a complementary direction of research has been towards the possibility of using the spin of the electron as the data bit (or spintronics). The electron spin has already been exploited for commercial applications such as GMR sensors and memory read/write heads in computer hard disks. The passive manipulation of the magnetization to change electronic properties may more properly be classified as magneto-electronics [232]. A more active approach is to transport spin-polarized currents, leading to spin valves and transistors [76, 103, 255, 356, 370]. For a recent review on the state of the field, see Reference [456].

Concomitantly, the study of low dimensional quantum confined structures has experienced rapid growth over the past thirty years, with great advances being made in fabrication

methods. Quantum well (QW) heterostructures, where the carriers are confined along the growth direction, have been extensively studied in the laboratory [37, 89, 210]. Commercial applications such as the quantum well laser and detectors that rely on the lowered dimensionality and quantum confinement in these systems now form the backbone of the current information revolution. The exciting possibilities of bandgap engineering for tunability and sensitivity, as well as lowered threshold current and higher gain in quantum cascade lasers shows the importance of quantum effects [60]. A natural extension of such research is therefore to consider the effects of confinement in the directions perpendicular to growth, leading to quantum wires and quantum dots (QDs). QDs refer to systems wherein the motion of charge carriers in semiconductors is confined in all three dimensions on the order of the de-Broglie wavelength of the particle. Due to the zero-dimensional nature of the confinement, the density of states for QDs is discrete [146, 345, 379]. The result is that a macroscopic collection ($\sim 10^3 - 10^6$) of atoms behaves like a single atom under optical or electronic excitation, leading to unusual properties. Hence, QDs are sometimes referred to as artificial atoms, and coupled QDs as artificial molecules. As a simple example of the tremendous change in the properties, consider the difference between a bulk semiconductor and a QD under optical excitation. As the excitation density increases, since a semiconductor can be well-modeled in a "quasi-particle" picture, more and more quasi-particles are excited corresponding to increase in occupation number of the mode. The system behaves as a harmonic oscillator, with any nonlinearities usually arising from the interactions between the quasi-particles. In a QD however, it is well established both theoretically and experimentally now that stimulated emission or Rabi oscillations take place instead, leading to higher probability that the quasi-particle will emit a photon and return the crystal to the ground state!

QD structures have been the subject of intense investigation for the past decade. With their discrete, atomic-like density of states and the availability of modern semiconductor processing technology that permits fabrication into compact integrated packages, they are attractive candidates for the next generation of technologies. QD detectors and lasers have already been demonstrated in several laboratories [153, 160, 313]. Inherently, QDs exhibit several quantum-mechanical properties that cannot be explained by classical physics, such as photon antibunching in the light emission [299]. This also makes them exciting sources of new devices such as QD single-photon sources [300, 388, 438, 439], and single-electron

transistors [190, 218]. We shall provide a brief review on the varieties of growth processes, devices and applications of QDs in Section 1.2.1.

Following Moore's law, the shrinking size of components in modern integrated circuits will soon reach the regime where quantum size effects become important. The synergy that is currently developing at the intersection of research into QDs, spintronics and information processing makes it a most exciting and fertile area of investigation. In particular, the emerging field of quantum information processing which utilizes the powerful resources of quantum entanglement and massive parallelism that are inherent in quantum mechanics [124, 281], provides an example of an area that would greatly benefit from research in this area. In Section 1.1 of this chapter, we will review the basic ideas of quantum information processing and survey a few of the experimental implementations being actively pursued, such as those based on ion traps, photons and nuclear magnetic resonance (NMR). Due to the natural advantages of mature technologies that are available for growing arrays of devices which enable large-scale integration, solid state implementations under investigation include donor nuclear spins in Silicon, superconducting circuits and QDs. In Section 1.2, we will summarize the key ideas behind QD quantum computing (QDQC). In Section 1.3, we discuss the importance of our work in the field of optical implementation of spin-based QDQC and provide an outline of the chapters that follow.

1.1 Motivation: Quantum Information Processing

The field of quantum information processing was originally suggested by Feynman [47]. The fundamental unit of the quantum computer is called a quantum bit (or qubit) and can exist in a superposition of quantum states $|0\rangle$ or $|1\rangle$. The central idea is to utilize the massive parallelism of quantum mechanical superpositions, combined with quantum interference during the unitary evolution, to achieve a desired computational result. Pioneering work by Deutsch and Bennett showed that quantum computers could, in principle, out-perform classical computers by exploiting the resources of quantum entanglement. For instance, the Deutsch-Jozsa algorithm [92] can decide whether a one-bit function is balanced or constant on a single run, while classical algorithms require at least two.

Entanglement refers to the property that the wavefunction of a system cannot be decomposed into the tensor product of its subsystems. As an example, denoting the state

of two spins by $|x,y\rangle$, $x,y = 0,1$, one such maximally entangled state is the Bell state $|\beta_{00}\rangle = \frac{|0,0\rangle+|1,1\rangle}{\sqrt{2}}$. Entanglement allows for non-local correlations that are at the heart of the Einstein-Podolsky-Rosen (EPR) paradox [1], so that the spin pair that comprises the Bell state is often referred to as an EPR pair. Bennett *et al.* showed that it is possible by means of shared EPR pairs and classical communication to achieve teleportation of an unknown quantum state [99], and to perform super-dense coding for quantum communication [90].

An obvious impediment to quantum computing (QC) is decoherence, which means the non-unitary collapse of the delicate quantum superpositions required for computations due to interactions of the quantum computer with the environment. The discovery of quantum error-correcting codes [171, 274] for fault-tolerant QC showed how to overcome this important issue. Peter Shor discovered a random algorithm, *i.e.* one that will eventually work, for the prime factors of large numbers that requires only polynomial steps as a function of the input size [120] (see Reference [151] for a clear review). It was (and still is) widely believed that this problem cannot be solved in polynomial steps by classical computers. The importance of Shor's algorithm lies in the fact that a number of modern-day cryptographic systems such as the RSA algorithm rely on this belief for their security. Similarly, Grover's search algorithm in an unsorted space showed that quantum algorithms could work faster than classical algorithms [183].

However, the problem of how to experimentally realize a working quantum computer was still monumental until it was realized that all the steps required for a computer could be constructed from universal quantum logic gates [124,125,141,281]. Combined with single qubit rotations, it was shown that two-qubit logic gates (for example, the controlled-NOT, or phase gate) are sufficient to enable QC. A discussion of the important requirements for QC is given by David DiVincenzo in Reference [285], which we paraphrase here:

1. A scalable physical system with well characterized (physically distinguishable) qubits.

2. The ability to initialize the state of the qubits to a simple fiducial state, such as $|000\ldots\rangle$ (state preparation).

3. Long relevant decoherence times, much longer than the gate operation time. Combined with error correction for fault-tolerant QC, this translates to the requirement that the decoherence time is $10^4 - 10^5$ times longer than the gate operation time.

4. A "universal" set of quantum logic gates.

5. A qubit-specific measurement capability (state readout).

Below, we briefly discuss the various experimental successes in other schemes for QC before moving on to discuss QDQC. Note that we have not considered so far another sub-field of quantum information processing, namely quantum communication which forms a highly interesting and active area of research in its own right. However, for QC with photons, the two fields are closely inter-related, so we shall discuss them together now.

1.1.1 Photon Quantum Computing

The use of photons for quantum communication is obviously attractive because of their rapidity and ease of transmission through long distances, either through free space or optical fibers. Furthermore, they are highly robust against decoherence processes, but unfortunately do not interact strongly with each other making it difficult to construct logic gates. The latter difficulty may be overcome using atom-cavity QED as discussed below. It has been shown however that quantum teleportation combined with linear optical elements can also be used to construct a scalable quantum computer [257, 339].

In most quantum teleportation experiments with photons, highly correlated photon pairs are created by parametric down-conversion in nonlinear crystals. These pairs are then used for demonstration of quantum teleportation, for example in Reference [176]. In that work, the authors use EPR pairs combined with post-selection (or conditional gating) for teleportation of unknown polarization states. The experiment usually ends up destroying the teleported photon, although this drawback was addressed in a subsequent work [412]. The entanglement and teleportation demonstrated in these experiments are usually random in nature due to the randomness of the source, relying on the post-selection for the high fidelity. Furusawa *et al.* attempted to address this criticism by using the amplitude and phase quadratures of squeezed light for continuous-variable teleportation [217]. Their experiment however suffered from poor fidelity compared to the polarization state teleportation. Quantum entanglement and teleportation have now been demonstrated for three [246, 302, 305], four [344] and even five [455] photons. Maximally entangled four-photon states, known as Greenberger-Horne-Zeilinger (GHZ) states are especially interesting as they can be shown theoretically and experimentally to form decoherence-free subspaces where the action of a

common-mode noise operator does not lead to decoherence [432]. While these challenging experiments certainly provide proof of principle, QC with linear optics requires a deterministic and bright source of entangled photons. Recently, such a source has been demonstrated with quantum dots for verification of the Bell's inequality violation [439], and for deterministic quantum teleportation with high fidelity [438].

As noted earlier, quantum communication with photons is in a much more advanced stage, particularly in demonstrations of quantum cryptographic protocols over long distances [391] (see Reference [301] also). Another active area in quantum communication is to network quantum computers at different nodes in a quantum network, wherein photons transmit the quantum information between nodes. A recent proposal in this regard shows that quantum communication can be achieved with tools that are currently available such as cold atomic ensembles and linear optics [325]. Significant experimental progress has already been made, with Kuzmich *et al.* showing that it was possible to transfer quantum information from photons into the atomic ensemble and store it for long times ($\sim$ 400 nsec in the experiment) [406]. We now leave behind the area of photon QC and discuss another extremely successful experimental deisgn, namely the trapped ions.

1.1.2 Trapped Ion Quantum Computing

The use of cold trapped ions for QC was originally suggested by Cirac and Zoller [123]. Trapped ions that have been cooled below the Lamb-Dicke limit, *i.e.* the average motion is smaller than a wavelength, can be individually addressed through laser excitation and coupled through vibrational modes of the trapped ion array ("bus" qubit). Demonstration of a controlled-NOT gate using the ion and bus qubit followed soon thereafter [134]. Scaling up the system presents some difficulties, although a recent proposal [372] offers promise in this regard. Both the Cirac-Zoller gate [418] and a geometric controlled π-phase gate [445] between two ions have been achieved experimentally. The geometric phase gate is based on the idea that depending on the internal atomic state of the ions (which is controllable), the combined state of motion of the ions will result in a geometric phase after a complete round-trip in the motion that depends on the area of the orbit in phase space. Since the geometric phase is less subject to the perturbations from the surrounding environment, higher fidelities were achieved ($F \sim 0.97$) as compared to the Cirac-Zoller gate ($F \sim 0.71$).

Deterministic entanglement between two [235], three [444,449] and four ions [306] has also been demonstrated. The problem of post-selection is avoided in these experiments, and have led to the demonstration of deterministic teleportation of the quantum states with high fidelity $\sim 78\%$ [430,448].

Atom-cavity QED schemes have also been proposed for networking ion trap quantum computers through photons via high-Q optical cavities and optical fibers [178]. Pellizzari *et al.* have shown how to use an ion trap enclosed in such a high-Q cavity to achieve gates between ions using photons rather than phonons as in the Cirac-Zoller scheme [137]. The experiment of Turchette *et al.* shows that cavity-QED may be utilized to generate strong nonlinear interactions between photons as required for the traditional linear optics QC proposals [142]. The experiments were however limited in nature as they relied on hot atomic beams which randomly interacted with the cavity photons [111, 142]. The strong coupling regime, wherein the coupling between the atom and the photon (inversely proportional to the cavity mode volume) is greater than the spontaneous emission rate of the atom and the cavity lifetime of the photon is hard to achieve, especially in a deterministic one-atom regime as required for the proposals in References [137, 178]. However, recent experiments using a magneto-optical trap from which cold atoms are dropped into the cavity shows how to overcome the limitations, and have realized deterministic generation of single photons [447] and the ultimate limit of strong-coupling: a single-atom laser [411]. In another recent experiment, Blinov *et al.* have demonstrated that trapped ions and photons can be entangled by employing an appropriate level scheme and detecting the spontaneously emitted photons along particular directions [431], thereby circumventing the experimental challenges of incorporating ion trap technologies and high-Q cavities. Their experiment thus shows that ions and photons may be used to build quantum networks and implement the quantum communication protocol proposed in Reference [325]. The trapped ion implementation clearly offers a viable scheme for building scalable quantum computers and quantum networks.

1.1.3 Bulk Nuclear Magnetic Resonance Quantum Computing

The next experimental paradigm that we consider for QC is using NMR in bulk materials, and the basic ideas were laid out by DiVincenzo in 1995 [124] and by Gershenfeld and

Chuang in 1997 [182]. Even though the qubits are not addressed individually, the NMR experiments can still extract information by considering the outcome of many computations running in the ensemble of molecules (to be thought of as individual quantum computers). The problem of different local magnetic fields experienced by different quantum computers can be overcome through the spin-echo technique, or "refocusing" sequences as they are known. Due to the advanced capabilities in the mature field of NMR, rapid progress was quickly realized, with demonstrations of the one-qubit Deutsch-Jozsa algorithm [209] and the four-state Grover's search algorithm in chloroform molecules [208]. Shor's algorithm for finding the prime factors of 15 with a seven-qubit designer molecule of perfluorobutadienyl has also been performed [355]. The above examples show that NMR QC is highly useful to test the basic concepts and algorithms of QC. However, NMR QC suffers from exponential degradation of the signal as the system is scaled up [247] and also from the fact that state preparation is limited by the thermal distribution of the states in the ensemble of molecules [200]. Finally, we note that NMR QC may be useful in a different context when we consider the implementations of QC with donor nuclei in solids, as discussed below.

1.1.4 Solid State Quantum Computing

Solid state implementations of QC have been pursued vigorously due to the obvious advantages in scaling and fabrication. The three most viable candidates at the moment appear to be superconducting Josephson junctions, donor nuclei in Silicon and QDs. We discuss the implementations with superconducting circuits and the donor nuclei in Silicon in this section. The concepts of QDQC will be discussed in greater detail in the next section.

The initial proposals used the charge states of a Josephson junction (explained below) as the qubit [195, 269]. A superconductor below the crossover temperature is comprised of Cooper pairs of electrons. By placing two superconductors (assumed to have only paired electrons) separated by a thin layer of normal metal, one obtains a Josephson junction. The difference in number of Cooper pairs on the two superconductors forms a qubit. By applying gate voltages, one can perform qubit rotations and by using inductive coupling, one can engineer two-qubit entanglement and logic gates. Coherent superpositions [272] and Rabi oscillations [341] of single Cooper-pair box states have been observed, first by Nakamura *et al.* and later by others [385, 387]. The latter experiments addressed the issue

of charge fluctuations leading to decoherence, by clever circuit design and biasing of the Josephson junctions in such a manner as to bring the two charge states to nearly the same average energy, thereby making the system immune to first-order charge fluctuations. The decoherence times so far reported are on the order of 0.5 μsec, and compare favourably with the operational time of a few hundred psec. Recently, entanglement between two macroscopic charge qubits has also been shown [413]. An alternative proposal was also made to use the quantized flux enclosed in superconducting persistent-current loops as the qubit [271]. Since the magnetic flux is only sensitive to fluctuating magnetic backgrounds, it can possess much longer coherence lifetimes. Coherent superpositions of flux qubits have also been demonstrated [288, 312].

As noted earlier, donor nuclear spins in semiconductors can form a qubit that can be easily manipulated through electron spin resonance (ESR) techniques. For instance, given the popularity of Si technology, the idea of using a phosphorous donor embedded in bulk Si would be an obvious choice for a qubit. The decoherence times of ^{31}P (nuclear spin $I = \frac{1}{2}$) donor nuclei in bulk Si was measured as early as 1958 through spin-echo techniques to be $\sim 200 - 500\,\mu$sec [11]. The same donor in isotopically purified Si was found recently to have even longer coherence times ($\sim$ 20 msec) [426]. This motivated the proposal by Kane in 1998 to consider an array of ^{31}P nuclei embedded just below the surface of a Si crystal [222]. The electron-nuclear hyperfine interaction can be controlled by means of electrical gates (the A gate), bringing different nuclei into resonance with an applied RF-magnetic field. The shift can be as great as 38 MHz for typical gate voltages, allowing one to perform coherent qubit rotations. Additionally, the exchange interaction between the electrons on different donors lowers the energy of the nuclear spin singlet with respect to the spin triplet, leading to controllable coupling between donor nuclei and the possibility of logic operations (the J gate). The shift is small, and places stringent requirements on the donor separation ($\sim$ 200 Å) as well as excellent control over the depth and location of the nuclei that stretches the limits of available technologies. Recent progress in the field indicates that the above technology is not out of reach however [419]. More recently, there have been proposals to use the random telegraph signal in silicon field effect transistors [314, 409, 429], the photocurrent in bulk Si [397] or single-electron transistors in silicon-germanium heterostructures [440] to read out the state of the electron spin trapped in paramagnetic defects. A recent measurement using ESR of the random

telegraph signal due to single electron capture and emission from a paramagnetic trap in a silicon field-effect transistor reveals a spin decoherence time $T_2 \sim 0.1\,\mu$sec [454].

1.2 Quantum Dot Quantum Computing

We begin the section with a brief review of various kinds of QDs, and then proceed to discuss the implementations of QDQC in Section 1.2.2. The review of QDs given here is by no means exhaustive, and we refer the reader in most cases to comprehensive reviews on the subject.

1.2.1 Review of QDs

For a good review article on nanocrystals, interface fluctuation QDs (IFQDs) and self-assembled QDs (SAQDs), see Reference [358]. We will also identify below other review articles related to each individual type of QD.

1.2.1.1 Lithographically Defined Quantum Dots

The first ideas for fabrication of QDs were an outgrowth of QW research, and it was attempted by means of electron-beam and ion-beam lithography to define patterns within the QW which would confine electrons. However, the damage and micro-roughness of the surfaces caused by etching resulted in quenching of optical and transport properties. The high mobilities observed in two-dimensional electron gases (2DEGs) formed by high-quality modulation doped QWs [33, 37] showed that electrons in those materials were largely free from scattering processes. By lithographically defining gates on the surface of the 2DEGs, it was possible to empty a region of the 2DEG completely of electrons, and then proceed to fill it sequentially. In this manner, Coulomb blockade effects became observable for the first time in the capacitance spectroscopy of these QDs [89, 95, 104]. Coulomb blockade is actually a classical effect that arises because it requires an energy $e^2/2C$ to load a charged QD (CQD) with an extra electron, where C is the capacitance of the CQD. An important many-body effect has been observed in these QDs, known as the Kondo effect [218], which refers to the increase in resistance below a certain temperature when an isolated electron spin forms a singlet state with a delocalized state.

The use of electrostatic gates to define QDs is extremely attractive as it allows for voltage control of the electronic charge, as well as between nearby QDs. Rabi oscillations with voltage pulses [403] as well as coupling between QD molecules [143] has been observed in these QD systems. Further, it is possible with the sophisticated lithographic techniques to arrange for periodic arrays and stacking of the QDs, thus allowing for scalability that is required for QC. However, the necessity for voltage control of the electronic state in the QD is actually a drawback as charge fluctuations in the environment can lead to dephasing of the charge qubit. Further, it is difficult to manufacture ultrafast voltage pulses that meet the requirement of being able to perform many gate operations within the decoherence time. This led to the proposal by Loss and DiVincenzo in 1998 to control the spin state of the electron in the lithographically defined QDs instead of the charge state, to be discussed below.

1.2.1.2 Nanocrystals

Nanocrystals are semiconductor clusters formed by chemical colloidal synthesis, with typical radii $\sim$ 10s of Å , unlike other QDs which are synthesized by molecular beam epitaxy (MBE) or metal organic chemical vapour deposition (MOCVD). The most common nanocrystals are formed from II-VI materials like CuCl or CdSe [73, 106, 146], although other material systems such as InAs [241] and InP [174] have also been developed. Single nanocrystal spectroscopy has been demonstrated by different groups [152, 263, 334], and discrete resonances due to the three-dimensional confinement with linewidths $\sim 100\,\mu$eV have been observed. Since they can be prepared as nearly perfect macroscopic crystallites of atoms in the gas phase, it might be presumed that they are perfect examples of semiconductor QDs. However, studies of nanocrystals showed that the optical properties and carrier dynamics are strongly influenced by the surface reconstruction which leads to the formation of surface states in the band gap of the semiconductor [117, 146, 298]. While possessing the advantage of simple synthesis procedures and wide tunability (CdSe nanocrystals can be made with wavelengths from 430 nm to 650 nm), one of the problems with nanocrystals is the spectral "blinking" after a few seconds [164, 263] and wandering of spectral lines [149] presumably due to the surface effects. While passivation with higher-bandgap material such as ZnS did alleviate the problem to an extent, it is not clear at present if nanocrystals can

serve as stable optical materials.

A variety of nonlinear optical spectroscopy techniques have been applied to nanocrystals to explain the broad homogeneous linewidth (short dephasing times) observed [96,117,224]. Recently, spectral hole burning measurements have shown that the broad linewidth is due to contributions from acoustic or surface phonon sidebands, in addition to the intrinsic radiative contribution to dephasing of $\sim 30\,\mu$eV [343]. Nanocrystals have been used to demonstrate many quantum-mechanical effects, such as photon antibunching [299], quantum-confined Stark effect [180], single-electron transistors [190] and stimulated emission for laser action [313].

1.2.1.3 Interface Fluctuation Quantum Dots

In normal growth of GaAs/Al_xGa_{1-x}As QWs by MBE, interface roughness occurs with a disorder lengthscale typically a few atomic diameters and is responsible for Anderson localization of mobile excitons [39,43]. However, it was discovered that by interrupting the growth at the interfaces of narrow QWs while subject to steady As flux, the subsequent interface formation shows large monolayer-high islands [39,91,113,121]. We will discuss the different localization mechanisms for IFQDs in Section 2.1.3. These islands are typically 40–100 nm in size (*i.e.* on the order of the Bohr radius of the exciton), and preferentially elongated along the [110] and [$\bar{1}$10] axis, giving rise to linearly polarized photoluminescence (PL) emission [155]. Extremely narrow linewidths in the PL emission ($\sim 25\,\mu$eV) [156], series of sharp resonances in photoluminescence excitation (PLE) spectra [128, 156], and strong suppression of spin relaxation processes [308, 309] confirms the zero-dimensional nature of the confinement in the islands.

A number of interesting experiments which exploit the zero-dimensional confinement of IFQDs have been performed with linear spectroscopic methods. The shift in the exciton Zeeman splitting, under the combined action of continuous optical excitation and magnetic field, due to the Overhauser effect (caused by electron-nuclear hyperfine interaction) has been observed, and used for optically detected NMR of single QDs [181, 206]. Direct absorption and modulation spectroscopy measurements on single QD excitons reveal large dipole moments [368, 381], consistent with theoretical predictions [239]. Coherent control techniques combined with PLE were applied to demonstrate elementary wavefunction engi-

neering in single QDs [205]. Besides single excitons, biexcitons have been observed in both GaAs [112,316] and CdTe IFQDs [282].

In addition to linear spectroscopy, a rich variety of nonlinear spectroscopy measurements have been performed, revealing that the dephasing dynamics of these QDs are primarily from the radiative recombination [204,382]. Near-field scanning optical microscopy (NSOM) techniques combined with nonlinear spectroscopy was used to directly image the center-of-mass wavefunction of localized excitons [332]. The optical stark effect, wherein strong excitation with a laser pulse can modify the polarization created by an earlier pulse has been observed [451]. Strong-field experiments confirm the atomic-like character of the excitonic states through the observation of exciton Rabi oscillations [353]. Biexciton Rabi oscillations in such dots have been used to demonstrate a quantum controlled-ROT gate [408]. Quantum entanglement between the bright exciton states has been experimentally shown both in the weak-field [284] and strong-field regime [446]. The large dipole moments of the QDs, and the lack of pure dephasing processes, makes them an ideal model system for study of the important physics that must be taken into account for QDQC.

1.2.1.4 Self-Assembled Quantum Dots

SAQDs have received a tremendous amount of attention in the semiconductor community. SAQDs are formed by growth of lattice-mismatched III-V or II-VI semiconductors (such as InAs on GaAs) in the coherent Stranski-Krastanow MBE growth mode. The use of this mode for the growth of SAQDs was proposed and achieved independently by Snyder *et al.* [88] and Leonard *et al.* [116]. See References [118,148,166,345] for excellent reviews on the growth processes that have been developed for SAQDs. The growth essentially occurs by the wetting action of 2–3 monolayers of the semiconductor during the MBE growth, followed by the self-organization of clumps of atoms around 10-100 nm in size which form QDs. The shape of the dots can be in the form of disks, lenses, pyramids, and even rings, depending on the growth conditions. The absence of interface dislocations during the process (hence the term coherent) allows for high optical-quality material.

Due to the extremely small size, and randomness of the self-organization process, there is a great deal of inhomogeneity in the size and shape leading to a large distribution in transition energies. Efforts to reduce the inhomogeneity involve usually vertical stacking

of layers of dots which tend to align naturally due to strain fields in the system. Another method is the growth of $In_xGa_{1-x}As$ islands on both (311)A and (311)B surfaces of GaAs, where the inhomogeneity was found to be considerably reduced. Two- and three-dimensional ordered arrays of SAQDs have also been demonstrated [162, 260, 266, 410], which is particularly useful for addressing the scalability issue in QC applications. Lateral alignment and size homogeneity can be induced through either strain patterning with a layer of stressor dots [264, 297], or on templates patterned by e-beam lithography [219, 293].

SAQDs have been investigated through electrical methods such as photocurrent spectroscopy [251, 252] and capacitance spectroscopy, but the optical techniques have primarily utilized cathodoluminescence [132], PL and PLE techniques. We will focus on optical studies of SAQDs, as the primary goal of the thesis is to study the physics of QDs for optically driven QC. An important effect predicted in SAQDs was the "phonon bottleneck", occurring because the energy levels in the QD are separated by a spacing that does not match the LO phonon energies in the material [82]. LA, TA and TO phonons are also found to be inefficient in causing energy relaxation (see Reference [220] for a detailed explanation). The "phonon bottleneck" gives rise to poor luminescence properties because it inhibits energy relaxation from the the higher excited states to the ground state, and should lead to the observation of peaks at the excited state energies even at low excitation intensity. However, the effect was not observed for a long time, and this led to some controversy regarding the models of energy relaxation. PLE spectra revealed the presence of a number of peaks separated by integer multiples of the LO phonon frequency [126, 157, 168], leading some authors to argue that multi-phonon processes were contributing to the relaxation, and masking the phonon bottleneck [93]. At high excitation intensity, Auger processes, involving the scattering of delocalized electrons with the QD electrons, can take place thereby leading to energy relaxation [167]. The existence of continuum and wetting layer states [275], could also contribute to the relaxation processes and ameliorate the phonon bottleneck. Recent measurements with pump-probe spectroscopy have shown however that the leading mechanism responsible for masking the phonon bottleneck was actually electron-hole exchange scattering [233], and further demonstrated the existence of the phonon bottleneck when the electron-hole scattering is suppressed [354].

Single QD spectroscopy has also been realized, with high spatial resolution achieved through NSOM [115, 275] or micro-PL experiments [112]. These techniques were extended

to the study of SAQDs and supported the claim of true zero-dimensional and discrete nature of the density of states [132, 165, 226]. Single SAQDs have also been studied by mesa-etching of samples which have a low surface density of dots [360]. Most of the earlier studies with NSOM [207,275] or micro-PL [165,211,226] reported extremely large linewidths ($\sim 100 - 200\,\mu$eV) which however did not agree with the calculated dephasing rates of $\sim 1\,\mu$eV. On the other hand, photon echo measurements performed on ensembles of SAQDs were found to be in good agreement with the calculated values [320, 321]. The discrepancy in the PL experiments is due to the long integration times, which makes the measurement especially sensitive to the fluctuating charge backgrounds. In comparison, the photon echo measurement occurs within the timescale of the decoherence, and faster than the spectral diffusion time (see Reference [52] for a detailed explanation on how to measure the spectral diffusion with the photon-echo method). It was found that, under resonant excitation in small mesa-etched structures, spectral diffusion due to the fluctuating charge background could be suppressed, leading to extremely narrow homogeneous linewidths ($\sim 2\,\mu$eV) [359].

Due to the discrete nature of QD states, they also exhibit complicated fine-structure which has been the focus of many studies on single SAQD emission. Fine-structure splitting and linear polarization of the bright exciton doublet (due to exchange and dot anisotropy) have been observed [242, 279], as well as the dark exciton states [360]. The dependence on magnetic field, and the g-factors of excitons have been studied for different orientations of the magnetic field [242, 360]. Biexcitonic lines [201, 207, 221, 225], and their fine structure caused by exchange and Coulomb interactions [265] have been resolved. Applications of SAQDs that range from detectors [319] and lasers [153,160,187,188,296,335] to information storage [268] and hole-burning memories [234] have already been demonstrated.

1.2.2 Implementations of Quantum Dot Quantum Computing

We now consider the proposals and experiments in the field of QDQC, which have involved two complementary ideas. Proposals to perform QC with QD electron spins [228,261] take advantage of the fact that since spins are inherently immune to long-range Coulomb interactions with environmental electric fields, they have extremely long coherence times, and hence should be perfect candidates for qubits. In the spin based implementation proposed by Loss and DiVincenzo [228], the electron spin in a gated (electrostatically-defined)

QD is used as the qubit, with qubit rotations applied either by pulsed ESR fields, or an electrically gated tunnel barrier between the QD and a nearby ferromagnetic QD. Similarly, an exchange coupling of the Heisenberg form $\mathcal{H}_s(t) = J(t)\mathbf{S}_1 \cdot \mathbf{S}_2$ can be induced by gating the tunnel barrier between adjacent dots. The above interactions were analyzed by Loss and DiVincenzo and it was shown that a $\sqrt{\text{SWAP}}$ gate could be implemented which is also a universal logic gate. The question of the spin coherence times in QDs is still a matter of theoretical and experimental investigation, and will be considered in this thesis (see Section 3.4.1 and Section 5.2). Previous works on spin coherence through Faraday rotation techniques have measured lifetimes limited by inhomogeneous broadening (T_2^*) of upto 100 ns in n-doped bulk GaAs [223], and ~ 3 ns in n-doped ZnSe QWs [189]. The mechanisms of decoherence are, however, very different in higher-dimensional structures, as compared to QDs. A similar experiment with neutral CdSe QDs shows that exciton spin coherence, even though limited by recombination, can be as long as 3 ns due to the zero-dimensional confinement [258]. A recent measurement of the spin relaxation time, which ultimately limits T_2, gives $T_1 \sim 1$ ms in gated GaAs QDs [437].

In the optically driven implementations of QDQC, optical excitation generates excitons in neutral QDs, and the absence or presence of the exciton can be mapped onto the Bloch vector [107,270]. The qubit $|0\rangle$ ($|1\rangle$) is related to the Bloch vector pointing down (up). Proposals for quantum logic operations involve coupling the excitons in different QDs through dipole [122] or electrostatic interactions [283, 311]. As noted in Section 1.2.1.3, significant progress has been made with demonstration of single qubit rotations [336, 353, 369, 390], quantum entanglement [284, 318] and controlled logic gates [408].

Following naturally from this work, the alliance of ultrafast optical techniques and the long coherence times of electron spin has been proposed by Imamoğlu *et al.* for optically driven spin-based QDQC [261]. In that work, the authors embedded the CQD in a high-Q cavity, and used cavity photons to engineer an XY type interaction $\mathcal{H}_s(t) = J(t)(S_{1,x}S_{2,x} + S_{1,y}S_{2,y})$ between the electron spins, where $J(t)$ is related to the Rabi frequency of the cavity mode. It is possible using this interaction to engineer a conditional phase-flip gate that is extremely fast. Another option for a two-qubit universal gate is to implement controlled-NOT gates through the application of bias voltages to the QDs, thereby tuning the resonance frequencies to an applied laser field [273]. Further, single qubit rotations can also be implemented with off-resonant stimulated Raman transitions

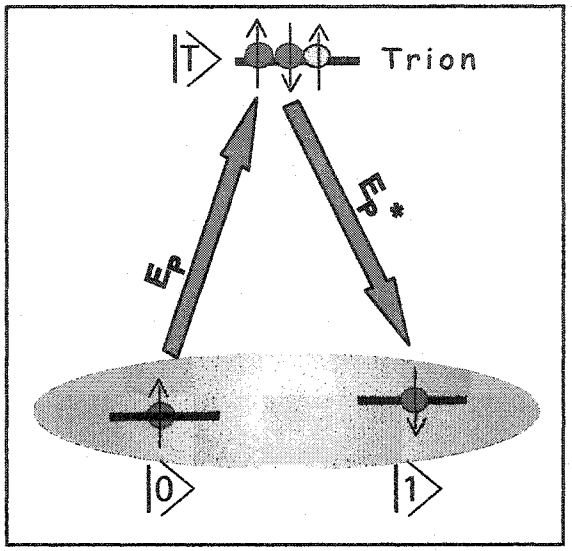

Figure 1.1: Proposal for optically driven spin-based quantum dot quantum computing. Simplified Λ energy level scheme for a single electron in a CQD, with optical excitation creating an intermediate trion state. Off-resonant Raman processes can be used to avoid populating the trion state, which would lead to undesirable decoherence.

to a charged exciton (trion) state as shown in Reference [292] (see Figure 1.1). A charged exciton is a three-particle electron-hole complex bound together by the Coulomb attraction between the particles. We will discuss charged excitons in great detail in this thesis, for example in Section 2.1.2 and Section 2.1.3. Optical control of the spin state in a dot by an adiabatic Raman process requires the laser fields to be detuned from the trion resonance [434]. The detuning is required to avoid populating the trion state, which can then lead to spontaneous emission and decoherence. Optical excitation of a continuum exciton state could also be used to coherently control the entanglement of electron spins in laterally separated CQDs. Piermarocchi *et al.* showed that the entanglement occurs through an RKKY type interaction which leads to a Heisenberg Hamiltonian similar to the one used by Loss and DiVincenzo [378]. Furthermore, by detuning from the resonance and pulse-shape engineering, an optically controlled two-spin $\sqrt{\text{SWAP}}$ gate can be implemented on ultrafast timescales.

Other ideas for controlled coupling between electron spins have also been proposed such as through Coulomb interactions between a vertically coupled quantum dot molecule [425]. In that work, if an electron in one of the dots (control qubit) is excited to a charged exciton state, the transition frequencies for the other dot are changed because of electrostatic

interactions and therefore one performs rotation based on whether the control qubit was 1 or 0. Pauli blocking has also been considered as a scheme for engineering the entanglement, whereby two laterally coupled dots interact through the dipole-dipole interaction between charged exciton states only if both the dots are occupied [399, 415]. The scheme utilizes the fact that a σ^+ laser field can excite the trion state $|\uparrow\downarrow\Uparrow\rangle$ only if the electron spin is in the state $|\uparrow\rangle$(Pauli blocking). Here $|\uparrow\rangle$ ($|\downarrow\rangle$) denotes electron spin up (down) and $|\Uparrow\rangle$ ($|\Downarrow\rangle$) denotes hole spin up (down). Another all-optical spin-based scheme involves coupling quantum dots directly through cavity photons, and utilizes the idea that logical qubits can be encoded in the state space of pairs of adjacent QDs [402]. The advantage of this coding is that it does not require single qubit rotations, and universal quantum computation can be carried out by two-qubit operations alone. This is an idea first proposed by DiVincenzo *et al.* [286], and requires approximately a factor of 3 more in number of devices and a factor of 10 more in computational steps. Later work by Lidar and Wu has shown how to reduce this requirement to a factor of only 2 more in the devices and a factor of 5 more in computational steps [374].

Another requirement for optical spin-based QDQC is the ability to perform state preparation and readout. A variety of schemes for initialization exist, such as allowing the electron spin to equilibriate in a large magnetic field at low temperature, applying local magnetic fields through gated interactions with nearby ferromagnetic dots [228], optically pumping an effective nuclear spin polarization that in turn polarizes the electron spin (Overhauser effect) [249, 405], or optical pumping through the trion state [420]. Spin-polarized currents can also be used for injection of a polarized electron into an empty dot which ties in with a large body of research in spintronics [456]. Read-out of the electron spin through electrical methods such as single-electron transistors was proposed [228], and has been experimentally demonstrated recently [437]. Other schemes involve spin filtering through leads attached to the dot that have different energy levels in an applied magnetic field, and thereby block certain spin states from tunneling [326, 417], or optical readout via the trion state combined with photon counting [365, 399, 420]. Spin-based quantum memories have also been proposed for the transfer of electron spin coherence into the nuclear spin state [423, 424], which has much longer decoherence lifetimes. Read out is performed either by experimentally demonstrated gate-voltage controlled interactions between the nuclear and electron spins [380, 442], or through optically induced AC stark shifts that bring the electron-nuclear

spin system into resonance [333, 405].

1.3 Thesis Outline

It is clear from the above discussion on optically driven spin-based QDQC that the intermediate trion state is crucial for the implementation. The trion dipole dephasing and decay times are important first measurements that are essential for progress towards implementing such proposals. Furthermore, as shown in References [292, 415, 420, 425], it is important to be able to resonantly access the optical transitions between the spin states and the trion states. Coherence between spin states may be optically induced at second order in the fields when both states are optically coupled to this common excited state (known as a Λ-energy level scheme), shown in Figure 1.1, and could be detected in the third-order polarization through ensemble measurements using, for example, photon echo techniques or homodyne-detected four-wave mixing (FWM) [215].

The focus of this thesis is the study of the resonant nonlinear optical response of trions in charged GaAs QDs. The experiments are motivated by the exciting possibility of coherent optical manipulation of single electron spins, for which it is important to understand the fundamental physics of trions in QDs. The thesis begins in Chapter 2 with an introduction to basic semiconductor theory of charged excitons in bulk and lower-dimensional semiconductor systems. The mechanism of modulation doping used to introduce electrons into the QDs is discussed, including the sample structure used for the experiments in this thesis. Finally, the results from PL experiments used to characterize the sample are presented.

It is essential for the optical approach to spin-based QDQC to characterize the transition from the spin state to the trion state both theoretically and experimentally. In Chapter 3, we discuss the selection rules for the transitions between the spin and trion states. As discussed earlier, Pauli blocking will prevent the absorption of light from the electron spin state $|\uparrow\rangle$ to the singlet trion state $|\uparrow\downarrow\Downarrow\rangle$, and these selection rules will be laid out from the point of view of the electromagnetic field interaction with the CQDs. The method employed to overcome the limitation of the vanishing dipole moment between these states, which is so essential for enabling stimulated Raman processes for qubit rotations, involves applying a magnetic field in the transverse direction. In the presence of the magnetic field, the CQD system corresponds closely to a four-level system with simple selection rules between the

states. The chapter concludes with a discussion of the various spin relaxation processes for electron spins in semiconductors, especially with respect to mobile and localized electron spins.

The resonant interaction between the electromagnetic field and matter leads to nonlinearities in the response. The fundamental tool used to analyze the outcome of this interaction, taking into account decay and decoherence, is the density matrix master equations that are introduced in Chapter 4. The method of the density matrix master equations allows us to compute the nonlinear optical signal that is expected in different experimental configurations such as differential transmission (DT), FWM and Faraday Rotation (FR). The experimental setup for both transient and frequency-domain nonlinear optical spectroscopy experiments will also be presented in this chapter.

Chapter 5 presents experimental studies using transient nonlinear spectroscopy to probe different parameters of the CQD system, such as the trion dipole decoherence and relaxation rates. Significantly, we will report on the coherent optical excitation of the electron spin coherence between the ground states of the CQD. The experimental data will show that the decoherence rate is at least an order of magnitude lesser for the spin than for the excitonic dipole (optical Bloch vector qubit) in neutral QDs. This important result shows that the spin state in a charged semiconductor QD is indeed viable as a qubit for optical implementation of QDQC. An unexpected and fascinating outcome of our experiment is the first observation of a vacuum field induced contribution to spin coherence from spontaneous emission of the trion state.

Chapter 6 will demonstrate that the spin coherence in the CQD can be controlled by a pair of phase-locked optical pulses. This is an important step towards showing that the spin coherence can not only be generated and detected by optical radiation, but also coherently manipulated. In a sense, these are the optical extension of ESR experiments that perform coherent manipulation of the spin polarization. We also demonstrate that by considering all the quantum-mechanical pathways for generation of the spin coherence, we can perform ultrafast optical control of the spin polarization.

Chapter 7 extends the study of the resonant nonlinear optical response of CQDs to a single QD regime. Single trions can be probed with frequency-stabilized continuous-wave (CW) laser fields, and an apertured mask allows us to spectrally and spatially select different CQDs from the inhomogeneous distribution. We shall show that the trion dipole transition

is indeed well modeled by a two-level system in the absence of magnetic fields, and that characteristic interference lineshapes due to coherent effects can be observed. Further, we demonstrate resonant optical access to the nominally forbidden transition from the state $|\uparrow\rangle$ to the trion state $|\uparrow\downarrow\Downarrow\rangle$, in the presence of a magnetic field. Finally, by coherent optical excitation with pulsed laser fields, we excite and detect the coherence of a single electron spin, and find that T_2 is not limited by the recombination of the trion dipole transition.

In Chapter 8, we conclude this work by discussing a few future directions such as electron spin state initialization and readout through optical methods, improving the measurements of the spin coherence time through either single QD techniques or Raman spin echo experiments and finally extending the weak-field spin polarization to perform complete coherent qubit rotations (spin Rabi oscillations). We also include two important theoretical results in the appendices. Appendix A demonstrates how the contribution to spin coherence can arise from the vacuum field that gives rise to spontaneous emission of the trion state. Appendix B shows how to analyze analytically the quantum interferogram created by finite bandwidth pump and control pulses in the coherent control experiment of Chapter 6, while including the inhomogeneous distribution of transition frequencies.

CHAPTER 2

Charged Excitons in Interface Fluctuation Quantum Dots : Basic Theory and Sample Structure

The discussion in Chapter 1 motivates a deeper examination of the nature of charged excitons in semiconductor QDs. In this chapter, the bandstructure of bulk GaAs is reviewed in Section 2.1.1 with particular attention to the crystal symmetry and its effects on the bandstructure as well as the effects of quantum confinement. The basic theoretical equations for the motion of charged excitons in bulk semiconductor materials are outlined in Section 2.1.2. The effect of lowering the dimensionality on the energy states of the charged excitons are then considered in Section 2.1.3. A brief review will also be given of the recent work on the physics of charged excitations in QW and QD nano-structures. The growth process and structure of the samples studied in this thesis as well as the aperture pattern on the sample surface are discussed in Section 2.2. Finally, we present some initial PL characterization experiments on the samples in Section 2.3.

2.1 Basic Semiconductor Theory

2.1.1 Properties of GaAs

The importance of GaAs as a semiconductor that empowers both opto-electronics applications and fundamental research cannot be overstated. The revolution in communication and information technologies that has occurred in the past few decades would not have been possible without key components like modulation doped field effect transistors (MODFET), solid state diode lasers and fast photodetectors that rely on GaAs. In this section, we devote some time to understand the essential features and properties of bulk GaAs. GaAs is

a direct band-gap semiconductor which crystallizes primarily in the zinc-blende structure, with a face-centered cubic (fcc) primitive lattice. The basis set of atoms in this structure consists of two elements, gallium and arsenic. The band-gap of GaAs at 0 K is 820 nm (1.519 eV) [338], and the unit cell constant is 5.6 Å at 300 K [324]. In the resulting crystal structure, each atom is surrounded by four nearest neighbours of the other species, forming a tetrahedron (similar to a methane molecule). The point group for GaAs, consisting of symmetry operations which leave the tetrahedron invariant, is denoted by T_d. The symmetry operations and multiplication table for T_d may be found in many standard texts on group theory in solids [22, 64, 191, 277].

The immediate consequence of the crystal symmetry is that the unit-cell components of the Bloch eigenfunctions can be expressed in a form such that they have definite transformation properties under the associated symmetry operations. To be exact, at the center of the Brillouin zone, the eigenfunctions must transform according to the basis functions that generate an irreducible representation of the point group. For GaAs, the topmost occupied band (the valence band), transforms according to the Γ_5 representation (Koster notation) and the lowest unoccupied band (the conduction band) transforms according to the Γ_1 representation. From the group-theoretical tables, one finds that the basis functions for the Γ_5 representation are $\{x, y, z\}$, which behave like the p-orbitals in atoms. This implies that under the symmetry operations of the group, the eigenfunctions in the valence band can be combined in such a manner that they will transform like eigenstates of the orbital angular momentum $\mathbf{l}$ with $l = 1$ given by $\{-(x + iy)/\sqrt{2}, (x - iy)/\sqrt{2}, z\}$. Likewise, the basis functions for the conduction band are similar to the s-orbitals ($\mathbf{l} = 0$). With the addition of spin, we may consider states of the total angular momentum $\mathbf{j} = \mathbf{l} + \mathbf{s}$. For $l = 1$ and $s = 1/2$, the eigenvalues of $\mathbf{j}$ are $j = 3/2$ and $j = 1/2$. For $l = 0$ and $s = 1/2$, the eigenvalue of $\mathbf{j}$ is $j = 1/2$. Thus, we have six degenerate states in the valence band and two degenerate states in the conduction band, in the absence of spin-orbit coupling. However, due to the spin-orbit interaction, there occurs a splitting of the states in the valence band, such that the $j = 1/2$ states are lowered by an energy Δ_0 compared to the $j = 3/2$ states. This is shown in Figure 2.1(a), with the magnitude of $\Delta_0 = 0.341$ eV for GaAs, an enormous number compared with the splitting due to quantum confinement or stress, and so we will always neglect the $j = 1/2$ states, known as the split-off (SO) band, from our considerations.

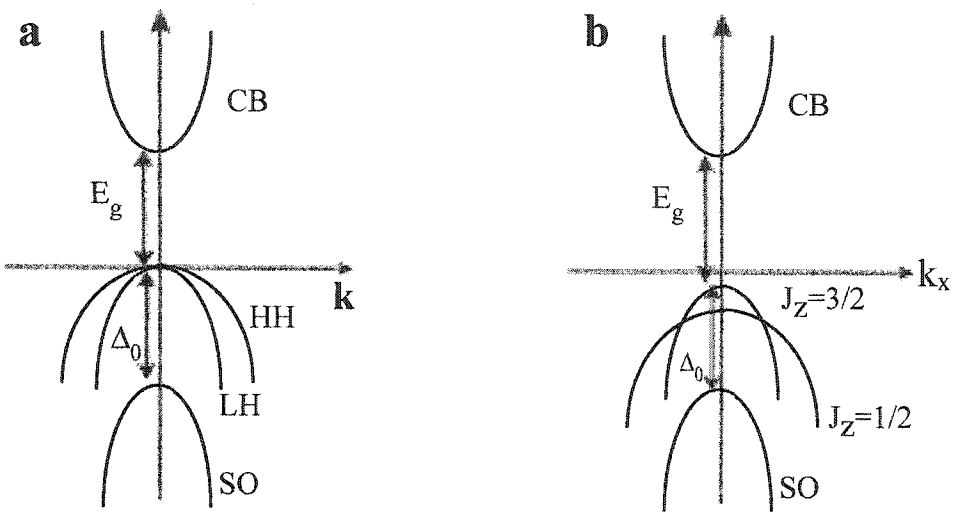

Figure 2.1: Bandstructure of bulk GaAs and the effect of quantum well growth. (a) The bandstructure of bulk GaAs along the direction [100], with the top filled valence bands energy taken to be zero. These bands correspond to the $j_z = \pm 3/2$ heavy hole (HH) and the $j_z = \pm 1/2$ light hole (LH) bands. The conduction band (CB) is higher in energy by the bandgap E_g. The $j = 1/2$ split-off (SO) band is lower in energy by $\Delta_0 = 0.341$ eV for GaAs. (b) The effect of quantum confinement along the [001] direction (taken to be the z-axis) on the bandstructure is shown. The energy versus wavevector in the k_x direction shows clearly that while the $j_z = \pm 3/2$ states are still heavier in the z-direction, they are lighter in the x-direction than the $j_z = \pm 1/2$ states. The band-gap is increased due to the quantum confinement.

The four remaining $j = 3/2$ states at zone-center are also broken up into $j_z = \pm 3/2$ heavy hole (HH) and $j_z = \pm 1/2$ light hole (LH) states, where the terms heavy (light) arise from the lower (higher) curvature of the band dispersions away from zone-center. The effect of quantum confinement, such as in a QW, on the holes may be seen by treating the QW potential as a perturbation to the $k = 0$ unperturbed states, and then by using the Luttinger Hamiltonian in the absence of a magnetic field [8],

$$H_{Lutt} = \frac{\hbar^2}{2m_0}\left[(\gamma_1 + \frac{5}{2}\gamma_2)k^2 - \gamma_2(\mathbf{k}\cdot\mathbf{J})^2 - 2\gamma_3(\{k_xk_y\}\{J_xJ_y\} + \{k_yk_z\}\{J_yJ_z\} + \{k_zk_x\}\{J_zJ_x\})\right] \tag{2.1}$$

where m_0 is the electron mass, $\gamma_1, \gamma_2, \gamma_3$ are the Luttinger parameters of the valence band and the symbols $\{\ldots\}$ represent anticommutators. In the simple spherical approximation, the last term in the Hamiltonian may be neglected.

Along a high-symmetry direction such as [001], the usual growth direction, the QW potential splits the HH and LH bands as shown in Figure 2.1(b), and the Luttinger terms will mix them for $\mathbf{k} \neq 0$ so that the terms heavy and light no longer have any meaning.

There is also crossing of the bands, which is removed when higher order terms in the Hamiltonian are taken into account. For our considerations near the zone-center, we may still use this terminology with the understanding that for the quantization axis along the growth direction, the heavy-hole bands are the $j_z = \pm 3/2$ states. Along the growth or confinement direction, the $j_z = \pm 3/2$ states have the heaviest mass, and therefore the smallest shift due to confinement. Hence, these states usually have the lowest transition energy in optical spectra. However, along the perpendicular directions the $j_z = \pm 3/2$ states have larger curvature, and are in fact *lighter* than the $j_z = \pm 1/2$ states, as can be verified from the Luttinger hamiltonian given above [46, 53, 54, 100]. It should be emphasized that this simple picture only holds along the high symmetry directions such as [001], and is much more complicated in case of growth along other directions. The application of uniaxial stress along high or low symmetry axes gives rise to similar results, with the stress axis playing an important role in determining the changes in the bandstructure. However, unlike the effects of QW growth, there is no crossing of the bands for the simple case of uniaxial stress along the [001] directions [14, 17]. In the remainder of this thesis, we shall restrict ourselves to only the heavy-hole states of the semiconductor.

2.1.2 Charged Excitons in Bulk Semiconductors

The ground state of a semiconductor at zero temperature consists of all the electrons in the valence band and none in the conduction band. In this simple picture, the Wannier exciton in direct band-gap materials is formed when an electron is promoted to the conduction band from the valence band leaving behind a hole in the electron sea. The Coulomb attraction between the electron and the hole leads to a bound state similar to a positronium atom which consists of an electron and positron. In view of the fact that even at zero temperature a semiconductor consists of over 10^{23} interacting electrons /cm^3 in the valence band, the positronium picture might initially seem naive and probably incorrect. Remarkably enough, it was shown by Sham and Rice in 1966 that one may replace the Schrödinger equation for the interacting electron gas by an effective mass equation for quasi-electron and quasi-hole particles moving in a dielectric [16]. This dramatic simplification allows us to understand and predict properties of the Wannier exciton such as binding energy, Bohr diameter and absorption oscillator strengths using the well-known quantum-mechanical solutions to the

positronium atom problem.

In this work, we are concerned with both neutral and charged excitons. The charged exciton (trion) can be formed by the addition of an extra electron (negative trion X^-) or extra hole (positive trion X^+) to the exciton, in analogy with H^- and H_2^+ ions, as first predicted in 1958 by Lampert [12]. We are primarily interested only in the negative trion in this thesis which we will denote by either T or X^-. The ground state of the semiconductor in this case can be viewed as having every electron still in the valence band, and a single electron in the conduction band. If an electron is now excited to the conduction band from the valence band, we must consider the Coulomb attraction between the two electrons in the conduction band and the hole left in the valence band. The binding energy of the trion, which is defined as the exciton energy minus the trion energy, must be positive for the trion to be stable against dissociation into an exciton and an electron.

The theoretical basis for charged excitons in three dimensions builds on the excitonic work, which is reviewed in [15, 40]. For the negative trion, we can write the trion wavefunction as a linear combination of the electron and hole Bloch wavefunctions,

$$\Psi(\mathbf{r}_{e1}, \mathbf{r}_{e2}, \mathbf{r}_h) = \sum_{\mathbf{k}_{e1}, \mathbf{k}_{e2}, \mathbf{k}_h} \Phi(\mathbf{k}_{e1}, \mathbf{k}_{e2}, \mathbf{k}_h) u_c(\mathbf{k}_{e1}, \mathbf{r}_{e1}) e^{i\mathbf{k_{e1}}\cdot\mathbf{r_{e1}}} u_c(\mathbf{k}_{e2}, \mathbf{r}_{e2}) e^{i\mathbf{k_{e2}}\cdot\mathbf{r_{e2}}} u_v(\mathbf{k}_h, \mathbf{r}_h) e^{i\mathbf{k_h}\cdot\mathbf{r_h}} \tag{2.2}$$

where the expansion coefficients $\Phi(\mathbf{k}_{e1}, \mathbf{k}_{e2}, \mathbf{k}_h)$ are functions of the wave-vectors $\mathbf{k}_i$, and position vectors $\mathbf{r}_i$, where $i = e1, e2, h$ denotes the three charge carriers. This wavefunction is governed by a Schrödinger equation which takes into account both the infinite crystal potential as well as the attraction between the charges. The task of solving such an equation is certainly daunting. To make any progress, we will have to assume that the wavevectors in the summation come from a small range around the zone-center. This in turn indicates that the trion wavefunction must be large compared to the dimensions of a unit cell for the assumption to be valid. Within this envelope function approximation (EFA), the unit cell components of the Bloch wavefunctions (u_c and u_v) must be slowly varying compared to the exponential terms. This allows us to take u_c and u_v out of the sum, and replace them by their values at the zone center. To be self-consistent, we must check the validity of the approximation at the end by showing that the dimension of the wavefunction is much larger than the unit cell size. Thus we get,

$$\begin{aligned}\Psi(\mathbf{r}_{e1},\mathbf{r}_{e2},\mathbf{r}_h) &\approx u_c(0,\mathbf{r}_{e1})u_c(0,\mathbf{r}_{e2})u_v(0,\mathbf{r}_h)\sum_{\mathbf{k}_{e1},\mathbf{k}_{e2},\mathbf{k}_h}\Phi(\mathbf{k}_{e1},\mathbf{k}_{e2},\mathbf{k}_h)e^{i\mathbf{k_{e1}}\cdot\mathbf{r_{e1}}}e^{i\mathbf{k_{e2}}\cdot\mathbf{r_{e2}}}e^{i\mathbf{k_h}\cdot\mathbf{r_h}} \\ &= u_c(0,\mathbf{r}_{e1})u_c(0,\mathbf{r}_{e2})u_v(0,\mathbf{r}_h)\Xi(\mathbf{r}_{e1},\mathbf{r}_{e2},\mathbf{r}_h) \qquad (2.3)\end{aligned}$$

where

$$\Xi(\mathbf{r}_{e1},\mathbf{r}_{e2},\mathbf{r}_h)=\sum_{\mathbf{k}_{e1},\mathbf{k}_{e2},\mathbf{k}_h}\Phi(\mathbf{k}_{e1},\mathbf{k}_{e2},\mathbf{k}_h)e^{i\mathbf{k_{e1}}\cdot\mathbf{r_{e1}}}e^{i\mathbf{k_{e2}}\cdot\mathbf{r_{e2}}}e^{i\mathbf{k_h}\cdot\mathbf{r_h}} \qquad (2.4)$$

is the *trion envelope function.* The effect of the crystal potential on the motion of the electrons and holes can be accounted for by using an effective mass, corresponding to the curvature of the conduction and valence bands near the zone center, in the Schrödinger equation. The Hamiltonian for this Schrödinger equation is given by,

$$H_{X^-}=\frac{\mathbf{p}_{e1}^2}{2m_e^*}+\frac{\mathbf{p}_{e2}^2}{2m_e^*}+\frac{\mathbf{p}_h^2}{2m_h^*}+V_{X^-} \qquad (2.5)$$

and V_{X^-} is the interaction potential given by

$$V_{X^-}=-\frac{e^2}{\epsilon}\left(\frac{1}{|\mathbf{r}_{e1}-\mathbf{r}_h|}+\frac{1}{|\mathbf{r}_{e2}-\mathbf{r}_h|}-\frac{1}{|\mathbf{r}_{e1}-\mathbf{r}_{e2}|}\right) \qquad (2.6)$$

where ϵ is the dielectric constant of the semiconductor, m_e^* and m_h^* are the effective masses of the electron and hole, and $\mathbf{p}_i, i=e1,e2,h$ are the conjugate momenta for the charges.

We now consider the transformation to relative coordinates for the three-body system of the charged exciton. This is done by the following set of definitions,

$$\mathbf{R}_{CM} = \frac{m_h^*\mathbf{r}_h+m_e^*\mathbf{r}_{e1}+m_e^*\mathbf{r}_{e2}}{M} \qquad (2.7)$$

$$\mathbf{r} = \mathbf{r}_{e2}-\mathbf{r}_{e1} \qquad (2.8)$$

$$\mathbf{R} = \frac{1}{2}(\mathbf{r}_{e2}+\mathbf{r}_{e1})-\mathbf{r}_h \qquad (2.9)$$

where $\mathbf{R}_{CM}$ denotes the center of mass (CM) coordinate, $\mathbf{r}$ is the relative separation between the two electrons, $\mathbf{R}$ is the coordinate of the hole measured from the CM of the two electrons and $M=2m_e^*+m_h^*$ is the total mass of the trion.

It can be shown that under this transformation, the motion of the center of mass is separable from the motion of the relative coordinates [58, 198, 199],

$$\Xi(\mathbf{r},\mathbf{R},\mathbf{R}_{CM})=\psi(\mathbf{R}_{CM})\varphi(\mathbf{r},\mathbf{R}) \qquad (2.10)$$

and in the case of a bulk semiconductor, the CM motion and the relative motion are governed by the following equations,

$$-\frac{\hbar^2}{2M}\nabla^2_{\mathbf{R}_{CM}}\psi(\mathbf{R}_{CM}) = E_{CM}\psi(\mathbf{R}_{CM}) \quad (2.11)$$

$$\left(-\frac{\hbar^2}{2\mu}\nabla^2_{\mathbf{r}} - \frac{\hbar^2}{2M_0}\nabla^2_{\mathbf{R}} + V_{X^-}\right)\varphi(\mathbf{r},\mathbf{R}) = E_R\varphi(\mathbf{r},\mathbf{R}) \quad (2.12)$$

where $\mu = m_e^*/2$ is the effective mass of the two electrons, and $M_0 = 2m_e^*m_h^*/M$ is the effective mass of both electrons and the hole. The Coulomb interaction in this coordinate system is given by

$$V_{X^-} = -\frac{e^2}{\epsilon}\left(\frac{2}{|2\mathbf{R}+\mathbf{r}|} + \frac{2}{|2\mathbf{R}-\mathbf{r}|} - \frac{1}{|\mathbf{r}|}\right) \quad (2.13)$$

The solutions to the CM equation are plane waves given by $\exp(i\mathbf{K}_{CM}\cdot\mathbf{R}_{CM})$, with energy $\hbar^2\mathbf{K}^2_{CM}/2M_0$. The plane wave implies that trions can be found anywhere in the crystal, or we can construct a wave packet by mixing a range of $\mathbf{K}_{CM}$. However, the tiny wave vector of light means that $K_{CM} \approx 0$ for optically generated trions and the motion of the center of mass can be ignored. The equation for the relative motion is not analytically tractable even in the bulk material case where there are no confining potentials. This adds a degree of complexity, as compared to neutral excitons, when trying to estimate the binding energy, Bohr diameter or absorption oscillator strength of the trion. For example, from the exciton work, it is well known that the excitonic binding energy which is defined as the energy difference between the exciton ground state and the bulk is on the order of 4.7 meV in bulk GaAs. Solution of the trion equation is only possible through numerical methods, such as variational approaches using trial wavefunctions to predict the binding energy [72]. The binding energy for trions in bulk GaAs was predicted to be extremely small (0.17 meV). This and other complexities in the measurements of bulk properties complicated the observation of trions in bulk semiconductors which was not made for nearly 30 years after they were first predicted [29, 32]. The wavefunction of a trion in bulk Ge was estimated as nearly 50 % larger than the exciton wavefunction [32], again indicative that they are weakly bound relative to the exciton.

2.1.3 Charged Excitons in Quantum Wells and Quantum Dots

We saw in Section 2.1.2 that the equation of motion for the relative coordinates cannot be easily solved even for bulk materials. Additional confinement naturally increases

the complexity of the problem to be solved. The effect of quantum confinement will be discussed only in very general terms here. It is known from the work on excitons, that separation of variables into CM and relative coordinates is possible only in the planar directions when the exciton is confined in a quantum well [38]. As before, we may ignore the CM motion in considering the energy. The confinement in the growth direction (the z-direction) is comparable to the Coulomb attraction between the electron and hole and now affects the relative motion of the exciton. A complete solution is possible through a variational approach, as described in [38, 42, 61]. For a strictly two-dimensional exciton, it can be shown that the binding energy in the ground state increases by a factor of four [89]. We may similarly expect that for charged excitons, the binding energy increases although the exact amount by which it increases varies depending on the numerical treatment and the semiconductor material. For lower dimensional systems, it was predicted that the binding energy should be larger [66, 72], because of the greater overlap between the electron and hole wavefunctions. For a strictly two-dimensional trion, Stebe and Ainane predicted that the binding energy would increase nearly ten times, to 2.3 meV in GaAs [72]. Their initial work did not take into account finite well width effects which should decrease the binding energy, as shown in later works [177, 198, 237, 287]. The theoretical calculations showed that in wide GaAs QWs, the trion binding energy is around 1.2 meV, which agrees well with experimental data [127].

In a modulation-doped QW, where the barriers are doped with shallow donors, electrons can transfer into the well layers to form a two-dimensional electron gas (2DEG). The spatial separation of the donors from the 2DEG using spacer layers is responsible for the extremely high mobilities that have been observed [89]. Control of the density in the well layers is possible through (a) controlling the density of the dopant or (b) application of voltages on the gate electrodes deposited on the surface of the sample. As the electron density is lowered in the wells, metal-insulator transitions were observed to occur in the conductivity. Optical experiments performed close to these densities showed the presence of sharp spectral lines that have been attributed to trions, for the first time in CdTe modulation-doped QWs [105]. This was followed up by work in GaAs QWs [127], and the positively charged exciton as well as the spin-triplet charged exciton states were also observed [139, 140]. The existence of bound states of electron-hole complexes in the presence of screening by the 2DEG was the subject of some controversy. Combining the techniques of PL spectroscopy

and near-field microscopy [127, 213] in gated GaAs/AlGaAs wide QWs, these issues were addressed in great detail. It is now believed that at the low carrier densities of the 2DEG in these QWs, localization of carriers occurs in the wells due to fluctuations in the electrostatic potential caused by ionized impurities in the barriers, reducing their effectiveness in screening the Coulomb interaction, and allowing formation of both excitons and trions. FWM measurements on trions in II-VI materials [248, 256] also tend to support these arguments. Recently, however, researchers have succeeded in observing the drift of free negative trions with electric fields in high quality GaAs samples [350]. The difficulty of distinguishing between X^+, X^- and donor-bound excitons is usually solved by relying on the binding energy behaviour, or the dependence on doping density. Shakeup processes also provide a very effective method of distinguishing the various species [154, 331]. Shakeup processes occur in a magnetic field when the electron and hole recombine and, instead of leaving behind the other electron in the ground state, the electron is left in a higher excited Landau level which is separated by energy $n\hbar\omega_c$, where ω_c is the cyclotron frequency.

Further confinement in the lateral dimensions leading to quantum wires and QDs will be treated only qualitatively in this section because of the additional complexities introduced into the trion properties in such nanostructures. We draw once again from the excitonic case wherein depending on the relative strengths of the confinement in the different directions, it is still possible in some limits to consider the CM motion separately from the relative motion. The approximation can be made in the "weak-confinement" regime, where the relative wavefunction of the exciton is smaller than the dimensions of the fluctuations in the quantum well potential. Disordered potentials in two-dimensional systems have been investigated for several decades and the topic of localization through the disorder mechanism is a subject of ongoing research [10,35,39,48,85,161]. Localization through disorder proceeds primarily through two mechanisms : Anderson localization and "box" localization. In the former type, the disorder length scale is much smaller than the particle wavefunction leading to localization arising from destructive interference between the scattering amplitudes from the potential. Without disorder, the excitons would be delocalized, and the strength of the localization depends on the transition energy, leading to the mobility edge that has been observed [43]. The localization is dependent on the phase of the wavefunction and could be destroyed by the action of magnetic fields that can perturb the phase. When the disorder length scale is comparable to or greater than the wavefunction diameter, we get localization

akin to that for a particle in a box, giving rise to zero dimensional confinement similar to that found in nanocrystals and SAQDs (see Section 1.2.1). Alternatively, for excitons, we may consider that box localization occurs when the potential strength is comparable to or weaker than the Coulomb attraction between the electron and hole. All of these considerations apply also to charged excitons, and "box" localization will occur when the fluctuations in the potential have a length scale on the order of the size of the trion. As in the excitonic case, we then consider that the fluctuations lead to a quantization of the CM motion in the plane, while leaving the relative motion unchanged.

The IFQDs, which are the subject of this thesis, are formed by monolayer (ML) fluctuations in the plane of a narrow QW. Figure 2.2(a) is a schematic depiction of the QW interface after two minute growth interruption (under steady As flux) of a narrow GaAs QW surface. In the figure, plateaus of thicker ML deposition lead to islands wherein the bandgap energy is lower, and excitons and trions can be confined by "box" localization. PL and PLE experiments on neutral IFQDs revealed sharp lines with excited state structure in the spectra, confirming that "box" localization does indeed occur [91, 113, 128, 155, 156]. Further evidence of confinement is shown in Figure 2.2(b), which is a NSOM image obtained using nonlinear spectroscopic probing from a sample with IFQDs. The peak in the figure represents a mapping of the CM wavefunction, indicating localization of the exciton in this region [332]. The strength of the lateral potential is $\sim 8 - 10$ meV for a 4.2 nm QW, as found from the splitting between the different ML regions in the PL spectra (Section 2.3). The simple picture of localized excitons in the larger ML regions is believed to hold, especially for states in the lower energy range of the spectrum. However, it was found that the excitons in the smaller ML regions are probably weakly localized as well due to the Anderson mechanism, and that there are delocalized states in the larger ML regions [253].

Most of the work on charged excitons in QDs has been carried out using self-organized III-V QD structures, although recently trions have been reported in II-VI QDs [361], and in type-II Ge/Si QDs [357]. Theoretically, charged excitons were expected to have even larger binding energy in QDs, as shown by the calculated binding energies for nanocrystals (~ 5.7 meV) [66]. The binding energy in SAQDs is highly dependent on the species of trion as well as the composition, size and the shape, with X^- and X^+ showing opposite binding behaviour for InGaAs spherical or cone-shaped dots [163]. Using capacitance spectroscopy, Coulomb blockade effects were observed in charged InGaAs SAQDs as the dots were sequentially

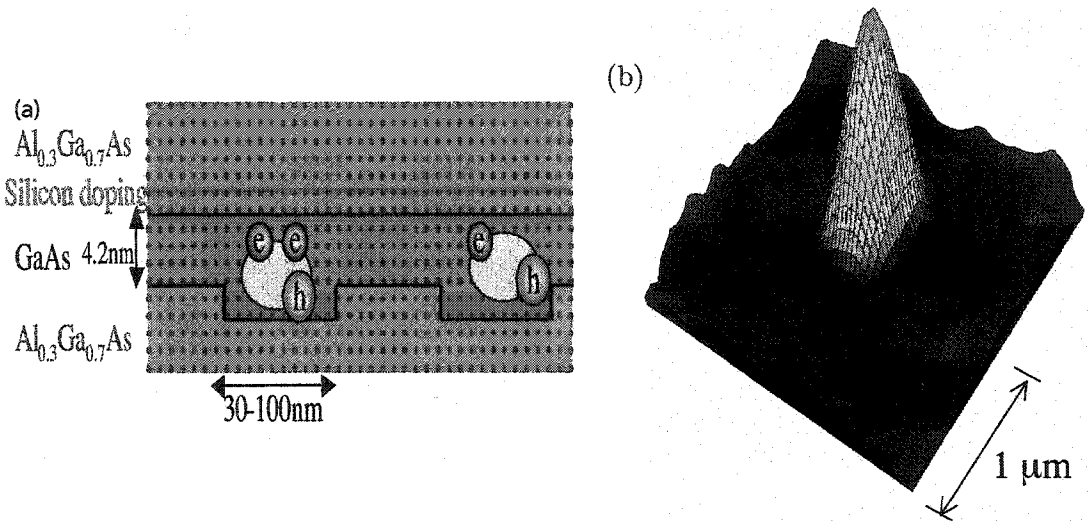

Figure 2.2: Localization due to interface fluctuations: Model and NSOM images. (a) shows a schematic representation of localization at the surface of a growth-interrupted 4.2 nm quantum well. An area with 15 MLs will have lower bandgap energy, compared to a 14 ML region, thus confining the excitons and trions laterally [155]. (b) shows a low temperature NSOM image obtained through nonlinear spectroscopy from a sample with neutral IFQDs. The peak in the figure represents a mapping of the CM wavefunction, showing localization of the exciton in this region. This figure is taken from Reference [332].

loaded with electrons [315]. PL spectroscopy on these single dots reveals the formation of X^-, X^{2-} and higher bound states accompanying the charging of the dots. The X^- binding energies have been reported as varying between 4.5–6 meV in most InGaAs SAQD structures [315,328,329], which is comparable to theoretical calculations yielding around 3–5 meV [144, 163, 383, 394]. Much higher binding energies of upto 22 meV have been observed in CdSe/ZnSe SAQDs [414] and CdTe SAQDs [361], due to the different semiconductor parameters such as the effective masses of the electrons and holes.

QDs that are charged with multiple electron-hole pairs were shown to possess statistical properties identical to a quantum light source of different emission energies [347]. The anti-bunching of photon emission from such nanostructures demonstrates the quantum nature of the trions captured in the QDs. Hartmann *et al.* have studied GaAs/AlGaAs QDs formed by epitaxial growth on patterned substrates, and have been able to observe multicharged excitonic states by controlling the electron density using above band-gap excitation [289]. Multi-charged excitons were shown to be highly sensitive probes of the electron-hole exchange interaction, without the need to apply strain or magnetic fields, because of the differences in pairing of electrons [427]. Near field microscopy on CQDs has also shown

that photoexcitation above the barrier can result in capture of electrons in the QD through relaxation mediated by acoustic and optical phonons, and diffusion [329,375].

Temperature mediated charging effects, wherein negatively charged QDs are created as the temperature is increased, can occur in SAQDs [337]. Because of the increase in the relaxation rate of photo-created excess carriers into the QDs as the number of phonons becomes larger with temperature, the temperature increases the probability of charging the QD, as does non-resonant excitation [329]. The issue of distinguishing X^+ and X^- trions is also problematic because the large inhomogeneous linewidth makes it difficult to separate them into two groups based on the lines observed in far-field PL. However, it is possible, by a careful study of the magnetic field behaviour [360], as well as through the different degrees of circular polarization in a Faraday magnetic field [361,433], to separate the X^- and excitons. CQDs that are formed in interface fluctuations can be separated in the far-field PL because of the narrow inhomogeneous distributions.

The dynamics of charged excitons have been investigated, and it was found that in CdSe SAQDs, the trion population decay time was comparable to the exciton decay time [414]. However, spin flip relaxation processes from the excited state to the ground state (*i.e.* triplet to singlet transitions) were found to be highly suppressed ($\tau_s \geq 200\,\mu$s) due to the Pauli blocking [367] in comparison to exciton spin-flip processes that are mediated by the exchange interaction. Rabi oscillations of the positive trion state in InGaAs SAQDs have been observed through resonant excitation of a higher excited state and detection of the PL from the positive trion state [393]. Recently, a charged SAQD was also found to exhibit correlations with the extended sea of electrons nearby, forming a hybridized state through phonon emission that could give rise to Kondo-like many-body effects [443]. Thus, charged excitons are an interesting multi-carrier complex capable of revealing new phenomena at the boundary of meso- and microscopic physics. The fact that they couple to a ground state that contains a single electron spin makes them especially attractive for our work.

2.2 Sample Structure and Growth

In this thesis, two samples, R990912F (henceforth referred to as 912F) and R010612F (referred to as 612F), provided by Dr. Allan S. Bracker at the Naval Research Laboratory were investigated. The sample structure and doping density are identical for the two sam-

ples. The growth was by means of MBE on a GaAs (001) substrate. The samples consisted of a GaAs buffer layer followed by five GaAs QWs of varying width (nominally 2.8, 4.2, 6.2, 8.5 and 14.2 nm) separated by 50 nm $Al_{0.3}Ga_{0.7}As$ barriers each containing a thin (3 nm) section doped with Si atoms at a distance of 10 nm from each well. The last barrier layer is followed by a 5 nm GaAs cap. The sample structure, as grown on the substrate is shown in Figure 2.3 (a). The carrier doping density in the barriers during growth was set to $\sim 3 \times 10^{10}$ cm^{-2}.

Growth interruptions at the interfaces lead to the formation of ML high islands which localize excitons and trions in the QD potentials, as discussed in the previous section. Figure 2.3 (b) shows the pattern of apertures that is opened using electron-beam lithography on a thin Aluminum mask (50 nm in thickness) laid down on the sample surface. The sub-micron diameter apertures occur in rows 2 through 8.

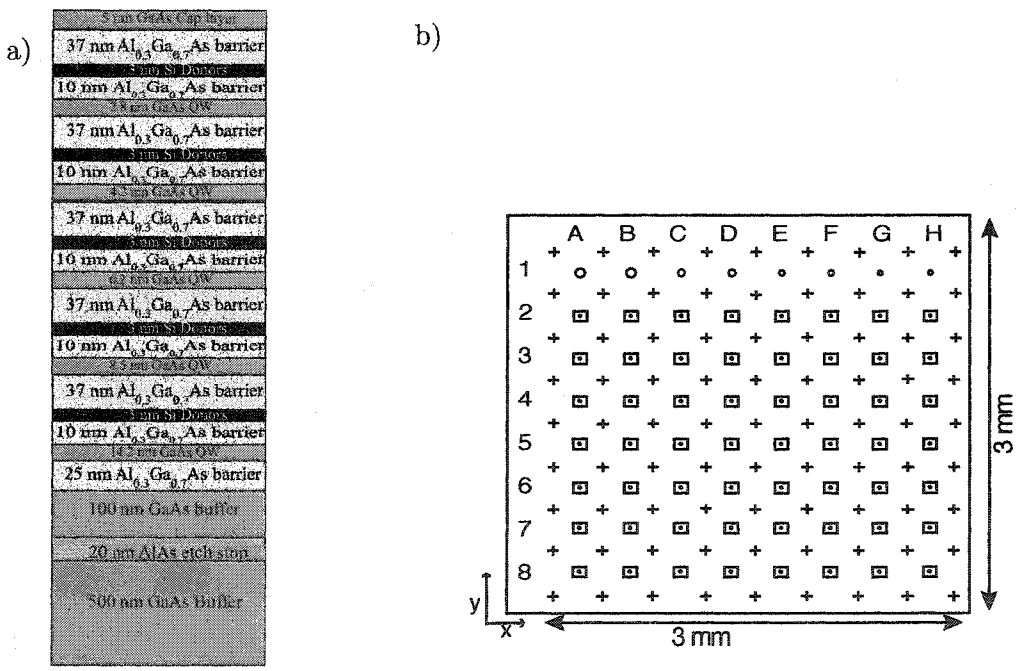

Figure 2.3: Sample structure and mask pattern. (a) The layers above the substrate in the sample structure are shown here. The important features are the five GaAs QWs with modulation doped barriers. The orange layers indicate GaAs, the blue layers are $Al_{0.3}Ga_{0.7}As$ and the black layers denote $Al_{0.3}Ga_{0.7}As$ with Si doping. (b) The aperture pattern on the samples is shown here. Row 1 contains large apertures of diameter 25 μm (A,B), 10 μm (C,D), 5 μm (E,F) and 2 μm (G,H). The rows below have apertures of diameter 710 nm, 690 nm, 700 nm, 678 nm, 464 nm, 428 nm and 439 nm respectively. The boxes around the apertures in the figure are there merely for the reader's convenience, and not on the actual sample.

The process of charging will be discussed now. The method used to charge the QDs

in the samples discussed in this thesis is through modulation doping. This method was first pioneered by Dingle and co-workers [33]. Essentially, the idea is to introduce electron donors in the barrier layers at a distance from the QW or QD that one wishes to dope as illustrated in Figure 2.2. Because the well (dot) forms a dip in the energy landscape of the heterostructure, the electrons donated by the dopant atoms tend to accumulate in the well(dot). The formation of a high density of mobile charge carriers without the associated large scattering rates that arise from the presence of dopant atoms has been used in QWs to produce mobilities as high as $10^6\,\mathrm{cm^2V^{-1}s^{-1}}$. Such high mobilities enable the MODFET and metal-oxide-silicon field effect transistors (MOSFET) that have revolutionized the computer and communication industries. Our interest here arises from the fact that this technique may be used to introduce electrons into the QDs formed by interface fluctuations without putting dopant atoms in the QD layer that might result in non-radiative recombination and poor optical quality of the samples. For this work, we will be working with lightly doped samples which will result in only a fraction of the dots being charged. The light doping is done as a precaution against state filling in the QDs that will mitigate against optical absorption. The effect of remote donors, that happen to be localized directly above a QD, on the excitons is a matter that deserves some investigation, however it is beyond the scope of this work. We shall not comment further on the effect, except to note that it should be small because the wavefunction of the exciton does not penetrate very far into the barrier layers, due to the strong confinement in the growth direction.

The band diagram of the sample as calculated from the grown sample structure is shown in Figure 2.5. The data is obtained through a self-consistent solution to the one-dimensional Poisson equation using the method of finite differences[1]. The most important parameter for the calculation is the density of dopant atoms, which was taken to be $N_d = 10^{17} cm^{-3}$ as calculated from the sheet density of dopants incorporated. The other important consideration to keep in mind for modelling the band diagram is the surface boundary condition. Since the sample was etched, the surfaces on both sides have an enormous number of dangling bonds, or surface states as they are known in the literature. The

[1]The numerical solution is performed by the routine "1D-Poisson/Schrödinger " written by Prof.Gregory Snider (Dept. of Electrical Engineering, Notre Dame University). The program is capable of also taking into account the Schrödinger equation for one of the wells if the exact quantum mechanical wavefunction is to be calculated.

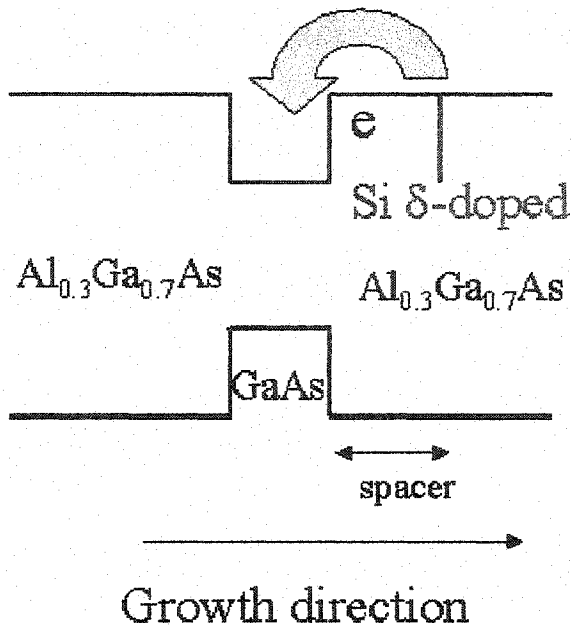

Figure 2.4: Illustration of the modulation doping process. Electrons donated by the Silicon atoms located in the barrier will tend to accumulate in the lowest energy region of the heterostructure such as the QDs or QWs. This leads to large carrier charge densities in the QW or QD without the accompanying scattering from the large Silicon ions.

rearrangement of the surface atoms to appropriately minimize the free energy leads to the formation of these surface states, which clamp the Fermi energy to be at approximately mid-bandgap ($\sim$ 0.7 eV for GaAs) unless the surface states are completely filled. For moderate doping levels, the Fermi energy therefore is far below the states in the QDs that are formed in the narrow QWs by the growth interruption process, as shown in Figure 2.5. In this equilibrium picture then, there are no electrons in the QDs. However, when the sample is illuminated by light, electrons appear to be introduced into the QDs, as will be seen in the subsequent section.

Three pieces of the apertured sample (referred to as 912F-2A, 612F-2A and 612F-3A) will be used for experiments at the single QD level, as described in Chapter 7. An unapertured piece of sample 612F (referred to as 612F-3NA) was also used for ensemble PL experiments described in Section 2.3 and for nonlinear spectroscopy measurements in Chapter 5 and Chapter 6.

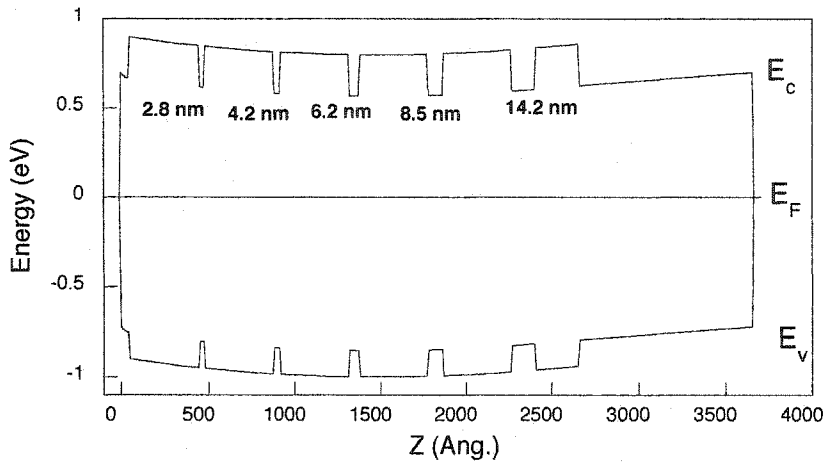

Figure 2.5: Calculated energy level structure for the etched, unapertured sample. A numerical solution to the one-dimensional Poisson equation was performed. The labels E_c, E_v and E_F stand for the conduction band, valence band and Fermi energy levels. The positions of the various QWs grown in the structure are marked as shown. The position of the Fermi level below the bandgap indicates that we do not have electrons in the QDs in the absence of any light on the sample.

2.3 Sample Characterization : Ensemble Photoluminescence Spectra

For the PL and nonlinear spectroscopy measurements, the sample 612F-3NA was mounted on a c-axis cleaved sapphire disk, and the substrate removed first through mechanical lapping, and then through a chemical etch. The etching solution consists of 6 ml H_2O_2 (30 % concentration) and 500 ml NH_4OH mixed together and maintained at 10° C. The sample after etching had a smooth, high optical quality surface. PL spectra were obtained by exciting the sample with laser radiation from either an Argon-ion laser or a Coherent model 699 dye laser operating at 1.738 eV. The PL is collected and dispersed through a 0.75 m double grating monochromator, and detected by a liquid nitrogen cooled charge coupled device (CCD). The measurements shown here were conducted in a continuous flow liquid helium cryostat (Janis model 8CNDT) at a temperature of 5 K, unless otherwise mentioned.

The spectrum obtained in Figure 2.6(a) shows the PL emission from all the QWs. While trion and exciton lines can be barely resolved in the other QWs, the 4.2 nm QW displays clear evidence of trion formation. The data shown in Figure 2.6(b) and (c) are from the 15 and 14 ML regions of the 42 Å QW. The spectral feature denoted by X^- is assigned to trions, localized by the interface fluctuation potential in the 15 and also in the 14 ML regions of the well. We can make this assignment on the basis of several

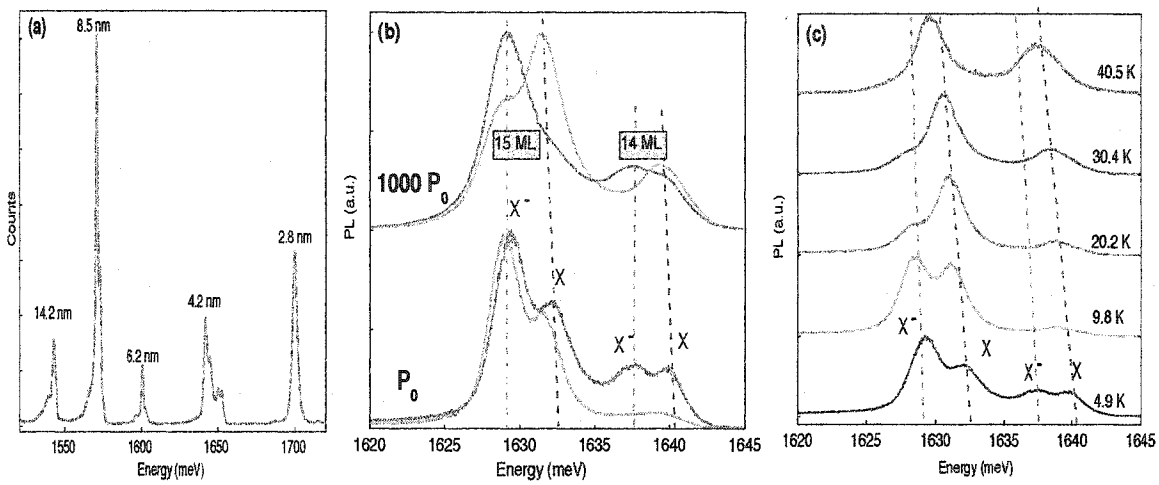

Figure 2.6: PL spectra from the unapertured sample. (a) PL spectrum displaying emission from all the QWs, with the 699 dye laser used as the exciting source. (b) PL spectra of the 4.2 nm QW for different excitation powers, using both Argon-ion laser (green) and 699 dye laser tuned to 1.738 eV (red), $P_0 \sim 2.6$ W/cm^2. (c) PL spectra as a function of temperature from the same well, using the 699 as the excitation laser.

observations from the data. The separation between the two peaks obtained by curve-fitting to double-Gaussian functions is 2.7 ± 0.1 meV, which is equal to the binding energy of the trion. In wider GaAs/AlGaAs QWs, binding energies for the negatively charged exciton have been reported as 1.2 meV [127, 384]. Clearly, the trion binding energy in the QDs is significantly larger than these reports in the QW, as expected due to the increased quantum confinement [66, 144, 163, 351, 383, 394]. Furthermore, we claim that this is not an exciton formed by binding to a neutral or charged donor in the dots (D^0X and D^+X), because to the best of our knowledge, the binding energy of such complexes for a 4.2 nm well is at most 1.3 meV [69, 212]. The linewidth of PL emission from donor bound excitons is governed by the Coulomb interactions with nearby donors, rather than the QD potential, and hence the large inhomogeneous broadening observed in our data also suggests that the peak is due to X^-. We characterized the power dependence and found the PL intensity grew linearly with the power for low powers (data not shown) and so the resonance is not due to a biexciton. PL and CW nonlinear spectroscopy through small apertures has also shown narrow resonances (to be discussed in Chapter 7), indicating that the doping level is not high enough to create a Fermi sea of electrons in the QWs leading to Fermi edge absorption singularities. It has also been observed that as the remote doping density is increased in

different samples, the trion peak increases in intensity, implying that the creation of X^- in the sample is not an effect of background doping [362, 398].

Figure 2.6 (b) shows the variation in the PL intensities of the peaks depending on the excitation above or below the AlGaAs barrier bandgap. While we do not fully understand the reasons for the wide range of intensity variations as a function of well width and laser wavelength below the barrier bandgap, X^- dominates at the lower intensities of "green" excitation as shown in Figure 2.6 (b). This behaviour has been observed in the literature and has been explained as due to efficient charging of the QDs when the green laser creates electron-hole pairs in the barrier layers throughout the sample. As the excitation intensity of the above-barrier laser is increased, the electron and hole pairs formed can separate due to local electric fields and can migrate and neutralize partly-ionized donors or acceptors and trapped carriers. This will lead to lower density of electrons in the QD region and hence lower intensity of the trion peak as observed. The trapping of electrons in surface states is largely responsible for depleting the charge densities in the well layers in the absence of light. Photo-created excess holes can combine with trapped surface electrons, leading to a band levelling effect and repopulating the quantum wells more efficiently with electrons [114, 158, 289]. Thus, the formation of trions under these non-equilibrium conditions is an indication of the fact that electrons do migrate into the QDs, as opposed to the equilibrium calculations presented in Section 2.2. While it is difficult to understand how photo-induced changes can lead to such a large redistribution of the carriers that the Fermi level moves close to the conduction band edge, it is possible that a more complete calculation of the energy level structure shown in Figure 2.5 needs to be made. Because it is difficult to characterize the exact level of background doping and impurities as well as the concentration of donors in the MBE chamber during the growth process, this latter possibility cannot be eliminated. Furthermore, the calculations did not take into account the nature of Si doping in $Al_xGa_{1-x}As$, where it is well known that for varying concentrations (x) of Al, the Si donor can behave either as a donor, acceptor or as a deep-level DX center. At present, we are unable to explain the discrepancy between the obtained data and the calculations.

Figure 2.6 (c) shows temperature dependence of the PL, using the 699 as the excitation laser. It is clear that X stays relatively unchanged, while X^- disappears around 30 K due to dissociation of the charged complex. This is also in accordance with earlier reports [384]

and with the binding energy of 2.7 meV obtained earlier. An attempt was made to fit the integrated PL intensities of the peaks as a function of temperature to a single-channel thermal activation model, but was unsuccessful, which suggests that this simple model is not sufficient to explain the PL temperature dependence. A more detailed calculation would have to take into account the surrounding energy states due to the donor atoms, continuum states, delocalized excitons and possible defects or deep levels in the semiconductor.

2.4 Chapter Summary

The preceding sections have presented some of the background required on the theory of semiconductors such as the properties of GaAs (Section 2.1.1), charged excitons in bulk semiconductors, QWs and QDs (Sections 2.1.2, 2.1.3). Details of the samples that will be investigated in this thesis were presented in Section 2.2 alongwith a discussion of the modulation doping process. Finally, some basic characterization experiments were presented in Section 2.3. In the next chapter, we will present some of the important theoretical concepts necessary to calculate the results of the experiments, along with a discussion on the mechanisms for electron spin relaxation in semiconductors.

CHAPTER 3

Theoretical Foundations for Charged Quantum Dots

The state of the spin vector of an excess electron in a CQD is an attractive candidate for a qubit in QC due to its anticipated long decoherence time. Optical implementation of QC requires knowledge of the transition strengths and selection rules. The theoretical foundations for understanding the optical spectroscopy experiments and data presented in the rest of this thesis will be laid in this chapter. We begin in Section 3.1 by calculating the optical selection rules for charged excitons in a CQD, and find that the transition between the trion state and one of the electron spin states is forbidden according to angular momentum conservation. This problem can be circumvented as we will see in Section 3.2 through the judicious application of a magnetic field perpendicular to the growth direction of the QDs (typically the [001] direction) known as the Voigt configuration. The selection rules are derived for the charged QD in the Voigt configuration in Section 3.2. An application of the Hamiltonian for GaAs QDs is presented in Section 3.3 where we demonstrate how knowledge of the fine structure and its variation with magnetic field can be used to distinguish between trions and excitons.

An interesting question to ask is what are the ultimate limits on the spin decoherence time, and we will consider in Section 3.4 the various theories of spin relaxation in a semiconductor, starting with the relaxation of bulk electron spins. The considerations of Section 3.4.1 will show that the hyperfine interaction between a localized electron spin and the 10^5–10^6 nuclei in the QD is the fundamental limit on the spin coherence time, yielding an estimate for the spin decoherence time $T_2 \sim 50\,\mu$s.

3.1 Selection Rules for Charged Quantum Dots

We saw in Section 2.1.1 that the heavy hole valence band states in GaAs are labeled by the total angular momentum projection along the growth direction $J_z = \pm 3/2$ and the conduction band electron states are labeled by $S_z = \pm 1/2$, with the understanding that the z-axis represents the growth direction. Selection rules for transitions between the ground states of a CQD and the trion states can be derived using group theory. In the absence of any optical excitation, the ground state of a CQD is assumed to be doubly degenerate as shown in Figure 3.1, with the two states corresponding to the electron in the $|S_z = \pm 1/2\rangle$ states labelled as $|z\pm\rangle$.

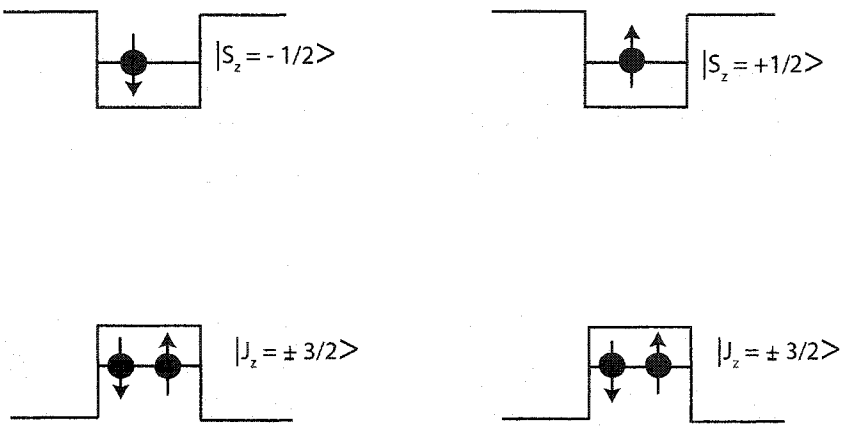

Figure 3.1: The conduction and heavy hole valence bands of the CQD, in the absence of any excitation. The conduction band ground state is doubly degenerate, as the electron spin can be pointing either up or down, with the quantization axis taken as the growth direction. In the valence band, the electrons are paired, resulting in the total angular momentum projection being zero in the valence band states.

When an incident laser field excites the CQD, a negative trion is created and the trion state is formed from two electrons and one heavy hole bound together. Due to the Pauli principle, only particular combinations of electron and hole angular momenta are allowed. When the electron is in the ground state $|z+\rangle$, the laser field can only excite an electron from the $J_z = -3/2$ valence band state to the $|z-\rangle$ conduction band state, as shown in Figure 3.2. The excitation leaves behind a hole with angular momentum projection $J_z = +3/2$. Thus the final trion state is labeled by $|S_{e1z} = +1/2, S_{e2z} = -1/2, J_{hz} = +3/2\rangle$. It must be noted that we are considering only the singlet trion states here, since both electrons are occupying the same envelope function state of the CQD and hence must have opposite spin orientation. It would also be possible to consider triplet trion states where the two electrons are in

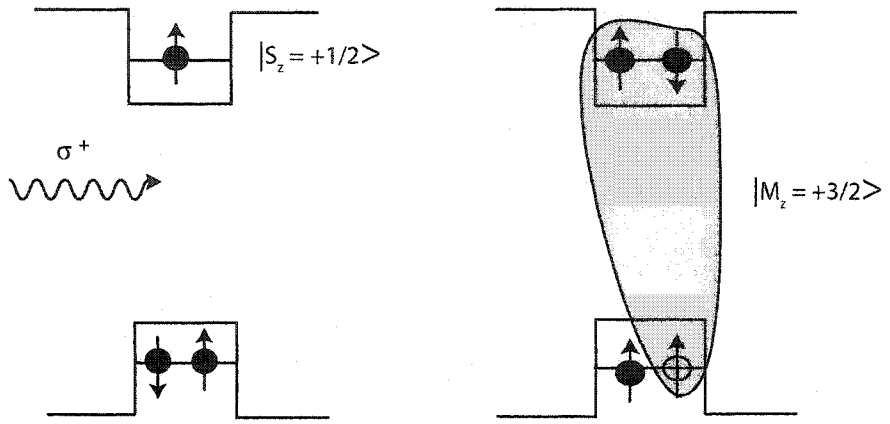

Figure 3.2: Electron hole picture of a CQD upon optical excitation. The figure illustrates the creation of the state $|t+\rangle$ from the state $|z+\rangle$. The incoming photon, denoted by the wavy arrow, promotes an electron from the filled valence band, leaving behind a hole. The angular momentum projection along the z-axis for the hole is $J_{hz} = +3/2$, resulting in the total angular momentum projection for the trion $M_z = +3/2$, because the electron spins are paired. As explained in the text, the incoming photon must be σ^+ polarized to excite this transition.

The total angular momentum projection defined by,

$$M_z = S_{e1z} + S_{e2z} + J_{hz} \tag{3.1}$$

will be equal to $+3/2$ in this case. The other trion state $|M_z = -3/2\rangle$ can be created from the ground state $|z-\rangle$. We will label the trion states $|M_z = \pm 3/2\rangle$ simply as $|t\pm\rangle$ in the following. We can convert from the electron-hole picture to an excitation level scheme as shown in Figure 3.3. The ground states in this viewpoint are the $|z\pm\rangle$ states and the upper states are the trion states $|t\pm\rangle$, giving rise to a four-level system. Let us now calculate the selection rules for the states in this scheme by introducing the electromagnetic field interaction potential,

$$V = -\boldsymbol{\mu} \cdot \mathbf{E} \tag{3.2}$$

where the dipole moment $\boldsymbol{\mu} = e\mathbf{r}$ and is the operator that acts on the states. In spherical vector form,

$$\boldsymbol{\mu} = -e(-r_{-1}\epsilon_{+1} - r_{+1}\epsilon_{-1} + r_0\epsilon_0) \tag{3.3}$$

$$\mathbf{E} = -E_{-1}\epsilon_{+1} - E_{+1}\epsilon_{-1} + E_0\epsilon_0 \tag{3.4}$$

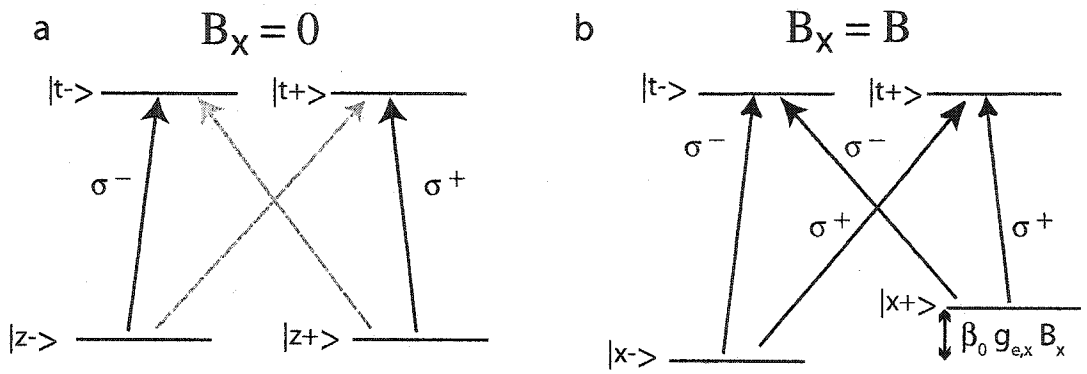

Figure 3.3: Excitation level picture for the CQD with and without a magnetic field in the Voigt geometry. (a) Excitation level picture for the CQD in the absence of the magnetic field, with the ground states consisting of electron spin pointing up or down ($|z\pm\rangle$), and the excited states consisting of the two possible singlet trion states ($|t\pm\rangle$). The selection rules derived in Section 3.1 are summarized by means of the polarizations that can excite the transition from one state to another in the direction of the arrow. (b) Excitation level picture of the CQD when there is a magnetic field in the Voigt configuration. As explained in Section 3.2, the field splits the ground states and mixes them resulting in the states $|x\pm\rangle$. The trion states are not mixed, and this results in the polarization selection rules shown.

where the spherical vector components of the position operator and the electric field are,

$$r_{\pm 1} = \mp\frac{(x \pm iy)}{\sqrt{2}}, r_0 = z, \tag{3.5}$$
$$E_{\pm 1} = \mp\frac{(E_x \pm iE_y)}{\sqrt{2}}, E_0 = E_z$$

and of the polarization unit vector are

$$\epsilon_{\pm 1} = \mp\frac{(\hat{\mathbf{x}} \pm i\hat{\mathbf{y}})}{\sqrt{2}}, \epsilon_0 = \hat{z} \tag{3.6}$$

with

$$\epsilon_{\pm 1} \cdot \epsilon_{\mp 1} = -1, \epsilon_0 \cdot \epsilon_0 = 1 \quad \text{and all other dot products vanishing.} \tag{3.7}$$

The above definitions are identical to the ones used when deriving the selection rules in atoms. It behooves us to consider how applicable such an approach is in a semiconductor. We know from Section 2.1.1 that the basis states must transform according to irreducible representations of the point group T_d, but we have not considered how the operators transform. The Hamiltonian in the effective-mass approximation and assuming semiclassical

electromagnetic fields in the Coulomb gauge is given by,

$$\begin{aligned} H_{em} &= \frac{1}{2m_e^*}(\mathbf{p} - e\mathbf{A})^2 + V_{conf}(\mathbf{r}) \\ &= \left(\frac{\mathbf{p}^2}{2m_e^*} + V_{conf}(\mathbf{r})\right) - \frac{e}{m_e^*}\mathbf{p}\cdot\mathbf{A} \end{aligned} \tag{3.8}$$

where $\mathbf{A}$ is the vector potential, and we neglect terms that are second-order in $\mathbf{A}$. The diagonalization of terms involving the confinement potential (V_{conf}) can be done using the EFA (see Section 2.1.2) to obtain the unperturbed eigenstates and energies. The last term in the Hamiltonian is the interaction term, which we have replaced in Eq. (3.2) by $V = -e\mathbf{r}\cdot\mathbf{E}$. In group theory, the selection rules are determined by the representations to which the operators and the basis states belong [64, 191]. Since we are replacing the interaction term by a term where the operators transform according to the same three-dimensional irreducible representation (Γ_5), the selection rules will remain the same. The advantage of doing so is that it allows us to derive the selection rules employing the tactics used in atomic physics, without resorting to the machinery of group theory. Let us consider as an example the matrix element

$$\langle t+|\boldsymbol{\mu}|z+\rangle = -e\langle +3/2|(-r_{-1}\epsilon_{+1} - r_{+1}\epsilon_{-1} + r_0\epsilon_0)|+1/2\rangle = -e\langle +3/2| - r_{+1}\epsilon_{-1}|+1/2\rangle$$

Hence we see that

$$\langle t+|\boldsymbol{\mu}|z+\rangle = \wp\epsilon_{-1} \tag{3.9}$$

where $\wp = \langle t||er||z\rangle$ indicates the strength of the dipole matrix element. Similarly we may work out the other matrix elements and the results are

$$\langle t-|\boldsymbol{\mu}|z-\rangle = \wp\epsilon_{+1} \tag{3.10}$$

$$\langle t-|\boldsymbol{\mu}|z+\rangle = \langle t+|\boldsymbol{\mu}|z-\rangle = 0 \tag{3.11}$$

The above equations imply that the transition $|z-\rangle \rightarrow |t-\rangle$ must be caused by a left circularly polarized (σ^- or LCP) field, since only $\epsilon_{-1}\cdot\epsilon_{+1} \neq 0$. Similarly the transition $|z+\rangle \rightarrow |t+\rangle$ can only be caused by a right circularly polarized (σ^+ or RCP) field. The selection rules are summarized in Figure 3.3 (a) which shows the allowed and forbidden transitions between the degenerate ground states corresponding to $|z\pm\rangle$ and the trion states $|t\pm\rangle$. In the figure, the direction of the arrows indicates that the polarization rules are for transitions from the ground states to the trion states.

In view of the above results arising from the angular momentum selection rules, the transitions from the states $|z\pm\rangle$ to the states $|t\mp\rangle$ are forbidden. The motivation behind this thesis work is to manipulate the electron spin states $|z\pm\rangle$ through optical excitation of the intermediate trion state requiring that the trion state couples to both spin states. At first glance, therefore, it might appear as though our cause is hopelessly lost. However, we must remember that since we are considering states in a semiconductor crystal, the rotational symmetries that we have used to label the states do not arise from the full rotation group in three dimensions but from the point group of the crystal T_d. What this means is that we may circumvent the "angular momentum" conservation by applying a perturbation that breaks the symmetry of the system for the electrons, relative to the holes. One such perturbation is the application of a magnetic field perpendicular to the growth direction, as we shall see in Section 3.2.

3.2 Selection Rules in the Presence of a Magnetic Field

The complete Hamiltonian for quantum dots in the presence of a magnetic field can be derived through either $\mathbf{k}\cdot\mathbf{p}$ perturbation theory [277, 428] or the method of invariants [8, 64, 186]. The latter method is based on group theory wherein operators, momenta and their products are decomposed and classified into various irreducible representations. Since the Hamiltonian is an invariant under the relevant point group symmetry (such as C_{2v} for a QW), only those products which contain a scalar (one-dimensional) representation are allowed. Thus, we obtain the Hamiltonian for quantum dots grown in the (001) direction [22, 186, 428],

$$H_{Zeeman} = \frac{\beta_0}{\hbar}(\mathbf{B}\cdot\bar{\bar{g}}_e\cdot\mathbf{S}) - \frac{\beta_0}{\hbar}(2\mathbf{B}\cdot\bar{\bar{\kappa}}\cdot\mathbf{J} + 2\mathbf{B}\cdot\bar{\bar{q}}\cdot\boldsymbol{\mathcal{J}}) \tag{3.12}$$

where $\beta_0 = e\hbar/2m_ec$ is the Bohr magneton (note that m_e is the free electron mass), $\bar{\bar{g}}_e$ is the electron g-factor tensor usually written in principal axes form, $\bar{\bar{\kappa}}$ is the corresponding hole g-factor tensor, and $\bar{\bar{q}}$ is the cubic correction to the hole g-factor tensor. $\mathbf{S}, \mathbf{J}$ are the angular momenta of the electron and hole respectively, and $\boldsymbol{\mathcal{J}}$ is the set of three four-dimensional matrices (J_x^3, J_y^3, J_z^3). The matrix J_x, for instance, contains matrix elements between the heavy hole $|+3/2\rangle$ and light hole $|+1/2\rangle$ state, but no term coupling the heavy holes between themselves, *i.e.* $\langle\pm3/2|J_x|\mp3/2\rangle = 0$. Only the matrices $\mathcal{J}_{x,y}$ contain terms that couple the heavy-hole states.

Under some approximations, we may simplify the terms in Eq. (3.12) as follows: since the heavy-light hole splitting is large, and usually $q \ll 1$, we may neglect the $|J_{hz} = \pm 1/2\rangle$ states, and treat the $|J_{hz} = \pm 3/2\rangle$ states as having a pseudo-angular momentum $\tilde{S}_{hz} = \mp 1/2$, reducing them to two-dimensional matrices. Note that Van Kesteren *et al.* [79] use the opposite convention, $|J_{hz} = \pm 3/2\rangle \equiv \tilde{S}_{hz} = \pm 1/2$, but we will follow this convention used by Ivchenko-Pikus [186]. To convert, we can just flip the sign of all the $\tilde{S}_{h,i}$ operators to obtain the Van Kesteren Hamiltonian.

The neglect of the light-hole states corresponds to neglecting terms proportional to $\bar{q}$. An additional caveat to this approximation is that the hole g-factors in directions perpendicular to the growth axis must vanish, because as seen from the exact Hamiltonian in (3.12), only terms that contain $\mathcal{J}$ can flip the hole spin from $|\pm 3/2\rangle$ to $|\mp 3/2\rangle$. These statements hold for the QDs grown by growth interrupts in GaAs QWs discussed in this thesis; however for heavily strained systems such as InAs/GaAs SAQDs, it is possible to find non-vanishing in-plane hole g-factors [280]. Due to the strong confinement in those systems in directions lateral to the growth, there is increased light-heavy hole mixing, and it is no longer possible to neglect those states. The Zeeman Hamiltonian, in the spherical approximation (derived from the neglect of the terms due to cubic symmetry), becomes,

$$H_{Zeeman} = \sum_{k} \sum_{i=x,y,z} \frac{\beta_0}{\hbar} (g_{e,i} S_{ek,i} + g_{h,i} \tilde{S}_{hk,i}) B_i \tag{3.13}$$

The full Hamiltonian can be written as the sum of two terms, one due to the exchange interaction and the other due to the Zeeman interaction with the magnetic field.

$$H = H_{exch} + H_{Zeeman} \tag{3.14}$$

The exchange interaction can be broken up into two parts: long-range and short-range. The exchange energy occurs because of the Coulomb attraction between electron and hole and the requirement of antisymmetry of the wavefunction because they are fermions. The magnitude of the exchange energy is given by,

$$\Delta \sim \frac{e^2}{\epsilon} \int\int dr\, dr' \, \frac{\psi_e^*(r)\psi_h(r)\psi_e(r')\psi_h^*(r')}{|r - r'|} \tag{3.15}$$

which can be separated into a short range and long range part [250, 308, 309]. It was shown in [250, 308] that the long-range exchange energy δ_b^{LR} can be written as the interaction energy between two polarization densities arising from the transition dipoles. Thus, the

long-range part is analogous to the interaction of the polarization density of a transition dipole moment in a single cell with a depolarization field which is created by all the other dipoles in the other unit cells of the dot.

$$\delta_b^{LR} = \frac{e^2}{\epsilon} \sum_{r_e \neq r'_e} f^*_{t\sigma}(r_e, r_h) f^*_{t\sigma}(r'_e, r'_h) \mu_{cv,t\sigma} \frac{[1 - 3\mathbf{n}' \cdot \mathbf{n}]}{|r_e - r'_e|^3} \mu_{vc,t'\sigma'} \tag{3.16}$$

where $f^*_{t\sigma}(r_e, r_h)$ is the envelope function, $\mu_{cv,t\sigma}$ is the dipole transition matrix element where c, v represent the conduction and valence band, t, σ represent the spin indices. $\mathbf{n}, \mathbf{n}'$ are the unit vectors between the electrons and holes in different unit cells. The depolarization field, E_{dep} (similar to a local field concept in a dielectric [262]) affects the transition energy of the exciton depending on the polarization density $P(r)$ created by the exciton.

$$\delta_b^{LR} \sim \int dr\, E_{dep}(r) P(r) \tag{3.17}$$

As a result, we see that an exciton in the $1s$ state polarized along the major axis of a dot leads to surface charge separation on the dot. The surface charge density in this case is lesser than in the case of an exciton polarized along the minor axis, and since the Coulomb attraction is larger in the second case this leads to longitudinal-transverse (LT) splitting of the exciton states. The exchange splitting will vanish for dots which preserve rotational symmetry in the plane, i.e. for circular dots. The splitting is therefore dependent on the exact orientation of the dot, as well as its shape.

The short-range exchange interaction δ_0 corresponds to the part of the exchange Coulomb interaction within a unit cell summed over all the cells and weighted by the envelope function.

$$\delta_0 = \int dr\, f^*_{t\sigma}(r, r) f_{t'\sigma'}(r, r) \tag{3.18}$$

The short-range exchange interaction is quite insensitive to the details of the dot shape and size and is usually determined by the strong confinement in the growth direction. Thus, the Hamiltonian for anisotropic quantum dots in the presence of a magnetic field is given by [79, 186, 330],

$$\begin{aligned} H = & \underbrace{\sum_k \sum_{i=x,y,z} \frac{\beta_0}{\hbar} (g_{e,i} S_{ek,i} + g_{h,i} \tilde{S}_{hk,i}) B_i}_{H_{Zeeman}} \\ & + \underbrace{\sum_k \Big[\frac{\delta_0}{\hbar^2} S_{ek,z} \tilde{S}_{hk,z} + \frac{\delta_b}{\hbar^2} (S_{ek,x} \tilde{S}_{hk,x} - S_{ek,y} \tilde{S}_{hk,y}) + \frac{\delta_d}{\hbar^2} (S_{ek,x} \tilde{S}_{hk,x} + S_{ek,y} \tilde{S}_{hk,y}) \Big]}_{H_{exch}} \end{aligned} \tag{3.19}$$

where the index k denotes all the electrons and holes in the CQD and $g_{e,i}$ ($g_{h,i}$) denote electron (hole) g-factors in the directions x, y, z respectively. The exchange part is clearly dependent on the orientation of the electron and hole spins with $\delta_{0,b,d}$ referring to the exchange interaction energies between the electron and hole. We note that the term proportional to δ_b, referred to as the anisotropic exchange term due to the long-range interaction as before, is responsible for both the splitting and the linear polarization of the bright exciton doublets that has been observed in elongated QDs at zero magnetic field [155,175,185,282]. The term proportional to δ_0 (due to the short-range exchange term) gives rise to exchange splitting between bright and dark excitons, and the term proportional to δ_d (again due to long-range interaction) leads to a splitting between dark exciton states. It is clear from the Hamiltonian that for arbitrary field directions, the various states will be mixed leading to a different set of selection rules.

From Eq. (3.19), we obtain the Hamiltonian in the total angular momentum basis for the exciton $\{|+1\rangle, |-1\rangle, |+2\rangle, |-2\rangle\}$ as,

$$H_X = \frac{1}{2} \times \begin{array}{c} \begin{array}{cccc} |+1\rangle & |-1\rangle & |+2\rangle & |-2\rangle \end{array} \\ \begin{pmatrix} \delta_0 - \beta_0(g_{e,z} + g_{h,z})B_z & \delta_b & \beta_0 g_{e,x} B_x & \beta_0 g_{h,x} B_x \\ \delta_b & \delta_0 + \beta_0(g_{e,z} + g_{h,z})B_z & \beta_0 g_{h,x} B_x & \beta_0 g_{e,x} B_x \\ \beta_0 g_{e,x} B_x & \beta_0 g_{h,x} B_x & -\delta_0 + \beta_0(g_{e,z} - g_{h,z})B_z & \delta_d \\ \beta_0 g_{h,x} B_x & g_{e,x}\beta_0 B_x & \delta_d & -\delta_0 - \beta_0(g_{e,z} - g_{h,z})B_z \end{pmatrix} \end{array} \tag{3.20}$$

The transverse magnetic field mixes the states, allowing observation of the "dark" states. The same equation gives us the Hamiltonian matrix for the trion state and the electron in the ground state of the charged QD,

$$H_T = \frac{1}{2} \begin{array}{c} \begin{array}{cc} |t+\rangle & |t-\rangle \end{array} \\ \begin{pmatrix} -\beta_0 g_{h,z} B_z & \beta_0 g_{h,x} B_x \\ \beta_0 g_{h,x} B_x & \beta_0 g_{h,z} B_z \end{pmatrix} \end{array} \quad H_e = \frac{1}{2} \begin{array}{c} \begin{array}{cc} |z+\rangle & |z-\rangle \end{array} \\ \begin{pmatrix} \beta_0 g_{e,z} B_z & \beta_0 g_{e,x} B_x \\ \beta_0 g_{e,x} B & -\beta_0 g_{e,z} B_z \end{pmatrix} \end{array} \tag{3.21}$$

It is seen immediately that the exchange terms dropped out of the matrix, since for the trion state, the two electrons are paired or in a singlet state. It is also possible to find trions in triplet states, but we shall not consider them, for that would require one of the electrons to be in an excited state of the CQD and would be at a higher energy.

Let us consider the matrix for the trion states upon application of a magnetic field $\mathbf{B} = (\mathrm{B}, 0, 0)$. This is a field perpendicular to the growth direction, also known as the Voigt configuration.

$$H_T = \begin{array}{c} \begin{array}{cc} |t+\rangle & |t-\rangle \end{array} \\ \begin{pmatrix} 0 & \frac{1}{2}\beta_0 g_{h,x} B \\ \frac{1}{2}\beta_0 g_{h,x} B & 0 \end{pmatrix} \end{array} \tag{3.22}$$

Similarly the matrix for the electron in the ground state of the CQD is

$$H_e = \begin{array}{c} \begin{array}{cc} |z+\rangle & |z-\rangle \end{array} \\ \begin{pmatrix} 0 & \frac{1}{2}\beta_0 g_{e,x} B \\ \frac{1}{2}\beta_0 g_{e,x} B & 0 \end{pmatrix} \end{array} \tag{3.23}$$

We may now diagonalize the matrices, and obtain the eigenstates and eigen-energies. The new eigenstates for the electron are given as

$$|x\pm\rangle = \frac{1}{\sqrt{2}}(|z+\rangle \pm |z-\rangle) \tag{3.24}$$

and the energy for the eigenstates are,

$$E_{x\pm} = \pm\frac{1}{2}\beta_0 g_{e,x} B$$

The reason for labelling the states of the electron as $|x\pm\rangle$ is also clear, because in the presence of the magnetic field, we expect the electron spin to be oriented along that direction. The trion eigenstates should similarly be diagonalized. However, we have already assumed in this approximation that the g-factors along directions perpendicular to the growth axis are negligible, and this assumption is also verified experimentally for our CQDs in [384]. Hence the trion states remain unperturbed, and we can now consider the selection rules arising from these new eigenstates. Let us consider,

$$\begin{aligned} \langle t+|\boldsymbol{\mu}|x+\rangle &= -e\langle +3/2|(-r_{-1}\epsilon_{+1} - r_{+1}\epsilon_{-1})(|+1/2\rangle + |-1/2\rangle) \\ &= -e\langle +3/2| - r_{+1}\epsilon_{-1}|+1/2\rangle = \wp\epsilon_{-1} \end{aligned} \tag{3.25}$$

Similarly we can work out all the others,

$$\langle t-|\boldsymbol{\mu}|x+\rangle = -e\langle -3/2|(-r_{-1}\epsilon_{+1} - r_{+1}\epsilon_{-1})(|+1/2\rangle + |-1/2\rangle) = \wp\epsilon_{+1} \tag{3.26}$$

$$\langle t+|\boldsymbol{\mu}|x-\rangle = -e\langle +3/2|(-r_{-1}\epsilon_{+1} - r_{+1}\epsilon_{-1})(|+1/2\rangle - |-1/2\rangle) = \wp\epsilon_{-1} \tag{3.27}$$

$$\langle t-|\boldsymbol{\mu}|x-\rangle = -e\langle -3/2|(-r_{-1}\epsilon_{+1} - r_{+1}\epsilon_{-1})(|+1/2\rangle - |-1/2\rangle) = -\wp\epsilon_{+1} \tag{3.28}$$

The application of the magnetic field has resulted in the dipole moments of the "forbidden" transitions becoming non-zero. We may wonder physically why the electron and hole behave differently. The reason arises from the bandstructure—as we saw in Section 2.1.1, the valence band consists of states that transform like p-orbitals, and are strongly affected by the confinement in the z-direction, causing the heavy and light hole bands to split. The energy separating the heavy and light hole states is a measure of how strongly the hole spin is "pinned" to the growth axis. In a semi-classical picture, the angular momentum vector of the hole cannot take on values other than those parallel or anti-parallel to the growth axis. It is only when the interaction energy of the magnetic field approaches the heavy-light hole separation, which is ~ 0.1 eV for the narrow quantum wells, that we may expect the hole spin to start aligning with the magnetic field.

3.3 Spectroscopy of Single Charged Quantum Dots

This section presents an application of the results of Section 3.2 to single-QD spectroscopy. To distinguish between trions and excitons at the single QD level, we perform magneto-PL spectroscopy through a small aperture on the sample 912F-2A. The apertured sample was placed in a magnetic cryostat in the Voigt configuration, where the magnetic field is parallel to the quantum well plane. PL was collected and dispersed through a 0.75-m double-grating monochromator and detected using a liquid nitrogen cooled CCD. Several apertures ranging in sizes from 1 μm to 400 nm were studied, and the data shown are from a nominally 0.7 μm aperture (2,B). As the magnetic field strength is varied, many of the states exhibit a peak which is ~ 98 μeV to the lower energy side of the peak at zero field, as seen in Figure 3.4C. However, there are also some states that do not display a well resolved lower energy transition, as shown in Figure 3.4F. We label the former as X and the latter as X^- for reasons that will be made clear shortly.

We interpret the fine structure of the X and X^- peaks as follows : X and X^- are both formed by electrons (with angular momentum projections $S_z = \pm 1/2$) and heavy holes ($J_z = \pm 3/2$) strongly confined by the QW in the z-direction and weakly confined in the lateral direction by interface fluctuations. X is formed by one electron and one heavy hole, thus giving rise to four possible states, characterized by angular momentum projection $M = \pm 1, \pm 2$ as shown in Figure 3.4. Due to the exchange interaction, the degeneracy between these

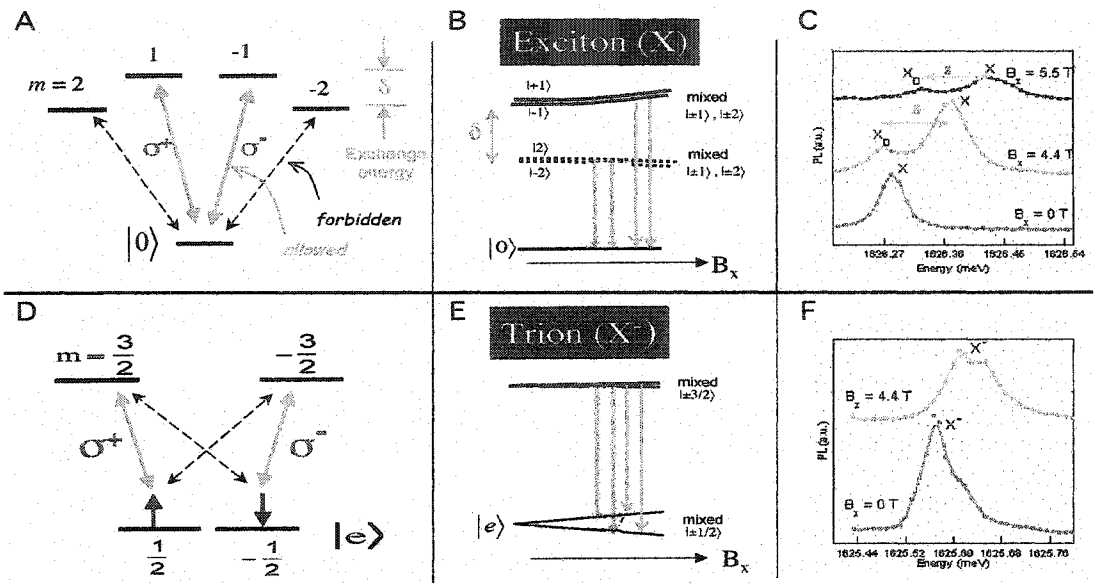

Figure 3.4: Magneto-PL spectroscopy of single neutral and charged QDs. **A.** Fine structure of an exciton in a neutral QD at zero magnetic field, labeled by the total angular momentum of exciton. **B.** Fine structure of the exciton with magnetic field in Voigt geometry, displaying all the allowed transitions. **C.** PL obtained from a 0.7 μm aperture (2,B) of sample 912F-2A, showing peaks due to transitions from previously inaccessible dark exciton states. **D.** Fine structure of a trion in a charged QD at zero magnetic field, labeled by the total angular momentum of trion. **E.** Fine structure of a trion with magnetic field in Voigt geometry, displaying all the allowed transitions. **F.** PL obtained from aperture (2,B) of sample 912F-2A, showing a peak identified as a trion.

states is broken even at zero magnetic field as shown in Figure 3.4A, and results in the M $= \pm 2$ states (or "dark" exciton states) lying at an energy δ below the "bright" (M $= \pm 1$) states [79, 110, 280]. We shall neglect δ_b, δ_d because as shown previously, they are typically $\leq 15\,\mu$eV [175]. The eigenvalues and eigenvectors can be calculated, and the energy is plotted as a function of the field in the Voigt profile (Figure 3.4B). The mixing between the bright and dark states allows for the observation of the previously forbidden transitions, and the splitting between the peaks corresponds to the exchange splitting $\delta_0 \sim 98\,\mu$eV. Note also that the center-of-mass between the peaks shifts to higher energy, due to the diamagnetic interaction, which can also be used as a further proof of the localization of the charges [363].

However, for the negative trion (X^-) which is formed from 2 electrons and 1 heavy hole, there are two singlet states where the two electrons are in the lowest state of the QD, have spins opposite to each other, and differ only by the heavy hole angular momentum as seen

in Figure 3.4D. Because of the pairing of the electrons, no exchange energy is present for this species. On recombination, a single electron is left behind in the ground state of the QD as shown in Figure 3.4D. In the Voigt geometry, four possible transitions are allowed as shown in Figure 3.4E. The absence of the exchange splitting in Figure 3.4F allows us to distinguish the trion from the exciton. Because the in-plane heavy-hole g-factors are close to zero (see Section 3.2) and the in-plane g-factor of the electron is small [384], it is difficult to resolve any of the four transitions, however their presence can be detected with high-resolution frequency-domain nonlinear spectroscopy as discussed in Section 7.1. We also note that the resonance X was stable as the temperature increased, however the resonance X^- vanishes as the temperature is increased beyond 15 K. This behaviour could be explained as due to either ionization of the electron from the trion complex or due to hopping of the electron from the QD being studied to another one nearby.

If $\mathbf{B} = (B\sin\theta, 0, B\cos\theta)$, then the energies of the transitions for bright (E_T^b) and dark (E_T^d) transitions becomes,

$$E_T^b = \pm\frac{\beta_0 B}{2}\left(\sqrt{(g_{h,z}\cos\theta)^2 + (g_{h,x}\sin\theta)^2} - \sqrt{(g_{e,z}\cos\theta)^2 + (g_{e,x}\sin\theta)^2}\right) \tag{3.29}$$

$$E_T^d = \pm\frac{\beta_0 B}{2}\left(\sqrt{(g_{h,z}\cos\theta)^2 + (g_{h,x}\sin\theta)^2} + \sqrt{(g_{e,z}\cos\theta)^2 + (g_{e,x}\sin\theta)^2}\right) \tag{3.30}$$

Since in the Voigt geometry, $\theta = 90°$, the transition splitting will grow linearly with the field, governed by the in-plane electron g-factor, as we indicated in Section 3.2. Further measurements of the transition energies as a function of the angle were carried out by our collaborators which allowed them to extract the g-factors $g_{h,x} \approx 0, g_{e,x} \sim 0.2, g_{e,z} \sim 0.2, g_{h,z} \sim -2$ [384].

3.4 Spin Relaxation

In this section we consider some of the key mechanisms of spin relaxation for electrons in solids. In contrast to the previous sections, we will not be concerned so much with trions or excitons but only with the electron spin. We have shown that the electron spin can be probed through the trion transition in the presence of a magnetic field in the Voigt profile. The standard description for the evolution of the spin polarization (or magnetization) of a

population of spins is through the Bloch equations [2],

$$\frac{\partial M_x}{\partial t} = \gamma_e(\mathbf{M} \times \mathbf{B})_x - \frac{M_x}{T_2} + D\nabla^2 M_x \tag{3.31}$$

$$\frac{\partial M_y}{\partial t} = \gamma_e(\mathbf{M} \times \mathbf{B})_y - \frac{M_y}{T_2} + D\nabla^2 M_y \tag{3.32}$$

$$\frac{\partial M_z}{\partial t} = \gamma_e(\mathbf{M} \times \mathbf{B})_z - \frac{M_z - M_z^0}{T_1} + D\nabla^2 M_z \tag{3.33}$$

where the magnetization $\mathbf{M}$ evolves under the influence of an applied magnetic field $\mathbf{B}(t) = B_0\hat{\mathbf{z}} + \mathbf{B}_1(t)$ which has a static longitudinal component, B_0, along the z-direction and a transverse oscillating component, $\mathbf{B}_1(t)$, perpendicular to $\hat{\mathbf{z}}$. $\gamma_e = \beta_0 g/\hbar$ is the electronic gyromagnetic ratio, D is the diffusion coefficient (taken for simplicity to be isotropic) and M_z^0 is the thermal equilibrium magnetization. The interaction of the magnetic moment of the electron spin with a magnetic field leads to spin precession around the vector $\mathbf{B}$ with a frequency, $\omega_c = \beta_0 g B/\hbar$. Other interactions can be treated as local, fluctuating magnetic fields. A single electron spin in the population undergoes spin precession about the effective magnetic field, while the fluctuations leads to either a spin-flip transition with an average rate referred to as $\Gamma_s = T_1^{-1}$ or an irreversible loss in the phase of the spin precession. The average time before the latter occurs is referred to as the single spin decoherence time (T_2) and corresponds to the qubit lifetime in quantum information processing.

The relaxation time T_1 represents the time taken for the longitudinal magnetization to relax back to equilibrium. It is sometimes also called the spin-lattice relaxation time since it represents the thermal equilibriation time with the lattice, and requires energy transfer from the spin system (for example through phonons) to the lattice. The time T_2 is the time for the transverse spin polarization of the ensemble spins which are initially in phase to irreversibly lose their phase coherence due to temporal fluctuations in the precessing frequencies of individual electron spins. The linewidths of NMR and ESR experiments are given by T_2. The correspondence between the Bloch equations and a microscopic picture of spin was first identified by Feynman, Vernon and Hellwarth [9] who established the equality of the Bloch equations to the density matrix equations for a two-level system.

Mobile electron spins have several sources of spin precession frequency fluctuations—for example, through slightly different g-factors or spin-flip rates in different momentum states. Scattering between states through momentum relaxation creates the fluctuations in the phase of the polarization. For mobile electrons, momentum scattering typically proceeds much faster than spin-flip scattering, and thus the broadening due to g-factor variations

can be inhibited by *motional narrowing* [3,7]. The principle behind motional narrowing is that if a spin is rotating with frequency ω_0, the spin phase changes by $\Delta\phi = \omega_0 t$ over a time t. If the spin is subject to a random force that is equally likely to make it precess clockwise and anti-clockwise, the average spin phase does not change. However, in a time τ_c before the next random impulse, the phase accumulated is $\omega_0\tau_c$. In a random walk model, the root-mean-square phase change increases with the square root of the number of steps (t/τ_c), which gives $(\langle\Delta^2\phi\rangle)^{1/2} \approx (\omega_0\tau_c)\sqrt{t/\tau_c}$. Here τ_c is the correlation time for the random force or intuitively the average time before the spin changes direction. The model is valid for rapid fluctuations, $\omega_0\tau_c \ll 1$. The phase relaxation time is then defined as the time over which the phase fluctuations $\sqrt{\langle\Delta^2\phi\rangle}$ reach unity: $\tau_\phi = 1/(\omega_0^2\tau_c)$.

For a localized electron spin, the momentum scattering analogy can be made to describe intersite hopping or exchange interactions between localized spins. Besides the changes in the magnetization due to spin-flips and g-factor broadening, localized spins also experience spatially inhomogeneous environments from one site to another, for example due to hyperfine fields or variations in the confinement affecting the spin-flip transition rates. Since the variation in frequency of different localized spins is static, the dephasing can be reversed in a spin-echo sequence that will refocus the spin vectors of different spins in the ensemble [4,71]. The spin dephasing time of ensemble spins is denoted by T_2^*, and generally $T_2^* \leq T_2$. We now consider the various mechanisms for spin relaxation in solids.

3.4.1 Mechanisms for Spin Relaxation

3.4.1.1 Mobile Electron Spins

In a seminal paper, Elliott showed in 1954 that conduction electron spins can relax via ordinary momentum scattering by phonons or impurities [5]. The source of the spin scattering is the spin-orbit interaction,

$$V_{so} = \frac{\hbar}{4m^2c^2}\nabla V_{cr} \times \hat{\mathbf{p}} \cdot \hat{\sigma} \tag{3.34}$$

where m is the free-electron mass, V_{cr} is the scalar periodic lattice potential, $\hat{\mathbf{p}} = -i\hbar\nabla$ is the linear momentum operator, and $\hat{\sigma}$ are the Pauli matrices. For example in metals and other solids with a center of symmetry, the eigenfunctions of $\hat{\sigma}_z$ are no longer the

single-electron Bloch wavefunctions but rather a mixture of the spin up and down states. Kramer's theorem states that $E_{\mathbf{k}\uparrow} = E_{-\mathbf{k}\downarrow} = E_{\mathbf{k}\downarrow}$, where the last step follows from inversion symmetry. Thus, one can create a superposition of states with opposite spin and same momentum $\mathbf{k}$, which leads to spin relaxation whenever momentum scattering takes place and couples the eigenstates. The Elliot-Yafet (EY) mechanism, as it is known, depends on the cause of the momentum relaxation either through phonons, impurities or interfaces. The EY spin-relaxation rate in the case of III-V semiconductors is given by [25],

$$\frac{1}{\tau_s(E_k)} = A_{EY}\left(\frac{\Delta_{so}}{\Delta_{so}+E_g}\right)^2\left(\frac{E_k}{E_g}\right)^2\frac{1}{\tau_p(E_k)} \tag{3.35}$$

where τ_p is the momentum relaxation time, Δ_{so} is the spin-orbit splitting, E_g is the bandgap and A_{EY} is a factor that varies depending on the type of scattering mechanism. The EY rate is important for small-gap semiconductors with large spin-orbit splitting (such as InSb).

In a bulk semiconductor such as GaAs, it is clear that spin is not a good quantum number because as we saw in Section 2.1.1 the spin-orbit interaction mixes states with different (l, s) quantum numbers giving the degenerate heavy and light hole bands with total angular momentum j. Further, from the Luttinger Hamiltonian (Eq. (2.1)) we see that the energy of the holes depends on the relative orientation of their momentum $\mathbf{k}$ and the angular momentum $\mathbf{J}$. The strong spin-orbit coupling leads to very rapid change in spin orientation whenever the momentum changes, and hence explains why the hole spin relaxation in bulk GaAs is very large.

For a free electron in the conduction band, the spin-orbit interaction is weaker but also plays a role in a different manner. In zinc blende semiconductors, the lack of inversion symmetry implies that $E_{\mathbf{k}\uparrow} \neq E_{\mathbf{k}\downarrow}$, although Kramer's theorem still holds $E_{\mathbf{k}\uparrow} = E_{-\mathbf{k}\downarrow}$. The non-centrosymmetric nature of the crystal leads to a term that is dependent on the third power of the wavevector projections along the cubic crystal axes [001], [010] and [100] and depends strongly on the vector direction. The spin-orbit interaction then leads to a precession around an effective magnetic field given by the Dresselhaus field [6],

$$\mathbf{B}_{dr} \propto k_x(k_y^2 - k_z^2)\mathbf{e_x} + k_y(k_z^2 - k_x^2)\mathbf{e_y} + k_z(k_x^2 - k_y^2)\mathbf{e_z} \tag{3.36}$$

The Dresselhaus field is directly responsible for the D'yakonov-Perel (DP) mechanism proposed for spin relaxation in a bulk non-centrosymmetric crystal [18, 19]. The spin relaxation rate is found to increase as the cube of the electron energy and therefore under

high-mobility or high temperature conditions the DP mechanism dominates over the EY mechanism. The basic difference between the DP and EY mechanisms is that in the EY process, the precession frequency is conserved between collisions and the loss of phase occurs during the collision (similar to collision broadening of the homogeneous linewidth in atomic gases). In the DP process, the precession frequency changes in between collisions due to the precession of electron spins with different momenta around the corresponding Dresselhaus field, thereby leading to loss of phase.

When the dimensionality of the system is reduced as in quantum wells or at the interface of a Schottky barrier, there is an additional field, known as the Rashba field which occurs from the interface asymmetry or due to the preferred direction of a built-in electric field. The Rashba field is given by,

$$\mathbf{B}_{rashba} = 2\alpha_{BR}(\mathbf{k} \times \mathbf{n}) \tag{3.37}$$

Here α_{BR} is a parameter depending on spin-orbit couplling and the asymmetry of the confining electrostatic potentials. The Rashba field is one example of a *structure inversion asymmetry* (SIA) which creates a corresponding spin splitting in the conduction band and is linear in $\mathbf{k}$. The Dresselhaus term is an example of *bulk inversion asymmetry* (BIA). The Rashba field can be tailored by changing the electrostatic potential, which provides a potential route to spin control [76]. Both SIA and BIA can be important contributors to the DP process in two-dimensional semiconductors, and the DP mechanism in QWs was proposed to be the primary source of spin relaxation in two-dimensional electron gases [55].

The third mechanism for spin relaxation was proposed by Bir, Aronov and Pikus [24,28]. The exchange interaction between electrons and holes acts as an effective magnetic field,

$$H = \alpha_{BAP}\mathbf{S} \cdot \mathbf{J}\delta(\mathbf{r}) \tag{3.38}$$

where α_{BAP} is proportional to the exchange integral between the conduction and valence band states, $\mathbf{J}$ is the angular momentum operator for holes, $\mathbf{S}$ is the electron spin operator, and $\mathbf{r}$ is the relative position of electrons and holes. Spin relaxation of conduction electrons in p-doped semiconductors then proceeds by scattering from the holes, accompanied by the spin exchange. The efficacy of the spin scattering depends on the state of the holes, for example whether the doping level is high enough to form a degenerate hole gas, or if they are bound on acceptors or free. The BAP rate for a bulk semiconductor in the case when

the holes are degenerate is given by,

$$\frac{1}{\tau_s} = \frac{3}{\tau_0} p a_B^3 \frac{\nu_{\mathbf{k}}}{\nu_B} \frac{k_B T}{E_{Fh}} \tag{3.39}$$

where $a_B = \hbar^2 \epsilon / e^2 m_e$ is the exciton Bohr radius, p is the density of free holes, τ_0 is an exchange splitting parameter given by $\hbar/\tau_0 = (3\pi/64)\,\delta_0^2/E_B$ where δ_0 is the exchange splitting of the exciton, E_B is the exciton Bohr energy ($E_B = \hbar^2/2m_e a_B^2$), $\nu_B = \hbar/m_e a_B$ is the exciton Bohr velocity, and E_{Fh} is the hole Fermi energy. In general, the BAP mechanism dominates in heavily-doped samples at low temperature but the DP mechanism becomes dominant at high temperatures even for large acceptor densities.

3.4.1.2 Localized Electron Spins

All three mechanisms proposed so far rely on momentum scattering as a mediator for spin relaxation, and thereby should be suppressed in QDs where the electron orbital state is highly localized and does not undergo elastic scattering events which lead to spin relaxation. The fourth mechanism for spin relaxation is due to the hyperfine interaction, which is the interaction between the magnetic moments of electrons and nuclei, and becomes highly effective for localized electrons. Localized electrons typically interact with around 10^4–10^6 nuclei, and experience the combined magnetic moments of many nuclei. In GaAs, all the lattice nuclei have a magnetic moment corresponding to $I = 3/2$, while in Si, the most abundant isotope ^{28}Si carries no spin and any hyperfine effects are due to ^{29}Si or the frequent donor ^{31}P which both carry nuclear spin $I = 1/2$. The effect of the hyperfine interaction is thereby much lesser in Si compared to GaAs.

The contribution to the decoherence in a QD is primarily through three processes: (i) spin-flip transitions which require energy transfer and affect Γ_s or T_1 and thereby T_2 (ii) pure dephasing events which affect the phase but not the population, which contribute only to T_2 (iii) inhomogeneities that result from varying local environments and affect T_2^*. We ignore the last contribution for now, although it will be extremely important for the experiments on an ensemble of spins described in Section 5.2, and consider only the other processes here. Let's consider the first contribution to decoherence, from the population decay time. For the localized orbital states, population transfer between Zeeman sublevels occur through hyperfine or spin-orbit couplings mediated by phonons. Inelastic scattering events require energy typically from the lattice or other carriers. At low temperatures and

densities, such events should not be significant. In fact, it was found theoretically that the time scales of spin relaxation between different orbital states in a QD mediated by one and two-phonon processes is on the order of milliseconds [295, 327]. Similarly, spin relaxation between the Zeeman sublevels of an electron in a single quantum dot orbital state due to spin-orbit scattering from acoustic phonons or due to the piezoelectric interaction were found to be ineffective, with $T_1 \sim 200$s [294]. We only need to consider the effect of the hyperfine interaction on the precession of the electron spin.

The effective Hamiltonian for the hyperfine interaction is the Fermi contact potential energy [71],

$$H = \frac{8\pi}{3}\frac{\mu_0}{4\pi} g_0 \beta_0 \sum_j \gamma_n \mathbf{S} \cdot \mathbf{I}_j \delta(\mathbf{r} - \mathbf{R}_j) \tag{3.40}$$

where μ_0 is the vacuum permeability, $g_0 = 2.0023$ is the free-electron g-factor, β_0 is the Bohr magneton, $\gamma_n = \beta_n g_n$ is the nuclear gyromagnetic ratio with β_n as the nuclear Bohr magneton, g_n as the nuclear g-factor and j represents the label for the nucleus at position $\mathbf{R}_j$. For localized electrons, the Hamiltonian for the interaction can be written by neglecting the higher lying energy levels,

$$\mathcal{H}_{en} = \frac{v_0}{2} \sum_j A_j \left|\psi(\mathbf{R}_j)\right|^2 (I_{j,z}\sigma_z + I_{j,x}\sigma_x + I_{j,y}\sigma_y) \tag{3.41}$$

where v_0 is the volume of the unit cell, $\psi(\mathbf{R}_j)$ is the electron envelope function evaluated at the jth nucleus, $I_{j,i}$ and σ_i are the spin projection operators on the coordinate axes $i = x, y, z$. In the above equation, $A_j = (16\pi\beta_0\gamma_n/3)\left|u_c(\mathbf{R}_j)\right|^2$, where $u_c(\mathbf{R}_j)$ is the electron Bloch function evaluated at the nucleus. In GaAs, the sum of the A_j over all the nuclei in the unit cell is $A = \sum_j A_j \approx 90\,\mu$eV. The electron Bloch functions are s-like and do not vanish at the nuclear positions, unlike the holes. This is the reason we can neglect hyperfine interactions for holes. The last two terms in the Hamiltonian are responsible for spin flips between the electron and nuclei, which would cause dephasing. The first term gives rise to an average field, which in combination with dynamical nuclear polarization, can cause the Overhauser shift [181, 330]. The Overhauser shift will be considered in more detail in Section 7.1.

In truth, the total Hamiltonian of the electron-nuclear spin system is given by,

$$\mathcal{H}_{tot} = \mathcal{H}_e + \mathcal{H}_n + \mathcal{H}_{en} \tag{3.42}$$

with

$$\mathcal{H}_e = \gamma_e \mathbf{B} \cdot \mathbf{S}_e \tag{3.43}$$

$$\mathcal{H}_n = -\gamma_n \sum_k \mathbf{B} \cdot \mathbf{I}_k + \mathcal{H}_{nn} \tag{3.44}$$

$$\mathcal{H}_{nn} = -4 \sum_{k<m} b_{km} I_{kz} I_{mz} + \sum_{k<m} b_{km} (I_{k+} I_{m-} + I_{k-} I_{m+}) \tag{3.45}$$

where $b_{km} = -\frac{1}{4}\gamma_n^2 \hbar \dfrac{1 - 3\cos^2\theta_{km}}{R_{km}^3}$ is the nuclear dipole-dipole interaction constant which depends on the angle between two nuclear spins θ_{km} and the distance between the spins R_{km}^3. For the time being, we ignore the nuclear spin-spin interactions given in $\mathcal{H}_{nn}$ and consider only the hyperfine interaction between the nuclei and the electron spin. The total spin $\mathbf{F} = \mathbf{S} + \sum_j \mathbf{I}_j$ of the electron-nuclear system must be conserved because it commutes with the total Hamiltonian given in Eq. (3.42) after neglecting $\mathcal{H}_{nn}$. In the absence of nuclear dipole interactions therefore, the total spin $\mathbf{F}$ and consequently the total nuclear spin $\mathbf{I}$ is conserved. The last part follows from the fact that $\mathbf{I} = \mathbf{F} - \mathbf{S} \approx \mathbf{F}$, since $F \gg S$. For timescales where the dipole-dipole interactions become important ($\sim 100\,\mu$s), the total nuclear spin is no longer conserved and the electron spin precession will be affected, leading to dephasing. In that case, only the component of the total spin along the magnetic field direction (taken as the z-axis) is conserved, *i.e.* $F_z = S_z + I_z \approx I_z$ is constant.

We consider two cases, when there is no magnetic field present present and when there is a strong external magnetic field. For the first case, the electron-nuclear spin flip mechanism is applicable for low fields, $B \leq \hbar\gamma_n |\psi(0)|^2 \ll 100$ G, where $|\psi(0)|^2 = 10^{22} - 10^{25}$ cm^{-3} is the electron probability density on a nucleus. This is in fact the mechanism proposed in [371], which showed that the single spin decoherence time for the low field case is $T_2 \sim \hbar N/A$ which gives $T_2 = 7.3\,\mu$s (for GaAs).

For the second case, the strong magnetic field implies a large electron Zeeman splitting which is much greater than the nuclear Zeeman splitting, and hence electron-nuclear spin flips are not possible due to energy conservation. When the field is increased, we enter the regime where the precession frequency of the electron spin is affected randomly whenever a nuclear spin flips, which implies we must take into account the term $\mathcal{H}_{nn}$. However, the dipole-dipole interaction does not conserve energy in the presence of the magnetic field (due to the nuclear Zeeman splitting), unless the spin flip of the nuclei is accompanied by a random change in the electron spin polarization. The energy conservation is satisfied by

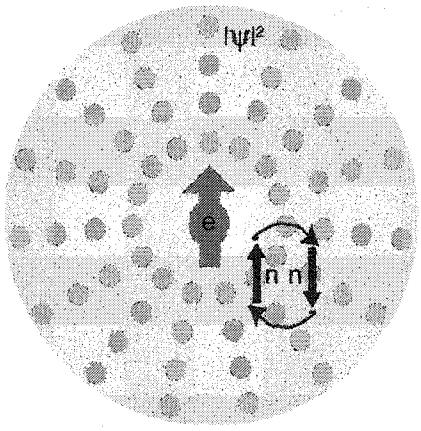

Figure 3.5: Illustration of the hyperfine interaction between electron and nuclear spins. The electron spin interacts with all the nuclei within the range where the magnitude of the wavefunction is non-zero. Nuclear spin flips lead to random shifts in the precession frequency of the electron spin giving rise to decoherence.

energy fluctuations in the Zeeman splitting of the electron. This is illustrated in Figure 3.5. The spin flip-flop of the nuclei must occur in pairs because I_z is conserved. The effect on the electron spin is to give a shift in the precession frequency, which we can term as *spectral diffusion* and leads to $T_2 \sim 50\,\mu$s for an electron spin in a GaAs QD [400,401]. We shall not consider further the hyperfine interaction in this section, but will consider its effect on the spin coherence in Chapter 5. This concludes the discussion on spin relaxation mechanisms in semiconductors.

3.5 Chapter Summary

We presented the essential concepts for understanding the nonlinear spectroscopy experiments on charged quantum dots. Sections 3.1–3.2 derived the selection rules under optical excitation for charged quantum dots and showed how to optically couple the electron spin states in a charged quantum dot. A fundamental question that arises is what causes spin polarization to relax in semiconductors in general, and we presented the basic mechanisms for relaxation in Section 3.4.1. The next chapter will discuss how to apply the models and selection rules derived in this chapter to the nonlinear spectroscopy experiments.

CHAPTER 4

Nonlinear Optical Spectroscopy: Theory and Experimental Setup

The simplest model for an atom, a two-level system, directly leads to a nonlinear interaction between light and matter. Nonlinear optical spectroscopy is used throughout our work to probe the light-matter interaction. An essential theoretical tool for physical interpretation of the results from the experiments is the density matrix, introduced in Section 4.1.1. The master equations of the density matrix, used to calculate the signals, are presented in the latter section, along with the most important approximations such as the **rotating-wave approximation (RWA)** and the **slowly varying envelope approximation (SVEA)** that are used to simplify the process of solving the equations. Section 4.1.2 derives the expressions necessary to calculate various nonlinear optical signals such as differential transmission (DT), four-wave mixing (FWM) and Faraday rotation (FR). While all of these techniques were used in the experiments presented in this thesis work, we concentrate primarily on DT where the bulk of the measurements were carried out.

Nonlinear optical spectroscopy both complements and supplements the information gleaned by linear spectroscopic methods such as photoluminescence, photoluminescence excitation and absorption. It is an excellent tool for studying dynamical processes in atoms, semiconductors and even complex biological systems [41, 62, 135, 170], and it is highly sensitive to many-body correlation effects that are unique to understanding semiconductor physics [322]. Recent advances in ultrafast lasers have yielded the ability to time resolve dynamics down to the single optical cycle regime. The experiments carried out in this work rely on both ultrafast mode-locked and frequency-stabilized laser systems, which will be described in Section 4.2 and Section 4.3, respectively. The common goal of both kinds of measurement techniques is to extract information on the coherent and incoherent dynamics in the system.

4.1 Theory for Nonlinear Spectroscopy Experiments

4.1.1 Density Matrix for the Four-Level System

The density matrix approach is a powerful theoretical tool used when considering the interactions of light with matter, especially when trying to incorporate the effects of decay and decoherence. Quantum mechanics defines a pure state as one where the system can be described by a single state vector $|\Psi\rangle$ in Hilbert space. However, when the system can exist with different probabilities in various pure states, then a complete description of the system can be obtained through the density operator [119],

$$\rho = \sum_{\Psi} \mathrm{P}_{\Psi} |\Psi\rangle\langle\Psi| \tag{4.1}$$

where P_{Ψ} represents the probability that the system is in any given pure state $|\Psi\rangle$. In some set of basis states $\{|i\rangle\}$, usually taken to be the energy eignestates of the unperturbed Hamiltonian H_0, we obtain the density matrix elements,

$$\rho_{ij} = \sum_{\Psi} \mathrm{P}_{\Psi} \langle i|\Psi\rangle\langle\Psi|j\rangle \tag{4.2}$$

The diagonal density matrix elements correspond to the population present in different energy eigenstates, while the off-diagonal elements carry information about the coherence or phase relationship between the state amplitudes. The preceding sections have shown that we need to consider a four-level model to simulate the nonlinear optical response from a CQD. The master equation of motion for the density matrix is given by,

$$\frac{d\rho}{dt} = \frac{1}{i\hbar}[H, \rho] + \left.\frac{\partial \rho}{\partial t}\right|_{relaxation} \tag{4.3}$$

We shall use the density matrix formalism to model all the experimental results obtained in this thesis. The first term on the right hand side arises from the deterministic, unitary evolution of the system under the influence of the system hamiltonian, while the second term arises from interactions with a reservoir or "bath" which causes decay of diagonal terms and decoherence of the off-diagonal terms. The nature and form of the decay can be derived depending on the kind of bath and the coupling to the reservoir. In our case, we shall restrict ourselves to only considering the bath consisting of the vacuum fluctuations in the electromagnetic field, and the corresponding decay terms arising from the dipole

interactions of the system with the vacuum field. We begin by writing out here in full the density matrix equations for the four level system described schematically in Figure 4.1. The decay rates for the diagonal density matrix elements are described in Figure 4.1. The dephasing rates for the off-diagonal density matrix elements ρ_{ij} are denoted by γ_{ij}. This gives the following set of equations,

$$\dot{\rho_{11}} = \Gamma_1\rho_{22} + \Gamma_2\rho_{33} + \Gamma_{41}(\rho_{44} - \rho_{11}) + \frac{1}{i\hbar}(V_{12}\rho_{21} - c.c.) + \frac{1}{i\hbar}(V_{13}\rho_{31} - c.c.) \tag{4.4}$$

$$\dot{\rho_{22}} = -(\Gamma_1 + \Gamma_2)\rho_{22} + \Gamma_{23}(\rho_{33} - \rho_{22}) + \frac{1}{i\hbar}(V_{21}\rho_{12} - c.c.) + \frac{1}{i\hbar}(V_{24}\rho_{42} - c.c.) \tag{4.5}$$

$$\dot{\rho_{33}} = -(\Gamma_1 + \Gamma_2)\rho_{33} - \Gamma_{23}(\rho_{33} - \rho_{22}) + \frac{1}{i\hbar}(V_{31}\rho_{13} - c.c.) + \frac{1}{i\hbar}(V_{34}\rho_{43} - c.c.) \tag{4.6}$$

$$\dot{\rho_{44}} = \Gamma_1\rho_{33} + \Gamma_2\rho_{22} - \Gamma_{41}(\rho_{44} - \rho_{11}) + \frac{1}{i\hbar}(V_{42}\rho_{24} - c.c.) + \frac{1}{i\hbar}(V_{43}\rho_{34} - c.c.) \tag{4.7}$$

$$\dot{\rho_{12}} = (i\omega_{21} - \gamma_{12})\rho_{12} + \frac{V_{12}}{i\hbar}(\rho_{22} - \rho_{11}) + \frac{V_{13}}{i\hbar}\rho_{32} - \frac{V_{42}}{i\hbar}\rho_{14} \tag{4.8}$$

$$\dot{\rho_{13}} = (i\omega_{31} - \gamma_{13})\rho_{13} + \frac{V_{13}}{i\hbar}(\rho_{33} - \rho_{11}) + \frac{V_{12}}{i\hbar}\rho_{23} - \frac{V_{43}}{i\hbar}\rho_{14} \tag{4.9}$$

$$\dot{\rho_{24}} = (i\omega_{42} - \gamma_{24})\rho_{24} + \frac{V_{24}}{i\hbar}(\rho_{44} - \rho_{22}) + \frac{V_{21}}{i\hbar}\rho_{14} - \frac{V_{34}}{i\hbar}\rho_{23} \tag{4.10}$$

$$\dot{\rho_{43}} = (i\omega_{34} - \gamma_{34})\rho_{43} + \frac{V_{43}}{i\hbar}(\rho_{33} - \rho_{44}) + \frac{V_{42}}{i\hbar}\rho_{23} - \frac{V_{13}}{i\hbar}\rho_{41} \tag{4.11}$$

$$\dot{\rho_{23}} = (i\omega_{32} - \gamma_{23})\rho_{23} + \frac{V_{21}}{i\hbar}\rho_{13} + \frac{V_{24}}{i\hbar}\rho_{43} - \frac{V_{13}}{i\hbar}\rho_{21} - \frac{V_{43}}{i\hbar}\rho_{24} \tag{4.12}$$

$$\dot{\rho_{14}} = (i\omega_{41} - \gamma_{14})\rho_{14} + \frac{V_{12}}{i\hbar}\rho_{24} + \frac{V_{13}}{i\hbar}\rho_{34} - \frac{V_{24}}{i\hbar}\rho_{12} - \frac{V_{34}}{i\hbar}\rho_{13} \tag{4.13}$$

where

$$V_{ij} = -\sum_l \boldsymbol{\mu}_{ij} \cdot \mathbf{E}_l,$$

$$\hbar\omega_{ij} = \mathsf{E}_i - \mathsf{E}_j,$$

and

$$\mathbf{E}_l = \frac{1}{2}(\mathbf{e}_l\mathcal{E}_l(t - \tau_l)e^{i(\mathbf{k}_l\cdot\mathbf{r} - \Omega_l(t-\tau_l))} + c.c.),$$

which gives

$$V_{ij} = \hbar(\mathcal{R}_{ij} + \mathcal{R}^*_{ij}), \tag{4.14}$$

with

$$\mathcal{R}_{ij} = -\frac{1}{2\hbar}\sum_l (\boldsymbol{\mu}_{ij}\cdot\mathbf{e}_l)\mathcal{E}_l(t-\tau_l)e^{i(\mathbf{k}_l\cdot\mathbf{r}-\Omega_l(t-\tau_l))},$$
$$\mathcal{R}^*_{ij} = -\frac{1}{2\hbar}\sum_l (\boldsymbol{\mu}_{ij}\cdot\mathbf{e}^*_l)\mathcal{E}^*_l(t-\tau_l)e^{-i(\mathbf{k}_l\cdot\mathbf{r}-\Omega_l(t-\tau_l))} \quad (4.15)$$

In the above equations, E_i is the energy of the state $|i\rangle$ and $\mathbf{E}_l$ is the electric field arriving at time τ_l, along the direction $\mathbf{k}_l$, with central frequency Ω_l, amplitude $\mathcal{E}_l$, and polarization vector $\mathbf{e}_l$. For experiments with CW laser fields, we would set the amplitude to be a constant, and all the arrival times $\tau_l = 0$.

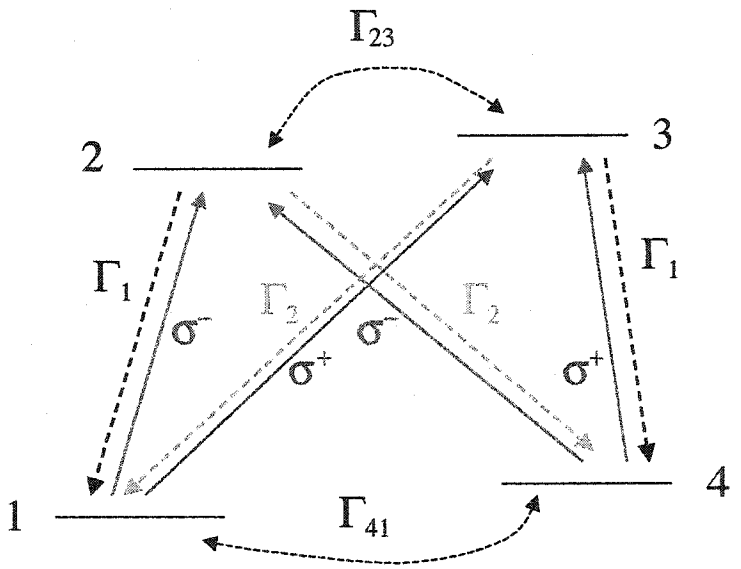

Figure 4.1: Illustration of the four level system that is used to model the experimental nonlinear optical signals obtained from the CQDs. The two ground levels (1 and 4) correspond to the electron spin states $|x-\rangle$ and $|x+\rangle$ respectively while the two upper levels (2 and 3) correspond to the trion states $|t-\rangle$ and $|t+\rangle$. The splitting between 2 and 3 is taken to be non-zero for generality but may later be set to zero. We have assumed that the relaxation pathways from 2 $\Rightarrow$ 1 and 3 $\Rightarrow$ 4 are the same (Γ_1), but different from the relaxation rates for 2 $\Rightarrow$ 4 or 3 $\Rightarrow$ 1 (Γ_2). The rates for 2 $\Leftrightarrow$ 3 and 3 $\Rightarrow$ 2 are assumed to be the same (Γ_{23}), but different from the rates for 1 $\Leftrightarrow$ 4 which is Γ_{14}.

The solution of the density matrix equations given above is greatly simplified in the **RWA** [107,169,270]. The physical basis for the approximation is as follows: when integrating the density matrix equations, those field components that oscillate with the same time dependence $e^{\pm i\Omega t}$ as the density matrix elements $e^{\pm i\omega t}$ lead to terms with denominators $\sim \frac{1}{\pm(\omega+\Omega)}$ for CW fields. Because the optical frequencies involved here are much larger

than either the dipole moments, or the decay rates, we may neglect these denominators corresponding to counter-rotating terms. The same holds true for pulsed laser fields, because the fast oscillations $e^{\pm i(\Omega+\omega)t}$ will be averaged out. In the RWA, the equations for the density matrix elements become,

$$\dot{\rho_{11}} = \Gamma_1\rho_{22} + \Gamma_2\rho_{33} + \Gamma_{41}(\rho_{44} - \rho_{11}) - i(\mathcal{R}^*_{12}\rho_{21} - h.c.) - i(\mathcal{R}^*_{13}\rho_{31} - h.c.) \tag{4.16}$$

$$\dot{\rho_{22}} = -(\Gamma_1 + \Gamma_2)\rho_{22} + \Gamma_{23}(\rho_{33} - \rho_{22}) - i(\mathcal{R}_{21}\rho_{12} - h.c.) - i(\mathcal{R}_{24}\rho_{42} - h.c.) \tag{4.17}$$

$$\dot{\rho_{33}} = -(\Gamma_1 + \Gamma_2)\rho_{33} - \Gamma_{23}(\rho_{33} - \rho_{22}) - i(\mathcal{R}_{31}\rho_{13} - h.c.) - i(\mathcal{R}_{34}\rho_{43} - h.c.) \tag{4.18}$$

$$\dot{\rho_{44}} = \Gamma_1\rho_{33} + \Gamma_2\rho_{22} - \Gamma_{41}(\rho_{44} - \rho_{11}) - i(\mathcal{R}^*_{42}\rho_{24} - h.c.) - i(\mathcal{R}^*_{43}\rho_{34} - h.c.) \tag{4.19}$$

$$\dot{\rho_{12}} = (i\omega_{21} - \gamma_{12})\rho_{12} - i\mathcal{R}^*_{12}(\rho_{22} - \rho_{11}) - i\mathcal{R}^*_{13}\rho_{32} + i\mathcal{R}^*_{42}\rho_{14} \tag{4.20}$$

$$\dot{\rho_{13}} = (i\omega_{31} - \gamma_{13})\rho_{13} - i\mathcal{R}^*_{13}(\rho_{33} - \rho_{11}) - i\mathcal{R}^*_{12}\rho_{23} + i\mathcal{R}^*_{43}\rho_{14} \tag{4.21}$$

$$\dot{\rho_{42}} = (i\omega_{24} - \gamma_{24})\rho_{42} + i\mathcal{R}^*_{42}(\rho_{44} - \rho_{22}) + i\mathcal{R}^*_{12}\rho_{41} - i\mathcal{R}^*_{43}\rho_{32} \tag{4.22}$$

$$\dot{\rho_{43}} = (i\omega_{34} - \gamma_{34})\rho_{43} - i\mathcal{R}^*_{43}(\rho_{33} - \rho_{44}) - i\mathcal{R}^*_{42}\rho_{23} + i\mathcal{R}^*_{13}\rho_{41} \tag{4.23}$$

$$\dot{\rho_{23}} = (i\omega_{32} - \gamma_{23})\rho_{23} - i\mathcal{R}_{21}\rho_{13} - i\mathcal{R}_{24}\rho_{43} + i\mathcal{R}^*_{13}\rho_{21} + i\mathcal{R}^*_{43}\rho_{24} \tag{4.24}$$

$$\dot{\rho_{14}} = (i\omega_{41} - \gamma_{14})\rho_{14} - i\mathcal{R}^*_{12}\rho_{24} - i\mathcal{R}^*_{13}\rho_{34} + i\mathcal{R}_{24}\rho_{12} + i\mathcal{R}_{34}\rho_{13} \tag{4.25}$$

The polarization can be calculated from the density matrix as,

$$\mathbf{P} = \mathrm{Tr}\,(\boldsymbol{\mu}\rho) \tag{4.26}$$

The solution to these equations usually proceeds in a perturbative manner, with some assumptions about the initial state of the system. We assume that initially (at $t = -\infty$) the system starts in the ground states 1 and 4 with no coherences, that is $\rho^{(0)}_{11} = N - \rho^{(0)}_{44} = N_0$. The equations can also be integrated numerically when exact solutions for a given pulseshape are required. The perturbative solution to the equations requires that we expand the density matrix as,

$$\rho = \rho^{(0)} + \rho^{(1)} + \rho^{(2)} + \rho^{(3)} + \ldots \tag{4.27}$$

where the superscripts denote higher orders in the field interaction. To any given order, we can then calculate the n^{th}-order polarization as,

$$\mathbf{P^{(n)}} = \mathrm{Tr}\,(\boldsymbol{\mu}\rho^{(n)}) \tag{4.28}$$

As an example, the 3^{rd}-order polarization for the four-level system in Figure 4.1 may be written as,

$$\mathbf{P^{(3)}} = (\boldsymbol{\mu}_{12}\rho^{(3)}_{21} + \boldsymbol{\mu}_{42}\rho^{(3)}_{24} + \boldsymbol{\mu}_{13}\rho^{(3)}_{31} + \boldsymbol{\mu}_{43}\rho^{(3)}_{34} + c.c.) \tag{4.29}$$

We note that Eq. (4.26) can be extended to inhomogeneously broadened systems by multiplying with the probability distribution that weights the number of oscillators at a given frequency and integrating over the distribution. In either case, the polarization will have negative and positive frequency components,

$$\mathbf{P} = \sum_l (\tilde{\mathbf{P}}_l(t) e^{i(\mathbf{k}_l \cdot \mathbf{r} - \Omega_l t)} + \tilde{\mathbf{P}}_l^*(t) e^{-i(\mathbf{k}_l \cdot \mathbf{r} - \Omega_l t)}) \tag{4.30}$$

which we can substitute in Maxwell's wave equations in a macroscopic medium,

$$\nabla^2 \mathbf{E} - \mu_0 \frac{\partial \mathbf{J}}{\partial t} - \frac{1}{c^2} \frac{\partial^2 \mathbf{E}}{\partial t^2} = \mu_0 \frac{\partial^2 \mathbf{P}}{\partial t^2} \tag{4.31}$$

where μ_0 is the magnetic permeability of the medium, taken to be the same as that of the vacuum, ϵ is the dielectric permittivity of the medium, $c = 1/\sqrt{\epsilon \mu_0}$ is the speed of light in the medium, and $\mathbf{J}$ is the current density in the medium. We drop the second term on the left side for the rest of the current discussion, as it does not apply to dielectric media. The above equation neglects transverse effects, i.e. the terms $\nabla(\nabla \cdot \mathbf{E})$, which are usually negligible in optics since the optical field vector hardly varies along the direction parallel to the propagation direction. The Maxwell wave equations allows us to find the electric field generated by the nonlinear polarization calculated using the density matrix equations, as described in the next section.

In general, the polarization may be expanded in powers of the field, with the susceptibility tensor forming the coefficients in the expansion,

$$P_i = \sum_j \chi_{ij}^{(1)} E_j + \sum_j \chi_{ijk}^{(2)} E_j E_k + \sum_j \chi_{ijkl}^{(3)} E_j E_k E_l + \ldots \tag{4.32}$$

where $\chi^{(n)}$ is the n^{th}-order susceptibility tensor. The fact that $\mathbf{P}^{(n)}$ is dependent on the n^{th} power of the electric field is very useful in experiments as it allows for distinguishability between signals due to nonlinear susceptibility $\chi^{(n)}$, and those from the first order susceptibility $\chi^{(1)}$ which gives rise to the usual effects of linear absorption and dispersion [262]. Thus, the density matrix theory allows us to directly predict the susceptibility tensors, which are of great interest in pursuing a variety of technological applications.

4.1.2 Calculation of Coherent Nonlinear Optical Signal

The experiments in this thesis are carried out typically in a standard pump and probe geometry [170], where the pump ($\mathbf{E}_1$) and probe ($\mathbf{E}_2$) fields are overlapped on the sample

and the probe field is then collected on a square-law detector. As seen in the previous section, the nonlinear polarization $\mathbf{P}^{(3)}$ created by the pump and probe fields will in turn create an electric field $\mathbf{E}_{NL}$ through the Maxwell equations. Physically, the picture is that the pump and probe beams resonantly interacting with the nonlinear oscillators gives rise to a macroscopic polarization. Maxwell's equations predict that the polarization will act as a source to generate fields coherently emitted along the phase-matched direction.

The calculation of the actual nonlinear field $\mathbf{E}_{NL}$ is then carried out by substituting Eq. (4.30) into Eq. (4.31), and making the **SVEA** which neglects second and higher derivatives in time and space. The SVEA implies that the envelope is varying slowly on the timescale of the optical period, which can be stated mathematically as,

$$\left|\frac{\partial U}{\partial t}\right| \ll \Omega|U| \tag{4.33}$$

where U is the envelope of either the electric field or the nonlinear polarization. To calculate the field from the nonlinear polarization then along some direction $\mathbf{k}$ (taken as the z-direction), we set

$$\mathbf{E}_{NL} = \tilde{\mathbf{E}}_{NL}(t)e^{i(\mathbf{k}\cdot\mathbf{r}-\Omega t)} + \tilde{\mathbf{E}}^{*}_{NL}(t)e^{-i(\mathbf{k}\cdot\mathbf{r}-\Omega_l t)}$$

and substitute this along with Eq. (4.30) into Eq. (4.31). This yields, after neglecting second-order derivatives,

$$(2ik\frac{\partial\tilde{\mathbf{E}}_{NL}}{\partial z} - k^2\tilde{\mathbf{E}}_{NL}) + \frac{1}{c^2}(2i\Omega\frac{\partial\tilde{\mathbf{E}}_{NL}}{\partial t} + \Omega^2\tilde{\mathbf{E}}_{NL}) = \mu\big(-2i\Omega\frac{\partial\tilde{\mathbf{P}}^{(3)}}{\partial t} - \Omega^2\tilde{\mathbf{P}}^{(3)}\big) \tag{4.34}$$

With the assumption of phase-matching *i.e.* $k^2 = \Omega^2/c^2$ and using the SVEA again we get the Maxwell-Bloch equations,

$$\frac{\partial\tilde{\mathbf{E}}_{NL}}{\partial z} = \frac{ik}{2\epsilon}\tilde{\mathbf{P}}^{(3)} \tag{4.35}$$

For optically thin samples of length L, this can be immediately integrated to give,

$$\tilde{\mathbf{E}}_{NL} = \frac{ikL}{2\epsilon}\tilde{\mathbf{P}}^{(3)} \tag{4.36}$$

The field so obtained, that we shall denote by $\mathbf{E}_{DT}$ is along the $\mathbf{k}_2$ direction for the case of DT experiments, is proportional to the pump and probe electric fields and is detected along with the probe beam. We shall assume a square-law detector, and hence the signal is just the time-average of the square of the absolute value of the total field incident on the detector. Typically, in the experiment, one modulates the pump and probe beams at some frequency and uses a lock-in amplifier for phase-sensitive detection at the difference

frequency. Thus, only those parts of the signal that are proportional to the intensities of the pump and probe beam will be detected, allowing us to drop all terms in Eq. (4.26) that are not of this form. Further, the first-order (linear) polarization gives rise to modifications in the probe and pump beams through the refractive index and absorption, but will not be picked up in the lock-in due to the modulation. We may therefore neglect the linear terms, and write the total photocurrent induced on the detector as,

$$I_{DT} = Q \int_{-\infty}^{\infty} \left| \mathbf{E}_{DT} + \mathbf{E}_2 \right|^2 dt \tag{4.37}$$

where Q is the detector response coefficient. The fields in this case no longer have any spatial variation because they are evaluated at the detector. Since we only detect terms that are sensitive to both pump and probe modulation, this gives,

$$\begin{aligned} I_{DT} &= 2Q\, \Re \left(\int_{-\infty}^{\infty} dt\, \tilde{\mathbf{E}}_{DT} \cdot \tilde{\mathbf{E}}_2^* \right) \\ &= \frac{QkL}{\epsilon}\, \Im \left(\int_{-\infty}^{\infty} dt\, \tilde{\mathbf{P}}^{(3)}(t) \cdot \tilde{\mathbf{E}}_2^*(t) \right) \end{aligned} \tag{4.38}$$

To normalize for the effects of changing pump and probe transmissions, we usually divide by the probe transmission,

$$I_T = Q \int_{-\infty}^{\infty} dt\, \left| \mathbf{E}_2(t) \right|^2 \tag{4.39}$$

Differential transmission as the name suggests, can be viewed as the differential signal obtained by subtracting the transmission of a probe beam when the pump beam is on from the transmission of the probe beam when the pump beam is off.

$$\mathrm{DT/T} = \frac{T_{pr}^{\text{pump on}} - T_{pr}^{\text{pump off}}}{T_{pr}^{\text{pump off}}} \tag{4.40}$$

While certainly correct, the above viewpoint obscures the fact that the transmission of a coherent laser pulse through the medium can imprint quantum coherences that will persist long after the pulse is gone, and can affect the properties of another pulse that arrives much later in time. That is why Eq. (4.38) should be used to calculate the actual DT signal that is measured [97].

It is an interesting question to ask whether the Maxwell-Bloch equations are valid in the limit of a single QD. Certainly when considering a single QD, it is meaningless to talk about phase-matching or plane-wave propagation of the nonlinear polarization and fields. The radiation pattern of a single dipole oscillator is no longer a plane-wave. However, one

may still ask the question of how much absorption the probe pulse undergoes in interacting with the single QD. The absorption of the probe pulse is proportional to the work done by the pulse, which in a time interval δt is given by [262]

$$\delta W = \delta t \, \mathbf{J} \cdot \mathbf{E}_2 = \delta t \, \frac{\partial \mathbf{P}}{\partial t} \cdot \mathbf{E}_2 \tag{4.41}$$

and integrating to obtain the total work done by the pulse,

$$W = \int_{-\infty}^{\infty} dt \, \dot{\mathbf{P}}(t) \cdot \mathbf{E}_2(t)$$

which gives for time-harmonic fields

$$W = -\Im\left(\int_{-\infty}^{\infty} dt \, \omega \tilde{\mathbf{P}}(t) \cdot \tilde{\mathbf{E}}_2^*(t) \right) \tag{4.42}$$

where we substituted $\mathbf{P} = \Re[\tilde{\mathbf{P}} e^{-i\omega t}]$ and a similar expression for $\mathbf{E}_2$, and used the SVEA to neglect terms that are derivatives of the envelope functions, to obtain Eq. (4.42). Then the DT signal can be written as $DT \propto -W$ which is the same as Eq. (4.38). Thus we can still use Eq. (4.38) to calculate the DT signal from a single QD after obtaining the nonlinear polarization using the density matrix equations.

We also carried out FWM experiments in this thesis, where the signal in the direction $2\mathbf{k}_2 - \mathbf{k}_1$ is detected directly using a sensitive photomultiplier tube. FWM is sensitive to different terms in the nonlinear polarization, and therefore can be used to obtain complementary information from DT. As an example, transient FWM in an inhomogeneously broadened 2-level system can be used to obtain the decoherence time (T_2^{dipole}) of the dipole transition [36], while transient DT is sensitive to the decay time of the dipole transition (T_1^{dipole}) [170]. The FWM signal is given by,

$$I_{FWM} \propto \int_{-\infty}^{\infty} dt \left| \mathbf{P}^{(3)} \right|^2 \tag{4.43}$$

An important technique used in previous experimental work that probed the spin coherence in semiconductors is FR [109, 189, 223, 258, 333]. FR experiments are performed in the pump-probe geometry, but measure the pump-induced rotation in the polarization of the linearly polarized probe beam, usually by setting up a polarization analyzer after the sample and using lock–in techniques to measure the signal from the detector at the difference of the modulation frequencies (for a typical experimental setup see Ref. [179]). The use of FR to probe quantum coherence is not new, and extends back several decades,

for example see Ref. [34]. The simplest way to understand the signal is by decomposing the probe beam into circularly polarized components, and calculating the birefringence caused by the pump [136, 227].

$$\Theta_F = \frac{L}{2I_0}\int_{-\infty}^{\infty} dt\, \Re(\tilde{P}_+\tilde{E}^*_{2,+} - \tilde{P}_-\tilde{E}^*_{2,-}) \tag{4.44}$$

where L is the length of the sample, I_0 is the probe intensity, and $P_\pm = \Re[\tilde{P}_\pm e^{-i\omega t}]$ are the left (right) circularly polarized components of the polarization, with similar expressions for E_2. Eq. (4.44) is not written in invariant form, but has to be applied separately for the cases when the probe is either s-polarized ($\tilde{E}^*_{2,+} = \tilde{E}^*_{2,-}$) or p-polarized ($\tilde{E}^*_{2,+} = -\tilde{E}^*_{2,-}$).

4.2 Experimental Setup for Transient Nonlinear Optical Spectroscopy

Figure 4.2 shows the experimental setup used for carrying out transient nonlinear spectroscopy measurements. The laser system used was a Coherent Mira-900D Ti:Sapphire oscillator system, operating at a repetition rate of 76 MHz. The Mira was pumped with either a Coherent Innova Saber argon-ion laser or a Coherent Verdi solid-state diode laser. The latter system showed significant improvement in performance categories such as stability, tuning range, ease of operation, and noise. The principles of Kerr lens mode-locked Ti:Sapphire oscillators are well known and will not be described here, but one may refer to the manuals for further information. The Mira-900D can be run in either femtosecond or picosecond modes. The femto-mode produces pulsewidths of $\sim$ 200 fsec while the pico-mode produces pulsewidths of $\sim$ 3 psec, with corresponding bandwidths of 7.5 meV and 0.4 meV around 760 nm. The pulsewidths change slightly as a function of the wavelength, but since our experiments are usually performed on the 4.2 nm QW whose emission is around 760 nm, we shall only report the numbers at that wavelength. The experiments presented in Chapter 5 use primarily the femto-mode, combined with a pulse-shaper which is described below.

The bandwidth of the Mira in femto-mode is much greater than even the inhomogeneously broadened PL linewidth ($\sim$ 1.5 meV) in our sample, and so we used pulse-shaping techniques to reduce the bandwidth for selective excitation. Another advantage of pulse-shaping is that one may use the same laser to drive different pulse-shapers thereby giving us the ability to perform non-degenerate measurements where two laser fields at different frequencies are used for the measurements. The two fields obtained are by definition highly

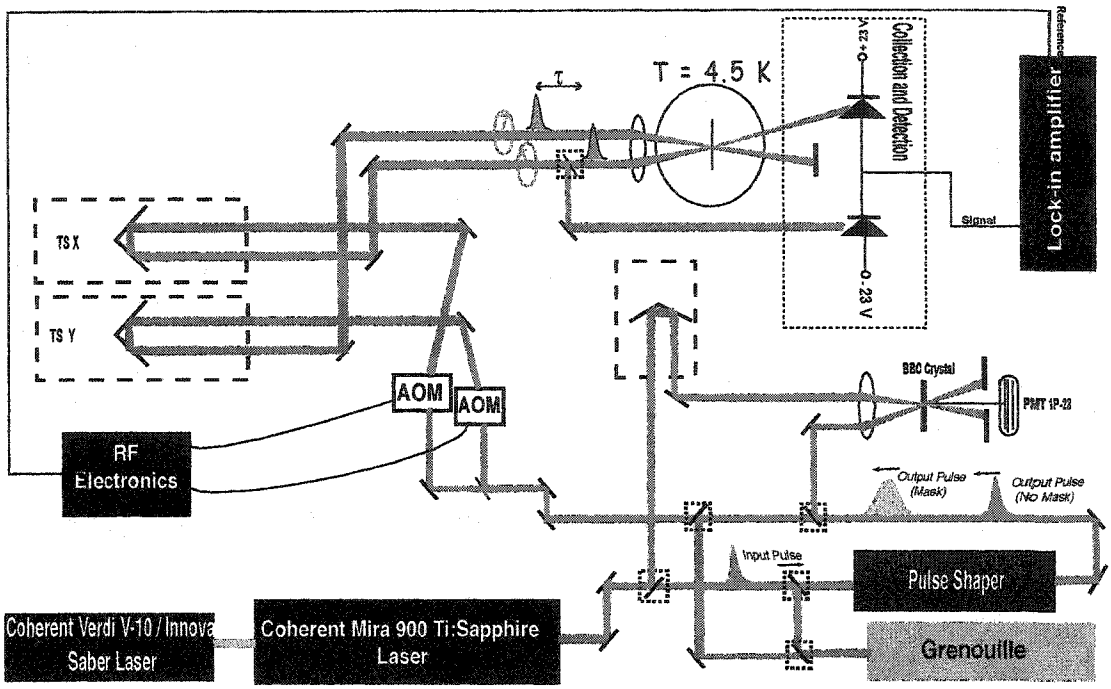

Figure 4.2: Experimental setup for transient nonlinear spectroscopy measurements. The pulses from the Mira can be shaped by the pulse-shaper or directly sent to the experiment using moveable mirrors. The pulses can be characterized in the time-domain using the GRENOUILLE or the cross-correlation setup, and in the frequency domain using a spectrometer. Traveling wave AOMs are used to impose modulation on both pump and probe beams, while simultaneously shifting the optical frequencies by 40 MHz. Mechanical delay lines (Newport model PM-500) allow us to change the relative timing between the pump and probe beams. The beams are focussed onto the sample placed in a magneto-optical cryostat using a 20 cm gradium lens.

mutually coherent which can be important when trying to probe quantum coherence that is excited through different coherent pathways [284, 407].

Figure 4.3 shows an idealized passive 4-f pulse shaper schematic. The incoming light is dispersed by the grating, and imaged in the Fourier plane by the first lens placed at a focal length away. The shaping occurs in this image plane, through a mask which filters various frequency components. The shaped pulse is then rebuilt through the other lens-grating pair. In the absence of any mask, the pulse shaper should be arranged to give rise to a dispersion-free pulse. In practice, the complete 4-f geometry can be made compact by using a mirror right after the mask. This is of course non-ideal and leads to a compromise between output power and the target pulse-shape. For our work, we used a 1800 grooves/mm grating blazed for 800 nm (ThermoRGL Model 83-06BK-330H) and an achromatic doublet lens of

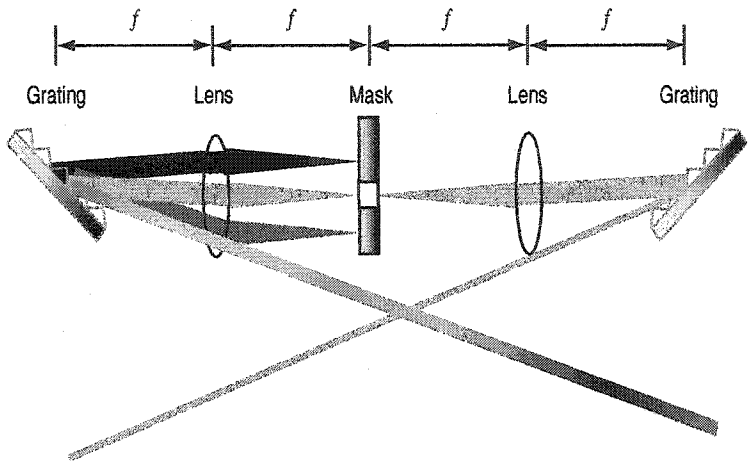

Figure 4.3: Passive 4-f pulse shaper schematic. The input light is dispersed by the grating, and shaped in the Fourier plane by the mask. The resulting pulse is rebuilt using the second lens-grating pair. The mask can also be replaced by an active element allowing for adaptive pulse shaping.

f = 20 cm.

The pulses emitted by the laser and after the pulse-shaper are characterized using both a second harmonic generation frequency resolved optical gating (SHG-FROG) instrument (Swamp optics model GRENOUILLE) as well as a cross(auto)-correlation setup. SHG-FROG allows one to characterize the intensity and phase of the pulses simultaneously, by spectrally resolving the auto-correlation of the pulse [310]. The GRENOUILLE is a variation of SHG-FROG where the thin nonlinear crystal is replaced by a thick nonlinear crystal which simultaneously provides the auto-correlation and spectral resolution functions, and the delay line is replaced by a Fresnel biprism. Since the traces are updated at 10 Hz, the instrument is an excellent tool for real time alignment of the pulse-shaper (by adjusting the lens distance) or the Mira laser (by adjusting the dispersion compensation prisms) for minimum area (time-bandwidth product) of the traces.

The alignment is reasonably verified for our pulse-shaper setup from Figure 4.4 (d) and (e) which shows the GRENOUILLE traces directly from the Mira and after passing through the pulse-shaper. As shown in Figure 4.4 (a), the pulse intensity is directly obtained from the GRENOUILLE trace (solid circles) while the autocorrelation trace is shown in open circles. The data was best fit to a Gaussian $I(t) = I_0 \exp(-\frac{4\ln 2 t^2}{\delta t^2})$ where δt is the full width at half maximum (FWHM) pulsewidth. From the GRENOUILLE trace we obtain an intensity pulsewidth (δt) of 203 fs, while the autocorrelation width (δt_a) is found to be 386.3 fs. For

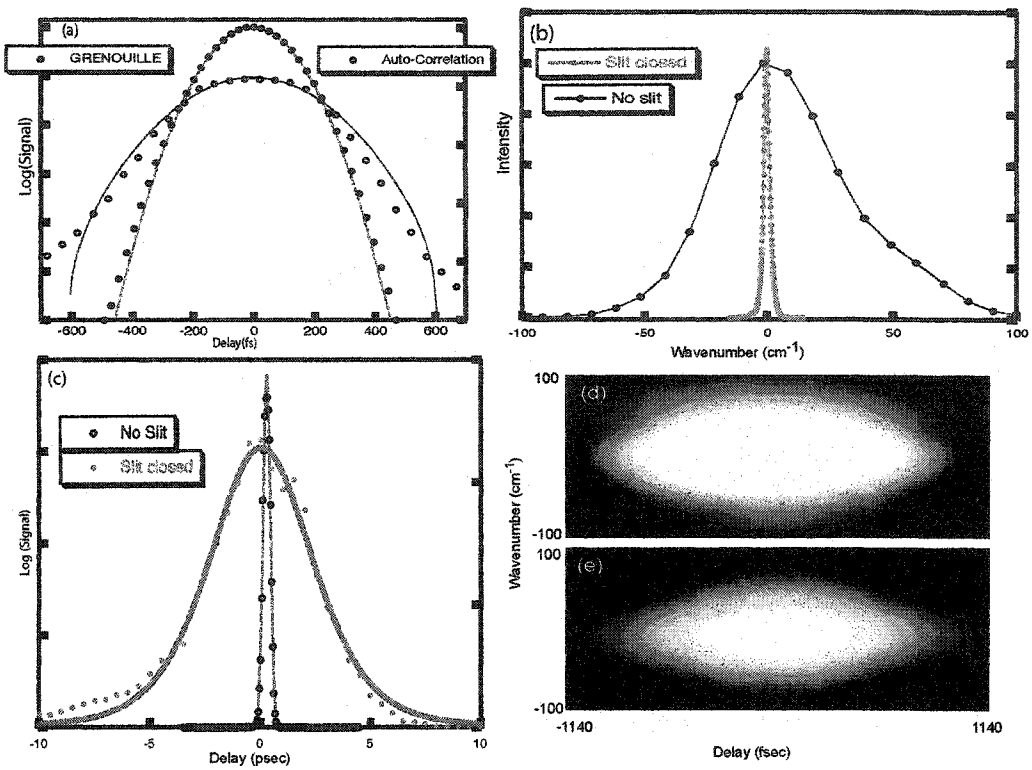

Figure 4.4: Experimental characterization of optical pulses. (a) Comparison of pulse intensity (after the pulse-shaper, without mask) as a function of time, obtained from the GRENOUILLE and auto-correlation. Solid lines show Gaussian fits, with the auto-correlation width = 386.3 fs and the actual pulsewidth from the GRENOUILLE trace = 203 fs. (b) Pulse intensity spectrum when there is no slit and with the slit closed down, with the corresponding FWHM $\delta\nu$ of 1.78 THz and 84.8 GHz respectively. (c) Corresponding time traces, as obtained through the cross-correlation. The FWHM of the cross-correlation trace, with the slit closed, is 5.36 ps. (d) GRENOUILLE trace obtained directly from the Mira-900D laser in femto-mode. (e) GRENOUILLE trace obtained after the pulse-shaper (without mask), showing that it is nearly dispersion free.

a transform limited Gaussian pulse, we expect $\delta t_a/\delta t = \sqrt{2}$, but we find the ratio here to be 1.9. Similarly, we also expect that the time-bandwidth product $\delta\nu\,\delta t = 0.44$. From Figure 4.4 (b) and (c) we found that for optimal slit width and position, $\delta\nu = 84.8$ GHz while $\delta t = 5.36$ ps which gives the product to be 0.46, again in reasonable agreement with Figures 4.4 (d) and (e) where the GRENOUILLE traces show that the pulse-shaper is nearly dispersion free. We will use this time-bandwidth product to estimate the pulsewidth for those cases when the slit width is not as narrow as shown in Figure 4.4. Note that to measure the laser spectrum when the slit is closed down, we used either a high-resolution single-grating spectrometer (Jobin-Yvon model HR-640) or a double-grating Raman spectrometer

(Jobin-Yvon model Spex 1403). The GRENOUILLE can measure spectra to approximately 1 nm resolution and pulsewidths lesser than $\sim$ 2.5 ps.

From Section 4.1.1, we know that the DT signal is proportional to the product of the pump and probe intensities. Lock-in detection leverages this fact to amplify the signal in a background-free manner, through modulation of the pump and probe intensities, and phase-sensitive detection at the difference or sum frequency. Two traveling-wave acousto-optic modulators (AOMs) were used to perform modulation of the pump and probe beams at a frequency of $\sim$ 1 MHz. The AOMs (IntraAction AOM-40N) were driven by the RF electronics setup shown in Figure 4.5.

The choice of modulation frequency around 1 MHz arises from several competing factors. Firstly, we cannot modulate higher than the repetition rate of the laser which would lead to "over-sampling" of the pulses. Secondly, the AOMs have a finite bandwidth of ≈ 5 MHz around their carrier frequency of 40 MHz, which implies we cannot modulate at higher frequencies. Thirdly, we would like to modulate at high frequencies since nonlinearities due to thermal effects and other slow processes should presumably be weak at those frequencies. It had been found in earlier neutral quantum dot samples that these effects were in fact suppressed at modulation frequencies $\geq$1 MHz [243, 244]. Finally, a useful fallout of modulating with AOMs is that the laser noise is significantly reduced at higher frequencies, as well as allowing one to pick higher reference frequencies to feed into the lock-in amplifiers, which diminishes the electrical noise. Further, the beams are taken from different diffraction orders (+1 and -1 respectively) which implies the optical frequencies differ by 80 MHz, resulting in damping of terms due to classical interference from mixing of the beams on the detector.

The setup shown in Figure 4.5 consists of two IntraAction ME405 AOM driver signal processors, which can synthesize a carrier frequency of 40 MHz modulated by an external output, and amplify the resulting signal to the levels needed to drive the AOMs. The modulation is supplied by two phase-locked Stanford DS-345 signal generators. The signal generators need to be phase-locked because they are subsequently used to generate the reference frequency for the lock-in amplifier, and any wandering in the phase of the reference signal will show up as phase noise in the lock-in, and could lead to artificial broadening of lines in frequency-domain nonlinear spectra. The reference frequency used is typically 40 kHz for the measurements. It should be noted that we introduced around 10 dB of

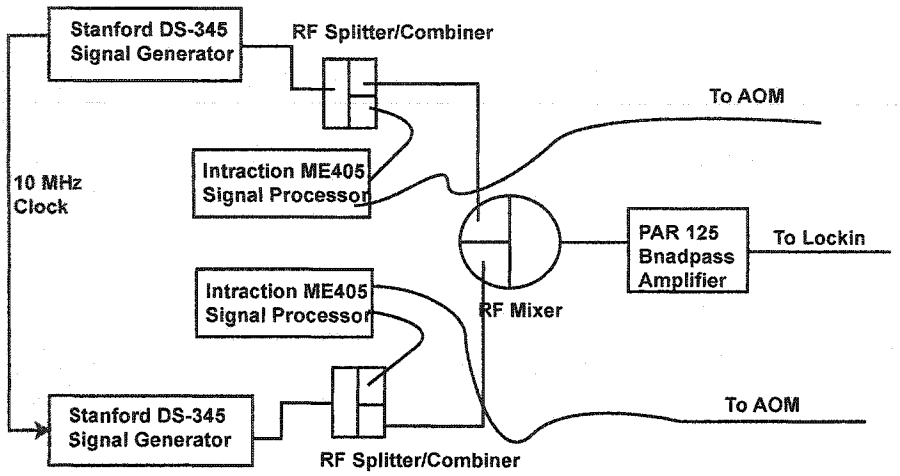

Figure 4.5: Circuit diagram for radio frequency electronics setup used to drive the AOMs. The mixer and band-pass amplifier together produce the reference frequency for the lock–in amplifier.

attenuation at both the inputs of the RF mixer used to generate the reference frequency. This is to avoid cross-talking between the pump and probe modulation arms caused by feedback through the RF mixer, otherwise we observe nonlinear signal without the pump beam on the sample. To regenerate the reference signal, a PAR125 bandpass amplifier is used to amplify the reference frequency to a level of 300 mV p-p required for the lock-in amplifiers (Stanford Research SRS830).

Figure 4.6 shows two typical collection setups for performing polarization sensitive measurements of either DT or FR. Figure 4.6(a) shows the setup used to detect simultaneously the DT signal when the pump and probe have the same or orthogonal circular polarizations. The probe can be viewed as a combination of left and right circular components, which the $\lambda/4$-waveplate converts to s- and p- polarizations, that are subsequently sent in different directions by the polarizing beamsplitter. The beams are detected on identical Silicon photodiodes that are reverse biased at 23 V by a battery, but the currents from the photodiodes are in opposite directions. Alternatively, we used the balanced detection setup shown in Figure 4.2 where the probe beam is split prior to the cryostat and collected on identical Silicon photodiodes that are reverse biased, and the currents are summed in a T-junction and sent to the lockin. The balanced detection was performed by adjusting the power on the reference arm, and monitoring a voltmeter. This approach requires that

we perform separate scans for same (orthogonal) circular polarization configurations. Both approaches yield similar results, since common-mode laser intensity noise is reduced by taking the difference of the signals.

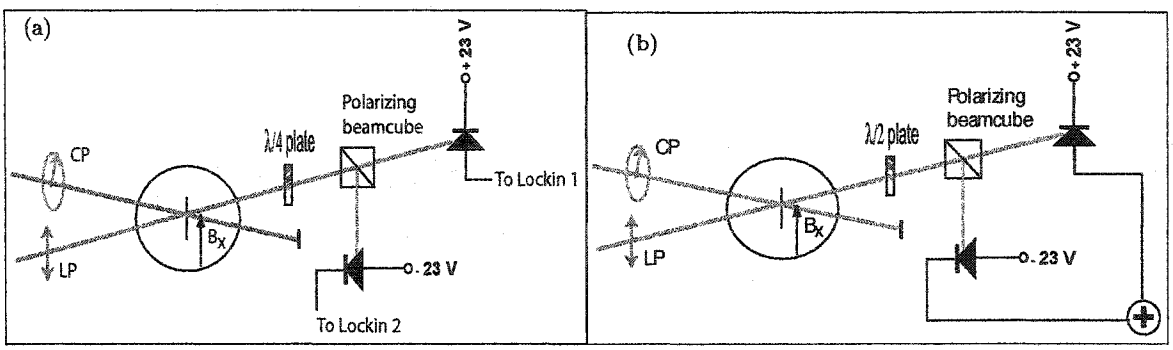

Figure 4.6: Collection optics setup for (a) simultaneous detection in DT and (b) FR. (a) Collection optics setup for simultaneous detection in DT. The linearly polarized (LP) light is a superposition of components parallel and orthogonal to the circularly polarized (CP) light, and lockin 1(2) detects the parallel (orthogonal) configuration. (b) Collection optics setup for FR experiments. The $\lambda/2$-waveplate after the sample is arranged at an angle for balancing the two photodiodes in the absence of the pump, *i.e.* by rotating LP light by 45°, and the difference signal is due to pump-induced rotation.

In Figure 4.6(b), the setup for FR is shown, where the linearly polarized probe is rotated after the sample by 45°, and the beamsplitter sends equal intensities of light to the two photodiodes. Pump-induced rotations will be picked up in the difference signal that is sent to the lock-in. FR was only briefly attempted in this thesis, but further improvements could be made in the setup by modulating the polarization rather than the intensity of the pump beam using for example a photoelastic modulator. In that case, the pump beam would vary between right and left circular polarizations, and the probe beam could be mechanically chopped [179]. The sample was placed in either a standard continuous-flow liquid helium cryostat (Janis model 10DT) or magneto-optical cryostat (Janis model 14CNDT). The latter cryostat was modified by placing large numerical aperture lenses close to the sample to enhance the collection efficiency for both single QD PL and DT studies.

4.3 Experimental Setup for Frequency Domain Nonlinear Optical Spectroscopy

Coherent and incoherent dynamics are both obtainable from transient DT and FWM measurements, but the availability of highly frequency-locked CW lasers provides an ex-

tremely sensitive tool for studying the nonlinear response of materials. Furthermore, it can be shown that the signals in the frequency domain nonlinear spectroscopy measurements are not merely the Fourier transform of the signals in transient measurements [41,135,363]. As an example, transient DT experiments cannot extract information about perturbation pathways that lead to zero-delay terms (the so-called "coherent artifacts") while such pathways lead to resonant denominators in CW non-degenerate DT experiments depending on the detuning of two independent mutually coherent CW laser fields [204,284]. Another example of the sensitivity of CW spectroscopy occurs when attempting to measure extremely long decay times of either coherent or incoherent processes, which would require unwieldy and bulky delay lines in the time domain, whereas their signature in the frequency domain is a narrow resonance that may be very precisely measured using highly frequency-stable lasers [50].

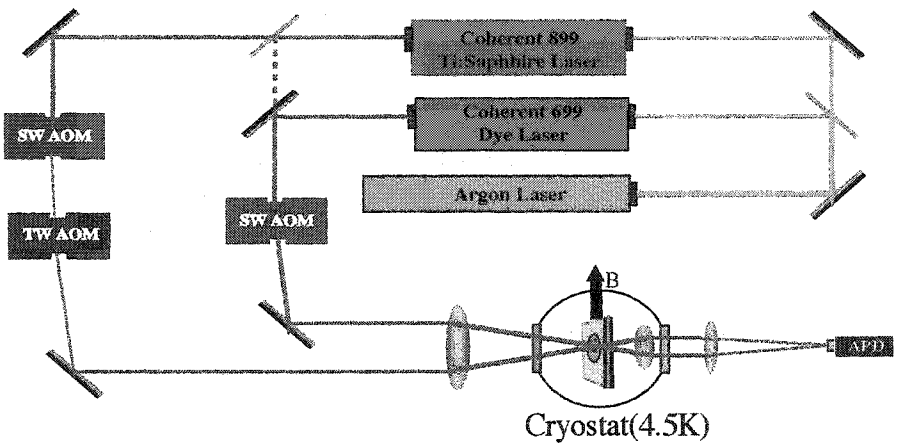

Figure 4.7: Experimental setup for frequency domain nonlinear spectroscopy measurements.

Figure 4.7 shows the experimental setup used for high-resolution frequency domain degenerate and non-degenerated nonlinear spectroscopy measurements. In degenerate experiments, the pump $(\mathbf{E_1}, \Omega_1)$ and probe $(\mathbf{E_2}, \Omega_2 = \Omega_1)$ beams are obtained from a Ti:Sapphire ring laser (Coherent model 899-29) which was frequency locked to a temperature-stabilized Fabry-Perot external reference cavity. For non-degenerate experiments (fixed Ω_1, scan Ω_2), the pump beam is from a frequency-stabilized dye ring laser (Coherent model 699-21), and the probe beam is from the 899-29. The 899-29 linewidth was found from measurements to be ≤ 1 MHz (4 neV) while the mutual coherence bandwidth between the two lasers was found to be ~ 4 MHz (16 neV).

A variety of modulation techniques were used in this work for the CW experiments, because the fields can be modulated at higher frequencies. One example is shown in Figure 4.7 where standing-wave AOMs (IntraAction SWM-502AE3) are used to modulate at frequencies of 100 MHz, and a traveling-wave AOM is used to shift the optical frequency by 40 MHz, for reasons similar to that described in Section 4.2. Other modulation options include using traveling-wave AOMs directly, or using mechanical choppers. Lower modulation frequencies may be needed when trying to detect processes with extremely slow relaxation times. Since DT can be visualized as the transmission with the pump on subtracted from the transmission with the pump off, if the process of interest is slow compared to the modulation period then there will be no change in the transmission due to that particular pathway, therefore washing out the expected signal.

We used a 20 cm gradium lens to focus the lasers onto the apertured sample for the experiments. A Silicon avalance photodiode (Hamamatsu model S3884) biased slightly below breakdown was used for detection, after determining that the bias voltage represents the best gain/noise ratio [352]. In this thesis work, we primarily used the CW spectroscopy in single QD studies so as to isolate narrow resonances from single charged QD trions or single neutral QD excitons, as detailed in Section 7.1. The degenerate experiments were used to measure the dipole decoherence time (T_2^{dipole}) and the non-degenerate experiments allowed us to investigate pure dephasing processes and to measure the population decay time (T_1^{dipole}).

4.4 Chapter Summary

Section 4.1.1 presented the four-level model and the density matrix master equations that are used to calculate the nonlinear polarization created in nonlinear spectroscopy experiments. Section 4.1.2 demonstrates the application of the nonlinear polarization to calculate the experimental signals that are anticipated for different experimental configurations. The chapter consisted of a description of the experimental techniques for transient nonlinear spectroscopy (Section 4.2) and frequency domain nonlinear spectroscopy (Section 4.3). In the former section, we elaborated on the characteristic of the laser system and pulse-shaping apparatus used to produce laser pulses, and on the modulation and collection techniques. The latter section consisted of a brief description of the experimental setup, and on the

advantages and utility of CW nonlinear spectroscopy. Starting from the next chapter, we will present the experimental results obtained using the nonlinear spectroscopy techniques that have been discussed.

CHAPTER 5

Transient Nonlinear Spectroscopy: Coherent Optical Excitation of Electron Spin Coherence

Semiconductor QDs feature prominently in many proposals for solid-state QC, due to the availability of a vast infrastructure for advanced fabrication techniques and the relative ease of integration into devices [228, 261, 285]. The qubit in optical implementations of QDQC schemes is usually represented by the state of the electron spin vector in the conduction-band ground state of a CQD [261, 378, 425], or the state of the excitonic optical Bloch vector denoting the presence or absence of an exciton in the QD [122, 283, 311]. In the latter case, considerable progress has been made in demonstrating many of the key DiVincenzo requirements for QC [285], such as single qubit rotations [336, 353, 369, 390], quantum entanglement [284] and conditional quantum logic gates [408]. However, the relatively short decoherence time associated with the excitonic transitions ($\sim$100 psec in large dots [204, 382] and $\sim$1 nsec in small self assembled dots [245, 320, 321]) represents a limitation in such systems for the implementation of quantum error correcting codes.

By contrast, the electron spin experiences relatively weak interactions with its crystal environment, and theoretical predictions for the single spin decoherence time (T_2) in GaAs QDs range from 1–100 μs [371, 376, 400, 401]. A recent measurement of the spin relaxation time (T_1), which ultimately limits T_2, in single GaAs QDs estimates $T_1 \sim 1\,\mathrm{ms}$ [437]. Long spin dephasing times (T_2^*), limited by inhomogeneous broadening, ranging from 3–100 ns have also been observed in bulk semiconductors [223, 366], n-doped ZnSe QWs [189] and chemically synthesized neutral nanocrystals [258]. However, the measurements in the latter mentioned work are limited by the recombination time of the excitons that are created, and therefore do not measure the true spin coherence of an electron in the ground state of the QD. To date, the only other measurement of the spin relaxation time was in self-assembled

InAs CQDs using nearly-resonant PL techniques to measure the degree of polarization of the recombining electron-hole pairs [365]. Their experiment does not, however, preserve coherence since the electron-hole pairs relax from continuum states and the spin polarization is created by incoherent optical pumping of the electron ground state, thereby only measuring the longitudinal spin relaxation time ($T_1 \sim 15$ ns). Therefore, it is important to excite and detect the spin coherence with resonant optical fields and measure the spin coherence time in CQDs, and to compare with theoretical predictions regarding the coherence lifetime. The alliance of ultrafast coherent optical control techniques and the long decoherence times of single electron spins in QDs was proposed for quantum computation through optical coupling of the QD electron spin to cavity photons [261, 273, 292] and charged excitons [378, 415, 420, 421, 425, 434] as discussed in Section 1.2. Hence, the study of the optical transitions of charged QDs is important for implementation of optically driven spin QC.

Section 5.1 exploits the power of transient nonlinear spectroscopy to measure the T_1 and T_2 times of the trion transition. In Section 5.2 we report on the coherent optical excitation of electron spin coherence in the ground state of charged GaAs QDs via the intermediate charged exciton (trion) state. Coherent optical fields are used for the creation and detection of the Raman spin coherence between the spin ground states of the charged quantum dot, which forms an integral part of proposals for optically driven spin based quantum computing [434]. The measured spin coherence time is likely limited by the nature of the spin ensemble, but approaches 10 ns at zero field. The results will further show that there are two contributions to the electron spin coherence: an induced part arising from coherent optical coupling of the spin states through stimulated Raman excitation, and a *spontaneously generated coherence (SGC)* arising from radiative recombination of the trion state into the spin states.

5.1 Ensemble Nonlinear Optical Spectroscopy

Under photo-excitation with an above-gap ultrafast laser pulse, the excited carriers undergo evolution back to thermal equilibrium with the lattice. The initial excitation is coherent with the exciting laser field, and creates a macroscopic optical polarization, which undergoes dephasing through scattering from other excitons, carriers, impurities or lattice vibrations. While the dephasing process proceeds on the timescale of T_2^{dipole}, the carriers

interact via Coulomb and phonon scattering to evolve from a non-thermal to a quasi-equilibrium Fermi-Dirac distribution. Finally the electrons and holes recombine to return the semiconductor to equilibrium on the timescale of T_1^{dipole}. In the absence of pure dephasing processes such as the scattering events described above, $T_2^{dipole} = 2T_1^{dipole}$. Probing the dynamics with DT and FWM reveals a wealth of information on the processes that underlie the evolution towards equilibrium, and on the differences between correlated systems such as semiconductors and non-interacting systems such as atoms. Several processes unique to many-body systems like band-gap renormalization, screening, phase-space filling and higher-order Coulomb-correlations impact the nonlinear spectroscopy measurements in semiconductors and semiconductor heterostructures and excellent reviews may be found in Refs. [101, 170, 322].

The setup for transient nonlinear spectroscopy measurements is shown in Figure 4.2 and discussed in Section 4.2. For the measurements discussed in this section, pump ($\mathbf{E_1}$) and probe ($\mathbf{E_2}$) pulses were obtained from the Mira-900D operating in femto-mode and subsequent pulse-shaping to reduce the bandwidth sufficiently to allow for selective excitation within the spectrum. The resulting pulse bandwidth (FWHM = 0.84 meV) is still much larger than the splitting between the electron spin states, which is crucial for the observation of the Raman coherence, as described in Section 5.2. Coherent transient pump-probe measurements show that we are able to resonantly excite and detect trion states in the ensemble. In this chapter, the sample used was 612F-3NA, an unapertured piece of sample 612F, which was mounted on a sapphire disk and etched for DT experiments as described in Section 2.3.

The DT spectrum is obtained by tuning the frequency of the laser fields using the pulse shaper while keeping the delay between the pulses at 6 psec. The DT signal was obtained by detecting only the probe beam, using balanced phase-sensitive detection, and the fields were modulated at $\sim$1 MHz for lock-in detection at the difference frequency. The homodyne detected collinear four-wave mixing response thus measured is sensitive to both incoherent and coherent dynamics (see Section 4.1.2). A 25 cm focal length lens was used to focus the pump and probe fields onto the sample kept in a standard continuous flow liquid helium cryostat (Janis Model 10DT). Figure 5.1 (a) shows the nonlinear response from the 15-monolayer region of the 4.2 nm quantum well, in comparison to the PL spectrum. The correspondence to peaks earlier identified in PL as trions (T) and excitons (X) is clear.

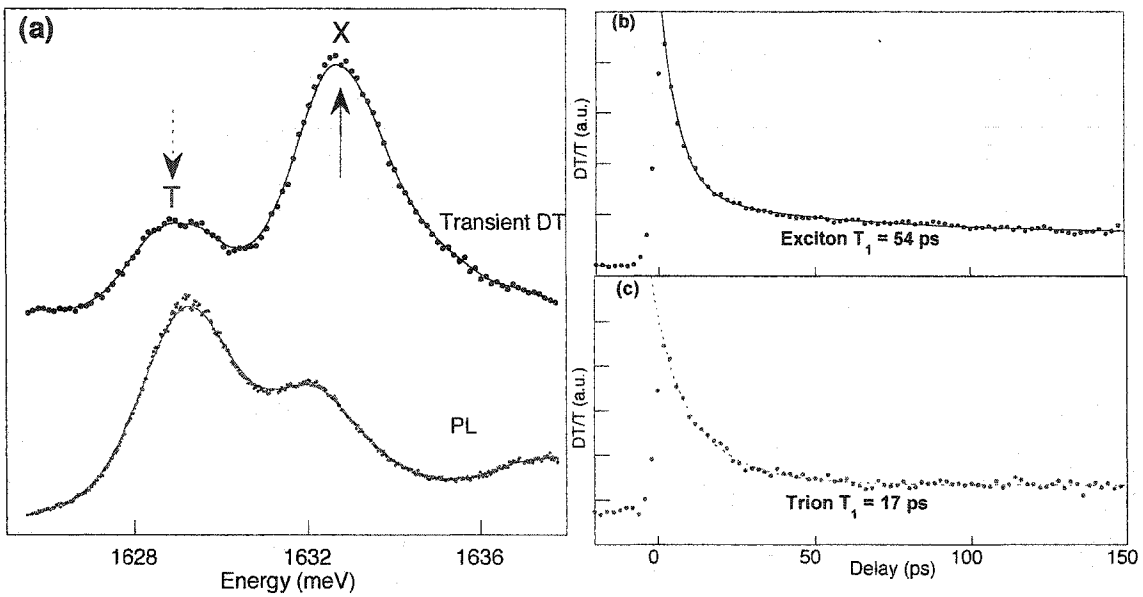

Figure 5.1: Differential transmission signal from an ensemble of CQDs. (a) Comparison of ensemble transient DT spectrum with PL spectrum. The delay between the pulses is fixed at 6 ps. (b) and (c) DT as a function of delay between pump and probe pulses. Data in (b) [(c)] corresponds to keeping the laser wavelength fixed at the solid [dashed] arrow shown in (a) denoting X[T]. Both curves are then fit to biexponentials, with slow components of 17.2 ± 4.8 psec (T), and 54.2 ± 8.5 psec (X). Fast decay times were found to be 7.3 ± 4.4 psec (T) and 6.1 ± 0.2 psec (X).

Figure 5.1 (b) and (c) show delay scans obtained with laser wavelength fixed at the X and T peaks respectively. Biexponential curve fits applied to the data yield fast and slow decay rates for both curves. For T, $T_{fast} \sim 7$ psec, while $T_{slow} \sim 17$ psec, whereas for X, $T_{fast} \sim 6$ psec, and $T_{slow} \sim 54$ psec. The slow decay times are attributed to radiative recombination (known as T_1^{dipole}), and the fast decay components to acoustic phonon-mediated spectral diffusion [214] which controls the establishment of thermal equilibrium among the excited carriers. Initial results from ensemble CW hole burning spectroscopy indicate narrow holes burned by the pump laser accompanied by spectral diffusion in these systems [435], and the radiative recombination times for X are in good agreement with earlier reports for the interface fluctuation QDs [204, 382]. Time-resolved PL measurements for T in wider QWs have reported timescales around 4–10 times longer than the values reported above [216, 307]. However, the additional confinement in QDs would tend to increase the electron-hole wavefunction overlap and thereby enhance the radiative decay rate. Thus, the results are consistent with a picture of localization of trions and excitons by the monolayer high

islands. The narrow resonances observed in single QD linear (Section 3.3) and nonlinear spectroscopy (Section 7.1) provide further evidence for the above picture.

In actual data analysis, however, difficulties arise from variations in the ensemble measurements as the laser frequency or position on the sample are changed, which make the interpretation harder. As noted in Chapter 2, the presence of a large number of surface states leads to a built-in electric field in the sample in the absence of illumination. Under non-equilibrium conditions such as photo-excitation, carriers that are possibly trapped in low-lying defect states or in donors that migrated to the QW region become localized by the dot potential, leading to the formation of trions under resonant excitation. As an example, excitation with a white-light source or a green HeNe laser or temperature drift leads to changes in the relative strength of the X and T peaks, as also observed in the PL spectrum (see Figure 2.6). Thus, it is clear that changes in the charge distribution in the sample could drastically affect the signal, and we observed variations both in the sign and magnitude of the relative amplitudes of the fast and slow exponential decay terms.

Self-diffracted FWM measurements, with signal detected on a photo-multiplier tube (Hamamatsu Model R928) in the $2\mathbf{k}_1 - \mathbf{k}_2$ direction, are shown in Figure 5.2. The FWM signal can be viewed as the diffraction of the pump field from the grating formed by the interference between the pump and probe fields. The measured FWM signal from the X (T) resonance decays exponentially on a time scale of ~ 3 (4) psec. In the presence of inhomogeneous broadening, the decay time in self-diffracted FWM corresponds to $T_2/4$ [36], which yields $T_2 \approx 13\,(15)$ for the exciton (trion). In the low-field $\chi^{(3)}$ regime, the signal strength is expected to vary as $I_1^2 I_2$, and our measurements were carried out in this regime but under near-saturation conditions for maximum signal to noise. However, by lowering the intensity further, changes in the decay times were observed. As shown in Figure 5.2 (b) T_2 as long as 28 psec for the trion were measured after performing a careful study of the power dependence of the decay times [407]. Again, slight variations in the decay time were noted with the laser frequency and position.

The power dependence arises because an ensemble of semiconductor QDs does not correspond to an ensemble of non-interacting two-level systems. As the intensity is increased, many-body effects come into play that lower the dephasing time. The study of many-body correlations using transient DT and FWM experiments is an area of intensive research, and a great deal of work has been done on modeling the nonlinear response in DT and FWM

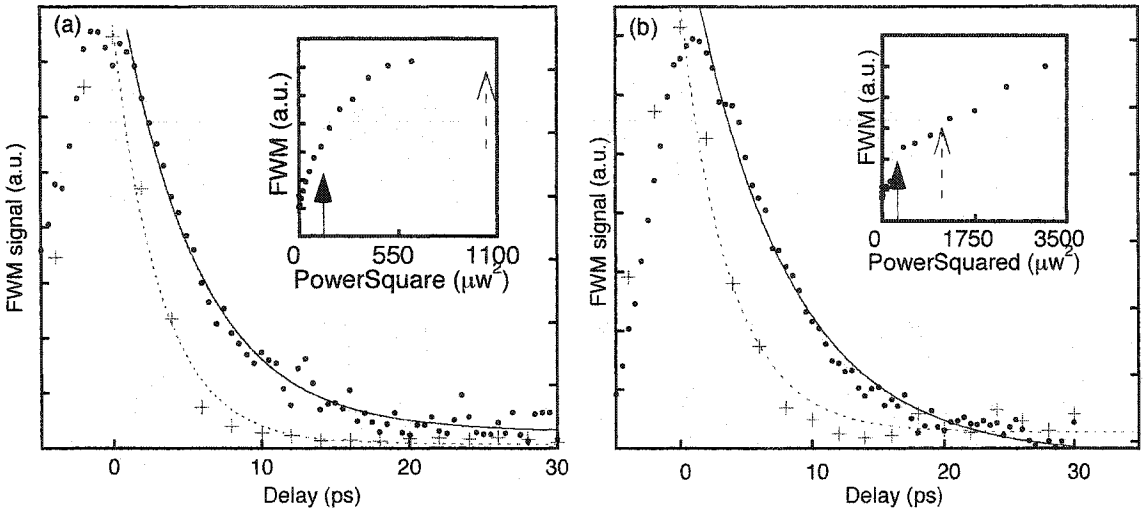

Figure 5.2: Four-wave mixing measurements on an ensemble of CQDs. (a) FWM signal obtained at the X resonance, as a function of the pump-probe delay. The symbols + (•) represent data taken with the power fixed at the dashed (solid) arrows shown in the inset. The data are fit to an exponentially decaying function (solid curves), yielding exponential decay times of 3.2 ± 0.2 ps (5.3 ± 0.2 ps), which then yields $T_2 = 12.8$ ps (16.2 ps). Inset: Plot of FWM signal strength as a function of the pump power I_1^2.(b) FWM signal obtained at the T resonance, as a function of the pump-probe delay. The symbols + (•) represent data taken with the power fixed at the dashed (solid) arrows shown in the inset. The data are fit to exponentials, yielding exponential decay times of 3.8 ± 0.4 ps (7.2 ± 0.3 ps), which then yields $T_2 = 15.2$ ps (28.8 ps). Inset: Plot of FWM signal strength as a function of the pump power I_1^2. Power dependence and low intensity FWM scans courtesy of Dr. Xiaoqin Li [407].

using modified semiconductor Bloch equations for a mean-field Hartree-Fock approach and quantum kinetics theory when the mean-field theory starts to fail [101, 170, 322]. The focus of this thesis work is however on the optical manipulation of the electron spin states in CQDs, rather than on the possible many-body effects that are present. We will therefore proceed to ignore these, except insofar as they might represent higher-order terms that would need to be taken into account in a more complete theory. The important point to note is that T_2 and T_1 obtained for the trion optical dipole transition do not seem to deviate significantly from that of the excitonic dipole. The above conclusions will be borne out further in Section 7.1 where single dot measurements using frequency-stabilized lasers are described.

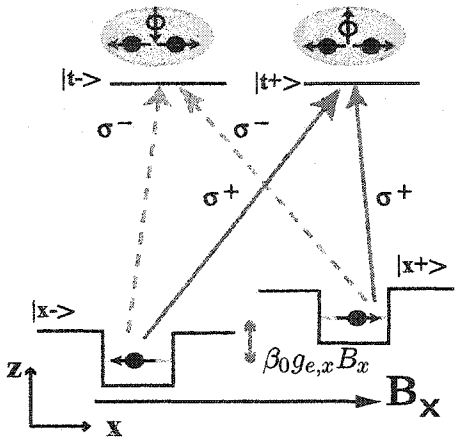

Figure 5.3: Excitation level scheme and selection rules for a CQD. In the excitation picture, the CQD ground states are labeled by electron spin states along the x-axis split by $\beta_0 g_{e,x} B_x$, and the trion states are labelled by the heavy-hole angular momentum projection along z-axis, as explained in the text. Solid (dashed) lines denote transitions excited by $\sigma^+(\sigma^-)$ light. The dipole matrix elements are derived in Section 3.2 to be $\mu_{t-,x-} = -\mu_{t-,x+} = -\wp\epsilon_+$, $\mu_{t+,x-} = \mu_{t+,x+} = \wp\epsilon_-$

5.2 Raman Quantum Beats Due To Electron Spin Coherence

An essential ingredient for quantum logic operations is the coherent manipulation of the qubit wavefunction, along with the ability to perform a complete bit flip, collectively known as qubit rotations or Rabi oscillations. In this section, we report on the coherent optical excitation of electron spin coherence in the ground state of a CQD ensemble via resonant excitation of the intermediate trion state. Coherent optical excitation, resonantly enhanced by dipole coupling to the trion state, leads to a quantum mechanical superposition of the electron spin states, which we detect through the time evolution of the quantum phase.

As shown in Section 3.1, the Hamiltonian for the electron in a CQD leads to the excitation level scheme shown in Figure 5.3. In the absence of any magnetic fields, the Zeeman sublevels ($|m_z = \pm 1/2\rangle \equiv |z\pm\rangle$) of the electron spin in the conduction band ground state of a CQD are assumed to be degenerate, where the z-axis is taken to be the growth direction. The singlet trion state consists of paired electron spins bound to a heavy-hole, which implies its total angular momentum projection is determined purely by the heavy-hole angular momentum direction ($|J_{hhz} = \pm 3/2\rangle \equiv |t\pm\rangle$). Application of a magnetic field (B_x) along the x-axis (Voigt geometry) aligns the electron spin states parallel and anti-parallel to the field, denoted by the eigenstates $|x\pm\rangle = (|z+\rangle \pm |z-\rangle)/\sqrt{2}$, and causes a splitting $\hbar\omega_c = \beta_0 g_{e,x} B_x$ between the eigenstates; where β_0 is the Bohr magneton and $g_{e,x}$ is the electron g-factor

along the x-axis. As discussed in Section 3.2, due to the large splitting between the heavy-hole and light-hole states induced by quantum confinement, the hole angular momentum is pinned to the growth direction and cannot follow the magnetic field, resulting in vanishing g-factors for the hole in the x-direction [77, 79, 110, 428]. Thus, the trion states are unaffected by the field and optical transitions can occur with $\sigma^-(\sigma^+)$ circular polarization between $|x\mp\rangle \rightarrow |t-\rangle(|t+\rangle)$, as shown in Figure 5.3.

The set of three levels $\{|t-\rangle, |x\pm\rangle\}$ and transitions thus engineered through the application of the magnetic field corresponds, in the language of quantum optics, to a Λ-system where the two nearly-degenerate ground states are not susceptible to decay. These systems, and their counterparts the V-systems, have been used to demonstrate a variety of fascinating phenomena such as electromagnetically induced transparency [83, 84, 184, 377, 416], lasing without inversion [56, 67, 70], slowing [259] and storage of light pulses [340, 346, 392]. The basis for all these effects is the non-radiative quantum coherence, often referred to as a Raman coherence, created between two closely-spaced levels that are coupled to a common state(s). Previous works have probed the Raman coherence quantum beats due to excitons in semiconductors by means of transient nonlinear spectroscopy [80, 215, 373, 446]. As reported in Section 3.3, the characteristic signatures of single QD trions and excitons

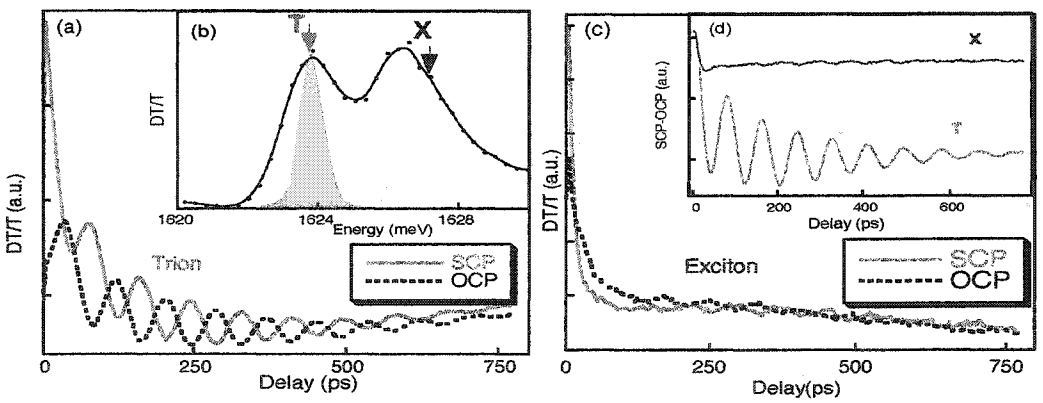

Figure 5.4: DT signal obtained for SCP and OCP configurations in the Voigt geometry at the trion and exciton resonances. (a) DT signal at an in-plane magnetic field $B_x = 6.6$ T obtained when the laser pulse is tuned to selectively excite the T resonance. Solid (dashed) lines show signal obtained for SCP (OCP) pump and probe fields. (b) DT spectrum with the pulse delay fixed at +10 ps. The shaded region is the pulse spectrum, and arrows at T (X) label the trion (exciton) resonances. (c) DT signal at the X resonance for $B_x = 6.6$ T showing no oscillations. (d) Data shown is difference between SCP and OCP signals at the T and X resonances.

in magnetic fields were detected from an apertured piece of a similar sample (912F-2A). Measurements by our collaborators on the sample 612F showed a vanishing hole g-factor as well as a small electron g-factor that implies a maximum splitting $\hbar\omega_c \sim 80$ μeV at the highest fields reached in our experiment [384]. The sample was placed in the superconducting magnetic cryostat and maintained at a temperature of 4.8 K in the Voigt geometry.

Figure 5.4(b) shows the spectrum obtained by fixing the delay between the pulses at +10 ps and tuning the laser, with two peaks corresponding to trions (T) and excitons (X) trapped in charged and neutral QDs, respectively. The binding energy for the trion of 2.7 meV extracted from the spectrum is in good agreement with that obtained in [384]. In Figure 5.4(a)[(c)], the data obtained as a function of delay when the laser is tuned to resonantly excite charged QDs at T[X] is shown. When the laser fields have the same (SCP) or orthogonal circular polarization (OCP), long-lived oscillations are observed that differ by a π-phase shift. We can isolate the oscillatory part of the signal by subtracting the SCP and OCP data, which is plotted in Figure 5.4(d) when the laser is tuned to X or T. We monitored the intensity dependence of the signal and all the data shown in this paper were taken in the $\chi^{(3)}$ regime. Note that there were no oscillations at the T resonance for any of the linear polarization configurations, and when the sample was placed in the Faraday geometry, with field parallel to the growth direction.

The long-lived oscillation at the trion energy shows the predominantly coherent evolution of the quantum mechanical superposition of the QD electron spin states. In contrast to the T resonance, tuning the laser to the X resonance results in vanishing of the beats. No oscillations are observed at the exciton energy in the Voigt geometry, due to overdamping caused by the small exciton g-factor and the short recombination time ($\sim$ 50-100 ps) that limits the coherence of optically injected electron spins in neutral interface fluctuation QDs [204, 284, 381, 382]. The absence of oscillations may be viewed from the standpoint that because QD excitons correspond to a V-system, where the upper states can decay due to exciton recombination, the Raman coherence lifetime cannot exceed the recombination time.

We performed a careful study of the magnetic field dependence of the oscillations at T, and the data at a few representative magnetic field values is shown in Figure 5.5. The data shown in Figure 5.5(a) was fitted using the equation,

$$DT_{scp-ocp} = C_1 e^{-2\Gamma_t \tau} + C_2 e^{-\gamma_s \tau} \cos(\omega_c \tau - \phi) \tag{5.1}$$

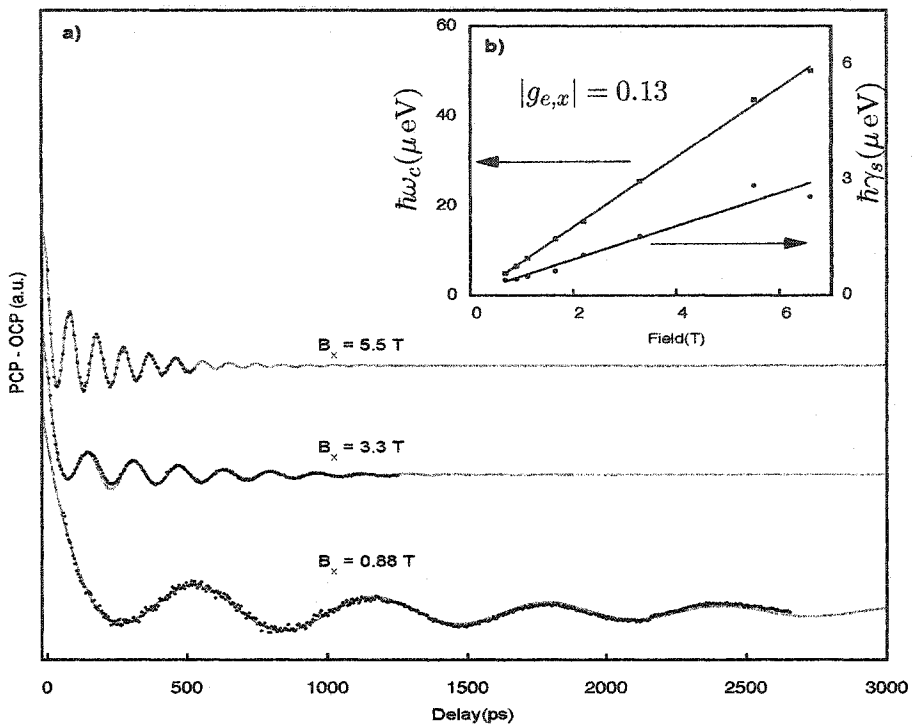

Figure 5.5: Magnetic field dependence of the spin quantum beats. (a) DT signal obtained by taking the difference between data for SCP and OCP configurations at different magnetic field values. Solid lines denote fits obtained using Eq. (5.1). (b) The fitted values for $\hbar\omega_c$ and $\hbar\gamma_s$ are plotted as a function of the field. The solid lines are linear fits to the data, which yields a in-plane g-factor $|g_{e,x}| = 0.13$. The zero-field intercept for $\hbar\gamma_s$ is $0.067\,\mu$eV, which implies a zero-field decay time of 9.8 ns.

and the resulting values for $\hbar\omega_c$ and $\hbar\gamma_s$ are plotted in Figure 5.5(b) as a function of the field. The oscillation frequency is expected to depend on the splitting between the states which allows us to extract the value of $|g_{e,x}|$ to be 0.13 in good agreement with [384]. This technique does not allow us, however, to determine the sign of $g_{e,x}$.

We can understand the results using the density matrix formulation for the four-level scheme shown in Figure 5.3, wherein the pump pulse coherently excites the Raman coherence ($\rho_{x+,x-}$) to second order in the field, and the probe pulse converts this to a nonlinear polarization ($\rho_{t-,x-}$) that co-propagates with the probe field. This polarization is phase-sensitively homodyne detected with the probe pulse by a square-law detector in the experiment. The coupled equations for the Raman coherence and the nonlinear polarization

between the levels $\{|x\pm\rangle, |t\pm\rangle\}$ are given in the rotating-wave approximation by,

$$\dot{\rho}_{t-,x-} = -i(\omega_g - i\gamma_t)\rho_{t-,x-} - i\frac{\wp}{2\hbar}E_+(t)(\rho_{t-,t-} - \rho_{x-,x-}) + i\frac{\wp}{2\hbar}E_-(t)\rho_{t-,t+} - i\frac{\wp}{2\hbar}E_+(t)\rho_{x+,x-} \tag{5.2}$$

$$\dot{\rho}_{t+,x-} = -i(\omega_g - i\gamma_t)\rho_{t+,x-} - i\frac{\wp}{2\hbar}E_-(t)(\rho_{t+,t+} - \rho_{x-,x-}) + i\frac{\wp}{2\hbar}E_+(t)\rho_{t+,t-} - i\frac{\wp}{2\hbar}E_-(t)\rho_{x+,x-} \tag{5.3}$$

$$\dot{\rho}_{x+,x-} = -i(\omega_c - i\gamma_s)\rho_{x+,x-} - i\frac{\wp}{2\hbar}E_+(t)\rho_{x+,t-} + i\frac{\wp}{2\hbar}E_+(t)\rho_{x+,t+} - i\frac{\wp}{2\hbar}E_+^*(t)\rho_{t-,x-} - i\frac{\wp}{2\hbar}E_-^*(t)\rho_{t+,x-} \tag{5.4}$$

where the electric field that appears in $\mathcal{R}_{ij}$ (see Eq. (4.15)) is given as,

$$\mathbf{E}_l = \frac{1}{2}(\boldsymbol{\epsilon}_+ E_{l-} + \boldsymbol{\epsilon}_- E_{l+} + c.c.) \tag{5.5}$$

with

$$E_{l\pm}(t) = \mathcal{E}_l(t - \tau_l)e^{i(\mathbf{k}_l\cdot\mathbf{r} - \Omega_l(t-\tau_l))} \tag{5.6}$$

and γ_t, γ_s are the dephasing rates for the trion and spin coherence, respectively, ω_g, ω_c are the energy splittings $\omega_{t-,x-}$ and $\omega_{x+,x-}$, respectively, $\wp$ is the magnitude of the dipole matrix elements, and $E_\pm(t)$ is the total field polarized along the $\boldsymbol{\epsilon}_\mp$ basis vectors. In addition to the above, there are several other equations describing the complete four-level system given in Eqns 4.16–4.25, and the calculation of the full third-order polarization involves solving them in a perturbative manner (see Section 4.1.1). However, Eqns 5.2–5.4 are sufficient for the purpose of gaining intuition regarding the behaviour of the signal. Note that the above equations have been obtained from Eqns 4.16–4.25 by setting the decay rates $\Gamma_{23} = 0, \Gamma_{41} = 0$, all population decay rates to be identically Γ_t and all dipole decoherence rates to be γ_t. The selection rules derived in Section 3.2 are also shown schematically in Figure 5.3. One possible pathway for reading out the Raman coherence through the pump and probe fields may be represented schematically as [21],

$$\rho_{x-,x-} \xrightarrow{\mathbf{E}_1(\sigma^-)} \rho_{t-,x-} \xrightarrow{\mathbf{E}_1^*(\sigma^-)} \rho_{x+,x-} \xrightarrow{\mathbf{E}_2(\sigma^\mp)} \begin{cases} \rho_{t-,x-} \\ \rho_{t+,x-} \end{cases}$$

The above Raman process leads to the third order nonlinear polarization along the $\mathbf{k}_2$

direction,

$$\rho^R_{t-,x-} = \frac{N_0}{(2\hbar)^3}\int_{-\infty}^{t} dt_1 \int_{-\infty}^{t_1} dt_2 \int_{-\infty}^{t_2} dt_3\, (-i\wp E_{2+}(t_1))e^{-i(\omega_g - i\gamma_t)(t-t_1)}\times$$
$$(-i\wp E^*_{1+}(t_2))e^{-i(\omega_c - i\gamma_s)(t_1-t_2)}(i\wp E_{1+}(t_3))e^{-i(\omega_g - i\gamma_t)(t_2-t_3)} \tag{5.7}$$
$$\rho^R_{t+,x-} = \frac{N_0}{(2\hbar)^3}\int_{-\infty}^{t} dt_1 \int_{-\infty}^{t_1} dt_2 \int_{-\infty}^{t_2} dt_3\, (-i\wp E_{2-}(t_1))e^{-i(\omega_g - i\gamma_t)(t-t_1)}\times$$
$$(-i\wp E^*_{1+}(t_2))e^{-i(\omega_c - i\gamma_s)(t_1-t_2)}(i\wp E_{1+}(t_3))e^{-i(\omega_g - i\gamma_t)(t_2-t_3)} \tag{5.8}$$

When we use δ-function pulse shapes for the optical fields, we get,

$$\rho^R_{t-,x-} = \frac{-iN_0\wp^3}{(2\hbar)^3}\Theta(t-\tau)\Theta(\tau)e^{-i(\omega_g - i\gamma_t)(t-\tau)}e^{-i(\omega_c - i\gamma_s)\tau} \tag{5.9}$$

and an identical expression for $\rho^R_{t+,x-}$, where the Heaviside unit step function is given by

$$\Theta(t) = \begin{cases} 0 & t < 0, \\ 1 & t \geq 0 \end{cases}$$

The third order polarization due to the Raman coherence at the frequency ω_g is therefore,

$$\tilde{\mathbf{P}}^R(\omega_g)(scp) = \boldsymbol{\mu}_{x-,t-}\rho^R_{t-,x-} = \boldsymbol{\epsilon}_- \frac{-iN_0\wp^4}{(2\hbar)^3}\Theta(t-\tau)\Theta(\tau)e^{-i(\omega_g - i\gamma_t)(t-\tau)}e^{-i(\omega_c - i\gamma_s)\tau} \tag{5.10}$$

$$\tilde{\mathbf{P}}^R(\omega_g)(ocp) = \boldsymbol{\mu}_{x-,t+}\rho^R_{t-,x+} = \boldsymbol{\epsilon}_+ \frac{iN_0\wp^4}{(2\hbar)^3}\Theta(t-\tau)\Theta(\tau)e^{-i(\omega_g - i\gamma_t)(t-\tau)}e^{-i(\omega_c - i\gamma_s)\tau} \tag{5.11}$$

The homodyne detection of the above nonlinear polarization with the corresponding probe pulse gives the DT signal, as defined in Eq. (4.38)

$$DT^R(scp) \propto -\Im\left(-i\int_{-\infty}^{\infty} dt\, \delta(t-\tau)e^{i\Omega_2(t-\tau)}\boldsymbol{\epsilon}^*_- \cdot \boldsymbol{\epsilon}_-\, e^{-i(\omega_g - i\gamma_t)(t-\tau)}e^{-i(\omega_c - i\gamma_s)\tau}\right)$$
$$= \cos(\omega_c\tau)\exp(-\gamma_s\tau) \tag{5.12}$$
$$DT^R(ocp) \propto -\Im\left(i\int_{-\infty}^{\infty} dt\, \delta(t-\tau)e^{i\Omega_2(t-\tau)}\boldsymbol{\epsilon}^*_+ \cdot \boldsymbol{\epsilon}_+\, e^{-i(\omega_g - i\gamma_t)(t-\tau)}e^{-i(\omega_c - i\gamma_s)\tau}\right)$$
$$= -\cos(\omega_c\tau)\exp(-\gamma_s\tau) \tag{5.13}$$

showing there is an oscillatory component to the DT signal at the frequency of the Zeeman splitting with a π-phase shift between the cases for SCP and OCP, as observed in the data. Further, for a circularly polarized pump and linearly polarized probe pulse, the nonlinear polarization is given by Eq. (5.10) $\pm$ Eq. (5.11) for s-polarized (p-polarized) probe fields. In either case, the DT signal due to the Raman coherence is given by,

$$DT^R(clp) \propto \Re\left(\int_{-\infty}^{\infty} dt\, \delta(t-\tau)e^{i\Omega_2(t-\tau)}(\boldsymbol{\epsilon}^*_- \pm \boldsymbol{\epsilon}^*_+)\cdot(\boldsymbol{\epsilon}_- \mp \boldsymbol{\epsilon}_+)e^{-i(\omega_g - i\gamma_t)(t-\tau)}e^{-i(\omega_c - i\gamma_s)\tau}\right) \tag{5.14}$$

which vanishes, in accordance with our experiments.

There are also many incoherent pathways, wherein diagonal density matrix elements corresponding to population are created in second order of the fields, which lead to a third-order polarization. One possible pathway is,

$$\rho_{x-,x-} \xrightarrow{\mathbf{E}_1(\sigma^-)} \rho_{t-,x-} \xrightarrow{\mathbf{E}_1^*(\sigma^-)} \rho_{t-,t-} \xrightarrow{\mathbf{E}_2(\sigma^\mp)} \begin{cases} \rho_{t-,x-} \\ \rho_{t+,x-} \end{cases}$$

The second order population created during this process is given by,

$$\rho^{(2)}_{t-,t-} = \frac{N_0}{(2\hbar)^2} \int_{-\infty}^{t} dt_1 \int_{-\infty}^{t_1} dt_2 \left[(-i\wp E^*_{1+}(t_1)) e^{-2\Gamma_t(t-t_1)} (i\wp E_{1+}(t_2)) e^{-i(\omega_g - i\gamma_t)(t_1-t_2)} + c.c. \right] \tag{5.15}$$

where $2\Gamma_t$ is the trion recombination rate, obtained by setting $\Gamma_1 = \Gamma_2 = \Gamma_t$ in Figure 4.1. We can then proceed to calculate the DT signal due to this incoherent pathway in the same manner as for the coherent process. In the limit of δ-function pulses, we performed the complete theoretical calculations by solving the coupled set of equations (Eqns 4.16–4.25) and obtained the signal to be,

$$DT^{th}_{scp-ocp} = \exp\left[-(\Gamma_1 + \Gamma_2 + 2\Gamma_{23})\tau\right] + \exp\left(-\gamma_{41}\tau\right)\cos(\omega_{41}\tau) \tag{5.16}$$

which reduces to that in Eq. (5.1) when $\Gamma_{23} = 0, \Gamma_1 = \Gamma_2 = \Gamma_t, \gamma_{41} = \gamma_s$, and $\omega_{41} = \omega_c$. The first term in Eq. (5.16) arises from the incoherent pathways mentioned earlier. The second term gives rise to the beats in the DT signal, and arises from the coherent pathways. Hole spin relaxation, which would give rise to decay between the two trion states or between the spin states is thus found to affect only the first term, but not to affect the beats. The approximation $\Gamma_{23} = 0$ is reasonable, since hole spin relaxation in QDs is theoretically expected to be much lower than electron spin relaxation, due to the vanishing hyperfine interaction with the nuclei [452]. Electron spin relaxation (Γ_{41}) does not affect the result either because the bandwidth of the laser pulse (in the δ-function limit as well as in the experiment) is much greater than the splitting, therefore the effect is lost when integrating over the change in population. We would like to call to the reader's attention the theoretical prediction that $\phi = 0, C_2 = 1$, which is in contradiction with the experimental results to be presented in Section 5.3.

It is important to note that, in agreement with the complete theory, we did not observe beats in the Faraday rotation signal (within the signal to noise of $\sim 5 \times 10^{-5}$ degrees) in our

experiments. The polarization symmetry of the dipole matrix elements leads to complete cancellation of all the terms in Eq. (4.44) for either s- or p-polarized probe fields. This is in contrast to earlier experiments that probed the spin coherence using Faraday rotation in undoped chemically synthesized nanocrystals [258], bulk n-doped GaAs [223] or in a two-dimensional electron gas [189]. The reason for the vanishing of FR beats in our experiments is due to the polarization symmetry, the on-resonant excitation and the small sample length traversed by the optical fields.

Figure 5.5(b) shows that the experimentally obtained decay rates depends on the field. A possible explanation for the observed trend is that the g-factors are inhomogeneously distributed because of differences in the quantum confinement potentials among the dots. Suppose that γ_s is truly a constant, independent of the field and that we have a Gaussian probability distribution for the Zeeman splittings,

$$W(\omega_c) = \frac{1}{\sqrt{\pi\delta_c^2}} \exp\left[-\left(\frac{\omega_c - \omega_c^0}{\delta_c}\right)^2\right] \tag{5.17}$$

where $\delta_c = \beta_0 \delta g_{e,x} B_x$ is the width of the distribution due to the variation in the g-factors. We can integrate Eq. (5.10) weighted by $W(\omega_c)$, and obtain,

$$\overline{\tilde{\mathbf{P}}^R(\omega_g)} \propto e^{-i(\omega_g - i\gamma_t)(t-\tau)} e^{-\gamma_s \tau} e^{-\left(\frac{\delta_c \tau}{2}\right)^2} e^{-i\omega_c^0 \tau} \epsilon_- \tag{5.18}$$

which clearly shows how the decay of the oscillations becomes Gaussian and can depend on the magnetic field, implying that we were probing T_2^*. We fit the oscillations to the function,

$$DT_{scp-ocp} = B_1 e^{-2\Gamma_t \tau} + B_2 e^{(-\gamma_s \tau)} e^{-\frac{\delta_c^2 \tau^2}{4}} \cos(\omega_c \tau - \phi) \tag{5.19}$$

and the resulting parameters $(\omega_c, \gamma_s, \delta_c)$ are plotted in Figure 5.6 as a function of the magnetic field. While the oscillation frequency is well described by a linear fit, the values for γ_s, δ_c do not conform to our expectations from the simple model above. We observe that γ_s is not a constant, nor is δ_c well fit to a straight line. There is also a clear anti-correlation between γ_s and δ_c, with γ_s increasing whenever δ_c decreases, showing that the fitting may not be entirely trustworthy, due to the many adjustable parameters. Therefore, either the data is not good enough at this time to test this model, or the model is incorrect. The field dependence is still not well understood at this point, but the zero-field intercept for the decay rate gives a dephasing time $T_2^* \sim 10$ ns, which is much smaller than the $T_2 \sim 50\,\mu$s predicted by theory (Section 3.4.1).

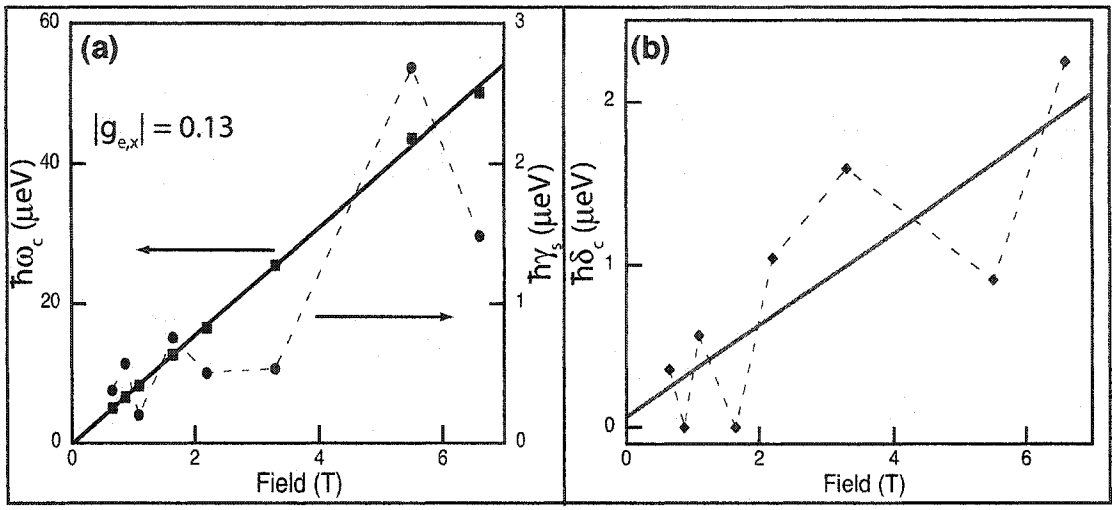

Figure 5.6: Fit parameters $\hbar\omega_c, \hbar\gamma_s, \hbar\delta_c$, obtained assuming a Gaussian distribution of g-factors. (a) Plot of $\hbar\omega_c$ and $\hbar\gamma_s$ obtained by fitting the data with Eq. (5.19) as the in-plane magnetic field is varied. The extracted g-factor from the Zeeman splitting is $g_{e,x} = \pm 0.13$. (b) Plot of $\hbar\delta_c$ obtained by fitting the data with Eq. (5.19) as a function of the in-plane magnetic field. The solid line is a rather poor linear fit to the data from which we obtain $\delta g = 0.005$.

In order to understand this discrepancy, we note that as per the discussion in Section 3.4.1, the primary mechanism for spin relaxation in GaAs QDs is hyperfine interactions with the $N \sim 10^6$ nuclei in the QD. That discussion did not consider the ensemble nature of the electron spins, but concentrated instead on the ultimate limits on T_2, the single spin decoherence time. The ensemble nature of the QDs however is obviously crucial in our experiment. The spin of an electron in an orbital state $\psi(\mathbf{r})$ experiences the magnetic field,

$$\mathbf{B}_n = \frac{v_0}{\beta_0 g_e} \left\langle \sum_j A_j \mathbf{I}_j |\psi(\mathbf{R}_j)|^2 \right\rangle_N \tag{5.20}$$

which is obtained by taking the expectation of Eq. (3.41) over the ensemble of nuclear wave functions.

Let us assume initially that the spin relaxation of an ensemble of localized electrons through the hyperfine interaction proceeds in the limit of complete decoupling between the orbital and spin states of neighbouring electrons. Hence, we may consider each electron in the QD ensemble to be interacting purely with the hyperfine field of nuclei within its wavefunction. We showed in Section 3.4.1.2 that fluctuations in the electron spin precession take place due to spectral diffusion caused by the hyperfine interaction. When considering an ensemble of CQDs, the electron spin in each CQD experiences a different $\mathbf{B}_n$. Thus,

spatial variations in $\mathbf{B}_n$ lead to inhomogeneous variations of the precession frequencies of different spins, with the distribution proportional to the rms of B_n, and depend on whether the nuclear spins are in a thermal or non-equilibrium distribution. The width of the distribution caused by the electron-nuclear interaction sets the ultimate limit on the spin dephasing time (T_2^*) at low magnetic fields. The effects of inhomogeneous broadening on T_2^* lead to broadening of ESR lines, for example, of donors in Silicon [13] or GaAs [196].

An order of magnitude estimate for the contribution to inhomogeneous broadening from the hyperfine interaction can be made as follows: the electron wavefunction interacts with N nuclei in the dot through the hyperfine coupling constant A ($\approx 90\,\mu$eV for GaAs), and hence the interaction per nuclei is $A_i \approx A/N$. The average rms phase gained can be obtained in a random walk phase model to be $(A/\hbar N)\sqrt{N}$. Hence, the time scale of the fluctuations in the electron spin coherence caused by the hyperfine spread in frequencies is $\hbar\sqrt{N}/A \approx 6$ ns for $N = 10^6$ nuclei, comparable to the zero-field intercept obtained above. For a localized electron in GaAs QDs, Merkulov *et al.* carried out a more detailed analysis, obtaining a decay time [376],

$$T_\Delta = \hbar\sqrt{\frac{3N}{16\sum_j I_j(I_j+1)(A_j)^2}} \tag{5.21}$$

where $\sum_j (A_j)^2 = 1.2 \times 10^{-3}\,\mathrm{meV}^2$, and $I_j = 3/2$ for all the nuclei. Again, for $N \sim 10^6$ nuclei, we obtain $T_\Delta \sim 4$ ns. Hanle effect measurements by our collaborators on a single charged QD, gives $T_\Delta \sim 4$ ns [433], in agreement with the above equation and our results. For a single electron, it is clear that the time-averaged measurement will also yield the same result as above. Due to the static nature of the broadening, it can be removed through spin-echo experiments, as shown for example in Si [11, 426].

As pointed out in Section 3.4.1.2, at high magnetic fields, we can ignore the electron-nuclear spin-flip mechanism. In that regime, temporal fluctuations in the precession frequency, which occur due to nuclear dipole-dipole interaction, are by nature irreversible causes of decoherence and ensemble spin dephasing. The electron Zeeman levels split by the hyperfine field will undergo shifts which vary randomly with time. The typical fluctuation time scale (τ_c) in GaAs is given by the precession of a nucleus in the field of neighbouring nuclei, which is on the order of 100 μs, while the precession frequency of the electron is $\omega_0 \sim 2\pi\,(1\text{ GHz})$ even in modest magnetic fields. Since the random kick imparted by the inter-nuclear interaction is in the regime $\omega_0\tau_c \gg 1$ it cannot lead to motional narrowing of

the electron spin coherence. The single spin decoherence time is primarily limited by the inter-nuclear interaction, as discussed in Section 3.4.1, and gives $T_2 \sim 50\,\mu$s. This corresponds to the limitation on the coherence due to the lifetime broadening caused by the rate of the spectral diffusion process.

The last point we wish to address is the long spin dephasing time ($T_2^* \sim 100$ ns) observed in n-doped bulk GaAs. Strong orbital correlations, for example due to intersite hopping, or spin correlations, for example due to direct exchange interaction, between neighbouring electrons can occur in bulk materials. Then motional narrowing (see Section 3.4) can take place, and the ensemble spin dephasing time (T_2^*) is much longer than the single spin decoherence time (T_2). The effect is pronounced for donor electrons in GaAs, because as the donor density is increased the overlap between different donor site wavefunctions is large even for low densities ($\approx 10^{14}$ cm^{-3}) but should be ineffective for a QD since presumably the electron is truly localized. References [223, 366] measured the ensemble spin dephasing time (T_2^*) as a function of the doping density in bulk GaAs and observed an increase in the dephasing time as the donor density was increased upto $\approx 10^{14}$ cm^{-3} and then a decrease. The decrease, as explained in Reference [366], arises from an increase in pure dephasing events that reduce the interaction time between localized electrons and nuclei thereby reducing the motional narrowing.

5.3 Anomalous Variation of Beat Amplitude and Phase: Evidence for SGC

Consider the data shown in Figure 5.7(a) and (b) where we have plotted the beat amplitude (C_2) and phase (ϕ) obtained from the fitting procedures (solid symbols) as a function of $\hbar\omega_c$. The data in the figure were obtained as follows: the DT data as a function of delay at each magnetic field were fitted either using the nonlinear Levenberg-Marquardt algorithm (as implemented in Mathematica and Kaleidagraph) with Eq. (5.1) as the fit function, or by a linear-prediction least square fitting procedure[1] that does not rely on initial parameter estimates [45, 63]. The mean of the fit parameters obtained was then plotted in Figure 5.7 and the error bars establish the systematic errors in the fitting procedure obtained from the standard deviation. The variation of the C_2 and ϕ parameters as a function of the splitting has not been observed in other quantum beat experiments using transient

[1]We would like to thank Dr. Andrea Bragas, Dr. Jiming Bao and Prof. R. Merlin for pointing out this technique and allowing us to use their code.

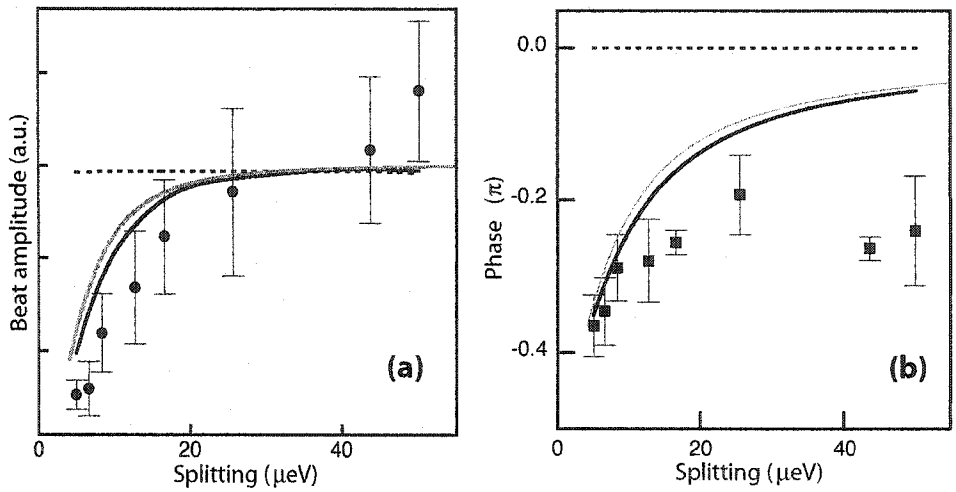

Figure 5.7: Anomalous variation of beat amplitude and phase. (a) and (b) show the changes in the amplitude (C_2) and phase (ϕ) of the oscillations as a function of the splitting, with the error bars establishing the systematic errors calculated. Solid (dashed) black lines denote theoretical predictions for these parameters with(without) the effects of SGC included. In numerical calculations, the optical pulses are assumed Gaussian with the intensity given by $\mathcal{I}(\omega) = \exp(-\omega^2/2\sigma^2)$ ($\sigma = 0.35$ meV). Gray lines are obtained by plotting the results assuming δ-function pulses given by Eq. (5.25) as a function of the splitting using the experimentally obtained values for Γ_t and γ_s.

nonlinear spectroscopy in semiconductors [80,215,373,446], or in experiments which probed the spin coherence using Faraday rotation [189,223,258].

This effect is unexpected since, in the limit where the pulse bandwidth is much greater than the Zeeman splitting and optical coupling of the spin states to the trion is independent of the splitting as shown in Figure 5.3, the amplitude and phase shift of the Raman coherence generated by the pump pulse should be a constant. Our intuition is further confirmed by the theory discussion in Section 5.2 which predicts in Eq. (5.16) that the amplitude and phase of the oscillatory component in the signal should remain unchanged as the field is varied. Numerical simulations with Gaussian pulses (dashed lines in Figure 5.7(a) and (b)), whose spectral power density is given by $\mathcal{I}(\omega) = \exp(-\omega^2/2\sigma^2)$ ($\sigma = 0.35$ meV, FWHM = 0.84 meV), are in close agreement with the calculation assuming δ-function pulses, and both are in contradiction with the experimental results [436]. The results cannot be explained either by a shift in the resonance, as we found that the nonlinear spectrum does not change as the magnetic field is varied (data not shown).

The magnetic field dependence confirms the existence of the spontaneous emission of the trion state into a coherent combination of the two spin states, known in the atomic physics literature as SGC [94, 102, 229]. Spontaneous emission is commonly considered to destroy coherence, but in the present case, the Zeeman splitting $\hbar\omega_c$ is comparable to or even smaller than the trion decay rate $2\Gamma_t \sim 7.8\,\mu$eV, so different transitions can couple to the same modes of the electromagnetic vacuum, for instance the transitions between $|t-\rangle$ and $|x\pm\rangle$ can couple to the same vacuum mode with polarization σ^-, and thus the vacuum fluctuation creates coherence between the final states ($|x\pm\rangle$) of the spontaneous emission process.

Hitherto, our discussion has neglected this term in the master equation for the Raman coherence where

$$\dot{\rho}_{x+,x-}\big|_{sgc} = \Gamma_t(\rho_{t+,t+} - \rho_{t-,t-}) \tag{5.22}$$

should be added to Eq. (5.4). The above term represents SGC due to the decay of the trion level, as predicted for Λ-systems when the transition dipole matrix elements are non-orthogonal (see Appendix A). This condition does not occur in most atomic or semiconductor systems where quantum beats have been observed [34, 80, 215, 373, 446]. One possible perturbation pathway for the SGC effect can be represented schematically as,

$$\rho_{x-,x-} \xrightarrow{\mathbf{E}_1(\sigma^-)} \rho_{t-,x-} \xrightarrow{\mathbf{E}_1^*(\sigma^-)} \left\{ \begin{array}{c} \rho_{t-,t-} \\ \downarrow \\ \rho_{x+,x-} \end{array} \right\} \xrightarrow{\mathbf{E}_2(\sigma^\mp)} \left\{ \begin{array}{c} \rho_{t-,x-} \\ \rho_{t+,x-} \end{array} \right.$$

Using Eq. (5.15), the above perturbation sequence (in the limit of δ-function pulses) leads to the polarization,

$$\begin{aligned}
\rho^{SGC}_{t-,x-} &= \frac{-N_0\Gamma_t}{(2\hbar)^3}\int_{-\infty}^{t} dt_1 \int_{-\infty}^{t_1} dt_2 \int_{-\infty}^{t_2} dt_3 \int_{-\infty}^{t_3} dt_4\, (-i\wp E_{2+}(t_1))e^{-i(\omega_g - i\gamma_t)(t-t_1)} \times \\
&\quad e^{-i(\omega_c - i\gamma_s)(t_1-t_2)} e^{-2\Gamma_t(t_2-t_3)} \left[(-i\wp E^*_{1+}(t_3))(i\wp E_{1+}(t_4))e^{-i(\omega_g - i\gamma_t)(t_3-t_4)} + c.c.\right] \\
&= \frac{2iN_0\Gamma_t\wp^3}{(2\hbar)^3}\Theta(t-\tau)\Theta(\tau)e^{-i(\omega_g - i\gamma_t)(t-\tau)}\left[\frac{e^{-2\Gamma_t\tau} - e^{-i(\omega_c - i\gamma_s)\tau}}{(2\Gamma_t - \gamma_s) - i\omega_c}\right]
\end{aligned} \tag{5.23}$$

We note that, in comparison to Eq. (5.7), the polarization created by the SGC term is of opposite sign. The amplitude also depends on the Zeeman splitting and the difference of the recombination rate and the spin decoherence rate. The DT signal is obtained in the usual manner to be,

$$DT^{sgc}_{scp-ocp} = \frac{2\Gamma_t\omega_c e^{-2\Gamma_t\tau}}{\omega_c^2 + (2\Gamma_t - \gamma_s)^2} - e^{-\gamma_s\tau}2\Gamma_t\left[\frac{(2\Gamma_t - \gamma_s)\cos(\omega_c\tau)}{\omega_c^2 + (2\Gamma_t - \gamma_s)^2} + \frac{\omega_c\sin(\omega_c\tau)}{\omega_c^2 + (2\Gamma_t - \gamma_s)^2}\right] \tag{5.24}$$

Thus, we see that the beats in the signal will have a varying amplitude and phase that depends on the Zeeman splitting and the recombination and spin decoherence rates. The total amplitude and phase of the beats obtained on combining Eq. (5.16) and Eq. (5.24) can be found,

$$C_2 = \sqrt{\frac{\gamma_s^2 + \omega_c^2}{\omega_c^2 + (2\Gamma_t - \gamma_s)^2}} \tag{5.25}$$
$$\phi = -\arctan\left(\frac{2\Gamma_t - \gamma_s}{\omega_c}\right) - \arctan\left(\frac{\gamma_s}{\omega_c}\right)$$

Taking into account the full four-level system, the above equations were still found to hold. Eq. (5.25) is plotted in Figure 5.7 (a) and (b) as indicated by the gray lines, and shows how the amplitude increases as the Zeeman splitting becomes large in comparison with the recombination rate, and also approaches the result expected in the absence of SGC (black dashed lines). When the magnetic field is weak, the trion decay is much faster than the spin precession, so the SGC cancels the conventional Raman coherence. In the strong magnetic field limit, the rapid spin precession averages the SGC to zero. This explains the observed field dependence of the spin beats in Figure 5.7. As the Zeeman splitting increases from zero to much larger than the radiative decay rate, the beat amplitude increases until it saturates at the value calculated without the SGC effect, and the phase shift increases from close to $-\pi/2$ to zero.

The solid black lines in Figure 5.7(a) and (b) represent the complete numerical calculations using Gaussian pulses whose spectral power density is given by $\mathcal{I}(\omega) = \exp(-\omega^2/2\sigma^2)$, with $\sigma = 0.35$ meV [436]. The only parameters in the theory were the recombination and spin decoherence rates, obtained from the experimental fits that were described earlier. The theoretical prediction for the trends in C_2 and ϕ closely matches with the experimental data, as well as the results for δ-function pulses, although there does seem to be significant deviation for ϕ from experiment at large splittings for both the numerical and analytical solutions.

One possibility for the deviation in the theory for ϕ could be due to the inhomogeneous Gaussian distribution in the splitting described in Eq. (5.17). Integrating Eq. (5.23) over the Gaussian distribution and combining with Eq. (5.16) gives,

$$DT_{beats}^{sgc-gauss} = e^{-\gamma_s\tau}e^{-\left(\frac{\delta_c\tau}{2}\right)^2}\Big[\cos(\omega_c\tau) + 2\Gamma_t\Big(\Theta(\tau-\tau_0)\Im[ie^{i\omega_c\tau}\mathcal{Z}(z_0 + i\frac{\delta_c\tau}{2})] \tag{5.26}$$
$$- \Theta(\tau_0-\tau)\Im[ie^{i\omega_c\tau}\mathcal{Z}(-z_0 - i\frac{\delta_c\tau}{2})]\Big)\Big]$$

where

$$\tau_0 = \frac{2(2\Gamma_t - \gamma_s)}{\delta_c^2}, \qquad z_0 = \frac{\omega_c}{\delta_c} - i\frac{(2\Gamma_t - \gamma_s)}{\delta_c}, \tag{5.27}$$

$$\mathcal{Z}(z) = \exp(-z^2)(1 + \mathrm{erf}(iz)) \qquad \text{is the plasma dispersion function,} \tag{5.28}$$

$$\mathrm{erf}(z) = \frac{2}{\sqrt{\pi}} \int_0^z dt\, e^{-t^2} \qquad \text{is the complex error function.} \tag{5.29}$$

Assuming a distribution in g-factors of $\delta g/g \sim 10\%$, we generated delay curves with Eq. (5.26) and fitted it with Eq. (5.1) from which we can extract the theory prediction for C_2 and ϕ. It was found that the presence of inhomogeneous broadening actually washes out the effect on the phase, and we found that the result approached the case where there was no SGC present. The analysis therefore seems to support our claim that inhomogeneous broadening does not seriously affect the spin quantum beats, and that the deviation between theory and experiment is still not well understood at this point.

The results still strongly support our conclusion that SGC plays an important role in affecting the Raman coherence, demonstrating the unanticipated and interesting effects that come into play when coupling between nearly degenerate ground states and a decaying excited state is taken into account. Because of the fundamental role of the SGC effect in the interaction between the dissipative environment and the multi-level system, including atoms and artificial atoms (as in the present case), there have been numerous theoretical studies since the early 1990's [59, 94, 102, 229, 278, 317, 386, 441], but there had been no experimental observation of an excited-state population decaying to a ground state Raman coherence. Vacuum field induced contributions to the coherence between ground states can also lead to a coherent combination of ground states that is "dark". Such "dark" states created by the spontaneous emission are responsible for the prediction of holes in spectral lines, known as *spontaneous emission cancellation (SEC)* [20, 27, 173, 231, 254]. Experimental observation of SEC has been reported [172], although the results are still a matter of controversy because the level scheme that the authors used for the demonstration can be similarity transformed into a basis that contains a metastable state [203]. There have been no convincing observations therefore in atoms of either SGC or SEC. In atoms, the difficulty of observing SGC arises from the very special conditions that must be simultaneously satisfied: (i) non-orthogonal transition dipole moments and (ii) the near-degeneracy of the ground states. However, the observation of atom-photon entanglement in $^{111}Cd^+$ ions by Blinov *et al.* demonstrates that such level schemes can be implemented in atoms and that

correlations between the spontaneous emission and the atomic state do exist [431]. The SGC effect is unambiguously demonstrated in our experiment by the observed field dependence of the spin beat amplitude and phase shift, and the significant agreement between theory and experiment. The observation of SGC in the IFQDs is favored not only by the relatively large radiative decay rate as compared to the spin precession rate, but also by the ability to tailor the quantum states in the artificial atoms by magnetic field and by doping.

5.4 Chapter Summary

In Section 5.1, we showed that the optical transition to the excited states of a charged QD, *i.e.* the singlet trion state, is characterized by T_2^{dipole} and T_1^{dipole} values that are similar to those for neutral excitons, and does not suffer from excess dephasing processes. The resonant optical generation of electron spin coherence through the stimulated Raman interaction with the trion states allowed us to observe spin coherence and measure the coherence lifetime in Section 5.2 although much remains to be understood about the dependence on the magnetic field and temperature. Theoretical calculations were presented for the signals observed, and found to be in discrepancy with the experimentally measured trend for the variation of beat amplitude and phase with magnetic field. Upon including a term in the master equation which takes into account the vacuum field induced contribution to the coherence from decay of the trion population into a coherent superposition of the spin ground state, we showed in Section 5.3 that we were able to nearly completely explain the functional behaviour of the amplitude and phase of the spin quantum beats. In the next chapter, we will show that the spin coherence generated by optical pulses can be coherently controlled.

CHAPTER 6

Transient Nonlinear Spectroscopy: Coherent Optical Control of Electron Spin Coherence

The advent of the laser has given scientists a new tool in the quest for control of the natural world. An immediate application of the laser, in particular high-power pulsed lasers, that suggested itself was for selective breaking of bonds in molecules to affect the yield of a chemical reaction. This approach was pursued intensively with a great deal of success until it became clear that the incoherent excitation of a bond in complex polyatomic molecules led to the redistribution of the energy into the normal modes of the system, thereby defeating the goal of selective control (see [108, 238, 348] and references therein). However, it was proposed in the late 1980s to use quantum interference, by harnessing the laser coherence, to achieve what incoherent techniques had failed to do. One idea involved quantum interference between single and multi-photon pathways to the same excited state [57, 197] while another proposed to initiate wavepacket dynamics with a laser pulse that undergoes quantum interference with wavepackets created by subsequent pulses [51]. Earlier work on atoms using phase-locked pulses had already shown the feasibility of using pairs of pulses, combined with the power of nonlinear processes to affect the final state of atoms [30, 31, 230]. Experimental demonstrations of such concepts were later realized for control of photoionization involving one-photon and three-photon pathways in atoms [74, 98] and molecules [86, 145]. Rapid progress followed in the field as phase-locked sequences of pulses and highly complex synthesized pulse-shapes were used to study molecular fluorescence [78, 87], control the photodissociation of molecules [81] and to map and control localized atomic wavepackets [65, 276]. References [108, 238, 304, 348] provide a review of the great progress that has been achieved, as well as providing some preview of future challenges in the area.

The application of coherent control techniques to solids did not lag far behind and shortly

thereafter, phase-locked pulses were used to coherently control the exciton density [130], orientation [192], and spin [333] in QWs. A staggering variety of control experiments with pulse sequences have been achieved including acoustic phonons in semiconductors [240,342], optical phonons in thin metal films [159], electron dynamics in metals [194], intraband coherences in micro-cavity enclosed QWs [267], electron-LO-phonon scattering in GaAs [236], and magnetization memory in thin ferromagnetic films [389]. The analog of the multi-photon quantum interference technique to generate pure charge and spin photocurrents in semiconductors was also proposed [68,147] and achieved [404,422].

However, the short dephasing times of the elementary excitations even in QW structures made significant progress in quantum control hard to achieve. Recently, neutral semiconductor QDs with their discrete density of states have been shown to have long decoherence times [204,321], and coherent control of the QD exciton population both in the weak and strong field regime have been demonstrated [205,353,453]. As shown in Chapter 5, long-lived spin coherence, with lifetimes at least an order of magnitude greater than the exciton coherence in neutral QDs, can be optically excited in CQDs with ultrashort laser pulses, and a natural direction to pursue is whether the spin coherence can also be controlled through coherent optical means. Furthermore, for quantum computation, it is important to have the capability to manipulate quantum superpositions between the spin states, and not just to generate and detect the coherence. In this chapter, we outline the results of a set of experiments which show that coherent optical fields can be used to control the spin coherence.

6.1 Quantum Interference of Control and Primary Two Photon Processes

Chapter 5 showed that the spin coherence between the nearly-degenerate ground states of a charged QD can be coherently generated and detected by taking advantage of the resonant enhancement with the trion dipole transition. The idea of using a stimulated Raman process (SRP) which couples two closely spaced ground levels to an excited state, and thereby mediates coherence or population transfer between the ground levels, has been used in atoms and molecules previously [26,202]. Stimulated Raman scattering (SRS), wherein sub-picosecond light pulses are used as the source of coherent energy supplied to the medium, has been widely used for exciting rotational wavepackets in molecules [290,

291, 303], surface acoustic waves [450], coherent plasma and phonon oscillations in bulk semiconductors [75, 129, 131, 138, 193] and QW structures [150]. Here we combine SRPs with phase control techniques to manipulate the spin coherence in the ground state of charged QDs.

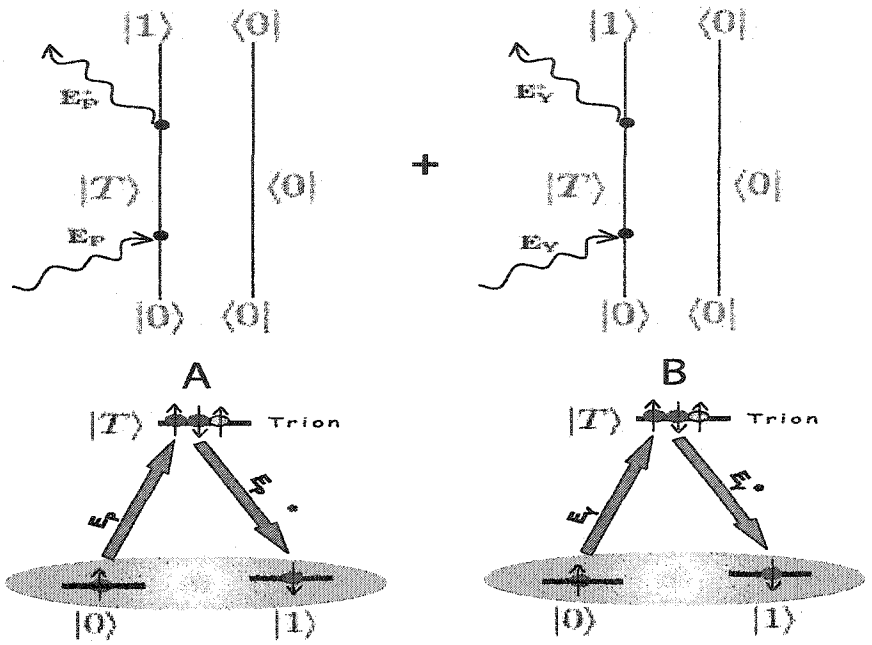

Figure 6.1: Double-sided Feynman diagrams illustrating two-photon processes leading to quantum interference. **A.** Double sided Feynman diagram wherein $\rho_{1,0}$ is created by a two-photon process initiated by the first pump pulse $\mathbf{E_P}$. The Λ-system model for the process is shown below the Feynman diagram. **B.** Double sided Feynman diagram wherein $\rho_{1,0}$ is created by a two-photon process initiated by the second pump pulse $\mathbf{E_Y}$.

As discussed in Section 5.2, the beats in the DT signal arise from the coherent pathway for the evolution of the third-order off-diagonal density matrix elements. Quantum interference can take place between two such coherent pathways as shown in Figure 6.1. Double-sided Feynman diagrams are used to illustrate the evolution of the density matrix elements [44]. We consider for simplicity the three level Λ-system illustrated in Figure 6.1, with two nearly degenerate ground states labeled $|0\rangle$ ($\equiv |x-\rangle$) and $|1\rangle$ ($\equiv |x+\rangle$) and an intermediate trion state labeled $|T\rangle$ ($\equiv |t-\rangle$). The diagram Figure 6.1A shows one possible coherent pathway for creation of the spin coherence $\rho_{1,0}$ in which one pump photon from the pump pulse creates the intermediate dipole coherence $\rho_{T,0}$ and the second photon from the pump pulse converts the dipole coherence to a spin coherence $\rho_{1,0}$. Figure 6.1B illustrates the corresponding two-photon SRP involving the control pulse, and the addition of the two

diagrams leads to the quantum interference. The perturbation sequence, to third order, corresponding to the first diagram is,

$$\rho_{0,0} \xrightarrow{\mathbf{E}_P(\sigma^-)} \rho_{T,0} \xrightarrow{\mathbf{E}_P^*(\sigma^-)} \rho_{1,0} \xrightarrow{\mathbf{E}_X(\sigma^+)} \rho_{T,0}$$

and the sequence for the second double-sided Feynman diagram is,

$$\rho_{0,0} \xrightarrow{\mathbf{E}_Y(\sigma^-)} \rho_{T,0} \xrightarrow{\mathbf{E}_Y^*(\sigma^-)} \rho_{1,0} \xrightarrow{\mathbf{E}_X(\sigma^+)} \rho_{T,0}$$

Figure 6.2 shows the modified Michelson interferometer for generating the pair of phase-locked pump pulses that will initiate and control the spin coherence. The input pump pulse is split by the first beam splitter, and one arm (labeled by τ_y) consisting of a right-angle prism mounted on a mechanized translation stage (labeled TS-Y, Newport model PM500) provides delay adjustments that can range from 100 fs to 1.2 ns. The other arm (labeled τ_p) consists of a mirror mounted on a piezoelectric translation stage (PZT) that can be controlled to sub-fs precision. The PZT is driven by a high voltage power supply (Stanford Research Systems PS325) that is GPIB controlled. The phase-locked pump pulse pair is recombined on the second beam splitter and then re-directed to the sample, while making sure that both pump and control fields have nearly the same power when they reach the sample. The probe pulse delay (τ_x) which is used to detect the effect of the pulse pair on the spin coherence is set as usual through another mechanized delay stage (TS-X). The collection optics setup is the same as in Figure 4.6 (a), which allows for detection of the difference between SCP and OCP DT signals on a single scan of the τ_x delay stage. The Mira laser is operated in pico-mode for the experiments, and tuned to the transition energy of the trion as shown in Figure 5.4. The sample (612F-3NA) is mounted in the magneto-optical cryostat in the Voigt geometry, and the magnetic field B_x is held at 2.2 T.

The data is collected by fixing the delay τ_y, and scanning the delay τ_x between 0 and 1.2 ns. Figure 6.3A shows the data obtained in a three-dimensional plot with τ_y varied from 100 to 400 ps. The vertical blue line in the figure marks the arrival of the pump pulse, and the diagonal blue line denotes the arrival of the second control pulse. The range of variation shown in τ_y corresponds to going through a full period in the spin coherence evolution *i.e.* $2\pi/\omega_c$. The starting point for τ_y is set as 100 ps, so as to avoid contributions to the signal from recombination, which has a decay time $\sim$ 85 ps. Constructive and destructive interferences take place between the spin coherence initialized by the first pump

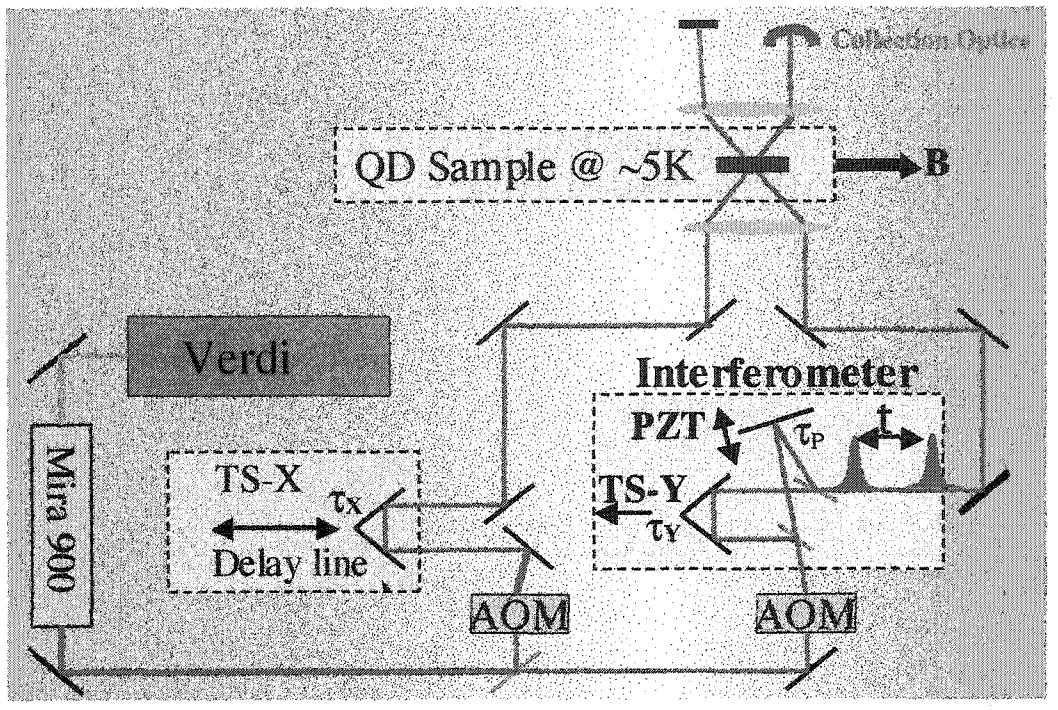

Figure 6.2: Experimental setup for coherent optical control of spin coherence. The modified Michelson interferometer creates a pair of phase-locked pump pulses, labeled by E_P and E_Y, with the delay between the two given by $t = \tau_y - \tau_p$. The probe pulse delay (τ_x) is controlled by another translation stage.

pulse and that initialized by the second control pulse, depending on the time delay between the pulses. A simple visual image of the process is to imagine that one strikes a (quantum) bell with a hammer that initiates ringing. The ringing may be enhanced or destroyed by a second hammer strike that is correctly phased to achieve the desired result. The stimulated Raman interaction provides the impulse necessary to begin the spin coherence evolution, as discussed in Section 5.2.

Figure 6.3B shows the complete destructive interference in the spin coherence caused by the arrival of the control pulse at $\tau_y = 120$ ps. The constructive interference caused by arrival of the control pulse at $\tau_y = 240$ ps (red) is shown in Figure 6.3C, where we have also plotted the spin coherence evolution (blue) as a function of the τ_x delay when there is no second control pulse. The green area marks the difference between the two. The theory will show that, due to the finite decoherence rate γ_s, the beat amplitude should be enhanced by a factor of ~ 1.73 through constructive interference. The experimental data is in the ratio $(6.78/3.79) \approx 1.8$, in good agreement with the theory.

The coherent control experiment was modeled for the complete four-level system of the

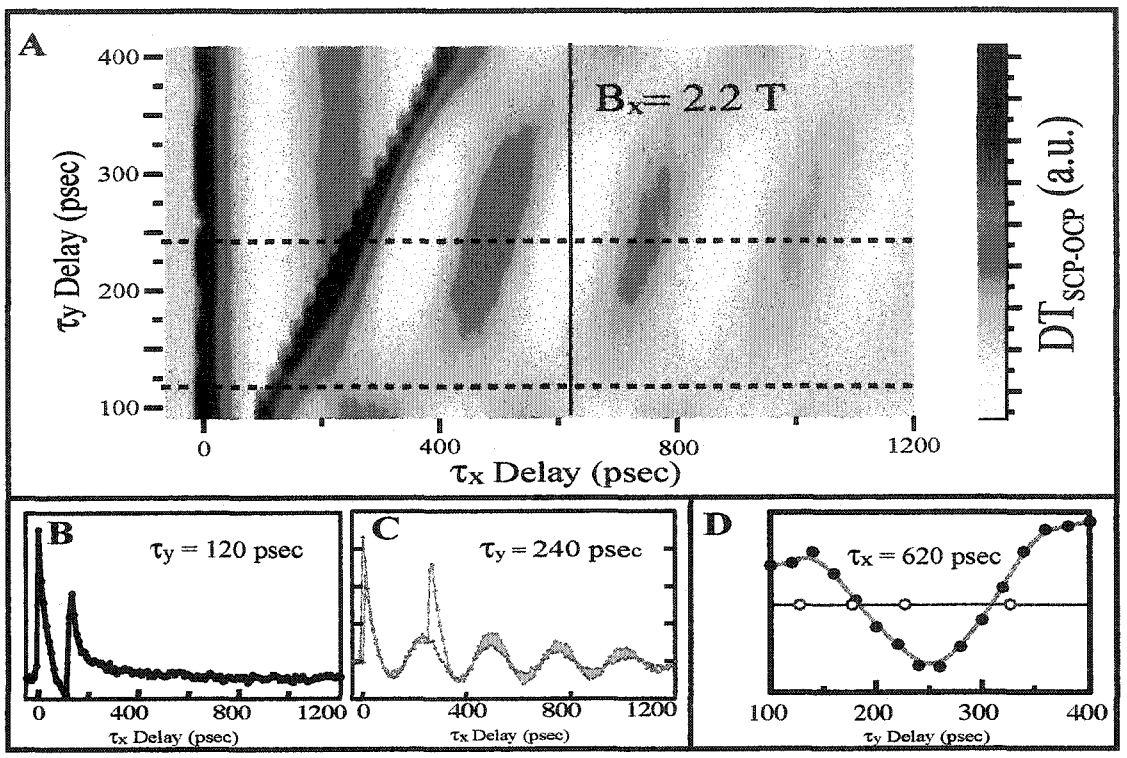

Figure 6.3: Experimental data demonstrating coherent optical control of electron spin coherence. **A.** DT signal plotted in color as a function of τ_x and τ_y. The signal plotted is the difference between SCP and OCP data. **B.** Lineout through the data in **A** (shown by horizontal dashed lines) at τ_y = 120 ps, showing complete destructive interference in the spin coherence. **C.** Lineout through the data in **A** (red) at τ_y = 240 ps, showing constructive interference in the spin coherence. Also shown is the data with only one pump pulse (blue) with the green area marking the difference. **D.** Vertical lineout through the data in **A** at τ_x = 620 ps, showing the interference as τ_y is varied (solid circles). The open blue circles are obtained from a classical first-order auto-correlation between the pump and control fields.

CQD as shown in Figure 5.3 using two pump fields and a probe field in the field-matter interaction potential, and the calculation carried out in a manner similar to that described in Chapter 5 with δ-function pulse shapes for all the fields. Taking the experimental conditions into account, the final expression for the expected DT signal when considering only the double-sided Feynman diagrams shown in Figure 6.1 is,

$$\begin{aligned} DT_{scp-ocp} \propto & \left[I_P \cos(\omega_c(\tau_x - \tau_p))e^{-\gamma_s(\tau_x-\tau_p)} + I_Y \cos(\omega_c(\tau_x - \tau_y))e^{-\gamma_s(\tau_x-\tau_y)}\right] \\ & + \left[I_P e^{-2\Gamma_t(\tau_x-\tau_p)} + I_Y e^{-2\Gamma_t(\tau_x-\tau_y)}\right] \end{aligned} \tag{6.1}$$

As expected from physical intuition, the first bracket corresponds to the quantum interference between the coherent pathways and the second bracket corresponds to quantum

interference between the incoherent pathways. We note that by setting the $\tau_x - \tau_y$ delay to be large compared to Γ_t^{-1}, we are able to neglect the second bracket and therefore consider only the quantum interference between spin coherence created by the pump and control fields. Theoretically, for complete constructive interference and assuming $\gamma_s = 0$, we expect the signal to be twice as large compared to the case for a single pump pulse. From the extracted value $\hbar\gamma_s \sim 0.88\,\mu$eV, we obtain an enhancement factor of 1.73. Further, Eq. (6.1) shows that as τ_y is increased, the spin coherence created by the first pump pulse is decaying, thus we cannot achieve complete constructive and destructive interference since the two terms will not have equal strengths. This is observed in the experiment for the larger τ_y delays as seen in Figure 6.3A where in the upper regions of the plot, the data no longer has a clear line of destructive interference.

6.2 Femtosecond Optical Control of Spin Coherence

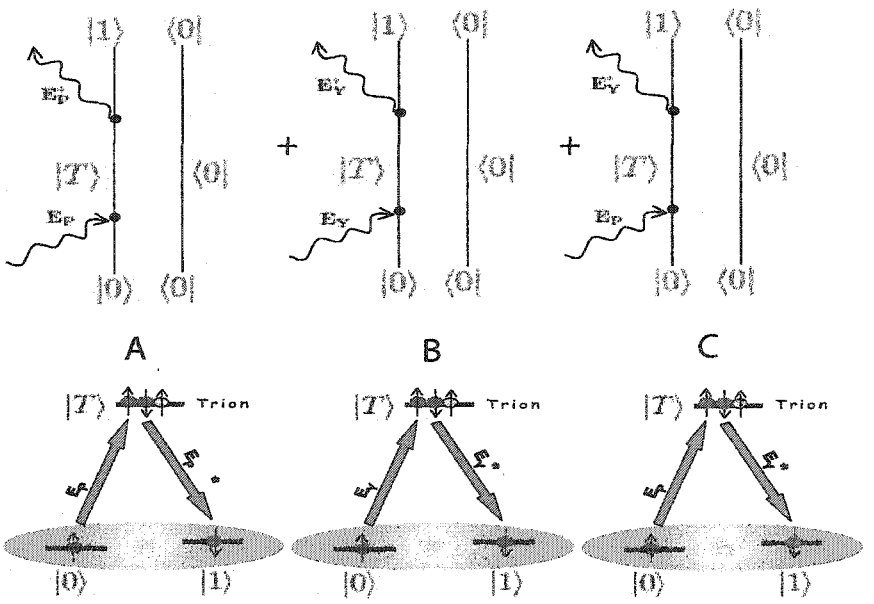

Figure 6.4: Complete set of double-sided Feynman diagrams for the two-photon processes leading to the spin coherence. The final diagram C occurs when the first photon is from the pump and the second photon from the control pulse, and only lasts as long as the intermediate trion coherence is preserved.

The previous section showed that the spin coherence can be manipulated with coherent optical fields by phasing a second optical pulse at the right time in the evolution of the spin coherence created by the initial pulse. The manipulation takes place on the time scale

set by the Zeeman splitting between the spin states of the CQD, which is $2\pi/\omega_c \approx 100$s of picoseconds due to the small g-factor in our particular GaAs QD system. It would be interesting however to ask the question if we can achieve control with femtosecond precision of the spin coherence using the time scale of the optical frequency instead. Quantum mechanics provides an affirmative answer, because of the fact that one must sum up all of the possible pathways which can lead to the spin coherence. Figure 6.4C includes another Feynman diagram that was missing in Figure 6.1 for the two-photon SRPs mediated by the pump and control photons that can lead to a spin coherence. Quantum mechanics demands that we include this pathway also in the theory, which leads to the following equation for the signal,

$$\begin{aligned} DT_{scp-ocp} \propto & \left[I_P \cos(\omega_c(\tau_x-\tau_p))e^{-\gamma_s(\tau_x-\tau_p)} + I_Y \cos(\omega_c(\tau_x-\tau_y))e^{-\gamma_s(\tau_x-\tau_y)}\right. \\ & \left. + 2\sqrt{I_P I_Y}\cos(\omega_g(\tau_y-\tau_p)+\omega_c(\tau_x-\tau_y))e^{-\gamma_s(\tau_x-\tau_y)}e^{-\gamma_t(\tau_y-\tau_p)}\right] + \left[I_P e^{-\Gamma_t(\tau_x-\tau_p)}\right. \\ & \left. + I_Y e^{-2\Gamma_t(\tau_x-\tau_y)} + 2\sqrt{I_P I_Y}\cos(\omega_g(\tau_y-\tau_p))e^{-\Gamma_t(\tau_x-\tau_y)}e^{-\gamma_t(\tau_y-\tau_p)}\right] \end{aligned} \tag{6.2}$$

We note that the third term in each bracket in Eq. (6.2), which is due to the third diagram in Figure 6.4, corresponds to a SRP where the first photon is provided by the pump pulse and the second photon by the control pulse. The intermediate quantum state is the trion dipole coherence, which decays with the rate γ_t, and experimentally was determined to be $\gamma_t^{-1} \sim 20-40$ ps (see Section 7.1). Hence, modulation in the intermediate state will affect the final spin coherence, and the natural optical frequency of the intermediate state implies ultrafast manipulation is possible. Once again by setting the probe delay $\tau_x - \tau_y$ to be large (227 ps) compared to the dipole decay time scales, we can neglect the entire second bracket. However, we also keep the control-probe separation $\tau_x - \tau_y$ fixed so as to avoid any changes in the amplitude due to this factor in the first bracket. As seen in Figure 6.5, we collected the DT data under the above conditions, while varying the τ_p delay on a femtosecond scale with the PZT. A quantum interferogram (QI) was taken by scanning the PZT at each different coarse delay (τ_y), thus varying τ_p on a femtosecond time scale, and a sample scan is shown in the inset to Figure 6.5 when $\tau_y = 7$ ps. Each scan is fit to a cosine from which the amplitude is extracted, and denoted by the solid circles in the data. The envelope shows a clear decay as expected, from which it should theoretically be possible to extract the trion coherence decay rate as shown in Eq. (6.2). However, inhomogeneous

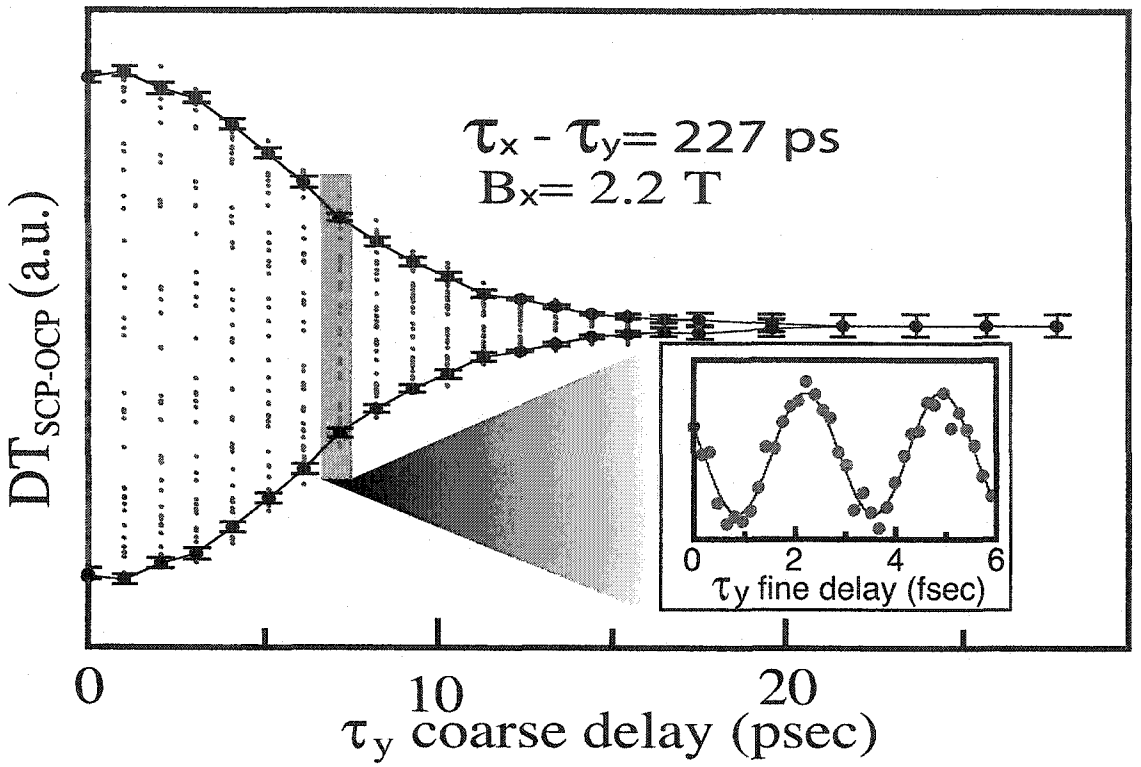

Figure 6.5: Quantum interferogram demonstrating femtosecond coherent optical control of the spin coherence. The τ_y coarse delay controlled by TS-Y translation stage is stepped, while the PZT (τ_p) is scanned. Inset: Expanded view of the gray region in the main plot, showing oscillations in the spin coherence as the phase is varied between the pump and control pulse.

broadening and finite pulsewidth effects complicate this simple picture.

Let us consider the Raman coherence created by the SRP involving the pump and control photons, by solving Eqns 5.2–5.4 to the second order,

$$\rho_{x+,x-}(t) = \frac{N_0}{(2\hbar)^2}\int_{-\infty}^{t} dt_1 \int_{-\infty}^{t_1} dt_2\,(-i\wp E^*_{y+}(t_1))e^{-i(\omega_c - i\gamma_s)(t-t_1)}(i\wp E_{p+}(t_2))e^{-i(\omega_g - i\gamma_t)(t_1-t_2)} \tag{6.3}$$

In Appendix B we show that this integral can be solved analytically for finite Gaussian pulses, under the approximation that the pulsewidth is much shorter than any of the decay rates in the problem. To be precise, we assume that the electric field amplitude is given in Eq. (5.5) by,

$$\mathcal{E}(t) = \mathcal{E}_0 \exp\left(-\frac{t^2}{s^2}\right) \tag{6.4}$$

with the Fourier transform defined by

$$\mathcal{E}(\omega) = \int_{-\infty}^{\infty} dt\, \mathcal{E}(t) e^{i\omega t} \tag{6.5}$$

$$= \mathcal{E}_0 \exp\left(-\frac{\omega^2}{4\sigma^2}\right) \tag{6.6}$$

where $\sigma = \frac{\delta\omega}{\sqrt{8\ln 2}} = (1/s)$, $s = \frac{\delta t}{\sqrt{2\ln 2}}$, and $\delta\omega, \delta t$ are the FWHM in the frequency and time domain of the intensity (as obtained from a spectrometer or autocorrelation). The assumption of Gaussian pulse-shapes is not strictly necessary for evaluating $\rho_{x+,x-}$, as shown in Appendix B, but allows the final DT signal including inhomogeneous broadening to be evaluated analytically. In fact, all that is required for the analytical evaluation of the integral is that we probe the signal at time $(\tau_x - \tau_y) \gg s$, which is certainly satisfied by our experimental conditions. Further, we will assume that all the fields $\mathbf{E}_l$ are degenerate and that the center frequency coincides with the center frequency of the inhomogenously broadened trion transition ($\Omega_l = \Omega = \omega_g^0$). We can show in Appendix B that the coherent contribution to the DT signal from SRP(C) including the inhomogeneous broadening of the trion transition is given by,

$$DT_{scp-ocp}^{SRPC} = e^{-\gamma_s(\tau_x-\tau_y)} e^{-\gamma_t(\tau_y-\tau_p)} e^{-\frac{(\tau_y-\tau_p)^2}{4\alpha}} \cos(\omega_g^0(\tau_y - \tau_p) + \omega_c(\tau_x - \tau_y)) \tag{6.7}$$

where $\alpha = \frac{1}{2\sigma^2} + \frac{1}{\eta_g^2}$, $\eta_g = \frac{\delta\omega_g}{\sqrt{4\ln 2}}$ and $\delta\omega_g$ is the FWHM of the Gaussian distribution in the transition frequency of the trion state. The equation shows that due to the large inhomogeneous broadening ($\delta\omega_g \sim 1.5$ meV) in the trion dipole transition, we expect the decay to be dominated by essentially the Gaussian decay in the pulseshape, since $\eta_g \gg \sigma$. Further, the equation also reproduces the result from Eq. (6.2) where we note the DT signal oscillates as a function of the delay between the pump and control photons at the frequency of the trion transition, *i.e.* on the femtosecond timescale. To extract the trion dipole decoherence time from fitting the above equation to the data directly is difficult. However, we may adopt an alternative approach as discussed below.

From Eq. (6.7) given above, we can consider only the envelope of the QI shown in Figure 6.5. We plot the envelope of the QI in Figure 6.6, and we also plot the envelope of the classical first-order autocorrelation function of the electric field, that is the classical interferogram (CI). The CI envelope is obtained in identical fashion as the QI, except that we remove the sample and allow the pump beams to fall on the detector directly, rather

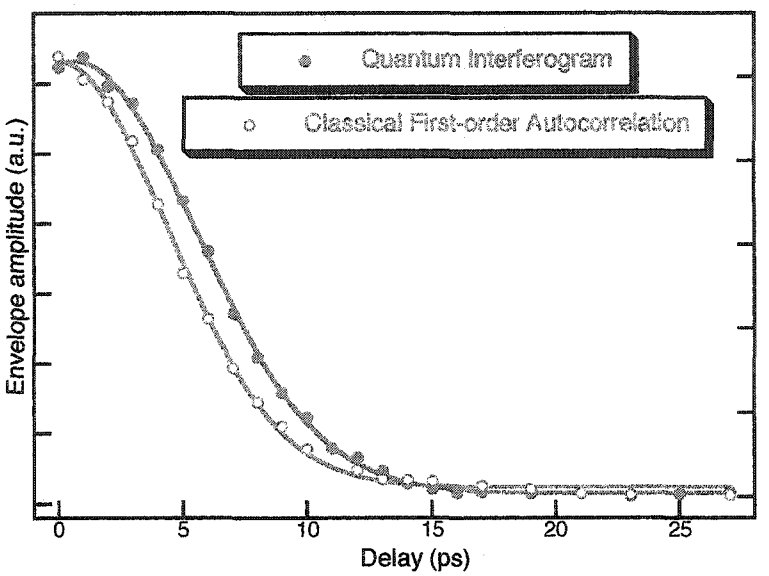

Figure 6.6: Comparison of the envelope obtained from the quantum interferogram and the classical interferogram. The delay here is between the pump and control pulse, *i.e.* $\tau_y - \tau_p$. The solid lines are Gaussian fits to the data, described by Eq. (6.8) for the classical interferogram envelope and Eq. (6.9) for the quantum interferogram envelope.

than the probe beam. Thus, from the Wiener-Kintchine theorem, we know that the CI is just the Fourier transform of the power spectral density [133],

$$\begin{aligned} CI_{env}(t) &= \int_{-\infty}^{\infty} d\omega\, \mathcal{E}_0^2 e^{-\frac{\omega^2}{2\sigma^2}} e^{-i\omega t} \\ &= \mathcal{E}_0^2 e^{-\frac{\sigma^2 t^2}{2}} \end{aligned} \tag{6.8}$$

where $t = \tau_y - \tau_p$ and we drop any constant factors from now onwards. From Eq. (6.7),

$$QI_{env}(t) = e^{-\frac{(t+2\gamma_t\alpha)^2}{4\alpha}} e^{\gamma_t^2\alpha} \tag{6.9}$$

It is clear from the above equations that the QI envelope should be displaced from the CI envelope backward in time by an amount $t_0 = 2\gamma_t\alpha$, and the shift is clearly reflected in the data of Figure 6.6. However, the shift predicted by theory seems to be the opposite of the shift in the experiment. Because we assumed in the theoretical calculations that the control pulse follows the pump pulse ($\tau_y - \tau_p > 0$), the above equation for the QI is not valid for negative delays. When the control pulse precedes the pump pulse, we obtain,

$$QI_{env} = e^{-\frac{(-(\tau_p-\tau_y)+2\gamma_t\alpha)^2}{4\alpha}} \tag{6.10}$$

The equation makes sense now when we interchange the role of the pump and control pulse, *i.e.* $\tau_y \Leftrightarrow \tau_p$. This yields a positive shift in the QI envelope relative to the CI envelope, as observed experimentally. We can thus obtain, by fitting the CI data as shown, the parameter σ. From this, and the fit to the QI data, we can obtain both the inhomogeneous width and the dipole dephasing time. The various parameters are given by,

$$s = \sigma^{-1} = 4.43\,\text{ps}, \quad t_0 = 0.658\,\text{ps}, \quad \alpha = 12.001\,\text{ps}^2$$

from which we obtain

$$\hbar\eta_g = 0.44\,\text{meV} \quad \text{and } \gamma_t = 0.0274\ \text{ps}^{-1} \implies T_2^{dip} = 36.5\ \text{ps}$$

The obtained inhomogeneous FWHM and trion dipole dephasing time is not in complete agreement with the numbers obtained from the DT and FWM data in Section 5.1, but are of the same order of magnitude and hence represent reasonable agreement of the theory and the experiment.

6.3 Chapter Summary

We have shown in this chapter that coherent optical control of the spin coherence can be achieved by taking advantage of the quantum interference between various pathways leading to the spin coherence. In the experiments covered in Section 6.1, we used the interference between two photon processes created separately by the pump pulse and the control pulse to enhance or reduce the spin coherence amplitude. In Section 6.2 we used interference between two photon processes where both pump and control fields were present to achieve femtosecond control by modulating the intermediate state.

CHAPTER 7

Coherent Nonlinear Optical Spectroscopy of Single Charged Quantum Dots

The experiments presented in Chapter 5 and Chapter 6 demonstrate that the trion state is clearly well suited for performing coherent optical manipulations of the electron spin in the ground state of charged QDs. However, the measurements were limited by the ensemble nature of the CQDs that were probed. A key requirement for optically driven spin based QD QC is the ability to coherently manipulate a single electron spin, and to drive qubit rotations (Rabi oscillations) between the spin states. Coherent optical control of a single electron spin through the trion state requires the ability to address a single spin, and demands a deeper understanding of the physical properties and parameters characterizing the optical transition between the ground states of a singly charged QD and the trion state. Exciton based quantum logic gates that have been demonstrated in our group [408] could not have been realized without the initial experiments on the linear and nonlinear optical properties of single QD excitons carried out by earlier workers [204, 244, 284, 332, 364, 368, 381, 382]. The first step in the pathway to QD spin QC with optical fields is therefore to characterize the optical transition between the spin states and the trion states at the single QD level. Section 7.1 is devoted to exploring measurements on the nonlinear optical spectroscopy of single charged quantum dots.

As shown in Section 5.2, the electron spin coherence in the ground state of charged QDs is extremely robust against dephasing, and persists up to 10 ns for vanishing magnetic field. However, due to the ensemble nature of the electron spins that were probed, the spatial fluctuations in the hyperfine interaction from one QD to another limited the observable coherence. In Section 7.2 we demonstrate the coherent excitation of electron spin coherence down to the single electron level. The measurements show no decay over the scan range of 600 ps, in contrast to the Raman coherence between excited states of a single neutral QD.

7.1 Nonlinear Spectroscopy of Single Charged QDs

In Section 5.1, transient DT and FWM measurements were presented on the unapertured sample (612F-3NA) which showed that the trion dipole decoherence time (T_2^{dipole}) and the population decay time (T_1^{dipole}) were comparable to that of the excitonic transition. For the remainder of this section, we drop the superscript with the understanding that we are only concerned with the optical transitions, and not the spin states. The drawback to the transient measurements presented in those sections were that they probe ensemble properties of CQDs, and furthermore, are sensitive to effects such as spatial and spectral diffusion over the area of the laser spot. Thus, we noted certain features like bi-exponential decays in the DT signal and a decrease in the FWM decay times as the power is increased.

By contrast, we will show in this section that when probed on length scales ~ 1 μm or lesser, the trion dipole transition is well described by a simple non-interacting two-level model. The data in this section is from the sample 912F-2A, however similar results were obtained from sample 612F-2A and 612F-3A as we will see in the subsequent sections. We performed frequency domain coherent nonlinear optical spectroscopy measurements, with the experimental setup described in Section 4.3. Modulation of the optical fields at $\sim$ 100 MHz using standing-wave AOMs, combined with homodyne detection on an avalanche photodiode and standard lock-in detection techniques, allows us to phase sensitively detect the coherent nonlinear optical signal (CNOS) in the sample.

7.1.1 Resonant Addressing of Single Trion States

Figure 7.1(a) shows a degenerate ($\Omega_1 = \Omega_2$) nonlinear spectrum taken with the Ti:Sapphire laser through a 0.7 μm aperture (2,B), at a temperature of 4.8 K, that exhibits sharp atomic-like resonances characteristic of the discrete density of states expected. The temperature dependence shown in Figure 7.1(b) was used to identify those peaks in the nonlinear spectrum that correspond to excitons and trions. The three narrow resonances that are clearly visible in Figure 7.1(a) with peak positions at 1631.87, 1632.22 and 1632.52 meV are labeled as *X*, *Ta*, and *Tb*, respectively, in Figure 7.1(b). The trion resonances labeled as *Ta* and *Tb* are seen to diminish in magnitude and disappear as the temperature is raised beyond 10 K as expected for trions. The exciton resonance however was found to be stable to much higher temperatures ($\sim$ 30 K). The temperature dependence observed here in the CNOS reflects

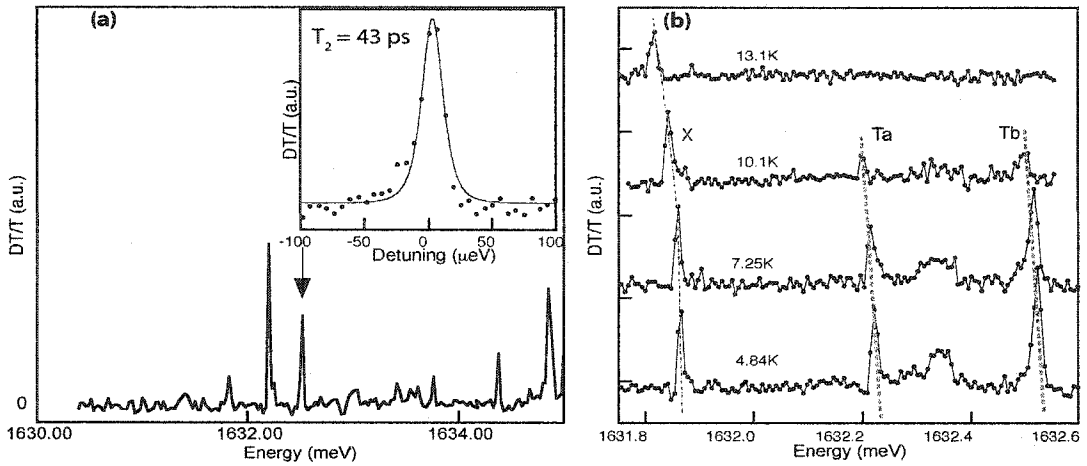

Figure 7.1: Degenerate nonlinear spectroscopy of single CQDs. (a) Degenerate nonlinear spectrum through a 0.7 μm aperture (2,B) of sample 912F-2A, at 4.8 K. The inset shows a high-resolution scan of the resonance marked by an arrow, with a Lorentzian squared fit yielding $\hbar\gamma = 15.2 \pm 1.1$ μeV. (b) Temperature dependence of the DT signal. The resonance marked X corresponds to an exciton, which is stable as the temperature increases. The resonances Ta and Tb are identified as trions, which decrease in magnitude and vanish as the temperature increases.

the temperature dependence observed in the single QD PL measurements (Section 3.3). In our experiments, the temperature at which the trion states disappear varies between 10 K to 20 K when probed through apertures. It should be noted that in Section 2.3, we presented data (Figure 2.6) which showed that the trion peak in the unapertured sample (612F-3NA) vanished at $T \sim 40$ K due to ionization of the trion complex. The discrepancy is not completely understood, but could possibly be due to hopping of the electron from one dot to another, thereby leaving the overall signal unchanged in the ensemble measurements.

To quantify the experimental data, we used the four-level density matrix master equations presented in Section 4.1.1 and reduced them to a three-level system or two-level system based on the appropriate experimental conditions. For the data in Figure 7.1 with no magnetic field, we can use a simple two-level model, and obtain the nonlinear polarization in the presence of the pump and probe CW fields as follows,

$$\tilde{P} = \frac{2iN_0\mu^3|E_1|^2E_2^*}{(2\hbar)^3}\frac{1}{\gamma_t - i\Delta_2}\left[\Gamma_t^{-1}\left(\frac{1}{\gamma_t - i\Delta_1} + \frac{1}{\gamma_t + i\Delta_1}\right) + \frac{1}{\Gamma_t - i(\Delta_2 - \Delta_1)}\left(\frac{1}{\gamma_t - i\Delta_2} + \frac{1}{\gamma_t + i\Delta_1}\right)\right]$$
$$+ \frac{2iN_0\mu^3|E_2|^2E_1^*}{(2\hbar)^3}\frac{1}{\gamma_t - i\Delta_1}\left[\Gamma_t^{-1}\left(\frac{1}{\gamma_t - i\Delta_2} + \frac{1}{\gamma_t + i\Delta_2}\right) + \frac{1}{\Gamma_t - i(\Delta_1 - \Delta_2)}\left(\frac{1}{\gamma_t - i\Delta_1} + \frac{1}{\gamma_t + i\Delta_2}\right)\right] \tag{7.1}$$

where γ_t is the trion dipole decoherence rate, N_0 is the initial population in the ground

state, Γ_t is the trion population relaxation rate, $\Delta_{1(2)} = \Omega_{1(2)} - \omega_g$ is the detuning between the pump (probe) frequency and the trion resonance frequency. The above equation takes into account the fact that we are detecting both pump and probe beams on the avalanche photodiode. For the degenerate experiments presented here $\Delta_1 = \Delta_2 = \Delta$, and in the experiments the pump and probe fields usually have equal magnitude. Therefore, the polarization becomes,

$$\tilde{P} = \frac{iN_0\mu^3|E|^2E^*}{\hbar^3}\Gamma_t^{-1}\frac{1}{\gamma_t - i\Delta}\frac{\gamma_t}{\gamma_t^2 + \Delta^2} \tag{7.2}$$

The DT signal is given by $DT \propto \Im(\tilde{P})$, hence we see that the lineshape is described by the square of a Lorentzian function. The inset to Figure 7.1(a) shows a high-resolution scan of the resonance Tb with peak position 1632.52 meV. The solid line is a fit with a Lorentzian squared function to the data, from which we extracted $\hbar\gamma_t = 15.2 \pm 1.1\,\mu$eV. Thus, we obtain the trion dipole dephasing time ($T_2 = \gamma_t^{-1}$) to be 43.8 ± 3.2 ps, comparable to T_2 for excitons in a neutral QD sample [204]. This is reassuring, since the charged nature of trions could conceivably increase their coupling to the environment, with excess scattering from other trions and charge carriers, hence reducing the coherence time. The narrow linewidths observed above in the degenerate nonlinear spectra for trions are significant since they show that remote doping has not resulted in a Fermi sea of electrons in the QW. Similarly, the measured $T_2 \sim 44$ ps is roughly an order of magnitude greater than that reported for trions in modulation-doped QW structures that are localized by fluctuations in the potential of the remote donors [248, 256], which is further proof of the "box" localization model due to quantum confinement discussed in Section 2.1.3.

Non-degenerate (fix Ω_1, scan Ω_2) spectroscopy allows us to study the contribution due to the decoherence from pure dephasing processes as well as to verify the two-level model adopted. See Section 4.3) for the description of the experimental setup. The data was taken by fixing the dye pump laser frequency at $\Omega_1 = 1632.52$ meV (the resonance Tb),and scanning the Ti:Sapphire probe laser frequency, Ω_2. The non-degenerate spectra are shown in the bottom panel of Figure 7.2(c), and the degenerate CNOS spectrum is also shown for reference at the top. From top to bottom, the scans were obtained for the pump detuning values $\Delta_1 = (0, 0.17, 0.67, 1.2)\,\gamma_t$, where $\hbar\gamma_t = 15.2\,\mu$eV as obtained from the degenerate spectrum. As expected for an isolated two-level system, the absence of any spectral hole burned by saturation of the resonance Tb implies that these are truly localized single trion states, and not a micro-ensemble under our laser spot, thus confirming the interpretation

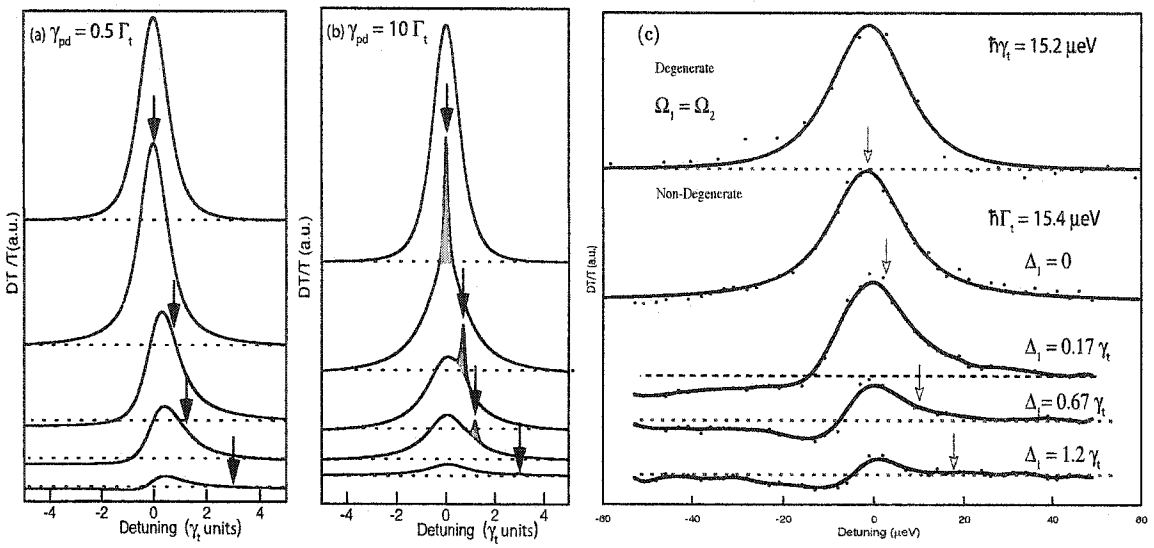

Figure 7.2: Theory and experiment for non-degenerate nonlinear spectroscopy of a single CQD. (a) Theory for non-degenerate spectrum assuming the pure dephasing rate $\gamma_{pd} = 0.5\Gamma_t$. (b) Theory for non-degenerate spectrum assuming $\gamma_{pd} = 10\,\Gamma_t$. The shaded regions in (b) represent the contribution to the dipole decoherence from recombination. The x-axis is the probe detuning (Δ_2) in units of the trion dipole decoherence rate (γ_t). For both (a) and (b), the order of the curves is (from top to bottom): degenerate, $\Delta_1 = 0$, $\Delta_1 = 0.7$, $\Delta_1 = 1.2$, $\Delta_1 = 3$.(c) Non-degenerate data : the arrows indicate pump frequency position, the x-axis is the probe detuning. The fit to the scan with $\Delta_1 = 0\,\mu$eV gives $\hbar\Gamma_t = 15.4 \pm 1.6\,\mu$eV, assuming the dipole decoherence rate is given by $\hbar\gamma_t = 15.2\,\mu$eV as obtained by fitting the degenerate spectrum. Solid lines on other scans are guides to the eye and scans are offset for clarity.

of our earlier PL data (Section 3.3).

From Eq. (7.1) and setting $\Delta_1 = 0$, we obtain the theoretical prediction for the signal. The resulting function was fitted to the data obtained in Figure 7.2(c) for $\Delta_1 = 0$, and we can extract $\hbar\Gamma_t = 15.4 \pm 1.6\,\mu$eV, which gives $T_1 = 42.7 \pm 4.4$ ps. In the absence of pure dephasing processes, we expect $T_2 = 2T_1$, which shows that the pure dephasing rate for the state under investigation is roughly comparable to the contribution from radiative recombination, *i.e.* $\gamma_{pd} \approx \Gamma_t/2$. The resulting decoherence rate is then $\gamma_t = \gamma_{pd} + \Gamma_t/2 \approx \Gamma_t$. This is in contrast to higher-dimensional systems where typically $\gamma_t \gg \Gamma_t$, providing further support to our claim that localized trion states are immune to the rapid dephasing processes which dominate the radiative contribution in bulk and QW structures. To investigate the effect of pure dephasing further on the spectral lineshape, we used Eq. (7.1) to generate theory curves for the predicted DT signal for two cases (a) $\gamma_t = \Gamma_t\,(\gamma_{pd} = \Gamma_t/2)$ and (b) $\gamma_t = 10.5\Gamma_t\,(\gamma_{pd} = 10\,\Gamma_t)$. The predicted signal is plotted in Figures 7.2 (a) and (b),

respectively.

In the theory, as Ω_1 is tuned away from the center of the resonance, the CNOS reduces in amplitude, as expected from physical intuition. Furthermore, as seen in Figure 7.2 (b), if the pure dephasing rate were significantly larger than the radiative contribution, a characteristic "Prussian helmet" shape would result which tracks the pump frequency, clearly absent in the data. The shaded regions in Figure 7.2(b) denote the contribution to the signal from the recombination, and the broader feature is due to the pure dephasing contribution. The non-degenerate data implies that pure dephasing has not overwhelmed contributions from the radiative decay, unlike in higher-dimensional structures. An extremely interesting feature of both the theory in Figure 7.2(a), for $\gamma_t = \Gamma_t$ ($\gamma_{pd} = \Gamma_t/2$), and the data in Figure 7.2(c), is the development of an interference lineshape as the pump detuning Δ_1 is increased. The interference lineshape is a key signature of the two-level model adopted for the trion, since it results from coherent population oscillations or "population pulsations" [204, 270]. The coherent population oscillations are a result of the population in second order oscillating at the frequency $\Omega_1 - \Omega_2$ of the grating created by the pump and the probe fields, which interferes with the usual incoherent contribution to the population. The coherent nature of the population pulsations is evident from the fact that if the detuning between the pump and probe fields grows large compared to the population relaxation rate Γ_t, the effect will be washed out. The data clearly show that this is not the case for the trion system, and is strong evidence for the localized two-level model that we have adopted. It is interesting to note that the dip in the spectral line caused by population pulsations has been used to demonstrate impeding of light pulses in ruby crystals [395] and superluminal and subluminal propagation in alexandrite crystals [396] at room temperature.

7.1.2 Resonant Addressing of Dark Transitions

In Section 3.3 we discussed the fine structure of trions and excitons, and used their dependence on the magnetic field as a signature to distinguish one from the other. We also pointed out that in the presence of an in-plane magnetic field (Voigt geometry), the formerly "dark" transitions of the trion become bright, due to mixing of the electron spin ground states (see Section 3.2). The appearance of spin quantum beats in Section 5.2 due to stimulated Raman excitation via the intermediate trion state, and the observation of

spontaneously generated coherence (Section 5.3), are also an indirect indicator that the theoretical picture presented for the ground and first excited states of a charged QD are correct. However, till now we have not presented direct evidence that we can resonantly access the dark transitions which enable the stimulated Raman process, and thereby form a key step in optical quantum computing with electron spins.

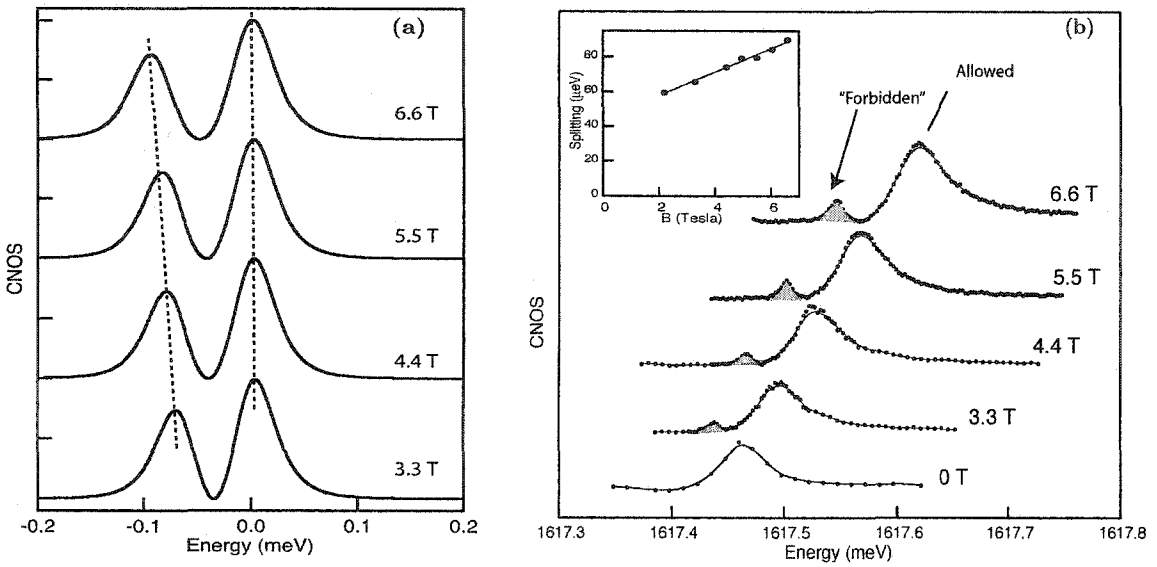

Figure 7.3: Theory and experiment for resonant addressing of the "dark" transition in a single CQD. (a) Theory for degenerate nonlinear spectrum of a single CQD in the Voigt geometry, modeled as a Λ system. (b) Degenerate nonlinear spectrum through aperture (3,C) of sample 612F-2A as a function of the magnetic field in the Voigt geometry. The peak at zero magnetic field is due to the allowed trion dipole transition. As the field is increased, the peak at lower energy arises due to the formerly dark transitions. Inset:The splitting between the peaks is plotted as a function of the field, and a linear fit yields the g-factor $|g_{e,x}| = 0.08$.

Figure 7.3 presents both experimental and theoretical results demonstrating direct resonant access to both the bright and dark transitions of the trion from the electron spin ground states. Degenerate nonlinear spectra were obtained from aperture (3,C) of the sample 612F-2A, as a function of the in-plane magnetic field. The data was obtained with both pump and probe linearly polarized. At zero magnetic field, there is a single peak due to the bright transition of the trion in the charged QD. The basic features of the signal as a function of the field are easily understood, for we note that as the field is increased there is a peak at lower energy that increases in separation from the bright trion resonance. This is explained by the fact that when the field is increased, the splitting between the electron spin states increases linearly, and because the in-plane hole g-factor is zero (Sections 3.2–3.3),

there are only two distinguishable transitions. However, some puzzling aspects of the data are that firstly, in the simple scheme that we have presented for the trion in Section 3.2 (see also Figure 5.3), all the transitions should be of equal strength, but the data clearly shows that the dark transition is initially weaker than the bright transition and grows in strength as the magnetic field is increased. Secondly, the dark transition should be expected to have nearly the same linewidth as the bright transition, but the data shows that the dark transition is narrower. Even taking into account the slope in the background signal (possibly due to non-resonant nonlinearities), this conclusion still holds. Thirdly, a plot of the peak separation versus the field shows that while the data is well fit by a line (inset to Figure 7.3(b)), there is a zero-field intercept for the splitting of $\sim 40\,\mu$eV.

To quantify the data, we proceed to calculate the expected DT signal. For simplicity, we modeled the signal using a Λ-level scheme, because as seen in Section 5.2, except for the polarization dependence, the basic physics is encapsulated in the Λ-system model upon application of the in-plane magnetic field. As in Section 5.2 we denote the electron spin levels in the ground state by $|x-\rangle$ and $|x+\rangle$, and the upper trion state by $|t-\rangle$. We take into account that the ground states are unequally populated due to the Zeeman splitting, and further that there is spin relaxation from the upper spin state $|x+\rangle$ to the lower state $|x-\rangle$ whose rate is denoted by Γ_s. The master equations and notation followed are the same as in Section 4.1.1, except for the reduction to a three-level system. We also write the Rabi frequencies $\mathcal{R}_{ij}$ as a sum over all the possible input fields,

$$\mathcal{R}_{ij} = \sum_l \mathcal{R}_{ij,l},\ \mathcal{R}^*_{ij} = \sum_l \mathcal{R}^*_{ij,l} \tag{7.3}$$

where

$$\begin{aligned}
\mathcal{R}_{ij,l} &= -\frac{1}{2\hbar}(\boldsymbol{\mu}_{ij}\cdot\mathbf{e}_l)\mathcal{E}_l e^{i(\mathbf{k}_l\cdot\mathbf{r}-\Omega_l(t-\tau_l))},\\
\mathcal{R}^*_{ij,l} &= -\frac{1}{2\hbar}(\boldsymbol{\mu}_{ij}\cdot\mathbf{e}^*_l)\mathcal{E}^*_l e^{-i(\mathbf{k}_l\cdot\mathbf{r}-\Omega_l(t-\tau_l))}
\end{aligned} \tag{7.4}$$

The incoherent contributions to the third-order dipole coherence, wherein population is

created in second order, are given by,

$$\rho^{inc}_{x-,t-} = -ie^{-i(\mathbf{k}_\gamma-\mathbf{k}_\beta+\mathbf{k}_\alpha)\cdot\mathbf{r}}e^{i(\Omega_\gamma-\Omega_\beta+\Omega_\alpha)t}\Big\{\sum_{\alpha,\beta,\gamma}\Big[\frac{N_0\mathcal{R}^*_{x-t-,\gamma}\mathcal{R}_{t-x-,\beta}\mathcal{R}^*_{x-t-,\alpha}}{i(\Omega_\gamma-\Omega_\beta+\Omega_\alpha-\omega_g)+\gamma_t}\times$$
$$\Big(\frac{1}{2\Gamma_t-i(\Omega_\beta-\Omega_\alpha)}\Big)\Big(\frac{1}{i(\Omega_\alpha-\omega_g)+\gamma_t}-\frac{1}{i(\Omega_\beta-\omega_g)-\gamma_t}\Big)\Big(2+\frac{\Gamma_t}{\Gamma_s-i(\Omega_\beta-\Omega_\alpha)}\Big)\Big]$$
$$+\Big[\frac{N_1\mathcal{R}^*_{x-t-,\gamma}\mathcal{R}_{t-x+,\beta}\mathcal{R}^*_{x+t-,\alpha}}{i(\Omega_\gamma-\Omega_\beta+\Omega_\alpha-\omega_g)+\gamma_t}\Big(\frac{1}{i(\Omega_\alpha-\omega_g-\omega_c)+\gamma_t}-\frac{1}{i(\Omega_\beta-\omega_g-\omega_c)-\gamma_t}\Big)\times$$
$$\Big(\frac{2}{2\Gamma_t-i(\Omega_\beta-\Omega_\alpha)}+\Big(\frac{\Gamma_t}{2\Gamma_t-i(\Omega_\beta-\Omega_\alpha)}-1\Big)\Big(\frac{1}{\Gamma_s-i(\Omega_\beta-\Omega_\alpha)}\Big)\Big)\Big]\Big\} \tag{7.5}$$

$$\rho^{inc}_{x+,t-} = -ie^{-i(\mathbf{k}_\gamma-\mathbf{k}_\beta+\mathbf{k}_\alpha)\cdot\mathbf{r}}e^{i(\Omega_\gamma-\Omega_\beta+\Omega_\alpha)t}\Big\{\sum_{\alpha,\beta,\gamma}\Big[\frac{N_0\mathcal{R}^*_{x+t-,\gamma}\mathcal{R}_{t-x-,\beta}\mathcal{R}^*_{x-t-,\alpha}}{i(\Omega_\gamma-\Omega_\beta+\Omega_\alpha-\omega_g-\omega_c)+\gamma_t}\times$$
$$\Big(\frac{1}{2\Gamma_t-i(\Omega_\beta-\Omega_\alpha)}\Big)\Big(\frac{1}{i(\Omega_\alpha-\omega_g)+\gamma_t}-\frac{1}{i(\Omega_\beta-\omega_g)-\gamma_t}\Big)\Big(1-\frac{\Gamma_t}{\Gamma_s-i(\Omega_\beta-\Omega_\alpha)}\Big)\Big]$$
$$+\Big[\frac{N_1\mathcal{R}^*_{x+t-,\gamma}\mathcal{R}_{t-x+,\beta}\mathcal{R}^*_{x+t-,\alpha}}{i(\Omega_\gamma-\Omega_\beta+\Omega_\alpha-\omega_g-\omega_c)+\gamma_t}\Big(\frac{1}{i(\Omega_\alpha-\omega_g-\omega_c)+\gamma_t}-\frac{1}{i(\Omega_\beta-\omega_g-\omega_c)-\gamma_t}\Big)\times$$
$$\Big(\frac{1}{2\Gamma_t-i(\Omega_\beta-\Omega_\alpha)}-\Big(\frac{\Gamma_t}{2\Gamma_t-i(\Omega_\beta-\Omega_\alpha)}-1\Big)\Big(\frac{1}{\Gamma_s-i(\Omega_\beta-\Omega_\alpha)}\Big)\Big)\Big]\Big\} \tag{7.6}$$

Similarly, the coherent contributions which involve Raman coherence created in second order,

$$\rho^{coh}_{0,T} = -ie^{-i(\mathbf{k}_\gamma-\mathbf{k}_\beta+\mathbf{k}_\alpha)\cdot\mathbf{r}}e^{i(\Omega_\gamma-\Omega_\beta+\Omega_\alpha)t}\sum_{\alpha,\beta,\gamma}\frac{\mathcal{R}^*_{x+t-,\gamma}\mathcal{R}_{t-x+,\beta}\mathcal{R}^*_{x-t-,\alpha}}{i(\Omega_\gamma-\Omega_\beta+\Omega_\alpha-\omega_g)+\gamma_t}\times$$
$$\Big(\frac{1}{\gamma_s-i(\Omega_\beta-\Omega_\alpha+\omega_c)}\Big)\Big[\frac{N_0}{i(\Omega_\alpha-\omega_g)+\gamma_t}-\frac{N_1}{i(\Omega_\alpha-\omega_g-\omega_c)+\gamma_t}\Big] \tag{7.7}$$

$$\rho^{coh}_{1,T} = -ie^{-i(\mathbf{k}_\gamma-\mathbf{k}_\beta+\mathbf{k}_\alpha)\cdot\mathbf{r}}e^{i(\Omega_\gamma-\Omega_\beta+\Omega_\alpha)t}\sum_{\alpha,\beta,\gamma}\frac{\mathcal{R}^*_{x-t-,\gamma}\mathcal{R}_{t-x-,\beta}\mathcal{R}^*_{x+t-,\alpha}}{i(\Omega_\gamma-\Omega_\beta+\Omega_\alpha-\omega_g-\omega_c)+\gamma_t}\times$$
$$\Big(\frac{1}{\gamma_s-i(\Omega_\beta-\Omega_\alpha-\omega_c)}\Big)\Big[\frac{N_0}{i(\Omega_\alpha-\omega_g-\omega_c)-\gamma_t}-\frac{N_1}{i(\Omega_\alpha-\omega_g)-\gamma_t}\Big] \tag{7.8}$$

We calculate the DT signal using the above equations for the given experimental conditions. The initial population in the ground states is taken to be,

$$N_0 = \frac{1}{1+\exp(-\hbar\omega_c/k_BT)},\quad N_1 = 1-N_0. \tag{7.9}$$

The theory prediction for the expected degenerate CNOS is plotted in Figure 7.3(a) as a function of the magnetic field taking the experimentally obtained values for the Zeeman splitting, decoherence (γ_t) and decay (Γ_t) rates. It is clear that theoretically, we should observe a peak at lower energy that remains constant in magnitude as the field is raised, which does not reproduce the experimental data. A complete calculation taking into ac-

count the other trion level was performed, and also found to be in agreement with this conclusion [435].

One possible reason for the observed behaviour is that the spin states are not degenerate at zero field. The Hamiltonian for the electron spin states written in the original basis of spin quantization along the z-axis is,

$$H_e = \begin{matrix} \langle z+| \\ \langle z-| \end{matrix} \begin{pmatrix} -\hbar\nu_0 & \hbar\nu_c \\ \hbar\nu_c & \hbar\nu_0 \end{pmatrix} \tag{7.10}$$

where $2\hbar\nu_0$ is the zero-field splitting and $\hbar\nu_c = (1/2)\beta_0 g_{e,x} B_x$. In that case, when the field is turned on, we see that it mixes the states $|z\pm\rangle$ unequally and the dipole moment matrix elements to the trion state are no longer of equal magnitude. The eigenvalues are now given by,

$$E_\pm = \pm\hbar\sqrt{\nu_0^2 + \nu_c^2} = \pm\frac{\hbar\omega_c}{2} \tag{7.11}$$

and the eigenstates are now given by,

$$|x+\rangle = \cos\theta|z+\rangle + \sin\theta|z-\rangle \tag{7.12}$$

$$|x-\rangle = -\sin\theta|z+\rangle + \cos\theta|z-\rangle \tag{7.13}$$

where

$$\theta = \arctan\left(\frac{\nu_c}{(\omega_c/2) - \nu_0}\right) \tag{7.14}$$

The dipole moments will now become,

$$\mu_{t-,x-} = \wp\cos\theta\epsilon_+, \quad \mu_{t-,x+} = \wp\sin\theta\epsilon_+ \tag{7.15}$$

thereby leading to a change in the strength of the dark transitions as the field is increased.

This picture is also borne out by the data in Figure 7.3 which shows that there is a non-zero splitting when the field vanishes. However, we need to consider the physical origin of the zero-field splitting. We also note that the zero-field splitting was not observed in the ensemble spin quantum beat measurements presented in Section 5.2 and cannot be the cause for the amplitude change observed in the beats as a function of the field (Section 5.3). It has been known that a non-zero splitting of excitonic lines at zero magnetic field can be caused by the Overhauser effect, described briefly in Section 3.4.1.2. The Overhauser effect

arises because of the hyperfine interaction, which we reproduce here from Section 3.4.1.2,

$$\mathcal{H}_{en} = \frac{v_0}{2}\sum_j A_j \left|\psi(\mathbf{R}_j)\right|^2 (I_{j,z}\sigma_z + I_{j,x}\sigma_x + I_{j,y}\sigma_y) \tag{7.16}$$

When there is no magnetic field present, the terms proportional to $I_x\sigma_x + I_y\sigma_y$ are responsible for electron-nuclear spin flip, thereby leading to exchange of spin between the electron and nuclear system. This in turn, changes the average nuclear magnetic field, leading to an effective magnetic field that affects the electron spin, and leads to a non-zero Zeeman splitting between the spin levels for the electron.

$$\mathbf{B}_{Ov} = \frac{A}{\beta_0 g_e}\left|\psi(\mathbf{R}_j)\right|^2 \langle \mathbf{I}_z \rangle_N \tag{7.17}$$

If there is a large magnetic field, then the difference in energy between the nuclear and electron Zeeman splittings makes the process highly forbidden due to energy conservation, and requires an assisting process such as emission of phonons, photons or other carriers [330]. Note that the smaller the g-factor, the larger the Overhauser field. For the effect to be large, the electron spin, the nuclear spin and the magnetic field direction needs to be strongly aligned, otherwise the spin flips will average out the effect of the nuclear field. Large nuclear spin polarizations are possible when the electron spin is predominantly aligned by the effect of the optical excitation along the z-axis.

Gammon *et al.* showed that the effect can contribute significantly, even at large Faraday magnetic fields, to the zero-field splitting of excitonic lines [330]. The hole does not contribute to the Overhauser field because, as noted previously (Section 3.4.1), the wavefunction of the hole at the nuclear sites vanishes. Because of electron-hole exchange however, the assisting process required to conserve energy during the electron-nuclear spin flip is mediated by the exchange interaction. Essentially, the rate at which the spin flip process takes place is inversely proportional in second-order perturbation theory to δ_0^2, where δ_0 is the exchange splitting. This energy is substantially lesser than the energy required to flip both electron and hole spins, *i.e.* for transition from one bright exciton state to another. Therefore, the rate is significantly increased and the exciton lines display complicated behavior which depends on the exchange, Zeeman and hyperfine interactions.

For trions, the situation is more complicated as the transitions occur from the trion state to a ground state with an electron spin. Firstly, for the singlet trion state, we note there is no exchange interaction because of the pairing of electron spins. Therefore, for the

electron spin to be flipped, we must promote one electron to a higher energy level, thereby making the process highly forbidden and the possibility of building up nuclear polarization extremely negligible. Hence, we need to consider only the electron spin in the conduction band ground state of the QD. Even at the lowest temperature and highest magnetic fields reached in our experiments, we note that the electron spin in the ground state is unpolarized as it is in thermal equilibrium with the surroundings. Unless we optically pump the electron spin preferentially into one of the spin states, its contribution to the nuclear polarization will be averaged out and we conclude that there should be no Overhauser effect in either the singlet trion state or in the ground states of the charged QD.

Other possibilities for the zero-field splitting include (a) we are actually probing a triplet trion state, for which there would be zero-field splitting due to the exchange interaction (b) presence of Dresselhaus and Rashba fields (introduced in Section 3.4.1) because of the non-centrosymmetric nature of the crystal as well as the built-in electric fields from interface asymmetry due to the QW growth. The latter effects should be relatively small however, and are most likely not the causes of the observed zero-field splitting. We cannot rule out the possibility that this is a triplet trion state with an exchange splitting of $\sim 40\,\mu$eV, as such states have been observed in single QD PL spectroscopy [362, 384]. At this point, we do not have a good explanation for the zero-field splitting but it is certainly a key factor responsible for the trends observed in the nonlinear spectroscopy measurements.

7.2 Single Electron Spin Coherence

Section 5.2 showed that coherent optical pulses can excite and detect the spin coherence between the ground states of an ensemble of charged QDs. With the power of high-resolution frequency domain spectroscopy and the spatial resolution obtainable by excitation through sub-micron diameter apertures, we now extend our ability to excite and detect the spin coherence down to the single electron level. The experimental setup for the time domain measurements is the same as that used previously in Section 5.2, and the collection optics setup is shown in Figure 4.6 (a).

The data obtained is from aperture (3,C) of sample 612F-3A, and is shown in Figure 7.4. The inset shows the degenerate frequency domain CNOS obtained as a function of the field. We note that there are clearly bright and dark transitions with increasing separations as

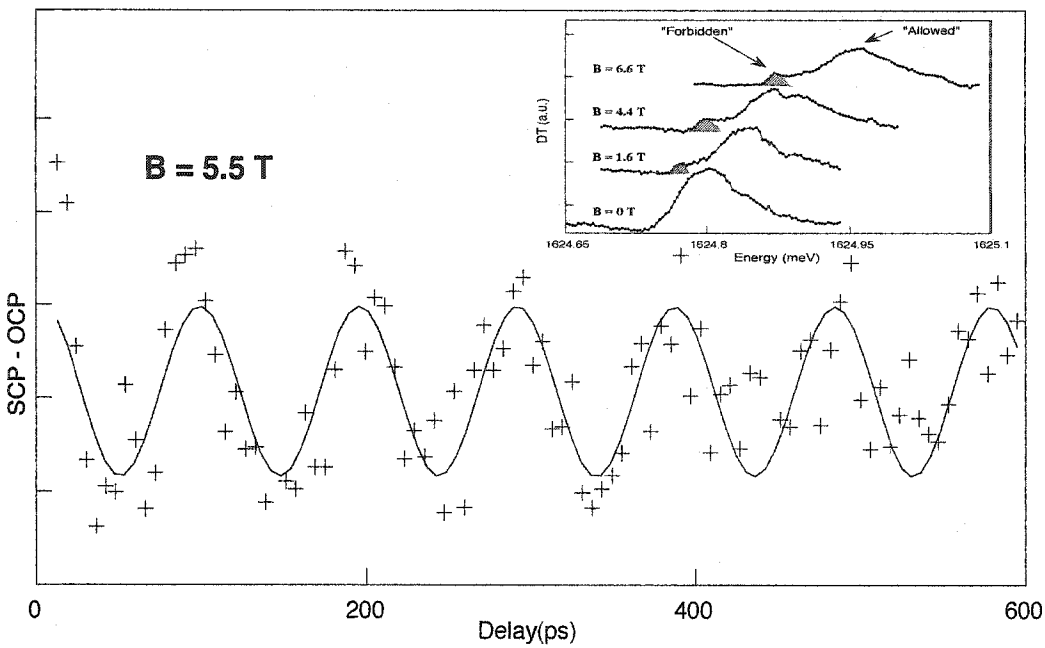

Figure 7.4: Single electron spin coherence excited by coherent optical pulses. The pulse width was ~ 5.6 ps. The data (+ symbols) shown is the difference between SCP and OCP configurations, taken through aperture (3,C) of sample 612F-3A. The solid line is a sinusoidal fit to the data. The inset shows the forbidden and allowed transitions of the trion state probed by frequency domain nonlinear spectroscopy.

the field increases. Once again, we observed zero-field splitting when plotting the splitting as a function of the field (data not shown). We however conclude that the state is most likely to be a trion state based on the discussion preceding this section. With optical access now to both the bright and dark transitions of a single charged QD, we were able to repeat the quantum beat measurements, but now at the single electron level.

The quantum beat data obtained by taking the difference between SCP and OCP configurations is shown in Figure 7.4, denoted by + symbols. The solid line is a sinusoidal fit to the data. A decaying sinusoidal fit was also attempted, and the decay time was found to be 465 ± 125 ps, with a larger χ^2 than for the fit displayed. Since the scan range is essentially the same as the decay time, we conclude that there is no decay over the range of data obtained. The experiment demonstrates that we have been able to excite spin coherence between the ground states of a single charged QD. The Raman decoherence time $T_2 \sim 600$ ps is an order of magnitude greater than the lifetime reported for the Raman coherence between excited states of a neutral QD, $T_2 \sim 60 - 100$ ps [373, 446]. The difference arises

from the fact that in neutral QDs, the Raman coherence between the bright exciton states is limited by the recombination lifetime of the excitons, corresponding to a V-system. The data demonstrates that since the Raman coherence between the spin ground states of a CQD resides in non-decaying states, corresponding to the ground states of a Λ-system, it is not limited by recombination of the trion state. The experiment has been repeated on a number of other CQDs, and currently the maximum decay time observed is ~ 5 nsec [435].

7.3 Chapter Summary

We have shown in this chapter that nonlinear optical spectroscopy constitutes a powerful tool to probe the decay dynamics, transition strengths and physical properties of trion states in single charged QDs. In Section 7.1.1, we used frequency domain nonlinear spectroscopy techniques to probe the dipole decoherence rate and radiative decay rates of single trions, and showed that pure dephasing processes do not contribute significantly to the decoherence. Section 7.1.2 showed that it is possible to resonantly access both the bright and spin-flip (or "forbidden") transitions between a single electron spin and the trion state. Finally, Section 7.2 presented experimental data where we used coherent optical fields to excite and detect the Raman coherence between the spin states of a single electron in the charged QD. The data showed no decay over the scan range ($\sim$ 600 ps), and was not limited by the recombination of the intermediate state.

CHAPTER 8

Summary and Future Directions

In this chapter, we summarize the work performed in this thesis, and provide some future directions of research. The key ideas that will be discussed are experiments to perform a spin Rabi oscillation and measurement of the spin coherence time using spin Raman echo. We will conclude with a discussion on how a spin-based quantum logic gate could be realized.

8.1 Summary

This work has concentrated on understanding the resonant nonlinear optical response of charged excitations in QDs. The experiments were motivated by the possibility of coherent optical manipulation of the electron spin in a CQD. We began by characterizing the basic linear optical properties of the CQD, both at the ensemble and single QD level, through PL. Transient nonlinear optical spectroscopy on the ensemble of CQDs allowed us to measure the T_1 and T_2 times of the trion dipole transitions, and showed that they did not deviate significantly from the excitonic dipole transition in neutral QDs. We further demonstrated that spin coherence can be excited via the stimulated Raman process involving the trion state. The spin coherence time, even though limited by the ensemble nature of the QD spins and the fluctuations in the nuclear hyperfine interactions, far exceeds the dipole coherence time of excitons that has been measured in both interface fluctuation QDs and SAQDs. An important outcome of the experiments was the observation of a contribution to the spin coherence from the vacuum-field induced decay of the trion state, known as SGC. SGC had been sought after unsuccessfully in atoms, where it was first predicted. However, due to the difficulty in engineering the correct level scheme, there was no earlier experimental observation of an excited state population decaying to a ground-state coherence. Since QDs

behave like artificial atoms, we were able to engineer the required properties in our QDs by magnetic field and doping.

Coherent optical control experiments, which form an extension of spin resonance techniques to the optical domain, were performed next. We showed that the spin coherence generated optically is indeed a true quantum coherence, because it is undergoes quantum mechanical interference. The quantum superposition principle allowed us to achieve femtosecond precision control over the state of the electron spin coherence, by modulation of the intermediate trion dipole coherence. The experiments, when carried into the strong-field regime, could also be used for measuring the spin relaxation time, as well as characterizing the physical density matrix of the spin state. Finally, we concluded by extending our ensemble measurements to the single QD level. We showed that, in the absence of a magnetic field and under optical excitation, the CQD indeed behaves like an isolated two-level system, even exhibiting the characteristic population pulsations that are observed in atoms. Upon applying a magnetic field in the Voigt geometry, we were able to resonantly access the spin-flip transition for the first time, since the inhomogeneity in linewidth was suppressed. Finally, using pulsed optical excitation, we excited and detected the spin coherence between spin states at the single electron level. The Raman coherence was found to be limited by the scan range, and not the recombination time of the trion state.

8.2 Future Directions

8.2.1 Spin Rabi Oscillations

The extension of coherent control measurements to the strong-field regime is essential for quantum logic operations. By demonstrating coherent qubit rotations or Rabi oscillations on the spin state, mediated by optical excitation, we would be able to perform single qubit logic operations, which along with two-qubit universal logic gates can be used to build a quantum computer. To begin with, it is necessary to initialize the spin state. Normally, the spin states are in thermal equilibrium, because $\hbar\omega_c \ll k_B T$, and so we must show that state preparation is possible. Several proposals exist for the initialization and the read-out of the spin population, as discussed in Section 1.2. Shabaev *et al.* have shown that the trion state can be used to optically pump the electron spin into a well-defined state, by

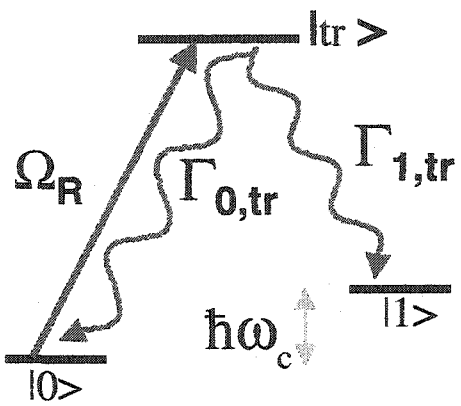

Figure 8.1: Initialization of electron spin state using resonant CW fields. The Rabi frequency Ω_R, and the decay rates $\Gamma_{0,tr}, \Gamma_{1,tr}$ must be much greater than the spin relaxation rate Γ_s. It is also assumed that the Zeeman splitting $\hbar\omega_c$ is larger than the linewidth $\gamma_{0,tr}, \gamma_{1,tr}$. Figure and theory courtesy of Yanwen Wu.

using a train of short optical π-pulses that is in phase with the spin precession caused by a permanent transverse magnetic field which lies in the plane of the QW [420]. A simpler protocol is also possible in the absence of a transverse magnetic field. A short σ^+ polarized optical π-pulse creates the singlet trion state $|\uparrow\downarrow\Uparrow\rangle$ from the electron spin state $|\uparrow\rangle$. The pulse cannot drive the transition from $|\downarrow\rangle$ because of Pauli blocking as explained before. At the same time, a short transverse magnetic field pulse can convert any population in the spin state $|\downarrow\rangle$ to the $|\uparrow\rangle$. Obviously, short magnetic pulses (pulse duration shorter than the trion recombination time) are hard to engineer, although g-tensor voltage modulation might overcome this problem [349]. Further, readout of the spin in the protocol is enabled through the same trion state by detecting the transient photon polarization upon excitation with intense $\sigma^+(\sigma^-)$ light, turned on after the N^{th} preparation pulse. Another scheme, that could be implemented with either a CW or pulsed laser field is shown in Figure 8.1.

The spin Rabi oscillation can now be performed through a fast optical pulse, which is detuned $\Delta \sim 2(1/T)$ where T is the pulsewidth. The detuning is required to avoid populating the intermediate trion state, thereby leading to a mixed state, and the calculations (see Figure 8.2) show that it is in principle possible to achieve nearly 100% coherent population transfer. See also Reference [434] for a similar approach using stimulated Raman adiabatic passage (STIRAP).

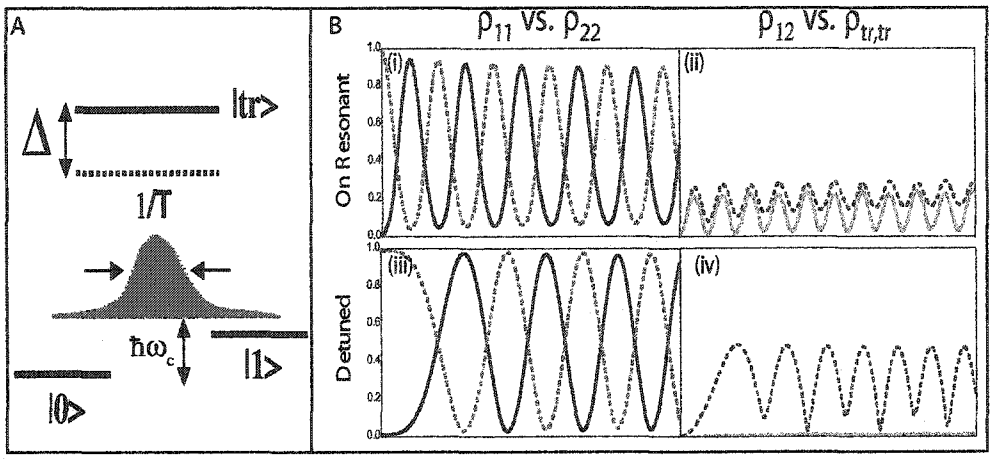

Figure 8.2: Theory for spin Rabi oscillation with ultrafast pulses. A. Level diagram and pulse properties used for calculation of spin Rabi oscillation. B. Numerical simulations showing ρ_{11} vs. ρ_{22} for on-resonant (i) and off-resonant (iii) pulsed excitation. The simulation shows that (ii) for detuning $\Delta = 0$, the trion population is non-zero, thereby creating a mixed state, (iv) for $\Delta \sim 2(1/T)$, the trion state is not populated, resulting in a coherent spin qubit rotation. Figure and theory courtesy of Yanwen Wu.

8.2.2 Spin Raman Echo for Measuring the Coherence Time

In Section 5.2, we demonstrated coherent optical excitation of the spin coherence in an ensemble of CQDs and showed that $T_2^* \sim 10\,\text{ns}$. In Section 7.2, we showed that the spin coherence of a single QD electron is much greater than the recombination time. In fact, recently our group has measured spin coherence times on single QD electrons of $\sim 5\,\text{ns}$ [435]. However, due to spectral diffusion caused by the nuclear hyperfine interactions, both measurements are limited by the ensemble or time averaging. To overcome the limitation of the inhomogeneous broadening from the spectral diffusion, we can perform a spin Raman echo measurement [23, 49]. The Raman echo is a six-photon process occurring in the Λ-level scheme, and allows us to eliminate the inhomogeneous broadening in both the trion frequency and the Zeeman splitting. The pulse sequence and perturbation chain are shown in Figure 8.3.

The technique adiabatically eliminates the upper trion states using a two-photon Raman process where the laser is detuned from the trion state, returning the treatment of the system back to a simple problem of photon echo on an effective two-level system. The adiabatic condition requires $\Omega_R/T \ll \Delta_{tr}^2$, where Ω_R is the Rabi frequency of the dipole transition, T is the pulse width and Δ_{tr} is the detuning from the upper trion state. After

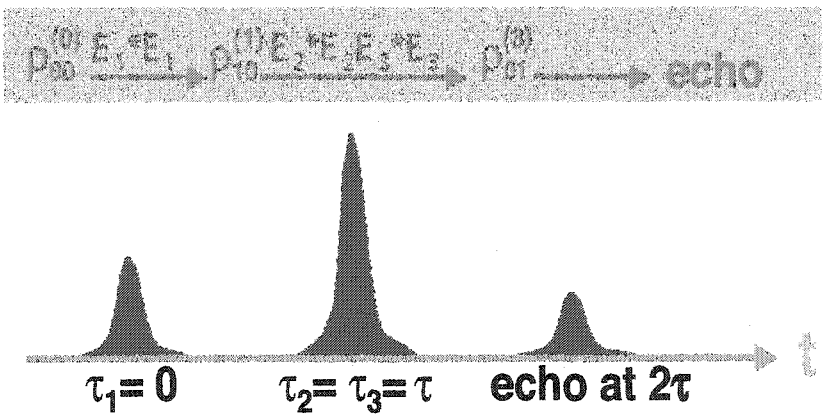

Figure 8.3: Pulse sequence and perturbation chain for the spin Raman echo. The spin Raman echo will allow us to measure the spin coherence time, even in the presence of inhomogeneous broadening caused by the nuclear spectral diffusion. The calculations show that the spin Raman echo occurs at a time τ after the second pulse, and radiates at the cyclotron frequency. Figure and theory courtesy of Yanwen Wu.

the elimination of the upper trion state, we derive the spin Raman echo signal using a third order perturbation calculation of the off-diagonal density matrix ρ_{01} in the interaction picture,

$$\rho_{01} \propto ie^{-\gamma_s(t-(\tau_3-\tau_2))}e^{-\Gamma_s(\tau_3-\tau_2)}(e^{-\frac{\sigma^2}{4}(t-(\tau_3-\tau_2))^2}+e^{-\frac{\sigma^2}{4}(t-(\tau_3+\tau_2))^2}) \tag{8.1}$$

where γ_s is the spin decoherence rate, Γ_s is the spin relaxation rate, σ is the inhomogeneous width of the spin state, and τ_2 and τ_3 are the time delay of the second and third pulses from the first pulse, which arrives at $t = 0$. By setting $\tau_2 = \tau_3 = \tau$ and selecting only the correct time ordering term, Eq. (8.1) simplifies to the following

$$\rho_{01} \propto ie^{-\gamma_s t}e^{-\frac{\sigma^2}{4}(t-2\tau)^2} \tag{8.2}$$

where we can clearly see that the echo occurs at the time of 2τ. Figure 8.3 shows the time ordering of the excitation pulses and the echo signal. By varying τ, the coherence time between the spin ground states, γ_s, is measured in the echo.

We note that here, the echo signal is real and is radiating at the cyclotron frequency, ω_c, which is in the microwave range. In order to detect the echo signal in the optical region, the optical dipole transition between one of the spin states and the trion state is excited with a detuned field when the spin raman echo is produced ($t = 2\tau$), and the signal can be observed via the Stokes radiation. Experimentally, the echo signal can be distinguished from signals of other orders by using proper amplitude modulations and lock-in detection.

8.2.3 Spin-based Controlled Logic Gate

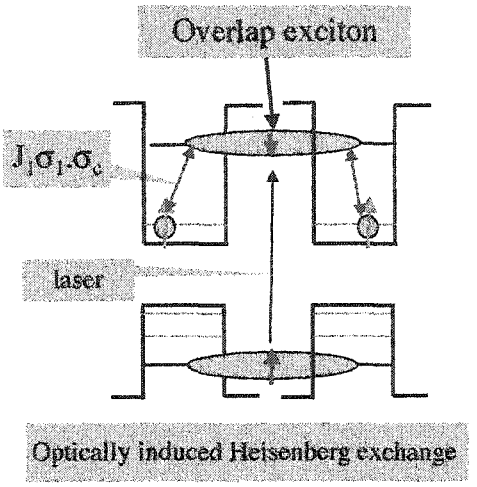

Figure 8.4: Scheme for optical gating of the coupling between CQDs. Optically induced Heisenberg exchange through the RKKY interaction couples electron spins in different QDs, through the common exciton or trion state that overlaps with the QD electron wavefunctions. Adapted from Reference [378].

There have been several proposals in the literature to implement controlled logic gates between two QD electron spins using the trion state. We reviewed some of these already in Section 1.2, and here we will just discuss the proposal by Piermarocchi *et al.* [378], which is schematically depicted in Figure 8.4. An ultrafast laser pulse excites a trion or exciton state that overlaps with the electron wavefunctions in both the QDs, thereby creating a Heisenberg exchange interaction $\mathcal{H}_s(t) = J(t)\boldsymbol{\sigma}_1 \cdot \boldsymbol{\sigma}_2$ where $\boldsymbol{\sigma}_i$ represents the spin vector of the electron in the i^{th} QD. The exchange coupling $J(t)$ depends on the Rabi frequency of the driving laser field, and will be present only during the optical gate. Therefore, we may engineer a $\sqrt{\text{SWAP}}$ gate, as long as the adiabatic Raman condition is satisfied, *i.e.* $T \gg \Omega_R/\Delta^2$, as before. The off-resonant process is required to avoid populating the overlap state, thereby leading to decoherence and loss of fidelity during the gate process. In the experiment, the optical pulses should be designed to maintain a relatively small detuning, otherwise two immediate problems will arise. First, other exciton or trion states in the same QD or other QDs will be excited. Second, increasing laser field strength with larger detuning becomes necessary to couple the trion state, and could result in excitation of delocalized or continuum states that are present in either IFQDs or SAQDs. The narrow linewidth of the trion state implies that we will be able to avoid these problems through

design of the optical pulses using pulse shaping techniques [304, 323].

The above ideas are just some of the possible exciting avenues of research that are now opening up for the pursuit of optically gated quantum computing with quantum dot electron spins. We expect that other new directions, and unexpected discoveries in the physics of charged excitations in semiconductors, will also arise as experiment and theory work together to meet the challenging requirements posed by this interesting and fruitful area of research.

APPENDICES

APPENDIX A

Spontaneously Generated Coherence

In Section 4.1.1, the equations that govern the time evolution of the density matrix elements were presented (Eqns 4.16–4.25). However, as shown in Section 5.3 it is necessary to include a term in the master equation for the Raman coherence due to SGC to fully account for the variation in the amplitude and phase of the spin quantum beats. It was claimed that the correct term is,

$$\dot{\rho}_{x+,x-}|_{sgc} = \Gamma_t(\rho_{t+,t+} - \rho_{t-,t-}) \tag{A.1}$$

The SGC term occurs because of the non-orthogonal dipole moments of the transitions from the trion state to the lower nearly-degenerate states. We will derive that term from first principles by considering the quantized electro-magnetic field and its interaction with a four level atomic system in this appendix. We work in the interaction picture with the three level Λ-system shown in Figure A.1. The interaction Hamiltonian is given by,

$$\mathcal{V} = \hbar \sum_{\mathbf{k},\mathbf{q},\lambda,\lambda'} \left[g^*_{ea,\mathbf{k}\lambda} |e\rangle\langle a| e^{i(\omega_{ea}-\nu_k)t} \hat{a}_{\mathbf{k},\lambda} + g^*_{eb,\mathbf{q}\lambda'} |e\rangle\langle b| e^{i(\omega_{eb}-\nu_q)t} \hat{a}_{\mathbf{q},\lambda'} + H.c. \right] \tag{A.2}$$

where ω_{ea}, ω_{eb} denote the transition frequencies, and ν_k, ν_q denote the quantized electro-magnetic field frequencies. The coefficients in the summation are defined as,

$$g_{ea,\mathbf{k}} = \sqrt{\frac{\nu_k}{2\epsilon_0 V\hbar}} (\mu_{ea} \cdot \epsilon_k^{\lambda}) \qquad\qquad g_{ea,\mathbf{q}} = \sqrt{\frac{\nu_q}{2\epsilon_0 V\hbar}} (\mu_{eb} \cdot \epsilon_q^{\lambda'}) \tag{A.3}$$

For ease of notation, we shall drop the polarization indices, except when we explicitly need to sum over them. In the interaction picture, the wavefunction is given by,

$$|\Psi(t)\rangle = C_{e,0}|e,0\rangle + \sum_{\mathbf{k}} C_{a,\mathbf{k}}|a,1_{\mathbf{k}}\rangle + \sum_{\mathbf{q}} C_{b,\mathbf{q}}|b,1_{\mathbf{q}}\rangle \tag{A.4}$$

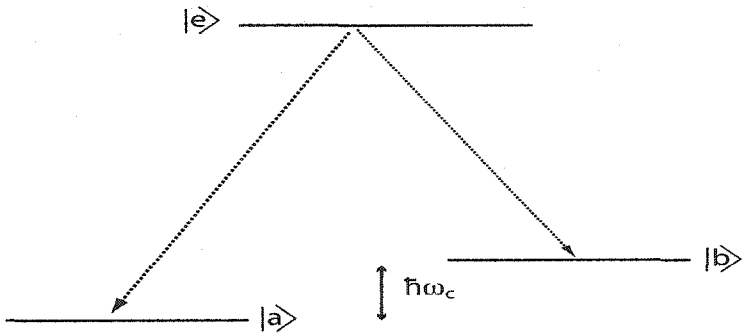

Figure A.1: The three level system which is used to derive the SGC term.

Note that the sum over $\mathbf{k}, \mathbf{q}$ also includes implicitly the sum over all the polarizations (λ, λ') of the field. We then have to solve the Schrodinger equation,

$$\frac{d|\Psi(t)\rangle}{dt} = -\frac{i}{\hbar}\mathcal{V}|\Psi(t)\rangle \tag{A.5}$$

subject to the initial conditions $C_{e,0}(0) = 1$ and all other coefficients vanishing. Substituting Eq. (A.2) and (A.4) into Eq. (A.5), we obtain the following set of coupled equations for the amplitudes,

$$\dot{C}_e(t) = -i\sum_{\mathbf{k}} g^*_{ea,\mathbf{k}} e^{i(\omega_{ea}-\nu_k)t} C_{a,\mathbf{k}} - i\sum_{\mathbf{q}} g^*_{eb,\mathbf{q}} e^{i(\omega_{eb}-\nu_k)t} C_{b,\mathbf{q}} \tag{A.6}$$

$$\dot{C}_{a,\mathbf{k}}(t) = -ig_{ea,\mathbf{k}} e^{-i(\omega_{ea}-\nu_k)t} C_e(t) \tag{A.7}$$

$$\dot{C}_{b,\mathbf{q}}(t) = -ig_{eb,\mathbf{q}} e^{-i(\omega_{eb}-\nu_q)t} C_e(t) \tag{A.8}$$

We can formally integrate the last two equations to yield,

$$C_{a,\mathbf{k}}(t) = -ig_{ea,\mathbf{k}} \int_0^t dt'\, e^{-i(\omega_{ea}-\nu_k)t'} C_e(t') \tag{A.9}$$

$$C_{b,\mathbf{q}}(t) = -ig_{eb,\mathbf{q}} \int_0^t dt'\, e^{-i(\omega_{eb}-\nu_q)t'} C_e(t') \tag{A.10}$$

Substituting Eq. (A.9) and Eq. (A.10) into Eq. (A.6),

$$\dot{C}_e(t) = -\sum_{\mathbf{k}} |g_{ea,\mathbf{k}}|^2 \int_0^t dt'\, e^{i(\omega_{ea}-\nu_k)(t-t')} C_e(t') - \sum_{\mathbf{q}} |g_{eb,\mathbf{q}}|^2 \int_0^t dt'\, e^{i(\omega_{eb}-\nu_q)(t-t')} C_e(t') \tag{A.11}$$

So far, the equation is exact, and we have just replaced the coupled differential equations Eqns A.6–A.8 by the single integro-differential equation Eq. (A.11). Let us look at the first term in the latter equation and make the replacement,

$$\sum_{\mathbf{k}} \to \sum_{\lambda} \int d\Omega_k \int d\nu_k \, \frac{\nu_k^2}{c^3} \frac{V}{2\pi^3}$$

The first term in Eq. (A.11) is then given by,

$$\sum_{\lambda} \int d\Omega_k \frac{(\boldsymbol{\mu_{ea}} \cdot \boldsymbol{\epsilon_k^{\lambda}})(\boldsymbol{\mu_{ae}} \cdot \boldsymbol{\epsilon_k^{\lambda *}})}{(2\pi c)^3 2\hbar\epsilon_0} \int_0^{\infty} d\nu_k \, \nu_k^3 \int_0^t dt' e^{i(\omega_{ea}-\nu_k)(t-t')} C_e(t') \tag{A.12}$$

This may be further simplified using the Wigner-Weisskopf approximation [107, 169, 270],

$$\int_0^{\infty} d\nu_k \, \nu_k^3 e^{i(\omega_{ea}-\nu_k)(t-t')} \approx \omega_{ea}^3 2\pi\delta(t-t') \tag{A.13}$$

which yields for the term,

$$\frac{\omega_{ea}^3 C_e(t)}{(2\pi)^2 c^3 2\epsilon_0 \hbar} \underbrace{\sum_{\lambda} \int d\Omega_k (\boldsymbol{\mu_{ea}} \cdot \boldsymbol{\epsilon_k^{\lambda}})(\boldsymbol{\mu_{ae}} \cdot \boldsymbol{\epsilon_k^{\lambda *}})} \tag{A.14}$$

The integral over solid angle and the sum over polarizations is denoted by $\mathcal{S}$,

$$\mathcal{S} = \sum_{\lambda} \int d\Omega_k (\boldsymbol{\mu_{ea}} \cdot \boldsymbol{\epsilon_k^{\lambda}})(\boldsymbol{\mu_{ae}} \cdot \boldsymbol{\epsilon_k^{\lambda *}}) \tag{A.15}$$

To evaluate $\mathcal{S}$, we use the linear polarization basis vectors perpendicular to $\hat{\mathbf{k}}$ ie $\hat{\boldsymbol{\theta}}_k$ and $\hat{\boldsymbol{\phi}}_k$,

$$\hat{k} = \sin\theta\cos\phi\,\hat{\mathbf{x}} + \sin\theta\sin\phi\,\hat{\mathbf{y}} + \cos\theta\,\hat{\mathbf{z}} \tag{A.16}$$

$$\hat{\boldsymbol{\epsilon}}_k^{(1)} = \cos\theta\cos\phi\,\hat{\mathbf{x}} + \cos\theta\sin\phi\,\hat{\mathbf{y}} - \sin\theta\,\hat{\mathbf{z}} \tag{A.17}$$

$$\hat{\boldsymbol{\epsilon}}_k^{(2)} = -\sin\phi\,\hat{\mathbf{x}} + \cos\phi\,\hat{\mathbf{y}} \tag{A.18}$$

And further assume that $(\boldsymbol{\mu_{ea}})_i = d_i, i = x, y, z$ to get,

$$\boldsymbol{\mu_{ea}} \cdot \boldsymbol{\epsilon_k^{\lambda}} = \sum_i d_i (\epsilon_k^{\lambda})_i \qquad\qquad \boldsymbol{\mu_{ae}} \cdot \boldsymbol{\epsilon_k^{\lambda *}} = \sum_i d_i^* (\epsilon_k^{\lambda *})_i \tag{A.19}$$

which gives,

$$\mathcal{S} = \sum_{i,j} d_i d_j^* \sum_{\lambda} \int d\Omega_k (\epsilon_k^{\lambda})_i (\epsilon_k^{\lambda *})_j = \sum_{i,j} d_i d_j^* \sum_{\lambda} \int_{-1}^{1} d(\cos\theta) \int_0^{2\pi} d\phi (\epsilon_k^{\lambda})_i (\epsilon_k^{\lambda *})_j \tag{A.20}$$

To evaluate $\mathcal{S}$, we note that those terms where $i \neq j$ will vanish because of the ϕ integration. The terms where $i = j$ are as follows,

$$\int d\Omega_k (\epsilon_k^{(1)})_x (\epsilon_k^{(1)*})_x = \int_{-1}^{1} d(\cos\theta) \int_0^{2\pi} d\phi \, \cos^2\theta \cos^2\phi = \frac{2\pi}{3}$$

$$\int d\Omega_k (\epsilon_k^{(1)})_y (\epsilon_k^{(1)*})_y = \int_{-1}^{1} d(\cos\theta) \int_0^{2\pi} d\phi \, \cos^2\theta \sin^2\phi = \frac{2\pi}{3}$$

$$\int d\Omega_k (\epsilon_k^{(1)})_z (\epsilon_k^{(1)*})_z = \int_{-1}^{1} d(\cos\theta) \int_0^{2\pi} d\phi \, \sin^2\theta = \frac{8\pi}{3}$$

$$\int d\Omega_k (\epsilon_k^{(2)})_x (\epsilon_k^{(2)*})_x = \int_{-1}^{1} d(\cos\theta) \int_0^{2\pi} d\phi \, \sin^2\phi = 2\pi$$

$$\int d\Omega_k (\epsilon_k^{(2)})_y (\epsilon_k^{(2)*})_y = \int_{-1}^{1} d(\cos\theta) \int_0^{2\pi} d\phi \, \cos^2\phi = 2\pi$$

This yields,

$$\mathcal{S} = \frac{8\pi}{3}\sum_i d_i d_j^* \delta_{ij} = \frac{8\pi}{3}\sum_i d_i d_i^* = \frac{8\pi}{3}\boldsymbol{\mu_{ea}}\cdot\boldsymbol{\mu_{ae}} \tag{A.21}$$

The first term in Eq. (A.11) becomes,

$$\frac{\omega_{ea}^3 \boldsymbol{\mu_{ea}}\cdot\boldsymbol{\mu_{ae}}}{3\pi\epsilon_0\hbar c^3} C_e(t)$$

The second term in Eq. (A.11) can be evaluated in identical fashion. By setting

$$\Gamma_{ea} = \frac{\omega_{ea}^3 \left|\mu_{ea}\right|^2}{3\pi\epsilon_0\hbar c^3} \qquad\qquad \Gamma_{eb} = \frac{\omega_{eb}^3 \left|\mu_{eb}\right|^2}{3\pi\epsilon_0\hbar c^3} \tag{A.22}$$

We get

$$\dot{C}_e(t) = -(\Gamma_{ea} + \Gamma_{eb})C_e(t) = -\Gamma_e C_e(t) \tag{A.23}$$

The density matrix element corresponding to the Raman coherence in the normal representation is given by,

$$\rho_{ba,\mathbf{qk}} = (C_{b\mathbf{q}}e^{i\omega_{eb}t})(C_{a\mathbf{k}}e^{i\omega_{ea}t})^* = C_{b\mathbf{q}}C_{a\mathbf{k}}^* e^{-i\omega_c t} = \tilde{\rho}_{ba,\mathbf{qk}}e^{-i\omega_c t} \tag{A.24}$$

where $\tilde{\rho}_{ba,\mathbf{qk}} = C_{b\mathbf{q}}C_{a\mathbf{k}}^*$ is the density matrix element in the interaction representation. The reduced density matrix element corresponding to the pure Raman coherence is obtained by taking the trace over the field modes, ie by setting $\mathbf{q} = \mathbf{k}$ and summing,

$$\begin{aligned}
\tilde{\rho}_{ba} &= \sum_{\mathbf{k}\lambda} C_{b\mathbf{k}\lambda}C_{a\mathbf{k}\lambda}^* \\
&= \sum_{\mathbf{k}\lambda}(-ig_{eb,\mathbf{k}\lambda})(+ig_{ea,\mathbf{k}\lambda}^*)\int_0^t dt'\, e^{-i(\omega_{eb}-\nu_k)t'}C_e(t')\int_0^t dt''\, e^{+i(\omega_{ea}-\nu_k)t''}C_e^*(t'') \\
&= \sum_\lambda \int d\Omega_k \int d\nu_k \frac{\nu_k^3}{2(2\pi c)^3\epsilon_0\hbar}(\boldsymbol{\mu_{eb}}\cdot\boldsymbol{\epsilon_k^\lambda})(\boldsymbol{\mu_{ea}}\cdot\boldsymbol{\epsilon_k^{\lambda *}})\int_0^t dt'\, e^{-i(\omega_{eb}-\nu_k)t'}C_e(t')\times \\
&\int_0^t dt''\, e^{+i(\omega_{ea}-\nu_k)t''}C_e^*(t'')
\end{aligned} \tag{A.25}$$

As before, we can perform the integral over solid angle and the sum over the polarizations,

$$\sum_\lambda \int d\Omega_k (\boldsymbol{\mu_{eb}}\cdot\boldsymbol{\epsilon_k^\lambda})(\boldsymbol{\mu_{ea}}\cdot\boldsymbol{\epsilon_k^{\lambda *}}) = \sum_\lambda\sum_{i,j}\int d\Omega_k d_i(\epsilon_k^\lambda)_i \bar{d}_j^*(\epsilon_k^{\lambda *})_j \tag{A.26}$$

the sum over polarizations gives as usual

$$\sum_\lambda \int d\Omega_k\, (\epsilon_k^\lambda)_i(\epsilon_k^{\lambda *})_j = \frac{8\pi}{3}\delta_{ij} \tag{A.27}$$

so that

$$\sum_{\lambda} \int d\Omega_k (\boldsymbol{\mu_{eb}} \cdot \boldsymbol{\epsilon_k^{\lambda}})(\boldsymbol{\mu_{ea}} \cdot \boldsymbol{\epsilon_k^{\lambda *}}) = \frac{8\pi}{3} \sum_i d_i \bar{d}_i^* \tag{A.28}$$

where $d_i = (\boldsymbol{\mu_{eb}})_i$, $\bar{d}_j = (\boldsymbol{\mu_{ea}})_j$ so that the Raman coherence is given by,

$$\tilde{\rho}_{ba} = \frac{(\boldsymbol{\mu_{eb}} \cdot \boldsymbol{\mu_{ae}})}{6\pi^2 c^3 \epsilon_0 \hbar} \int_0^{\infty} d\nu_k \, \nu_k^3 \, e^{i\nu_k (t'-t'')} \int_0^t dt' \, e^{-i\omega_{eb} t'} C_e(t') \int_0^t dt'' \, e^{+i\omega_{ea} t''} C_e^*(t'') \tag{A.29}$$

There is some ambiguity at this point in applying the Wigner-Weisskopf approximation, since the integral over ν_k clearly diverges. It is not clear at what frequency the integral over ν_k should be evaluated. Since we already chose before to evaluate the integral at the atomic transition frequency, we proceed by making the substitution $\nu_k = z - \bar{\omega}$ and we will pick $\bar{\omega}$ later on as some "average" of the atomic transition frequencies. With this transformation,

$$\tilde{\rho}_{ba} = \frac{(\boldsymbol{\mu_{eb}} \cdot \boldsymbol{\mu_{ae}})}{6\pi^2 c^3 \epsilon_0 \hbar} \int_{\bar{\omega}}^{\infty} dz \, (z-\bar{\omega})^3 \, e^{i(z-\bar{\omega})(t'-t'')} \int_0^t dt' \, e^{-i\omega_{eb} t'} C_e(t') \int_0^t dt'' \, e^{+i\omega_{ea} t''} C_e^*(t'') \tag{A.30}$$

We can now use the Wigner-Weisskopf approximation on the integral over z to obtain,

$$\int_{\bar{\omega}}^{\infty} dz \, (z-\bar{\omega})^3 \, e^{i(z-\bar{\omega})(t'-t'')} \approx 2\pi \, \bar{\omega}^3 \delta(t'-t'') \tag{A.31}$$

which gives,

$$\begin{aligned} \tilde{\rho}_{ba} &= \frac{(\boldsymbol{\mu_{eb}} \cdot \boldsymbol{\mu_{ae}}) \, \bar{\omega}^3}{3\pi c^3 \epsilon_0 \hbar} \int_0^t dt' \int_0^t dt'' \, \delta(t'-t'') e^{-i\omega_{eb} t'} C_e(t') \, e^{+i\omega_{ea} t''} C_e^*(t'') \\ &= \frac{(\boldsymbol{\mu_{eb}} \cdot \boldsymbol{\mu_{ae}}) \, \bar{\omega}^3}{3\pi c^3 \epsilon_0 \hbar} \int_0^t dt' e^{+i(\omega_{ea} - \omega_{eb}) t'} \rho_{ee}(t') \end{aligned} \tag{A.32}$$

Substituting the last line of the above equation back into Eq. (A.24),

$$\rho_{ba} = \frac{(\boldsymbol{\mu_{eb}} \cdot \boldsymbol{\mu_{ae}}) \, \bar{\omega}^3}{3\pi c^3 \epsilon_0 \hbar} \int_0^t dt' e^{+i\omega_c (t'-t)} \rho_{ee}(t') \tag{A.33}$$

We can take the time derivative of the last equation, and obtain,

$$\boxed{\dot{\rho}_{ba} = \frac{(\boldsymbol{\mu_{eb}} \cdot \boldsymbol{\mu_{ae}}) \, \bar{\omega}^3}{3\pi c^3 \epsilon_0 \hbar} \rho_{ee}(t) = -\Gamma_{sgc} \rho_{ee}(t)} \tag{A.34}$$

At this point, we can finally put in the selection rules, and also choose the frequency $\bar{\omega} = \sqrt{\omega_{eb} \, \omega_{ea}}$ which is the geometric mean of the transition frequencies. We can also include another level (denoted by e') which is coupled to the states a, b in the same manner,

and the above derivation can be repeated. The selection rules are given as in Section 3.2 to be

$$\mu_{eb} = \wp\epsilon_+ \qquad \mu_{ea} = -\wp\epsilon_+ \tag{A.35}$$

$$\mu_{e'b} = \wp\epsilon_- \qquad \mu_{e'a} = \wp\epsilon_- \tag{A.36}$$

where we have made the correspondence

$$|e\rangle \rightarrow |t-\rangle \qquad |e'\rangle \rightarrow |t+\rangle \tag{A.37}$$

$$|a\rangle \rightarrow |x-\rangle \qquad |b\rangle \rightarrow |x+\rangle \tag{A.38}$$

The decay rates are evaluated to be,

$$\Gamma_{ea} = \frac{\omega_{ea}^3 |\wp|^2}{3\pi\epsilon_0\hbar c^3} \qquad \Gamma_{eb} = \frac{\omega_{eb}^3 |\wp|^2}{3\pi\epsilon_0\hbar c^3} \tag{A.39}$$

which gives for the SGC rate

$$\Gamma_{sgc}|_e = -\frac{(\omega_{eb}\,\omega_{ea})^{3/2}(-|\wp|^2)}{3\pi\epsilon_0\hbar c^3} = \sqrt{\Gamma_{eb}\Gamma_{ea}} \tag{A.40}$$

Similarly the other contribution to the SGC gives,

$$\Gamma_{sgc}|_{e'} = -\frac{(\omega_{e'b}\,\omega_{e'a})^{3/2}(+|\wp|^2)}{3\pi\epsilon_0\hbar c^3} = -\sqrt{\Gamma_{e'b}\Gamma_{e'a}} \tag{A.41}$$

If we assume that $\Gamma_{eb} \approx \Gamma_{ea} = \Gamma_e$, and similarly that $\Gamma_{e'b} \approx \Gamma_{e'a} = \Gamma_{e'} \approx \Gamma_e$we get,

$$\boxed{\dot{\rho}_{x+,x-}|_{sgc} = \Gamma_t(\rho_{t+,t+} - \rho_{t-,t-})} \tag{A.42}$$

This completes the derivation of the spontaneously generated coherence term in the master equations.

APPENDIX B

Finite Pulse Effects on the Quantum Interferogram

In Section 6.2, experimental results were presented for the quantum interferogram created when the pump and control photons combine in a stimulated Raman process (SRP) to create the spin coherence ($\rho_{x+,x-}$). We will now derive Eq. (6.7) which gives the coherent contribution to the DT signal taking into account the finite pulsewidth and the inhomogeneous broadening in the trion transition. We start with the second order Raman coherence created by the SRP involving pump and control photons,

$$\rho_{x+,x-}(t) = \frac{N_0}{(2\hbar)^2}\int_{-\infty}^{t} dt_1 \int_{-\infty}^{t_1} dt_2\,(-i\wp E^*_{y+}(t_1))e^{-i(\omega_c - i\gamma_s)(t-t_1)}(i\wp E_{p+}(t_2))e^{-i(\omega_g - i\gamma_t)(t_1-t_2)} \tag{B.1}$$

and substitute Eq. (5.5) to obtain,

$$\rho_{x+,x-}(t) = \frac{N_0\wp^2}{(2\hbar)^2}\int_{-\infty}^{t} dt_1 \int_{-\infty}^{t_1} dt_2\,\mathcal{E}^*(t_1-\tau_y)\mathcal{E}(t_2-\tau_p)e^{i\Omega(t_1-\tau_y)}e^{-i\Omega(t_2-\tau_p)}\times \\ e^{-i(\omega_c - i\gamma_s)(t-t_1)}e^{-i(\omega_g - i\gamma_t)(t_1-t_2)} \tag{B.2}$$

We shall drop factors pertaining to the strength of the Raman coherence such as $\frac{N_0\wp^2}{(2\hbar)^2}$, and concentrate purely on the time dependence. Let us also define,

$$\xi_t = \omega_g - i\gamma_t \tag{B.3}$$

$$\xi_c = \omega_c - i\gamma_s \tag{B.4}$$

Then, we need to consider the integral,

$$\rho_{x+,x-} = e^{-i\Omega(\tau_y-\tau_p)}\int_{-\infty}^{t} dt_1\,\mathcal{E}^*(t_1-\tau_y)e^{-i\xi_c(t-t_1)}\int_{-\infty}^{t_1} dt_2\mathcal{E}(t_2-\tau_p)e^{-i(\Omega-\xi_t)(t_2-t_1)} \tag{B.5}$$

Consider the second integral, with the substitution $t' = t_1 - t_2$,

$$I_2 = -\int_{\infty}^{0} dt'\mathcal{E}(t_1-\tau_p-t')e^{i(\Omega-\xi_t)t'} \tag{B.6}$$

Introduce the inverse Fourier transform as ,

$$\mathcal{E}(t') = \int_{-\infty}^{\infty} \frac{d\omega}{2\pi} \mathcal{E}(\omega) e^{-i\omega t'} \tag{B.7}$$

and we get,

$$\begin{aligned} I_2 &= \int_0^{\infty} dt' \int_{-\infty}^{\infty} \frac{d\omega}{2\pi} \mathcal{E}(\omega) e^{-i\omega(t_1-\tau_p-t')} e^{i(\Omega-\xi_t)t'} \\ &= \int_{-\infty}^{\infty} \frac{d\omega}{2\pi} \mathcal{E}(\omega) \int_0^{\infty} dt'\, e^{-i\omega(t_1-\tau_p)} e^{i(\omega+\Omega-\xi_t)t'} \\ &= i \int_{-\infty}^{\infty} \frac{d\omega}{2\pi} \frac{\mathcal{E}(\omega) e^{-i\omega(t_1-\tau_p)}}{\omega+\Omega-\xi_t} \end{aligned} \tag{B.8}$$

When we substitute this back into Eq. (B.5), we get,

$$\begin{aligned} \rho_{x+,x-} &= ie^{-i\Omega(\tau_y-\tau_p)} \int_{-\infty}^{t} dt_1\, \mathcal{E}^*(t_1-\tau_y) e^{-i\xi_c(t-t_1)} \int_{-\infty}^{\infty} \frac{d\omega}{2\pi} \frac{\mathcal{E}(\omega) e^{-i\omega(t_1-\tau_p)}}{\omega+\Omega-\xi_t} \\ &= ie^{-i\Omega(\tau_y-\tau_p)} \int_{-\infty}^{\infty} \frac{d\omega}{2\pi} \frac{\mathcal{E}(\omega)}{\omega+\Omega-\xi_t} \int_{-\infty}^{t} dt_1 \mathcal{E}^*(t_1-\tau_y) e^{-i\xi_c(t-t_1)} e^{-i\omega(t_1-\tau_p)} \\ &= ie^{-i\Omega(\tau_y-\tau_p)} \int_{-\infty}^{\infty} \frac{d\omega}{2\pi} \frac{\mathcal{E}(\omega) e^{-i\omega(\tau_y-\tau_p)}}{\omega+\Omega-\xi_t} \int_{-\infty}^{\infty} \frac{d\omega'}{2\pi} \frac{\mathcal{E}^*(\omega') e^{i(\omega'-\omega)(t-\tau_y)}}{i(\omega'-\omega+\xi_c)} \end{aligned} \tag{B.9}$$

where to obtain the third line, we introduced the inverse Fourier transform again and substituted $t'' = t_1 - \tau_y$ to do the integration over t_1. Note that we have made no approximations regarding the pulseshapes to this point. Consider the second integral over ω', and make the substitution $x = \omega' - \omega$,

$$I_3 = \int_{-\infty}^{\infty} \frac{dx}{2\pi} \frac{\mathcal{E}^*(x+\omega) e^{ix(t-\tau_y)}}{x+\xi_c} \tag{B.10}$$

Let us now make the assumption that the Fourier transform $\mathcal{E}(\omega)$ is analytic in the complex plane, *i.e.* there are no singularities. The assumption is satisfied for Gaussian pulseshapes, but not for hyperbolic secant or one-sided exponential functions. We shall show at the very end that even this assumption may be relaxed for times much larger than the pulsewidth, but the Gaussian pulse assumption will allow us to solve for the DT signal now. Extend the integral into the complex plane, and evaluate over the contour shown in Figure B.1. The contour integral is broken into two parts, and we will now show that the integral over the

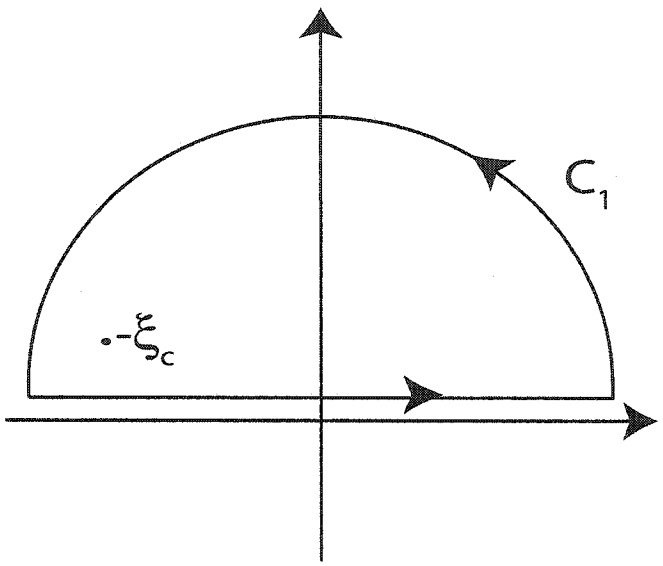

Figure B.1: Contour used for evaluating the integral I_3.

part C_1 vanishes,

$$\begin{aligned}\oint_{C_1} \frac{dz}{2\pi} \frac{\mathcal{E}^*(z+\omega)e^{iz(t-\tau_y)}}{z+\xi_c} &= \lim_{R\to\infty} \int_0^\pi d\theta \frac{\mathcal{E}^*(Re^{i\theta}+\omega)e^{i(R\cos\theta+iR\sin\theta)(t-\tau_y)}}{Re^{i\theta}+\xi_c} \\ &\leq \lim_{R\to\infty} \int_0^\pi d\theta \left|\frac{\mathcal{E}^*(Re^{i\theta}+\omega)e^{i(R\cos\theta+iR\sin\theta)(t-\tau_y)}}{Re^{i\theta}+\xi_c}\right| \\ &\leq \lim_{R\to\infty} \int_0^\pi d\theta \frac{\left|\mathcal{E}^*(R\cos\theta+iR\sin\theta+\omega)e^{-R\sin\theta(t-\tau_y)}\right|}{\left|Re^{i\theta}\right|-\left|\xi_c\right|} \\ &\to 0 \end{aligned} \tag{B.11}$$

because $\sin\theta \geq 0$ for $0 \leq \theta \leq \pi$. Further, because we assumed that there are no singularities other than at $z = -\xi_c$, we get from the Residue theorem,

$$I_3 = \frac{1}{2\pi}(2\pi i)\mathcal{E}^*(\omega-\xi_c)e^{-i\xi_c(t-\tau_y)} \tag{B.12}$$

and the analytic continuation of the Fourier transform into the complex plane is defined by,

$$\mathcal{E}(z) = \int_{-\infty}^{\infty} \mathcal{E}(t)e^{izt}\,dt \qquad\qquad \mathcal{E}^*(z) = \int_{-\infty}^{\infty} \mathcal{E}^*(t)e^{-izt}\,dt \tag{B.13}$$

where it should be noted that,

$$(\mathcal{E}(z^*))^* = \mathcal{E}^*(z) \neq (\mathcal{E}(z))^*$$

We will now use the property that the pulse width $s \ll \gamma_s^{-1}$, since

$$\mathcal{E}^*(\omega - \omega_c + i\gamma_s) = \int_{-\infty}^{\infty} dt\, \mathcal{E}^*(t) e^{-i(\omega-\omega_c+i\gamma_s)t} \approx \int_{-\infty}^{\infty} dt\, \mathcal{E}^*(t) e^{-i(\omega-\omega_c)t}$$

where the final step follows because $e^{\gamma_s t}$ does not vary over the pulse width, and hence

$$\mathcal{E}^*(\omega - \omega_c + i\gamma_s) \approx \mathcal{E}^*(\omega - \omega_c) \tag{B.14}$$

Finally, by substituting Eq. (B.12) into Eq. (B.9) and using Eq. (B.14) we get for the Raman coherence,

$$\begin{aligned}\rho_{x+,x-} &= ie^{-i\Omega(\tau_y-\tau_p)} e^{-i\xi_c(t-\tau_y)} \int_{-\infty}^{\infty} \frac{d\omega}{2\pi} \frac{\mathcal{E}(\omega)\mathcal{E}^*(\omega-\omega_c)e^{-i\omega(\tau_y-\tau_p)}}{\omega + \Omega - \xi_t} \\ &= ie^{-i\Omega(\tau_y-\tau_p)} e^{-i\xi_c(t-\tau_y)} \int_{-\infty}^{\infty} \frac{dz}{2\pi} \frac{\mathcal{E}(z)\mathcal{E}^*(z-\omega_c)e^{-iz(\tau_y-\tau_p)}}{z - (\xi_t - \Omega)}\end{aligned} \tag{B.15}$$

Once again, we can perform the contour integral, this time over the lower half plane, since the pole is at $z = \xi_t - \Omega = (\omega_g - \Omega) - i\gamma_t$. Similarly the integral over the semi-circle in the lower half-plane will vanish, and we get,

$$\rho_{x+,x-} = e^{-i(\omega_c - i\gamma_s)(t-\tau_y)} e^{-i(\omega_g - i\gamma_t)(\tau_y-\tau_p)} \mathcal{E}(\omega_g - \Omega - i\gamma_t)\mathcal{E}^*(\omega_g - \Omega - \omega_c - i\gamma_t) \tag{B.16}$$

Again, since the pulsewidth $s \ll \gamma_t^{-1}$, we have,

$$\rho_{x+,x-} = e^{-i\omega_c(t-\tau_y)} e^{-\gamma_s(t-\tau_y)} e^{-i\omega_g(\tau_y-\tau_p)} e^{-\gamma_t(\tau_y-\tau_p)} \mathcal{E}^*(\omega_g - \Omega - \omega_c)\mathcal{E}(\omega_g - \Omega) \tag{B.17}$$

Note in the above equation that the first photon is at frequency detuning $\Delta = \omega_g - \Omega$, and the second photon is at the detuning $\Delta - \omega_c$ satisfying the two-photon resonance condition. Since the Zeeman splitting $\omega_c \ll \omega_g, \Omega$ we can write,

$$\rho_{x+,x-} = e^{-i\omega_c(t-\tau_y)} e^{-\gamma_s(t-\tau_y)} e^{-i\omega_g(\tau_y-\tau_p)} e^{-\gamma_t(\tau_y-\tau_p)} \left|\mathcal{E}(\omega_g - \Omega)\right|^2 \tag{B.18}$$

Substituting the above into Eq. (5.2), we obtain the Raman contribution to the third order dipole coherence (Eq. (5.7)) assuming that the probe pulse is a δ-function,

$$\rho^R_{t-,x-} = \frac{-iN_0\wp^3}{(2\hbar)^3} e^{-i\omega_g(t-\tau_x)} e^{-\gamma_t(t-\tau_x)} e^{-i\omega_c(\tau_x-\tau_y)} e^{-\gamma_s(\tau_x-\tau_y)} e^{-i\omega_g(\tau_y-\tau_p)} e^{-\gamma_t(\tau_y-\tau_p)} \left|\mathcal{E}(\omega_g - \Omega)\right|^2 \tag{B.19}$$

from which the nonlinear polarization is given by

$$\begin{aligned}\tilde{\mathbf{P}}^R = \epsilon_- \frac{-iN_0\wp^4}{(2\hbar)^3} \left|\mathcal{E}(\omega_g - \Omega)\right|^2 e^{-i\omega_g(t-\tau_x)} e^{-\gamma_t(t-\tau_x)} e^{-i\omega_c(\tau_x-\tau_y)} e^{-\gamma_s(\tau_x-\tau_y)} \times \\ e^{-i\omega_g(\tau_y-\tau_p)} e^{-\gamma_t(\tau_y-\tau_p)}\end{aligned} \tag{B.20}$$

and we now have to integrate over the inhomogeneous Gaussian distribution in the trion transition frequencies,

$$W(\omega_g) = \frac{1}{\sqrt{\pi\delta_g^2}} \exp\left(-\frac{(\omega_g - \omega_g^0)^2}{\eta_g^2}\right) \tag{B.21}$$

The assumption of δ-function probe pulse can easily be relaxed to accommodate finite pulsewidths again. However, the only condition that the probe pulse needs to satisfy (as we will show at the end of the section) is that $(\tau_x - \tau_y) \gg s$, where s is the pulsewidth in the time. On that time scale, we may as well treat the probe as a δ-function. The only integral to be evaluated is,

$$I_4 = \int_{-\infty}^{\infty} d\omega_g \, e^{-\frac{(\omega_g - \omega_g^0)^2}{\eta_g^2}} e^{-i\omega_g(t-\tau_x+\tau_y-\tau_p)} \left|\mathcal{E}(\omega_g - \Omega)\right|^2$$

and when we substitute a Gaussian pulse shape (Eq. (6.6)) for the electric field

$$\Longrightarrow I_4 = \int_{-\infty}^{\infty} d\omega_g e^{-\frac{(\omega_g - \omega_g^0)^2}{\eta_g^2}} e^{-i\omega_g(t-\tau_x+\tau_y-\tau_p)} e^{-\frac{(\omega_g-\Omega)^2}{2\sigma^2}} \tag{B.22}$$

The integral gives,

$$I_4 = e^{-i\omega_g^0(t-\tau_x+\tau_y-\tau_p)} e^{-\frac{\Delta_0^2}{2\sigma^2}} e^{\frac{\beta^2}{4\alpha}} \tag{B.23}$$

where

$$\alpha = \frac{1}{2\sigma^2} + \frac{1}{\eta_g^2} \tag{B.24}$$

$$\beta = \frac{\Delta_0}{2\sigma^2} - i(t - \tau_x + \tau_y - \tau_p) \tag{B.25}$$

and $\Delta_0 = \omega_g^0 - \Omega$ is the detuning from the center frequency of the inhomogeneously broadened transition, that we will take to be zero. We can then solve for the DT signal by using Eq. (4.38),

$$\begin{aligned} DT &\propto \Re\{e^{-i\omega_c(\tau_x-\tau_y)} e^{-\gamma_s(\tau_x-\tau_y)} e^{-i\omega_g^0(\tau_y-\tau_p)} e^{-\gamma_t(\tau_y-\tau_p)} e^{-\frac{(\tau_y-\tau_p)^2}{4\alpha}}\} \\ &= e^{-\gamma_s(\tau_x-\tau_y)} e^{-\gamma_t(\tau_y-\tau_p)} e^{-\frac{(\tau_y-\tau_p)^2}{4\alpha}} \cos(\omega_g^0(\tau_y - \tau_p) + \omega_c(\tau_x - \tau_y)) \end{aligned} \tag{B.26}$$

as shown in Eq. (6.7).

Addendum: Non-Analytic Pulseshapes

We now demonstrate that the assumption of analytical pulse shape is not strictly necessary. Consider once again the integral,

$$\begin{aligned} I_3 &= \oint_C \frac{dz}{2\pi} \frac{\mathcal{E}^*(z+\omega)e^{iz(t-\tau_y)}}{z+\xi_c} \\ &= \oint_C \frac{dz}{2\pi} \frac{\mathcal{E}^*(z)e^{izt}e^{-i\omega t}}{z-\omega+\xi_c} \end{aligned} \tag{B.27}$$

with the substitutions $z \rightarrow z+\omega$ and $t \rightarrow t-\tau_y$. The worst possibility is a pulse with infinitely many singularities. For example, the hyperbolic secant pulse, $\mathcal{E}(\omega) = \mathrm{sech}(\omega/\sigma) = \frac{2}{e^{\omega/\sigma}+e^{-\omega/\sigma}}$ has infinitely many singularities (simple poles) along the imaginary axis, $z_n = (2n+1)i\pi\sigma/2$. In general, the distance of the singularities from the origin will be proportional to $\sigma \propto 1/s$ where s is the pulsewidth in time. We now evaluate the contribution to the contour integral from the residue at the singularity $z_0 = i\pi\sigma/2$,

$$2\pi i \lim_{z\rightarrow z_0}(z-z_0)\frac{2}{ie^{(z-z_0)/\sigma}-ie^{-(z-z_0)/\sigma}}\frac{1}{z-\omega+\xi_c}e^{izt}e^{-i\omega t} = \frac{2\pi\sigma e^{-(\pi/2)\sigma t}e^{-i\omega t}}{(\omega_c-\omega)+i(\pi/2)\sigma-i\gamma_s} \tag{B.28}$$

which is obtained by expanding the exponentials in powers of $(z-z_0)/\sigma$. Unfortunately, the denominator is exactly cancelled by the contribution to the residue from the singularity at z_0 in the limit $\gamma_s \ll \sigma$, else we could have neglected this residue in comparison to the term already calculated in Eq. (B.12). However, in the same limit, we see that for $t \gg s \propto (1/\sigma)$, the above residue becomes negligible. Residues at the other poles $z_n = (2n+1)z_0$ will die out even faster, and hence can also be neglected. Therefore, as stated earlier, the integral becomes exact for $(t-\tau_y) \gg s$.

BIBLIOGRAPHY

BIBLIOGRAPHY

[1] A. Einstein, B. Podolsky, N. Rosen, "Can Quantum-Mechanical Description of Physical Reality Be Considered Complete?", *Phys. Rev.* **47**, 777 (1935).

[2] F. Bloch, "Nuclear Induction", *Phys. Rev.* **70**, 460 (1946).

[3] N. Bloembergen, R. Purcell, R. Pound, "Relaxation Effects in Nuclear Magnetic Resonance Absorption", *Phys. Rev.* **73**, 679 (1948).

[4] E. L. Hahn, "Spin Echoes", *Phys. Rev.* **80**, 580 (1950).

[5] R. J. Elliott, "Theory of the effect of spin-orbit coupling on magnetic resonance in some semiconductors", *Phys. Rev.* **96**, 266 (1954).

[6] G. Dresselhaus, "Spin-Orbit Coupling Effects in Zinc Blende Structures", *Phys. Rev.* **100**, 580 (1955).

[7] D. Pines, C. P. Slichter, "Relaxation times in Magnetic Resonance", *Phys. Rev.* **100**, 1014 (1955).

[8] J. M. Luttinger, "Quantum Theory of Cyclotron Resonance in Semiconductors : General Theory", *Phys. Rev.* **102**, 1030 (1956).

[9] R. P. Feynman, F. L. Vernon, R. W. Helwarth, "Geometrical representation of the Schrodinger equation for solving maser problems", *Journal of Applied Physics* **28**, 49 (1957).

[10] P. W. Anderson, "Absence of diffusion in certain random lattices", *Phys. Rev.* **109**, 1492 (1958).

[11] J. P. Gordon, K. G. Bowers, "Microwave Spin Echoes From Donor Electrons in Silicon", *Phys. Rev. Lett.* **1**, 368 (1958).

[12] M. A. Lampert, "Mobile and Immobile effective-mass complexes in nonmetallic solids", *Phys. Rev. Lett.* **1**, 450 (1958).

[13] G. Feher, E. A. Gere, "Electron Spin Resonance Experiments in Silicon. II Electron Spin Relaxation Effects", *Phys. Rev.* **114**, 1245 (1959).

[14] J. C. Hensel, G. Feher, "Cyclotron resonance experiments in Uniaxially stressed Silicon : Valence Band parameters and Deformation potentials", *Phys. Rev.* **129**, 1041 (1963).

[15] R. S. Knox, *Theory of Excitons*, Solid State Phys., Suppl. 5, Academic Press Inc., New York (1963).

[16] L. J. Sham, T. M. Rice, "Many-Particle Derivation of the Effective-Mass Equation for the Wannier Exciton", *Phys. Rev.* **144**, 708 (1966).

[17] F. H. Pollak, M. Cardona, "Piezo-Electroreflectance in Ge, GaAs and Si", *Phys. Rev.* **172**, 816 (1968).

[18] M. I. D'Yakonov, V. I. Perel, "Spin orientation of electrons associated with the interband absorption of light in semiconductors", *Sov. Phys. JETP* **33**, 1053 (1971).

[19] M. I. D'Yakonov, V. I. Perel, "Spin relaxation of conduction electrons in noncentrosymmetric semiconductors", *Sov. Phys. Solid State* **13**, 3023 (1971).

[20] R. Fontana, R. P. Srivastava, "Holes in Spectral Lines", *Phys. Rev. A* **7**, 1866 (1973).

[21] I. M. Beterov, V. P. Chebotaev, "Three-Level Gas Systems and Their Interactions with Radiation", *Prog. Quant. Electron.* **3**, 1 (1974).

[22] G. L. Bir, G. E. Pikus, *Symmetry and strain-induced effects in semiconductors*, John Wiley and Sons, Inc., New York (1974).

[23] P. Hu, S. Geschwind, T. M. Jedju, "Spin-Flip Raman Echo in n-Type CdS", *Phys. Rev. Lett.* **37**, 1357 (1974).

[24] G. L. Bir, A. G. Aronov, G. E. Pikus, "Spin relaxation of electrons due to scattering by holes", *Sov. Phys. JETP* **42**, 705 (1975).

[25] J. N. Chazalviel, "Spin relaxation of conduction electrons in n-type indium arsenide at low temperature", *Phys. Rev. B* **11**, 1555 (1975).

[26] D. Grischkowsky, M. M. T. Loy, P. F. Liao, "Adiabatic following model for two-photon transitions: Nonlinear mixing and pulse propagation", *Phys. Rev. A* **12**, 2514 (1975).

[27] R. M. Whitley, C. R. Stroud, Jr., "Double Optical Resonance", *Phys. Rev. A* **14**, 1498 (1976).

[28] G. Fishman, G. Lampel, "Spin relaxation of photoelectrons in p-type gallium arsenide", *Phys. Rev. B* **16**, 820 (1977).

[29] T. Kawabata, K. Muro, S. Narita, "Observation of Cyclotron-resonance absorptions due to excitonic ion and excitonic molecule ion in silicon", *Solid State Communications* **23**, 267 (1977).

[30] M. M. Salour, C. Cohen-Tannoudji, "Observation of Ramsey's Interference Fringes in the Profile of Doppler-Free Two-Photon Resonances", *Phys. Rev. Lett.* **38**, 757 (1977).

[31] R. Teets, J. Eckstein, T. W. Hänsch, "Coherent Two-Photon Excitation by Multiple Light Pulses", *Phys. Rev. Lett.* **38**, 760 (1977).

[32] G. A. Thomas, T. M. Rice, "Trions, Molecules and Excitons above the Mott density in Ge", *Solid State Communications* **23**, 359 (1977).

[33] R. Dingle, H. L. Störmer, A. C. Gossard, W. Wiegmann, "Electron mobilities in modulation-doped semiconductor heterojunction superlattices", *Appl. Phys. Lett.* **33**, 665 (1978).

[34] W. Lange, J. Mlynek, "Quantum beats in transmission by time-resolved polarization spectroscopy", *Phys. Rev. Lett.* **40**, 1373 (1978).

[35] E. Abrahams, P. W. Anderson, D. C. Licciardello, T. V. Ramakrishnan, "Scaling theory of localization: Absence of quantum diffusion in two-dimensions", *Phys. Rev. Lett.* **42**, 673 (1979).

[36] T. Yajima, Y. Taira, "Spatial optical coupling of picosecond light pulses and transverse relaxation effect in resonant media", *J. Phys. Soc. Jpn.* **47**, 1620 (1979).

[37] T. Ando, A. B. Fowler, F. Stern, "Electronic properties of two-dimensional systems", *Rev. Mod. Phys.* **54**, 437 (1982).

[38] G. Bastard, E. E. Mendez, L. L. Chang, L. Esaki, "Exciton binding energy in quantum wells", *Phys. Rev. B* **26**, 1974 (1982).

[39] J. Hegarty, M. D. Sturge, C. Weisbuch, A. C. Gossard, W. Wiegmann, "Resonant Rayleigh Scattering from an Inhomogeneously Broadened Transition: A New Probe of the Homogeneous Linewidth", *Phys. Rev. Lett.* **49**, 930 (1982).

[40] E. I. Rashba, M. D. Sturge (eds.), *Excitons*, North Holland Publ., Amsterdam (1982).

[41] S. Stenholm, *Foundations of Laser Spectroscopy*, John Wiley & Sons, Inc., New York (1983).

[42] R. L. Greene, K. K. Bajaj, D. E. Phelps, "Energy levels of Wannier excitons in GaAs-$Ga_{1-x}Al_xAs$ quantum-well structures", *Phys. Rev. B* **29**, 1807 (1984).

[43] J. Hegarty, L. Goldner, M. D. Sturge, "Localized and delocalized two-dimensional excitons in GaAs-AlGaAs multiple-quantum-well structures", *Phys. Rev. B* **30**, 7346 (1984).

[44] Y. R. Shen, *The principles of nonlinear optics*, John Wiley and Sons, New York (1984).

[45] H. Barkhuijsen, R. D. Beer, W. M. M. J. Bovée, D. van Ormondt, "Retrieval of Frequencies, Amplitudes, Damping Factors, and Phases from Time-Domain Signals Using a Linear Least-Squares Procedure", *J. Magnetic Resonance* **61**, 465 (1985).

[46] D. A. Broido, L. J. Sham, "Effective masses of holes at GaAs-AlGaAs heterojunctions", *Phys. Rev. B* **31**, 888 (1985).

[47] R. P. Feynman, "Quantum Mechanical Computers", *Optics News* **11**, 11 (1985).

[48] P. A. Lee, T. V. Ramakrishnan, "Disordered electronic systems", *Rev. Mod. Phys.* **57**, 287 (1985).

[49] R. F. Loring, S. Mukamel, "Selectivity in coherent transient Raman measurements of vibrational dephasing in liquids", *J. Chem. Phys.* **83**, 2116 (1985).

[50] D. G. Steel, S. C. Rand, "Ultranarrow Nonlinear Optical Resonances in Solids", *Phys. Rev. Lett.* **55**, 2285 (1985).

[51] D. J. Tannor, S. A. Rice, "Control of selectivity of chemical reaction via control of wave packet evolution", *J. Chem. Phys.* **83**, 5013 (1985).

[52] A. M. Weiner, S. D. Silvestri, E. P. Ippen, "Three-pulse scattering for femtosecond dephasing studies: theory and experiment", *J. Opt. Soc. Am. B* **2**, 654 (1985).

[53] S.-R. E. Yang, D. A. Broido, L. J. Sham, "Holes at GaAs-$Al_xGa_{1-x}As$ heterojunctions in magnetic fields", *Phys. Rev. B* **32**, 6630 (1985).

[54] D. A. Broido, L. J. Sham, "Valence-band coupling and Fano-resonance effects on the excitonic spectrum in undoped quantum wells", *Phys. Rev. B* **34**, 3917 (1986).

[55] M. I. D'Yakonov, V. Y. Kachorovskiĭ, "Spin relaxation of two-dimensional electrons in noncentrosymmetric semiconductors", *Sov. Phys. Semicond* **20**, 110 (1986).

[56] O. A. Kocharovskaya, Y. I. Khanin, "Population trapping and coherent bleaching of a three-level medium by a periodic train of ultrashort pulses", *Sov. Phys. JETP* **63**, 945 (1986).

[57] M. Shapiro, P. Brumer, "Laser control of product quantum state populations in unimolecular reactions", *J. Chem. Phys.* **84**, 4103 (1986).

[58] B. Stébé, E. Feddi, G. Munschy, "Landau oscillations of excitonic trions", *J. of Phys. C : Solid State Phys.* **19**, 699 (1986).

[59] W. Wöger, H. King, R. J. Glauber, J. W. Haus, "Spontaneous generation of coherent optical beats", *Phys. Rev. A* **34**, 4859 (1986).

[60] F. Capasso, "Band-Gap Engineering: From Physics and Materials to New Semiconductor Devices", *Science* **235**, 172 (1987).

[61] U. Ekenberg, M. Altarelli, "Exciton binding energy in a quantum well with inclusion of valence-band coupling and nonparabolicity", *Phys. Rev. B* **35**, 7585 (1987).

[62] M. D. Levenson, S. S. Kano, *Introduction to Nonlinear Laser Spectroscopy*, Academic Press, Inc., San Diego (1987).

[63] F. W. Wise, M. J. Rosker, G. L. Millhauser, C. L. Tang, "Application of Linear Prediction Least-Squares Fitting to Time-Resolved Optical Spectroscopy", *J. Quant. Elect.* **23**, 1116 (1987).

[64] W. Ludwig, C. Falter, *Symmetries in Physics : Group theory applied to physical problems*, Springer-Verlag, Berlin Heidelberg (1988).

[65] J. A. Yeazell, C. R. Stroud, Jr., "Observation of Spatially Localized Atomic Electron Wave Packets", *Phys. Rev. Lett.* **60**, 1494 (1988).

[66] A. L. Efros, A. V. Rodina, "Confined excitons, trions and biexcitons in semiconductor microcrystals", *Solid State Communications* **72**, 645 (1989).

[67] S. E. Harris, "Lasers without Inversion: Interference of Lifetime-Broadened Resonances", *Phys. Rev. Lett.* **62**, 1033 (1989).

[68] G. Kurizki, M. Shapiro, P. Brumer, "Phase-coherent control of photocurrent directionality in semiconductors", *Phys. Rev. B* **39**, 3435 (1989).

[69] D. C. Reynolds, C. E. Leak, K. K. Bajaj, C. E. Stutz, R. L. Jones, K. R. Evans, P. W. Yu, W. M. Theis, "Determination of the binding energy of excitons to neutral donors located in the center or edge of the well or at the center of the barrier in $Al_xGa_{1-x}As/GaAs$ multiple-quantum-well structures", *Phys. Rev. B* **40**, 6210 (1989).

[70] M. O. Scully, S. Y. Zhu, A. Gavrielides, "Degenerate Quantum-Beat Laser: Lasing without Inversion and Inversion without Lasing", *Phys. Rev. Lett.* **62**, 2813 (1989).

[71] C. P. Slichter, *Principles of Magnetic Resonance*, Springer-Verlag, Berlin, 3rd edition (1989).

[72] B. Stébé, A. Ainane, "Ground state energy and optical absorption of excitonic trions in two dimensional semiconductors", *Superlatt. Microstruct.* **5**, 545 (1989).

[73] M. G. Bawendi, W. L. Wilson, L. Rotheberg, P. J. Carroll, T. M. Jedju, M. L. Steigerwald, L. E. Brus, "Electronic Structure and Photoexcited-Carrier Dynamics in Nanometer-Size CdSe Clusters", *Phys. Rev. Lett.* **65**, 1623 (1990).

[74] C. Chen, Y. Y. Yin, D. S. Elliott, "Product State control through Interfering Excitation Routes", *Phys. Rev. Lett.* **64**, 507 (1990).

[75] G. C. Cho, W. Kütt, H. Kurz, "Subpicosecond Time-Resolved Coherent-Phonon Oscillations in GaAs", *Phys. Rev. Lett.* **65**, 764 (1990).

[76] S. Datta, B. Das, "Electronic analog of the electro-optic modulator", *Appl. Phys. Lett.* **56**, 665 (1990).

[77] R. W. Martin, R. J. Nicholas, G. J. Rees, S. K. Haywood, N. J. Mason, P. J. W. Walker, "Two-dimensional spin confinement in strained-layer quantum wells", *Phys. Rev. B* **42**, 9237 (1990).

[78] N. F. Scherer, A. J. Ruggiero, M. Du, G. R. Fleming, "Time resolved dynamics of isolated molecular systems studied with phase-locked femtosecond pulse pairs", *J. Chem. Phys.* **93**, 856 (1990).

[79] H. W. van Kesteren, C. E. Cosman, W. A. J. A. van der Poel, C. T. Foxon, "Fine structure of excitons in type-II GaAs/AlAs quantum wells", *Phys. Rev. B* **41**, 5283 (1990).

[80] S. Bar-Ad, I. Bar-Joseph, "Absorption Quantum Beats of Magnetoexcitons in GaAs Heterostructures", *Phys. Rev. Lett.* **66**, 2491 (1991).

[81] T. Baumert, M. Grosser, R. Thalweiser, G. Gerber, "Femtosecond Time-Resolved Molecular Multiphoton Ionization: The Na_2 System", *Phys. Rev. Lett.* **67**, 3753 (1991).

[82] H. Benisty, C. M. Sotomayer-Torres, "Intrinsic mechanism for the poor luminescence properties of quantum-box systems", *Phys. Rev. B* **44**, 10495 (1991).

[83] K. J. Boller, A. Imamoğlu, S. E. Harris, "Observation of Electromagnetically Induced Transparency", *Phys. Rev. Lett.* **66**, 2593 (1991).

[84] J. E. Field, K. H. Hahn, S. E. Harris, "Observation of Electromagnetically Induced Transparency in Collisionally Broadened Laser Vapor", *Phys. Rev. Lett.* **67**, 3062 (1991).

[85] D. Gammon, B. V. Shanabrook, D. S. Katzer, "Excitons, phonons, and interfaces in GaAs/AlAs quantum-well structures", *Phys. Rev. Lett.* **67**, 1547 (1991).

[86] S. M. Park, S. P. Lu, R. J. Gordon, "Coherent laser control of the resonance-enhanced multiphoton ionization of HCl", *J. Chem. Phys.* **94**, 8522 (1991).

[87] N. F. Scherer, R. J. Carlson, A. Matro, M. Du, A. J. Ruggiero, V. Romero-Rochin, J. A. Cina, G. R. Fleming, S. A. Rice, "Fluorescence-detected wave packet interferometry: Time resolved molecular spectroscopy with sequences of femtosecond phase-locked pulses", *J. Chem. Phys.* **95**, 1487 (1991).

[88] C. W. Snyder, D. Barlett, B. G. Orr, P. K. Bhattacharya, J. Singh, "The molecular beam epitaxy growth of InGaAs on GaAs(100) studied by *in situ* scanning tunneling microscopy and reflection high-energy electron diffraction", *J. of Vac. Sci. and Tech. B* **9**, 2189 (1991).

[89] C. Weisbuch, B. Vinter, *Quantum Semiconductor Structures*, Academic Press Inc., New York (1991).

[90] C. H. Bennett, S. J. Wiesner, "Communication via one- and two-particle operators on Einstein-Podolsky-Rosen states", *Phys. Rev. Lett.* **69**, 2881 (1992).

[91] K. Brunner, U. Bockelmann, G. Abstreiter, M. Walther, G. Böhm, G. Tränkle, G. Weimann, "Photoluminescence from a single GaAs/AlGaAs quantum dot", *Phys. Rev. Lett.* **69**, 3216 (1992).

[92] D. Deutsch, R. Jozsa, "Rapid solution of problems by quantum computation", in *Proceedings of the Royal Society of London A*, pages 439–553 (1992).

[93] T. Inoshita, H. Sakaki, "Electron relaxation in a quantum dot: Significance of multiphonon processes", *Phys. Rev. B* **46**, 7260 (1992).

[94] J. Javanainen, "Effect of State Superpositions Created by Spontaneous Emission on Laser-Driven Transitions", *Europhys. Lett.* **17**, 407 (1992).

[95] M. A. Kastner, "The single-electron transistor", *Rev. Mod. Phys.* **64**, 849 (1992).

[96] S. Nomura, T. Kobayashi, "Exciton-LO-phonon couplings in spherical semiconductor microcrystallites", *Phys. Rev. B* **45**, 1305 (1992).

[97] S. Schmitt-Rink, D. Bennhardt, V. H. an P. Thomas, P. Haring, G. Maidorn, H. Bakker, K. Leo, D. S. Kim, J. Shah, K. Köhler, "Polarization dependence of heavy- and light-hole quantum beats", *Phys. Rev. B* **46**, 10460 (1992).

[98] Y. Y. Yin, C. Chen, D. S. Elliott, A. V. Smith, "Product State control through Interfering Excitation Routes", *Phys. Rev. Lett.* **69**, 2353 (1992).

[99] C. H. Bennett, G. Brassard, C. Crepeau, R. Jozsa, A. Peres, W. K. Wootters, "Teleporting an Unknown Quantum State via Dual Classical and Einstein-Podolsky-Rosen Channels", *Phys. Rev. Lett.* **70**, 1895 (1993).

[100] G. Goldoni, A. Fasolino, "Hole states in quantum wells in in-plane magnetic fields: Implications for resonant magnetotunellling spectroscopy", *Phys. Rev. B* **48**, 4948 (1993).

[101] H. Haug, S. W. Koch, *Quantum Theory of the Electronic and Optical Properties of Semiconductors*, World Scientific, Singapore (1993).

[102] G. C. Hegerfeldt, M. B. Plenio, "Coherence with incoherent light: A new type of quantum beats for a single atom", *Phys. Rev. A* **47**, 2186 (1993).

[103] M. Johnson, "Bipolar Spin Switch", *Science* **260**, 320 (1993).

[104] M. A. Kastner, "Artificial Atoms", *Physics Today* **46**, 24 (1993).

[105] K. Kheng, R. T. Cox, Y. M. d'Aubigné, F. Bassani, K. Saminadayar, S. Tatarenko, "Observation of negatively charged exciton X^- in Semiconductor quantum wells", *Phys. Rev. Lett.* **71**, 1752 (1993).

[106] C. B. Murray, D. J. Norris, M. G. Bawendi, "Synthesis and Characterization of Nearly Monodisperse CdE (E = S, Se, Te) Semiconductor Nanocrystallites", *J. Am. Chem. Soc.* **115**, 8706 (1993).

[107] M. Sargent III, M. O. Scully, W. E. Lamb, Jr., *Laser physics*, Perseus books, Reading, MA (1993).

[108] W. S. Warren, H. Rabitz, M. Dahleh, "Coherent Control of Quantum Dynamics: The Dream is Alive", *Science* **259**, 1581 (1993).

[109] J. J. Baumberg, D. D. Awschalom, N. Samarth, H. Luo, J. K. Furdyna, "Spin beats and Dynamical Magnetization in Quantum Structures", *Phys. Rev. Lett.* **72**, 717 (1994).

[110] E. Blackwood, M. J. Snelling, R. T. Harley, S. R. Andrews, C. T. B. Foxon, "Exchange interaction of excitons in GaAs heterostructures", *Phys. Rev. B* **50**, 14246 (1994).

[111] M. Brune, P. Nussenzveig, F. Schmidt-Kaler, F. Bernardot, A. Maali, J. M. Raimond, S. Haroche, "From Lamb shift to light shifts: vacuum and subphoton cavity fields measured by atomic phase sensitive detection", *Phys. Rev. Lett.* **72**, 3339 (1994).

[112] K. Brunner, G. Abstreiter, G. Böhm, G. Tränkle, G. Weimann, "Sharp-Line Photoluminescence and two-photon Absorption of Zero-Dimensional Biexcitons in a GaAs/AlGaAs Structure", *Phys. Rev. Lett.* **73**, 1138 (1994).

[113] K. Brunner, G. Abstreiter, G. Böhm, G. Tränkle, G. Weimann, "Sharp-line photoluminescence of excitons localized at GaAs/AlGaAs quantum well inhomogeneities", *Appl. Phys. Lett.* page 3320 (1994).

[114] M. Hayne, A. Usher, A. S. Plaut, K. Ploog, "Optically induced density depletion of the two-dimensional electron system in GaAs/$Al_xGa_{1-x}As$ heterojunctions", *Phys. Rev. B* **50**, 17208 (1994).

[115] H. F. Hess, E. Betzig, T. D. Harris, "Near-Field Spectroscopy of the Quantum Constituents of a Luminescent System", *Science* **264**, 1740 (1994).

[116] D. Leonard, S. Fafard, K. Pond, Y. H. Zhang, J. L. Merz, P. M. Petroff, "Structural and optical properties of self-assembled InGaAs quantum dots", *J. of Vac. Sci. and Tech. B* **12**, 2516 (1994).

[117] D. M. Mittleman, R. W. Schoenlein, J. J. Shiang, V. L. Colvin, A. P. Alivisatos, C. V. Shank, "Quantum size dependence of femtosecond electronic dephasing and vibrational dynamics in CdSe nanocrystals", *Phys. Rev. B* **49**, 14435 (1994).

[118] P. M. Petroff, S. P. DenBaars, "MBE and MOCVD Growht and Properties of Self-Assembling Quantum Dot Arrays in III-V Semiconductor Structures", *Superlatt. Microstruct.* **15**, 15 (1994).

[119] J. J. Sakurai, *Modern Quantum Mechanics*, Addison-Wesley Publishing Company, Inc., Reading, MA (1994).

[120] P. W. Shor, "Polynomial-Time Algorithms for Prime Factorization and Discrete Logarithms on a Quantum Computer", in 35^{th} *Annual Symposium on Foundations of Computer Science* (available online at arXiv e-print quant-ph/9508027), IEEE Computer Society Press (1994).

[121] A. Zrenner, L. V. Butov, M. Hagn, G. Abstreiter, G. Böhm, G. Weimann, "Quantum dots formed by interface fluctuations in AlAs/GaAs coupled quantum well structures", *Phys. Rev. Lett.* **72**, 3382 (1994).

[122] A. Barenco, D. Deutsch, A. Ekert, R. Jozsa, "Conditional Quantum Dynamics and Logic Gates", *Phys. Rev. Lett.* **74**, 4083 (1995).

[123] J. I. Cirac, P. Zoller, "Quantum Computations with Cold Trapped Ions", *Phys. Rev. Lett.* **74**, 4091 (1995).

[124] D. P. DiVincenzo, "Quantum computation", *Science* **270**, 255 (1995).

[125] D. P. DiVincenzo, "Two-bit Gates are Universal for Quantum Computation", *Phys. Rev. A* **50**, 1015 (1995).

[126] S. Fafard, R. Leon, D. Leonard, J. L. Merz, P. M. Petroff, "Phonons and radiative recombination in self-assembled quantum dots", *Phys. Rev. B* **52**, 5752 (1995).

[127] G. Finkelstein, H. Shtrikman, I. Bar-Joseph, "Optical Spectroscopy of a Two-Dimensional Electron Gas near the Metal-Insulator Transition", *Phys. Rev. Lett.* **74**, 976 (1995).

[128] D. Gammon, E. S. Snow, D. S. Katzer, "Excited State Spectroscopy of Excitons in Single Quantum Dots", *Appl. Phys. Lett.* **67**, 2391 (1995).

[129] G. A. Garrett, T. F. Albrecht, J. F. Whitaker, R. Merlin, "Coherent THz Phonons Driven by Light Pulses and the Sb Problem: What is the Mechanism?", *Phys. Rev. Lett.* **74**, 4273 (1995).

[130] A. P. Heberle, J. J. Baumberg, K. Köhler, "Ultrafast Coherent Control and Destruction of Excitons in Quantum Wells", *Phys. Rev. Lett.* **75**, 2598 (1995).

[131] A. V. Kuznetsov, C. J. Stanton, "Coherent phonon oscillations in GaAs", *Phys. Rev. B* **51**, 7555 (1995).

[132] R. Leon, P. M. Petroff, D. Leonard, S. Fafard, "Spatially Resolved Visible Luminescence of Self-Assembled Semiconductor Quantum Dots", *Science* **267**, 1966 (1995).

[133] L. Mandel, E. Wolf, *Optical coherence and quantum optics*, Cambridge University Press, Cambridge, UK (1995).

[134] C. Monroe, D. M. Meekhoff, B. E. King, W. M. Itano, D. J. Wineland, "Demonstration of a Fundamental Quantum Logic Gate", *Phys. Rev. Lett.* **75**, 4714 (1995).

[135] S. Mukamel, *Principles of nonlinear optical spectroscopy*, Oxford University Press, New York (1995).

[136] T. Östreich, K. Schönhammer, L. J. Sham, "Theory of spin beatings in Faraday rotation of semiconductors", *Phys. Rev. Lett.* **75**, 2554 (1995).

[137] T. Pellizzari, S. A. Gardiner, J. I. Cirac, P. Zoller, "Decoherence, Continuous observation, and Quantum Computing : A Cavity QED model", *Phys. Rev. Lett.* **75**, 3788 (1995).

[138] W. Sha, A. L. Smirl, W. F. Tseng, "Coherent Plasma Oscillations in Bulk Semiconductors", *Phys. Rev. Lett.* **74**, 4273 (1995).

[139] A. J. Shields, J. L. Osborne, M. Y. Simmons, M. Pepper, D. A. Ritchie, "Magneto-optical spectroscopy of positively charged excitons in GaAs quantum wells", *Phys. Rev. B* **51**, R5523 (1995).

[140] A. J. Shields, M. Pepper, M. Y. Simmons, D. A. Ritchie, "Spin-triplet negatively charged excitons in GaAs quantum wells", *Phys. Rev. B* **52**, 7841 (1995).

[141] T. Sleator, H. Weinfurter, "Realizable Universal Quantum Logic Gates", *Phys. Rev. Lett.* **74**, 4087 (1995).

[142] Q. A. Turchette, C. J. Hood, W. Lange, H. Mabuchi, H. J. Kimble, "Measurement of conditional phase shifts for quantum logic", *Phys. Rev. Lett.* **75**, 4710 (1995).

[143] F. R. Waugh, M. J. Berry, D. J. Mar, R. M. Westervelt, K. L. Campman, A. C. Gossard, "Single-Electron Charging in Double and Triple Quantum Dots with Tunable Coupling", *Phys. Rev. Lett.* **75**, 705 (1995).

[144] A. Wojs, "Negatively charged magnetoexcitons in quantum dots", *Phys. Rev. B* **51**, 10880 (1995).

[145] L. Zhu, V. Kleiman, X. Li, S. P. Lu, K. Trentelman, R. J. Gordon, "Coherent Laser Control of the Product Distribution Obtained in the Photoexcitation of HI", *Science* **270**, 77 (1995).

[146] A. P. Alivisatos, "Semiconductor Clusters, Nanocrystals, and Quantum Dots", *Science* **271**, 933 (1996).

[147] R. Atanasov, A. Hacheé, J. L. P. Hughes, H. M. van Driel, J. E. Sipe, "Coherent Control of Photocurrent generation in Bulk Semiconductors", *Phys. Rev. Lett.* **76**, 1703 (1996).

[148] D. Bimberg, N. N. Ledentsov, M. Grundmann, N. Kirstaeder, O. G. Schmidt, M. H. Mao, V. M. Ustinov, A. Y. Egorov, A. E. Zhukov, P. S. Kopev, Z. I. Alferov, S. S. Ruvimov, U. Gösele, J. Heydenreich, "InAs-GaAs Quantum Dots: From Growth to Lasers", *Phys. Stat. Sol. (b)* **194**, 159 (1996).

[149] S. A. Blanton, M. A. Hines, P. Guyot-Sionnest, "Photoluminescence wandering in single CdSe nanocrystals", *Appl. Phys. Lett.* **69**, 3905 (1996).

[150] T. Dekorsy, A. M. T. Kim, G. C. Cho, H. Kurz, A. V. Kuznetsov, A. Förster, "Subpicosecond coherent carrier-phonon dynamics in semiconductor heterostructures", *Phys. Rev. B* **53**, 1531 (1996).

[151] A. Ekert, R. Jozsa, "Quantum computation and Shor's factoring algorithm", *Rev. Mod. Phys.* **68**, 733 (1996).

[152] S. A. Empedocles, D. J. Norris, M. G. Bawendi, "Photoluminescence Spectroscopy of Single CdSe Nanocrystallite Quantum Dots", *Phys. Rev. Lett.* **77**, 3873 (1996).

[153] S. Fafard, K. Hinzer, S. Raymond, M. Dion, J. McCaffrey, Y. Feng, S. Charbonneau, "Red-Emitting Semiconductor Quantum Dot Lasers", *Science* **274**, 1350 (1996).

[154] G. Finkelstein, H. Shtrikman, I. Bar-Joseph, "Negatively and positively charged excitons in GaAs/$Al_xGa_{1-x}As$ quantum wells", *Phys. Rev. B* **53**, R1709 (1996).

[155] D. Gammon, E. S. Snow, B. V. Shanabrook, D. S. Katzer, D. Park, "Fine Structure Splitting in the Optical Spectra of Single GaAs Quantum Dots", *Phys. Rev. Lett.* **76**, 3005 (1996).

[156] D. Gammon, E. S. Snow, B. V. Shanabrook, D. S. Katzer, D. Park, "Homogeneous Linewidths in the Optical Spectrum of a Single Gallium Arsenide Quantum Dot", *Science* **273**, 87 (1996).

[157] M. Grundmann, N. N. Ledentsov, O. Stier, D. Bimberg, V. M. Ustinov, P. S. Kopev, Z. I. Alferov, "Excited states in self-organized InAs/GaAs quantum dots: Theory and experiment", *Appl. Phys. Lett.* **68**, 979 (1996).

[158] R. Hartmann, J. Kraus, G. Schaack, K. Panzlaff, "Spectroscopic investigations of photoinduced changes of the spatial distribution of charge carriers in modulation-doped quantum-well structures", *Phys. Rev. B* **53**, 13011 (1996).

[159] M. Hase, K. Mizoguchi, H. Harima, S. Nakashima, M. Tani, K. Sakai, M. Hangyo, "Optical control of coherent optical phonons in bismuth films", *Appl. Phys. Lett.* **69**, 2474 (1996).

[160] K. Kamath, P. Bhattacharya, T. Sosnowski, T. Norris, J. Phillips, "Room-temperature operation of $In_{0.4}Ga_{0.6}As$/GaAs self-organised quantum dot lasers", *Electronics Letters* **32**, 1374 (1996).

[161] S. V. Kravchenko, D. Simonian, M. P. Sarachik, W. Mason, J. Furneaux, "Electric field scaling at a B = 0 metal-insulator transition", *Phys. Rev. Lett.* **77**, 4938 (1996).

[162] N. N. Ledentsov, M. Grundmann, N. Kirstaeder, O. G. Schmidt, R. Heitz, J. Böhrer, D. Bimberg, V. M. Ustinov, V. A. Shchukin, A. Y. Egorov, A. E. Zhukov, S. Zaitsev, P. S. Kopev, Z. I. Alferov, S. S. Ruvimov, A. O. Kosogov, P. Werner, U. Gösele, J. Heydenreich, "Ordered Arrays of Quantum Dots: Formation, Electronic Spectra, Relaxation Phenomena, Lasing", *Solid-State Electronics* **40**, 785 (1996).

[163] P. Lelong, G. Bastard, "Binding energies of excitons and charged excitons in GaAs/Ga(In)As quantum dots", *Solid State Communications* **98**, 819 (1996).

[164] M. Nirmal, B. O. Dabbousi, M. G. Bawendi, J. J. Macklin, J. K. Trautman, T. D. Harris, L. E. Brus, "Fluorescence intermittency in single cadmium selenide nanocrystals", *Nature* **383**, 802 (1996).

[165] M. Notomi, T. Furuta, H. Kamada, J. Temmyo, T. Tamamura, "Microscopic excitation spectroscopy for zero-dimensional quantized states of individual $In_xGa_{1-x}As/Al_yGa_{1-y}As$ quantum dots", *Phys. Rev. B* **53**, 15743 (1996).

[166] R. Nötzel, "Self-organized growth of quantum-dot structures", *Semicond. Sci. Technol.* **11**, 1365 (1996).

[167] B. Ohnesorge, M. Albrecht, J. Oshinowo, A. Forchel, Y. Arakawa, "Rapid carrier relaxation in self-assembled $In_xGa_{1-x}As/GaAs$ quantum dots", *Phys. Rev. B* **54**, 11532 (1996).

[168] K. H. Schmidt, G. Medeiros-Ribeiro, M. Oestreich, P. M. Petroff, G. H. Döhler, "Carrier relaxation and electronic structure in InAs self-assembled quantum dots", *Phys. Rev. B* **54**, 11346 (1996).

[169] M. O. Scully, M. S. Zubairy, *Quantum Optics*, Cambridge University Press, Cambridge, UK (1996).

[170] J. Shah, *Ultrafast Spectroscopy of Semiconductors and Semiconductor Nanostructures*, Springer-Verlag, New York (1996).

[171] A. M. Steane, "Error Correcting Codes in Quantum Theory", *Phys. Rev. Lett.* **77**, 793 (1996).

[172] H. R. Xia, C. Y. Ye, S. Y. Zhu, "Experimental Observation of Spontaneous Emission Cancellation", *Phys. Rev. Lett.* **77**, 1032 (1996).

[173] S. Y. Zhu, M. O. Scully, "Spectral Line Elimination and Spontaneous Emission Cancellation via Quantum Interference", *Phys. Rev. Lett.* **76**, 388 (1996).

[174] U. Banin, C. J. Lee, A. A. Guzelian, C. J. Bardeen, A. P. Alivisatos, C. V. Shank, "Quantum Confinement and Ultrafast Dephasing Dynamics in InP Nanocrystals", *Phys. Rev. B* **55**, 7059 (1997).

[175] N. H. Bonadeo, G. Chen, D. G. Steel, D. Gammon, "Single Quantum dot nonlinear optical spectroscopy", *Phys. Status Solidi (a)* **221**, 5 (1997).

[176] D. Bouwmeester, J.-W. Pan, K. Mattle, M. Eibl, H. Weinfurter, A. Zeilinger, "Experimental quantum teleportation", *Nature* **390**, 575 (1997).

[177] J. R. Chapman, N. F. Johnson, V. N. Nicopoulos, "Stability of optically active charged excitons in quasi-two-dimensional systems", *Phys. Rev. B* **55**, 10221 (1997).

[178] J. I. Cirac, P. Zoller, H. J. Kimble, H. Mabuchi, "Quantum state transfer and entanglement distribution among distant states of a quantum network", *Phys. Rev. Lett.* **78**, 3221 (1997).

[179] S. A. Crooker, D. D. Awschalom, J. J. Baumberg, F. Flack, N. Samarth, "Optical spin resonance and transverse spin relaxation in magnetic semiconductor quantum wells", *Phys. Rev. B* **56**, 7574 (1997).

[180] S. A. Empedocles, M. G. Bawendi, "Quantum-Confined Stark Effect in Single CdSe Nanocrystallite Quantum Dots", *Science* **278**, 2114 (1997).

[181] D. Gammon, S. W. Brown, E. S. Snow, T. A. Kennedy, D. S. Katzer, D. Park, "Nuclear Spectroscopy in Single Quantum Dots: Nanoscopic Raman Scattering and Nuclear Magnetic Resonance", *Science* **277**, 85 (1997).

[182] N. H. Gershenfeld, I. L. Chuang, "Bulk Spin-Resonance Quantum Computation", *Science* **275**, 350 (1997).

[183] L. K. Grover, "Quantum Mechanics Helps in Searching for a Needle in a Haystack", *Phys. Rev. Lett.* **79**, 325 (1997).

[184] S. E. Harris, "Electromagnetically Induced Transparency", *Physics Today* **July**, 36 (1997).

[185] E. L. Ivchenko, "Fine structure of excitonic levels in semiconductor nanostructures", *Phys. Status Solidi (a)* **164**, 487 (1997).

[186] E. L. Ivchenko, G. E. Pikus, *Superlattices and Other Heterostructures : Symmetry and Optical Phenomena*, Springer Series in Solid-State Sciences, Springer-Verlag, Berlin Heidelberg, 2nd edition (1997).

[187] K. Kamath, N. Chervela, K. K. Linder, T. Sosnowski, H. T. Jiang, T. Norris, J. Singh, P. Bhattacharya, "Photoluminescence and time-resolved photoluminescence characteristics of $In_xGa_{1-x}As/GaAs$ self-organized single- and multiple-layer quantum dot laser structures", *Appl. Phys. Lett.* **71**, 927 (1997).

[188] K. Kamath, J. Phillips, H. Jiang, J. Singh, P. Bhattacharya, "Small-signal modulation and differential gain of single-mode self-organized $In_{0.4}Ga_{0.6}As/GaAs$ quantum dot lasers", *Appl. Phys. Lett.* **70**, 2952 (1997).

[189] J. M. Kikkawa, I. P. Smorchkova, N. Samarth, D. D. Awschalom, "Room-temperature Spin memory in two-dimensional electron gases", *Science* **277**, 1284 (1997).

[190] D. L. Klein, R. Roth, A. K. L. Lim, A. P. Alivisatos, P. L. McEuen, "A single-electron transistor made from a cadmium selenide nanocrystal", *Nature* **389**, 699 (1997).

[191] C. F. Klingshirn, *Semiconductor optics*, Springer-Verlag, Berlin Heidelberg (1997).

[192] X. Marie, P. LeJeune, T. Amand, M. Brousseau, J. Barrau, M. Paillard, R. Planel, "Coherent Control of the Optical Orientation of Excitons in Quantum Wells", *Phys. Rev. Lett.* **79**, 3222 (1997).

[193] R. Merlin, "Generating Coherent THz Phonons with Light Pulses", *Solid State Communications* **102**, 207 (1997).

[194] H. Petek, A. P. Heberle, W. Nessler, H. Nagano, S. Kubota, S. Matsunami, N. Moriya, S. Ogawa, "Optical Phase Control of Coherent Electron Dynamics in Metals", *Phys. Rev. Lett.* **79**, 4649 (1997).

[195] A. Schnirman, G. Schön, Z. Hermon, "Quantum Manipulations of Small Josephson Junctions", *Phys. Rev. Lett.* **79**, 2371 (1997).

[196] D. R. Seck, M. Potemski, P. Wyder, "High-field spin resonance of weakly bound electrons in GaAs", *Phys. Rev. B* **56**, 7422 (1997).

[197] M. Shapiro, P. Brumer, "Quantum control of chemical reactions", *J. Chem. Soc., Faraday Trans.* **93**, 1263 (1997).

[198] B. Stébé, G. Munschy, L. Stauffer, F. Dujardin, J. Murat, "Excitonic trion X^- in semiconductor quantum wells", *Phys. Rev. B* **56**, 12454 (1997).

[199] A. Thilagam, "Two-dimensional charged-exciton complexes", *Phys. Rev. B* **55**, 7804 (1997).

[200] W. S. Warren, "The Usefulness of NMR Quantum Computing", *Science* **277**, 1688 (1997).

[201] M. Bayer, T. Gutbrod, A. Forchel, V. D. Kulakovskii, A. Gorbunov, M. Michel, R. Steffen, K. H. Wang, "Exciton complexes in $In_xGa_{1-x}As$/GaAs quantum dots", *Phys. Rev. B* **58**, 4740 (1998).

[202] K. Bergmann, H. Theuer, B. W. Shore, "Coherent population transfer among quantum states of atoms and molecules", *Rev. Mod. Phys.* **70**, 1003 (1998).

[203] P. R. Berman, "Analysis of dynamical suppression of spontaneous emission", *Phys. Rev. A* **58**, 4886 (1998).

[204] N. H. Bonadeo, G. Chen, D. Gammon, D. S. Katzer, D. Park, D. G. Steel, "Nonlinear Nano-Optics: Probing One Exciton at a Time", *Phys. Rev. Lett.* **81**, 2759 (1998).

[205] N. H. Bonadeo, J. Erland, D. Gammon, D. Park, D. S. Katzer, D. G. Steel, "Coherent Optical Control of the Quantum State of a Single Quantum Dot", *Science* **282**, 1473 (1998).

[206] S. W. Brown, T. A. Kennedy, D. Gammon, "Optical NMR from single quantum dots", *Sol. State Nuc. Mag. Res.* **11**, 49 (1998).

[207] A. Chavez-Pirson, J. Temmyo, H. Kamada, H. Gotoh, H. Ando, "Near-field optical spectroscopy and imaging of single InGaAs/AlGaAs quantum dots", *Appl. Phys. Lett.* **72**, 3494 (1998).

[208] I. L. Chuang, N. Gershenfeld, M. Kubinec, "Experimental Implementation of Fast Quantum Searching", *Phys. Rev. Lett.* **80**, 3408 (1998).

[209] I. L. Chuang, L. M. K. Vandersypen, X. Zhou, D. W. Leung, S. Lloyd, "Experimental realization of a quantum algorithm", *Nature* **393**, 143 (1998).

[210] J. H. Davies, *The physics of low-dimensional semiconductors : an introduction*, Cambridge University Press., Cambridge, U.K.:New York (1998).

[211] E. Deckel, D. Gershoni, E. Ehrenfreund, D. Spektor, J. M. Garcia, P. M. Petroff, "Optical spectroscopy of a single self-assembled quantum dot", *Physica E* **2**, 694 (1998).

[212] J. L. Dunn, C. A. Bates, M. J. Pye, D. Boffety, A. M. Vasson, A. Vasson, J. Leymarie, "Binding energy of bound excitons D^0X in quantum wells", *Phys. Rev. B* **58**, 7970 (1998).

[213] G. Eytan, Y. Yayon, M. Rappaport, H. Shtrikman, I. Bar-Joseph, "Near-field Spectroscopy of a Gated Electron gas : A direct evidence for Electron Localization", *Phys. Rev. Lett.* **81**, 1666 (1998).

[214] X. Fan, T. Takagahara, J. E. Cunningham, H. Wang, "Pure dephasing induced by exciton-phonon interactions in narrow GaAs quantum wells", *Solid State Communications* **108**, 857 (1998).

[215] K. B. Ferrio, D. G. Steel, "Raman Quantum beats of Interacting excitons", *Phys. Rev. Lett.* **80**, 786 (1998).

[216] G. Finkelstein, V. Umansky, I. Bar-Joseph, V. Ciulin, S. Haacke, J. D. Ganiére, B. Deveaud, "Charged Exciton Dynamics in GaAs quantum wells", *Phys. Rev. B* **58**, 12637 (1998).

[217] A. Furusawa, J. L. Sørensen, S. L. Braunstein, C. A. Fuchs, H. J. Kimble, E. S. Polzik, "Unconditional Quantum Teleportation", *Science* **282**, 706 (1998).

[218] D. Goldhaber-Gordon, H. Shtrikman, D. Mahalu, D. Abusch-Magder, U. Meirav, M. A. Kastner, "Kondo effect in a single-electron transistor", *Nature* **391**, 156 (1998).

[219] T. Ishikawa, S. Kohomoto, K. Asakawa, "Site control of self-organized InAs dots on GaAs substrates by *in situ* electron-beam lithography and molecular-beam epitaxy", *Appl. Phys. Lett.* **73**, 1712 (1998).

[220] L. Jacak, P. Hawrylak, A. Wojs, *Quantum Dots*, Springer-Verlag, Berlin Heidelberg (1998).

[221] H. Kamada, H. Ando, J. Temmyo, T. Tamamura, "Excited-state optical transitions of excitons and biexcitons in a single $In_xGa_{1-x}As$ quantum disk", *Phys. Rev. B* **58**, 16243 (1998).

[222] B. E. Kane, "A silicon-based nuclear spin quantum computer", *Nature* **393**, 133 (1998).

[223] J. M. Kikkawa, D. D. Awschalom, "Resonant Spin Amplification in n-type GaAs", *Phys. Rev. Lett.* **80**, 4313 (1998).

[224] V. Klimov, D. W. McBranch, "Femtosecond $1P$-to$1S$ Electron Relaxation in Strongly Confined Semiconductor Nanocrystals", *Phys. Rev. Lett.* **80**, 4028 (1998).

[225] A. Kuther, M. Bayer, A. Forchel, A. Gorbunov, V. B. Timofeev, F. Schäffer, J. P. Reithmaier, "Zeeman splitting of exciton and biexcitons in single $In_{0.60}Ga_{0.40}As/GaAs$ self-assembled quantum dots", *Phys. Rev. B* **58**, R7508 (1998).

[226] L. Landin, M. S. Miller, M.-E. Pistol, C. E. Pryor, L. Samuelson, "Optical Studies of Individual InAs Quantum Dots in GaAs: Few-Particle Effects", *Science* **280**, 262 (1998).

[227] M. Linder, L. J. Sham, "Theory of the coherent spin dynamics in magnetic semiconductor quantum wells", *Physica E* **2**, 412 (1998).

[228] D. Loss, D. P. DiVencenzo, "Quantum computation with quantum dots", *Phys. Rev. A* **57**, 120 (1998).

[229] S. Menon, G. S. Agarwal, "Effects of spontaneously generated coherence on the pump-probe response of a Λ system", *Phys. Rev. A* **57**, 4014 (1998).

[230] D. Meshulach, Y. Silberberg, "Coherent quantum control of two-photon transitions by a femtosecond laser pulse", *Nature* **396**, 239 (1998).

[231] E. Paspalakis, P. L. Knight, "Phase Control of Spontaneous Emission", *Phys. Rev. Lett.* **81**, 293 (1998).

[232] G. A. Prinz, "Magnetoelectronics", *Science* **282**, 1660 (1998).

[233] T. S. Sosnowski, T. B. Norris, H. Jiang, J. Singh, K. Kamath, P. Bhattacharya, "Rapid carrier relaxation in $In_{0.4}Ga_{0.6}As/GaAs$ quantum dots characterized by differential transmission spectroscopy", *Appl. Phys. Lett.* **73**, 1712 (1998).

[234] Y. Sugiyama, Y. Nakata, S. Muto, T. Futatsugi, N. Yokoyama, "Characteristics of Spectral-Hole Burning of InAs Self-Assembled Quantum Dots", *IEEE J. of Sel. Topics Quant. Elect.* **4**, 880 (1998).

[235] Q. A. Turchette, C. S. Wood, B. E. King, C. J. Myatt, D. Leibfried, W. M. Itano, C. Monroe, D. J. Wineland, "Deterministic Entanglement of Two Trapped Ions", *Phys. Rev. Lett.* **81**, 3631 (1998).

[236] M. U. Wehner, M. H. Ulm, D. S. Chemla, M. Wegener, "Coherent Control of Electron-LO-Phonon Scattering in Bulk GaAs", *Phys. Rev. Lett.* **80**, 1992 (1998).

[237] J. M. Whittaker, A. J. Shields, "Theory of X^- at high magnetic fields", *Phys. Rev. B* **56**, 15185 (1998).

[238] R. N. Zare, "Laser Control of Chemical Reactions", *Science* **279**, 1875 (1998).

[239] L. C. Andreani, G. Panzarini, J. M. Gérard, "Strong-coupling regime for quantum boxes in pillar microcavities: Theory", *Phys. Rev. B* **60**, 13276 (1999).

[240] V. M. Axt, M. Herbst, T. Kuhn, "Coherent control of phonon quantum beats", *Superlatt. Microstruct.* **26**, 117 (1999).

[241] U. Banin, Y. Cao, D. Katz, O. Millo, "Identification of atomic-like electronic states in indium arsenide nanocrystal quantum dots", *Nature* **400**, 542 (1999).

[242] M. Bayer, A. Kuther, A. Forchel, A. Gorbunov, V. B. Timofeev, F. Schäfer, J. P. Reithmaier, T. L. Reinecke, S. N. Walck, "Electron and Hole g Factors and Exchange Interactions from Studies of the Exciton Fine Structure in $In_{0.60}Ga_{0.40}As$ Quantum Dots", *Phys. Rev. Lett.* **82**, 1748 (1999).

[243] N. H. Bonadeo, *Coherent nonlinear optical spectroscopy and control of single GaAs quantum dots*, Ph.D. thesis, The University of Michigan, The Harrison M. Randall Laboratory of Physics, Ann Arbor, MI 48109-1120 (1999).

[244] N. H. Bonadeo, A. S. Lenihan, G. Chen, J. R. Guest, D. G. Steel, D. Gammon, D. S. Katzer, D. Park, "Single Quantum Dot States Measured by Optical Modulation Spectroscopy", *Appl. Phys. Lett.* **75**, 2933 (1999).

[245] P. Borri, W. Langbein, J. Mørk, J. M. Hvam, "Heterodyne pump-probe and four-wave mixing in semiconductor optical amplifiers using balanced lock-in detection", *Opt. Commun.* **169**, 317 (1999).

[246] D. Bouwmeester, J.-W. Pan, M. Daniell, H. Weinfurter, A. Zeilinger, "Observation of three-photon Greenberger-Horne-Zeilinger Entanglement", *Phys. Rev. Lett.* **82**, 1345 (1999).

[247] S. L. Braunstein, C. M. Caves, R. Jozsa, N. Linden, S. Popescu, R. Schack, "Separability of Very Noisy Mixed States and Implications for NMR Quantum Computing", *Phys. Rev. Lett.* **83**, 1054 (1999).

[248] D. Brinkmann, J. Kudrna, P. Gilliot, B. Hönerlage, A. Arnoult, J. Cibert, S. Tatarenko, "Trion and Exciton dephasing measurements in modulation-doped quantum wells : A probe for trion and carrier localization", *Phys. Rev. B* **60**, 4474 (1999).

[249] G. Burkard, D. Loss, D. P. DiVincenzo, "Coupled quantum dots as quantum gates", *Phys. Rev. B* **59**, 2070 (1999).

[250] K. Cho, "Mechanisms for LT Splitting of Polarization Waves: a Link between Electron-Hole Exchange Interaction and Depolarization Shift", *J. Phys. Soc. Jpn.* **68**, 683 (1999).

[251] L. Chu, M. Arzberger, A. Zrenner, G. Böhm, G. Abstreiter, "Polarization dependent photocurrent spectroscopy on InAs/GaAs quantum dots", *Appl. Phys. Lett.* **75**, 2247 (1999).

[252] L. Chu, A. Zrenner, G. Böhm, G. Abstreiter, "Normal-incident intersubband photocurrent spectroscopy on InAs/GaAs quantum dots", *Appl. Phys. Lett.* **75**, 3599 (1999).

[253] J. Erland, J. C. Kim, N. H. Bonadeo, D. G. Steel, D. Gammon, D. S. Katzer, "Non-exponential photon echo decays from nanostructures: Strongly and weakly localized degenerate exciton states", *Phys. Rev. B* **60**, R8497 (1999).

[254] Z. Ficek, T. Rudolph, "Quantum interference in a driven two-level atom", *Phys. Rev. A* **60**, 4245 (1999).

[255] R. Fiederling, M. Keim, G. Reuscher, W. Ossau, G. Schmidt, A. Waag, L. W. Molenkamp, "Injection and detection of a spin-polarized current in a light-emitting diode", *Nature* **402**, 787 (1999).

[256] P. Gilliot, D. Brinkmann, J. Kudrna, O. Cregut, R. Levy, A. Arnoult, J. Cibert, S. Tatarenko, "Quantum Beats between trion and exciton transitions in modulation-doped CdTe quantum wells", *Phys. Rev. B* **60**, 5797 (1999).

[257] D. Gottesman, I. L. Chuang, "Demonstrating the viability of universal quantum computation using teleportation and single-qubit operations", *Nature* **402**, 390 (1999).

[258] J. A. Gupta, D. D. Awschalom, X. Peng, A. P. Alivisatos, "Spin Coherence in semiconductor quantum dots", *Phys. Rev. B* **59**, 10421 (1999).

[259] L. V. Hau, S. E. Harris, Z. Dutton, C. H. Behroozi, "Light speed reduction to 17 metres per second in an ultracold atomic gas", *Nature* **397**, 594 (1999).

[260] Huaizhe Xu, W. Jiang, B. Xu, W. Zhou, Z. Wang, "Two-dimensional ordering of self-assembled $In_xGa_{1-x}As$ quantum dots grown on GaAs(311)B surfaces", *J. of Crystal Growth* **206**, 279 (1999).

[261] A. Imamoğlu, D. D. Awschalom, G. Burkard, D. P. DiVincenzo, D. Loss, M. Sherwin, A. Small, "Quantum Information Processing using quantum dot spins and Cavity QED", *Phys. Rev. Lett.* **83**, 4204 (1999).

[262] J. D. Jackson, *Classical Electrodynamics*, John Wiley and Sons, Inc., Hoboken, NJ, 3rd edition (1999).

[263] F. Koberling, A. Mews, T. Basché, "Single-dot spectroscopy of CdS nanocrystals and CdS/HgS heterostructures", *Phys. Rev. B* **60**, 1921 (1999).

[264] S. Krishna, K. Linder, P. Bhattacharya, "Photoluminescence linewidth of self-organized $In_{0.4}Ga_{0.6}As$ quantum dots grown on InAlAs stressor dots", *Journal of Applied Physics* **86**, 4691 (1999).

[265] V. D. Kulakovskii, G. Bacher, R. Weigand, T. Kimmel, A. Forchel, E. Borovitskaya, K. Leonardi, D. Hommel, "Fine Structure of Biexciton Emission in Symmetric and Asymmetric CdSe/ZnSe Single Quantum Dots", *Phys. Rev. Lett.* **82**, 1780 (1999).

[266] S. Lan, K. Akahane, K.-Y. Jang, T. Kawamura, Y. Okada, M. Kawabe, "The Procedure to Realize Two-Dimensional Quantum Dot Superlattices: From Incoherently Coupled to Coherently Coupled Quantum Dot Arrays", *Jpn. J. Appl. Phys.* **38**, 1090 (1999).

[267] Y. S. Lee, T. B. Norris, M. Kira, F. Jahnke, S. W. Koch, G. Khitrova, H. M. Gibbs, "Quantum Correlations and Intraband Coherences in Semiconductor Cavity QED", *Phys. Rev. Lett.* **83**, 5338 (1999).

[268] T. Lundstrom, W. Schoenfeld, H. Lee, P. M. Petroff, "Exciton Storage in Semiconductor Self-Assembled Quantum Dots", *Science* **286**, 2312 (1999).

[269] Y. Makhlin, G. Schön, A. Schnirman, "Josephson-junction qubits with controlled couplings", *Nature* **398**, 305 (1999).

[270] P. Meystre, M. Sargent III, *Elements of Quantum Optics*, Springer-Verlag, Berlin-Heidelberg (1999).

[271] J. E. Mooij, T. P. Orlando, L. Levitov, L. Tian, C. H. van der Wal, S. Lloyd, "Josephson Persistent-Current Qubit", *Science* **285**, 1036 (1999).

[272] Y. Nakamura, Y. A. Pashkin, J. S. Tsai, "Coherent control of macroscopic quantum states in a single-Cooper-pair box", *Nature* **398**, 786 (1999).

[273] M. S. Sherwin, A. Imamoğlu, T. Montroy, "Quantum computation with quantum dots and terahertz cavity quantum electrodynamics", *Phys. Rev. A* **60**, 3508 (1999).

[274] A. M. Steane, "Efficient fault-tolerant quantum computing", *Nature* **399**, 124 (1999).

[275] Y. Toda, O. Moriwaki, M. Nishioka, Y. Arakawa, "Efficient Carrier Relaxation Mechanism in InGaAs/GaAs Self-Assembled Quantum Dots Based on the Existence of Continuum States", *Phys. Rev. Lett.* **82**, 4114 (1999).

[276] T. C. Weinacht, J. Ahn, P. H. Bucksbaum, "Controlling the shape of a quantum wavefunction", *Nature* **397**, 233 (1999).

[277] P. Y. Yu, M. Cardona, *Fundamentals of Semiconductors*, Springer-Verlag, Berlin Heidelberg (1999).

[278] G. S. Agarwal, "Anisotropic Vacuum-Induced Interference in Decay Channels", *Phys. Rev. Lett.* **84**, 5500 (2000).

[279] M. Bayer, O. Stern, P. Hawrylak, S. Fafard, A. Forchel, "Hidden symmetries in the energy levels of excitonic 'artificial atoms'", *Nature* **405**, 923 (2000).

[280] M. Bayer, O. Stern, A. Kuther, A. Forchel, "Spectroscopic study of dark excitons in $In_xGa_{1-x}As$/GaAsself-assembled quantum dots by a magnetic-field-induced symmetry breaking", *Phys. Rev. B* **61**, 7272 (2000).

[281] C. H. Bennett, D. P. DiVincenzo, "Quantum information and computation", *Nature* **404**, 247 (2000).

[282] L. Besombes, K. Kheng, D. Martrou, "Exciton and Biexciton Fine Structure in Single Elongated Islands Grown on a Vicinal Surface", *Phys. Rev. Lett.* **85**, 425 (2000).

[283] E. Biolatti, R. C. Iotti, P. Zanardi, F. Rossi, "Quantum Information Processing with Semiconductor Macroatoms", *Phys. Rev. Lett.* **85**, 5647 (2000).

[284] G. Chen, N. H. Bonadeo, D. G. Steel, D. Gammon, D. S. Katzer, D. Park, L. J. Sham, "Optically Induced Entanglement of Excitons in a Single Quantum Dot", *Science* **289**, 1906 (2000).

[285] D. P. DiVincenzo, "The Physical Implementation of Quantum Computation", *Fortschr. Phys.* **48**, 771 (2000).

[286] D. P. DiVincenzo, D. Bacon, J. Kempe, G. Burkard, K. B. Whaley, "Universal quantum computation with the exchange interaction", *Nature* **408**, 339 (2000).

[287] A. Esser, E. Runge, R. Zimmermann, W. Langbein, "Photoluminescence and radiative lifetime of trions in GaAs quantum wells", *Phys. Rev. B* **62**, 8232 (2000).

[288] J. R. Friedman, V. Patel, W. Chen, S. K. Tolpygo, J. E. Lukens, "Quantum superposition of distinct macroscopic states", *Nature* **406**, 43 (2000).

[289] A. Hartmann, Y. Ducommun, E. Kapon, U. Hohenester, E. Molinari, "Few-Particle Effects in Semiconductor Quantum Dots : Observation of Multicharged Excitons", *Phys. Rev. Lett.* **84**, 5648 (2000).

[290] E. Hertz, O. Faucher, B. Lavorel, R. Chaux, "Controlling molecular alignment rephasing through interference of Raman-induced rotational coherence", *J. Chem. Phys.* **113**, 6132 (2000).

[291] E. Hertz, O. Faucher, B. Lavorel, F. D. Via, R. Chaux, "Quantum control of ground-state rotational coherence in a linear molecule", *Phys. Rev. A* **61**, 033816 (2000).

[292] A. Imamoğlu, "Quantum Computation Using Quantum Dot Spins and Microcavities", *Fortschr. Phys.* **48**, 987 (2000).

[293] T. Ishikawa, T. Nishimura, S. Kohomoto, K. Asakawa, "Site controlled InAs single quantum-dot structures on GaAs surfaces patterned by *in situ* electron-beam lithography", *Appl. Phys. Lett.* **76**, 167 (2000).

[294] A. V. Khaetskii, Y. V. Nazarov, "Spin-flip transitions between Zeeman sublevels in semiconductor quantum dots", *Phys. Rev. B* **61**, 12639 (2000).

[295] A. V. Khaetskii, Y. V. Nazarov, "Spin relaxation in semiconductor quantum dots", *Phys. Rev. B* **61**, 12639 (2000).

[296] S. Krishna, O. Qasaimeh, P. Bhattacharya, P. J. McCann, K. Namjou, "Room-temperature far-infrared emission from a self-organized InGaAs/GaAs quantum-dot laser", *Appl. Phys. Lett.* **76**, 3355 (2000).

[297] S. Krishna, J. Sabarinathan, K. Linder, P. Bhattacharya, B. Lita, R. S. Goldman, "Growth of high density self-organized (In,Ga)As quantum dots with ultranarrow photoluminescence linewidths using buried In(Ga,Al)As stressor dots", *J. of Vac. Sci. and Tech. B* **18**, 1502 (2000).

[298] P. Malý, J. Kudrna, F. Trojánek, D. Mikeš, P. Němec, A. C. Maciel, J. F. Ryan, "Dominant role of surface states in photoexcited carrier dynamics in CdSe nanocrystalline films prepared by chemical deposition", *Appl. Phys. Lett.* **77**, 2352 (2000).

[299] P. Michler, A. Imamoğlu, M. D. Mason, P. J. Carson, G. F. Strouse, S. K. Buratto, "Quantum correlation among photons from a single quantum dot at room temperature", *Nature* **406**, 968 (2000).

[300] P. Michler, A. Kiraz, C. Becher, W. V. Schoenfeld, P. M. Petroff, L. Zhang, E. Hu, A. Imamoğlu, "A quantum dot single-photon turnstile device", *Science* **290**, 2282 (2000).

[301] M. A. Nielsen, I. L. Chuang, *Quantum Computation and Quantum Information*, Cambridge University Press, Cambridge, UK (2000).

[302] J.-W. Pan, D. Bouwmeester, M. Daniell, H. Weinfurter, A. Zeilinger, "Experimental test of quantum nonlocality in three-photon Greenberger-Horne-Zeilinger entanglement", *Nature* **421**, 721 (2000).

[303] R. Pausch, M. Held, T. Chen, H. Schwoerer, W. Kiefer, "Quantum control by stimulated Raman scattering", *J. Raman. Spectrosc.* **31**, 7 (2000).

[304] H. Rabitz, R. de Vivie-Riedle, M. Motzkus, K. Kompa, "Whither the Future of Controlling Quantum Phenomena?", *Science* **288**, 824 (2000).

[305] A. Rauschenbeutel, G. Nogues, S. Osnaghi, P. Bertet, M. Brune, J. M. Raimond, S. Haroche, "Step-by-step engineered multiparticle entanglement", *Science* **288**, 2024 (2000).

[306] C. A. Sackett, D. Kielpinski, B. E. King, C. Langer, V. Meyer, C. J. Myatt, M. A. Rowe, Q. A. Turchette, W. M. Itano, D. J. Wineland, C. Monroe, "Experimental entanglement of four particles", *Nature* **404**, 256 (2000).

[307] D. Sanvitto, R. A. Hogg, A. J. Shields, D. M. Whittaker, M. Y. Simmons, D. A. Ritchie, M. Pepper, "Rapid Radiative Decay of Charged Excitons", *Phys. Rev. B* **62**, R13294 (2000).

[308] T. Takagahara, "Theory of exciton doublet structure and polarization relaxation in single quantum dots", *Phys. Rev. B* **62**, 16840 (2000).

[309] T. Takagahara, "Theory of Exciton Fine Structure and Extremely Slow Spin Relaxation in Single Quantum Dots", *J. Lum.* **87**, 308 (2000).

[310] R. Trebino, *Frequency-resolved optical gating: the measurement of ultrashort laser pulses*, Kluwer Academic Publishers, Boston (2000).

[311] F. Troiani, U. Hohenester, F. Molinari, "Exploiting exciton-exciton interactions in semiconductor quantum dots for quantum-information processing", *Phys. Rev. B* **62**, 2263 (2000).

[312] C. H. van der Wal, A. C. J. ter Haar, F. K. Wilhelm, K. N. Schouten, C. J. P. M. Harmans, T. P. Orlando, J. E. Mooij, S. Lloyd, "Quantum superposition of macroscopic persistent-current states", *Science* **290**, 773 (2000).

[313] V.Klimov, A. A. Mikhailovsky, S. Xu, A. Malko, J. A. Hollingsworth, C. A. Leatherdale, H.-J. Eisler, M. G. Bawendi, "Optical Gain and Stimulated Emission in Nanocrystal Quantum Dots", *Science* **290**, 314 (2000).

[314] R. Vrijen, E. Yablonovitch, K. Wang, H. W. Jiang, A. Balandin, V. Roychowdhury, T. Mor, D. DiVincenzo, "Electron-spin-resonance transistors for quantum computing in silicon-germanium heterostructures", *Phys. Rev. A* **62**, 012306 (2000).

[315] R. J. Warburton, C. Schäflein, D. Haft, F. Bickel, A. Lorke, K. Karrai, J. M. Garcia, W. Schoefeld, P. M. Petroff, "Optical Emission from a charge-tunable quantum ring", *Nature* **405**, 926 (2000).

[316] Q. Wu, R. D. Grober, D. Gammon, D. S. Katzer, "Excitons, biexcitons, and electron-hole plasma in a narrow 2.8-nm GaAs/$Al_xGa_{1-x}As$ quantum well", *Phys. Rev. B* **62**, 13022 (2000).

[317] G. S. Agarwal, A. K. Patnaik, "Vacuum-induced coherences in radiatively coupled multilevel systems", *Phys. Rev. A* **63**, 043805 (2001).

[318] M. Bayer, P. Hawrylak, K. HInzer, S. Fafard, M. Korkusinski, Z. R. Wasilewski, O. Stern, A. Forchel, "Coupling and Entangling of Quantum States in Quantum Dot Molecules", *Science* **291**, 451 (2001).

[319] P. Bhattacharya, S. Krishna, J. Phillips, P. J. McCann, K. Namjou, "Carrier dynamics in self-organized quantum dots and their application to long-wavelength sources and detectors", *J. Crystal Growth* **227**, 27 (2001).

[320] D. Birkedal, K. Leosson, J. M. Hvam, "Long Lived Coherence in Self-Assembled Quantum Dots", *Phys. Rev. Lett.* **87**, 227401 (2001).

[321] P. Borri, W. Langbein, S. Schneider, U. Woggon, R. L. Sellin, D. Ouyang, D. Bimberg, "Ultralong Dephasing Time in InGaAs Quantum Dots", *Phys. Rev. Lett.* **87**, 157401 (2001).

[322] D. S. Chemla, J. Shah, "Many-body and correlation effects in semiconductors", *Nature* **411**, 549 (2001).

[323] P. Chen, C. Piermarocchi, L. J. Sham, "Control of Exciton Dynamics in Nanodots for Quantum Operations", *Phys. Rev. Lett.* **87**, 067401 (2001).

[324] Collaboration: Authors and Editors of the LB Volumes III/17A-22A-41A1A (ed.), *Group IV Elements, IV-VI and III-V Compounds, Part a - Lattice Properties*, volume III/41A1A of *Landolt-Börnstein - Group III Condensed Matter*, Springer-Verlag Heidelberg (2001).

[325] L. M. Duan, M. D. Lukin, J. I. Cirac, P. Zoller, "Long-distance quantum communication with atomic ensembles and linear optics", *Nature* **414**, 413 (2001).

[326] H.-A. Engel, D. Loss, "Detection of Single Spin Decoherence in a Quantum Dot via Charge Currents", *Phys. Rev. Lett.* **86**, 4648 (2001).

[327] S. I. Erlingsson, Y. V. Nazarov, V. I. Falko, "Nucleus-mediated spin-flip transitions in GaAs quantum dots", *Phys. Rev. B* **64**, 195306 (2001).

[328] F. Findeis, M. Baier, A. Zrenner, M. Bichler, G. Abstreiter, U. Hohenester, E. Molinari, "Optical excitations of a self-assembled artificial ion", *Phys. Rev. B* **63**, 121309 (2001).

[329] J. J. Finley, A. D. Ashmore, A. Lemaître, D. J. Mowbray, M. S. Skolnick, I. E. Iskevitch, P. A. Maksym, M. Hopkinson, T. F. Krauss, "Charged and neutral exciton complexes in individual self-assembled In(Ga)As quantum dots", *Phys. Rev. B* **63**, 073307 (2001).

[330] D. Gammon, A. L. Efros, T. A. Kennedy, M. Rosen, D. S. Katzer, D. Park, S. W. Brown, V. L. Korenev, I. A. Merkulov, "Electron and Nuclear spin interactions in the Optical Spectra of Single GaAs Quantum Dots", *Phys. Rev. Lett.* **86**, 5176 (2001).

[331] S. Glasberg, H. Shtrikman, I. Bar-Joseph, "Photoluminescence of a low-density two-dimensional hole gas in a GaAs quantum well: Observation of valence-band Landau levels", *Phys. Rev. B* **63**, 201308 (2001).

[332] J. R. Guest, T. H. Stievater, G. Chen, E. A. Tabak, B. G. Orr, D. G. Steel, D. Gammon, D. S. Katzer, "Near-field coherent spectroscopy and microscopy of a quantum dot system", *Science* **293**, 2224 (2001).

[333] J. A. Gupta, R. Knobel, N. Samarth, D. D. Awschalom, "Ultrafast manipulation of Electron Spin coherence", *Science* **292**, 2458 (2001).

[334] J. Hu, L.-S. Li, W. Yang, L. Manna, L.-W. Wang, A. P. Alivisatos, "Linearly Polarized Emission from Colloidal Semiconductor Quantum Rods", *Science* **292**, 2060 (2001).

[335] X. Huang, A. Stintz, H. Li, F. Lester, J. Cheng, K. J. Malloy, "Passive mode-locking in 1.3 μm two-section InAs quantum dot lasers", *Appl. Phys. Lett.* **78**, 2825 (2001).

[336] H. Kamada, H. Gotoh, J. Temmyo, T. Takagahara, H. Ando, "Exciton Rabi Oscillation in a Single Quantum Dot", *Phys. Rev. Lett.* **87**, 246401 (2001).

[337] K. F. Karlsson, E. S. Moskalenko, P. O. Holtz, B. Monemar, W. V. Schoenfeld, J. M. Garcia, P. M. Petroff, "Temperature influence on optical charging of self-assembled InAs/GaAs semiconductor quantum dots", *Appl. Phys. Lett.* **78**, 2952 (2001).

[338] C. Klingshirn (ed.), *Optical Properties, Part 1*, volume III/34/C1 of *Landolt-Börnstein - Group III Condensed Matter*, Springer-Verlag Heidelberg (2001).

[339] E. Knill, R. LaFlamme, G. J. Milburn, "A scheme for efficient quantum computation with linear optics", *Nature* **409**, 46 (2001).

[340] C. Liu, Z. Dutton, C. H. Behroozi, L. V. Hau, "Observation of coherent optical information storage in an atomic medium using halted light pulses", *Nature* **409**, 490 (2001).

[341] Y. Nakamura, Y. A. Pashkin, J. S. Tsai, "Rabi Oscillations in a Josephson-Junction Charge Two-Level System", *Phys. Rev. Lett.* **87**, 246601 (2001).

[342] U. Özgür, C. W. Lee, H. O. Everitt, "Control of Coherent Acoustic Phonons in Semiconductor Quantum Wells", *Phys. Rev. Lett.* **86**, 5604 (2001).

[343] P. Palinginis, H. Wang, "High-resolution spectral hole burning in CdSe/ZnS core-shell nanocrystals", *Appl. Phys. Lett.* **78**, 1541 (2001).

[344] J.-W. Pan, M. Daniell, S. Gasparoni, G. Weihs, A. Zeilinger, "Experimental Demonstration of Four-Photon Entanglement and High-Fidelity Teleportation", *Phys. Rev. Lett.* **86**, 4435 (2001).

[345] P. M. Petroff, A. Lorke, A. Imamoğlu, "Epitaxially Self-Assembled Quantum Dots", *Physics Today* **54**, 46 (2001).

[346] D. F. Phillips, A. Fleischhauer, A. Mair, R. L. Walsworth, M. D. Lukin, "Storage of Light in Atomic Vapor", *Phys. Rev. Lett.* **86**, 783 (2001).

[347] D. V. Regelman, U. Mizrahi, D. Gershoni, E. Ehrenfreund, W. V. Schoenfeld, P. M. Petroff, "Semiconductor Quantum Dot : A quantum light source of Multicolor photons with tunable statistics", *Phys. Rev. Lett.* **87**, 257401 (2001).

[348] S. A. Rice, "Interfering for the good of a chemical reaction", *Nature* **409**, 422 (2001).

[349] G. Salis, Y. Kato, K. Ensslin, D. C. Driscoll, A. C. Gossard, D. D. Awschalom, "Electrical control of spin coherence in semiconductor nanostructures", *Nature* **414**, 619 (2001).

[350] D. Sanvitto, F. Pulizzi, A. J. Shields, P. C. M. Christianen, S. N. Holmes, M. Y. Simmons, D. A. Ritchie, J. C. Maan, M. Pepper, "Observation of Charge Transport by Negatively Charged Excitons", *Science* **294**, 837 (2001).

[351] J. Shumway, A. Franceschetti, A. Zunger, "Correlation versus mean-field contributions to excitons, multiexcitons, and charging energies in semiconductor quantum dots", *Phys. Rev. B* **63**, 155316 (2001).

[352] T. H. Stievater, *Transient Nonlinear Spectroscopy of Single Quantum Dots*, Ph.D. thesis, The University of Michigan, The Harrison M. Randall Laboratory of Physics, Ann Arbor, MI 48109-1120 (2001).

[353] T. H. Stievater, X. Li, D. G. Steel, D. Gammon, D. S. Katzer, D. Park, C. Piermarocchi, L. J. Sham, "Rabi oscillations of excitons in single quantum dots", *Phys. Rev. Lett.* **87**, 133603 (2001).

[354] J. Urayama, T. B. Norris, J. Singh, P. Bhattacharya, "Observation of Phonon Bottleneck in Quantum Dot Electronic Relaxation", *Phys. Rev. Lett.* **86**, 4930 (2001).

[355] L. M. K. Vandersypen, M. Steffen, G. Breyta, C. S. Yannoni, M. H. Sherwood, I. L. Chuang, "Experimental realization of Shor's quantum factoring algorithm using nuclear magnetic resonance", *Nature* **414**, 883 (2001).

[356] S. A. Wolf, D. D. Awschalom, R. A. Buhrman, J. M. Daughton, S. von Molnár, M. L. Roukes, A. Y. Chtchelkanova, D. M. Treger, "Spintronics: A Spin-Based Electronics Vision for the Future", *Science* **294**, 1488 (2001).

[357] A. I. Yakimov, A. V. Dvurechenskii, N. P. Stepina, A. V. Nenashev, A. I. Nikiforov, "Spatially indirect excitons in self-assembled Ge/Si quantum dots", *Nanotechnology* **12**, 441 (2001).

[358] A. D. Yoffe, "Semiconductor quantum dots and related systems: electronic, optical, luminescence and related properties of low dimensional systems", *Adv. Phys.* **50**, 1 (2001).

[359] M. Bayer, A. Forchel, "Temperature dependence of the exciton homogeneous linewidth in $In_{0.4}Ga_{0.6}As$ self-assembled quantum dots", *Phys. Rev. B* **65**, 041308 (2002).

[360] M. Bayer, G. Ortner, O. Stern, A. Kuther, A. A. Gorbunov, A. Forchel, P. Hawrylak, S. Fafard, K. Hinzer, T. L. Reinecke, S. N. Walck, J. P. Reithmaier, F. Klopf, F. Schäfer, "Fine structure of neutral and charged excitons in self-assembled In(Ga)As/(Al)GaAs quantum dots", *Phys. Rev. B* **65**, 195315 (2002).

[361] L. Besombes, K. Kheng, L. Marsal, H. Mariette, "Few-particle effects in single CdTe quantum dots", *Phys. Rev. B* **65**, 121314 (2002).

[362] A. S. Bracker, "unpublished data", (2002).

[363] G. Chen, *Coherent optical spectroscopy and manipulation of GaAs quantum dots*, Ph.D. thesis, The University of Michigan, The Harrison M. Randall Laboratory of Physics, Ann Arbor, MI 48109-1120 (2002).

[364] G. Chen, T. H. Stievater, E. T. Batteh, X. Li, D. G. Steel, D. Gammon, D. S. Katzer, D. Park, L. J. Sham, "Biexciton quantum coherence in a single quantum dot", *Phys. Rev. Lett.* **88**, 117901 (2002).

[365] S. Cortez, O. Krebs, S. Laurent, M. Senes, X. Marie, P. Voisin, R. Ferreira, G. Bastard, J. M. Gérard, T. Amand, "Optically Driven Spin Memory in n-doped InAs-GaAs Quantum Dots", *Phys. Rev. Lett.* **89**, 207401 (2002).

[366] R. I. Dzhioev, V. L. Korenev, I. A. Merkulov, B. P. Zakharchenya, D. Gammon, A. L. Efros, D. S. Katzer, "Manipulation of the spin memory of electrons in n-GaAs", *Phys. Rev. Lett.* **88**, 256801 (2002).

[367] T. Fujisawa, D. G. Austing, Y. Tokura, Y. Hirayama, S. Tarucha, "Allowed and Forbidden Transitions in Artificial Hydrogen and Helium Atoms", *Nature* **419**, 278 (2002).

[368] J. R. Guest, T. H. Stievater, X. Li, J. Cheng, D. G. Steel, D. Gammon, D. S. Katzer, D. Park, C. Ell, A. Thranhardt, G. Khitrova, H. M. Gibbs, "Measurement of optical absorption by a single quantum dot exciton", *Phys. Rev. B* **65**, 241310 (2002).

[369] H. Htoon, T. Takagahara, D. Kulik, O. Baklenov, A. L. Holmes, Jr., C. K. Shih, "Interplay of Rabi Oscillations and Quantum Interference in Semiconductor Quantum Dots", *Phys. Rev. Lett.* **88**, 087401 (2002).

[370] F. J. Jedema, H. B. Heersche, A. T. Filip, J. J. A. Baselmans, B. J. van Wees, "Electrical detection of spin precession in a metallic mesoscopic spin valve", *Nature* **416**, 713 (2002).

[371] A. V. Khaetskii, D. Loss, L. Glazman, "Electron spin decoherence in quantum dots due to interaction with nuclei", *Phys. Rev. Lett.* **88**, 186802 (2002).

[372] D. Kielpinski, C. Monroe, D. J. Wineland, "Architecture for a large-scale ion-trap quantum computer", *Nature* **417**, 709 (2002).

[373] A. S. Lenihan, M. V. G. Dutt, D. G. Steel, S. Ghosh, P. K. Bhattacharya, "Raman quantum beats from entangled polarization eigenstates of InAs quantum dots", *Phys. Rev. Lett.* **88**, 223601 (2002).

[374] D. A. Lidar, L.-A. Wu, "Reducing Constraints on Quantum Computer Design by Encoded Selective Recoupling", *Phys. Rev. Lett.* **88**, 017905 (2002).

[375] M. Lomascolo, A. Vergine, T. K. Johal, R. Rinaldi, A. Passaseo, R. Cingolani, S. Patanè, M. Labardi, M. Allegrini, F. Troiani, E. Molinari, "Dominance of charged excitons in single-quantum-dot photoluminescence spectra", *Phys. Rev. B* **66**, 041302 (2002).

[376] I. A. Merkulov, A. L. Efros, M. Rosen, "Electron spin relaxation by nuclei in semiconductor quantum dots", *Phys. Rev. B* **65**, 205309 (2002).

[377] M. Phillips, H. Wang, "Spin Coherence and Electromagnetically Induced Transparency via Exciton Correlations", *Phys. Rev. Lett.* **89**, 186401 (2002).

[378] C. Piermarocchi, P. Chen, L. J. Sham, D. G. Steel, "Optical RKKY Interaction between charged semiconductor quantum dots", *Phys. Rev. Lett.* **89**, 167402 (2002).

[379] S. M. Reimann, M. Manninen, "Electronic structure of quantum dots", *Rev. Mod. Phys.* **74**, 1283 (2002).

[380] J. H. Smet, R. A. Deutschmann, F. Ertl, W. Wegscheider, G. Abstreiter, K. von Klitzing, "Gate-voltage control of spin interactions between electrons and nuclei in a semiconductor", *Nature* **415**, 281 (2002).

[381] T. H. Stievater, X. Li, J. R. Guest, D. G. Steel, D.Gammon, D. S. Katzer, D. Park, "Wavelength modulation spectroscopy of single quantum dots", *Appl. Phys. Lett.* **80**, 1876 (2002).

[382] T. H. Stievater, X. Li, D. G. Steel, D. Gammon, D. S. Katzer, D. Park, "Transient nonlinear spectroscopy of excitons and biexcitons in single quantum dots", *Phys. Rev. B* **65**, 205319 (2002).

[383] B. Szafran, B. Stébé, J. Adamowski, S. Bednarek, "Excitonic trions in single and double quantum dots", *Phys. Rev. B* **66**, 165531 (2002).

[384] J. G. Tischler, A. S. Bracker, D. Gammon, D. Park, "Fine Structure of Trions and Excitons in Single GaAs Quantum Dots", *Phys. Rev. B* **66**, 081310 (2002).

[385] D. Vion, A. Aassime, A. cottet, P. Joyez, H. Pothier, C. Urbina, D. Esteve, M. H. Devoret, "Manipulating the Quantum state of an Electrical Circuit", *Science* **296**, 886 (2002).

[386] W. H. Xu, J. H. Wu, J. Y. Gao, "Effects of spontaneously generated coherence on transient process in a Λ system", *Phys. Rev. A* **66**, 063812 (2002).

[387] Y. Yu, S. Han, X. Chu, S.-I. Chu, Z. Wang, "Coherent Temporal Oscillations of Macroscopic Quantum States in a Josephson Junction", *Science* **296**, 889 (2002).

[388] Z. Yuan, B. E. Kardynal, R. M. Stevenson, A. J. Shields, C. J. Lobo, K. Cooper, N. S. Beattie, D. A. Ritchie, M. Pepper, "Electrically driven single photon source", *Science* **295**, 102 (2002).

[389] Q. Zhang, A. V. Nurmikko, A. Angueloch, G. Xiao, A. Gupta, "Coherent Magnetization Rotation and Phase Control by Ultrashort Optical Pulses in CrO_2 Thin Films", *Phys. Rev. Lett.* **89**, 177402 (2002).

[390] A. Zrenner, E. Beham, S. Stufler, F. Findeis, M. Bichler, G. Abstreiter, "Coherent properties of a two-level system based on a quantum-dot photodiode", *Nature* **418**, 612 (2002).

[391] M. Aspelmeyer, H. R. Böhm, T. Gyatso, T. Jennewein, R. Kaltenbaek, M. Lindenthal, G. Molina-Terriza, A. Poppe, K. Resch, M. Taraba, R. Ursin, P. Walther, A. Zeilinger, "Long-Distance Free-Space Distribution of Quantum Entanglement", *Science* **301**, 621 (2003).

[392] M. Bajcsy, A. S. Zibrov, M. D. Lukin, "Stationary pulses of light in an atomic medium", *Nature* **426**, 638 (2003).

[393] L. Besombes, J. J. Baumberg, J. Motohisa, "Coherent Spectroscopy of Optically Gated Charged Single InGaAs Quantum Dots", *Phys. Rev. Lett.* **90**, 257402 (2003).

[394] G. Bester, A. Zunger, "Compositional and size-dependent spectroscopic shifts in charged self-assembled $In_xGa_{1-x}As/GaAs$ quantum dots", *Phys. Rev. B* **68**, 073309 (2003).

[395] M. S. Bigelow, N. N. Lepeshkin, R. W. Boyd, "Observation of Ultraslow Light Propagation in a Ruby Crystal at Room Temperature", *Phys. Rev. Lett.* **90**, 113903 (2003).

[396] M. S. Bigelow, N. N. Lepeshkin, R. W. Boyd, "Superluminal and Slow Light Propagation in a Room-Temperature Solid", *Science* **301**, 200 (2003).

[397] C. Boehme, K. Lips, "Electrical Detection of Spin Coherence in Silicon", *Phys. Rev. Lett.* **91**, 246603 (2003).

[398] A. S. Bracker, J. G. Tischler, V. L. Korenev, D. Gammon, "Polarized electrons, trions and nuclei in charged quantum dots", *Phys. Stat. Sol. (b)* **238**, 266 (2003).

[399] T. Calarco, A. Datta, P. Fedichev, E. Pazy, P. Zoller, "Spin-based all-optical quantum computation with quantum dots: Understanding and suppressing decoherence", *Phys. Rev. A* **68**, 012310 (2003).

[400] R. de Sousa, S. D. Sarma, "Electron spin coherence in semiconductors: Considerations for a spin-based solid-state quantum computer architecture", *Phys. Rev. B* **67**, 033301 (2003).

[401] R. de Sousa, S. D. Sarma, "Theory of nuclear -induced spectral diffusion: Spin decoherence of phosphorous donors in Si and GaAs quantum dots", *Phys. Rev. B* **68**, 115322 (2003).

[402] M. Feng, I. D'Amico, P. Zanardi, F. Rossi, "Spin-based quantum information processing with semiconductor quantum dots and cavity QED", *Phys. Rev. A* **67**, 014306 (2003).

[403] T. Hayashi, T. Fujisawa, H. D. Cheong, Y. H. Jeong, Y. Hirayama, "Coherent Manipulation of Electronic States in a Double Quantum Dot", *Phys. Rev. Lett.* **91**, 226804 (2003).

[404] J. Hübner, W. W. Rühle, M. Klude, D. Hommel, R. D. R. Bhat, J. E. Sipe, H. M. van Driel, "Direct Observation of Optically Injected Spin-Polarized Currents in Semiconductors", *Phys. Rev. Lett.* **90**, 216601 (2003).

[405] A. Imamoğlu, E. Knill, L. Tian, P. Zoller, "Optical Pumping of Quantum-Dot Nuclear Spins", *Phys. Rev. Lett.* **91**, 017402 (2003).

[406] A. Kuzmich, W. P. Bowen, A. D. Boozer, A. Boca, C. W. Chou, L. M. Duan, H. J. Kimble, "Generation of nonclassical photon pairs for scalable quantum communication with atomic ensembles", *Nature* **423**, 731 (2003).

[407] X. Li, *Coherent Transient Nonlinear Optical Spectroscopic Studies of Single Semiconductor Quantum Dots: Applications to Quantum Information Processing*, Ph.D. thesis, The University of Michigan, The Harrison M. Randall Laboratory of Physics, Ann Arbor, MI 48109-1120 (2003).

[408] X. Li, Y. Wu, D. Steel, D. Gammon, T. H. Stievater, D. S. Katzer, D. Park, C. Piermarocchi, L. J. Sham, "An All-Optical Quantum Gate in a Semiconductor Quantum Dot", *Science* **301**, 809 (2003).

[409] I. Martin, D. Mozyrsky, H. W. Jiang, "A scheme for electrical detection of single electron spin resonance", *Phys. Rev. Lett.* **90**, 018301 (2003).

[410] Y. I. Mazur, W. Q. Ma, X. Wang, Z. M. Wang, G. J. Salamo, M. Xiao, T. D. Mishima, M. B. Johnson, "InGaAs/GaAs three-dimensionally-ordered array of quantum dots", *Appl. Phys. Lett.* **83**, 987 (2003).

[411] J. McKeever, A. Boca, A. D. Boozer, J. R. Buck, H. J. Kimble, "Experimental realization of a one-atom laser in the regime of strong coupling", *Nature* **425**, 268 (2003).

[412] J.-W. Pan, S. Gasparoni, M. Aspelmeyer, T. Jennewein, A. Zeilinger, "Experimental realization of freely propagating teleported qubits", *Nature* **421**, 721 (2003).

[413] Y. A. Pashkin, T. Yamamoto, O. Astafiev, Y. Nakamura, D. V. Averin, J. S. Tsai, "Quantum oscillations in two coupled charge qubits", *Nature* **421**, 823 (2003).

[414] B. Patton, W. Langbein, U. Woggon, "Trion, biexciton, and exciton dynamics in single self-assembled CdSe quantum dots", *Phys. Rev. B* **68**, 125316 (2003).

[415] E. Pazy, E. Biolatti, T. Calarco, I. D'Amico, P. Zanardi, F. Rossi, P. Zoller, "Spin-based optical quantum computation via Pauli blocking in semiconductor quantum dots", *Europhys. Lett.* **62**, 175 (2003).

[416] M. Phillips, H. Wang, I. Rumyantsev, N. H. Kwong, R. Takayama, R. Binder, "Electromagnetically Induced Transparency in Semiconductors via Biexciton Coherence", *Phys. Rev. Lett.* **91**, 183602 (2003).

[417] M. Pioro-Ladriére, M. Ciorga, J. Lapointe, P. Zawadzki, M. Korkusiński, P. Hawrylak, A. S. Sachrajda, "Spin-Blockade Spectroscopy of a Two-Level Artificial Molecule", *Phys. Rev. Lett.* **91**, 026803 (2003).

[418] F. Schmidt-Kaler, H. Häffner, M. Riebe, S. Gulde, G. P. T. Lancaster, T. Deuschle, C. Becher, C. F. Roos, J. Eschner, R. Blatt, "Realization of the Cirac-Zoller controlled-NOT quantum gate", *Nature* **422**, 408 (2003).

[419] S. R. Schofield, N. J. Curson, M. Y. Simmons, F. J. Rueb, T. Hallam, L. Oberbeck, R. G. Clark, "Atomically Precise Placement of Single Dopants in Si", *Phys. Rev. Lett.* **91**, 136104 (2003).

[420] A. Shabaev, A. L. Efros, D. Gammon, I. A. Merkulov, "Optical readout and initialization of an electron spin in a single quantum dot", *Phys. Rev. B* **68**, 201305 (2003).

[421] C. Sifel, U. Hohenester, "A turnstile electron-spin entangler in semiconductors", *Appl. Phys. Lett.* **83**, 153 (2003).

[422] M. J. Stevens, A. L. Smirl, R. D. R. Bhat, A. Najmaie, J. E. Sipe, H. M. van Driel, "Quantum Interference Control of Ballistic Pure Spin Currents in Semiconductors", *Phys. Rev. Lett.* **90**, 136603 (2003).

[423] J. M. Taylor, C. M. Marcus, M. D. Lukin, "Controlling a Mesoscopic Spin Environment by Quantum Bit Manipulation", *Phys. Rev. Lett.* **91**, 246802 (2003).

[424] J. M. Taylor, C. M. Marcus, M. D. Lukin, "Long-Lived Memory for Mesoscopic Quantum Bits", *Phys. Rev. Lett.* **90**, 206803 (2003).

[425] F. Troiani, E. Molinari, U. Hohenester, "High-Finesse Optical Quantum Gates for Electron Spins in Artificial Molecules", *Phys. Rev. Lett.* **90**, 206802 (2003).

[426] A. M. Tyryshkin, S. A. Lyon, A. V. Astashkin, A. M. Raitsimring, "Electron spin relaxation times of phosphorous donors in silicon", *Phys. Rev. B* **68**, 193207 (2003).

[427] B. Urbaszek, R. J. Warburton, K. Karrai, B. D. Gerardot, P. M. Petroff, J. M. Garcia, "Fine Structure of Highly Charged Excitons in Semiconductor Quantum Dots", *Phys. Rev. Lett.* **90**, 247403 (2003).

[428] R. Winkler, *Spin–Orbit Coupling Effects in Two-Dimensional Electron and Hole Systems*, Springer Tracts in Modern Physics, Springer-Verlag Heidelberg (2003).

[429] M. Xiao, I. Martin, H. W. Jiang, "Probing the Spin State of a Single Electron Trap by Random Telegraph Signal", *Phys. Rev. Lett.* **91**, 078301 (2003).

[430] M. D. Barrett, J. Chiaverini, T. Schaetz, J. Britton, W. M. Itano, J. D. Jost, E. Knill, C. Langer, D. Leibfried, R. Ozeri, D. J. Wineland, "Deterministic quantum teleportation with atomic qubits", *Nature* **429**, 737 (2004).

[431] B. B. Blinov, D. L. Moehring, L. M. Duan, C. Monroe, "Observation of entanglement between a single trapped atom and a single photon", *Nature* **428**, 153 (2004).

[432] M. Bourennane, M. Eibl, S. Gaertner, C. Kurtsiefer, A. Cabello, H. Weinfurter, "Decoherence-Free Quantum Information Processing with Four-Photon Entangled States", *Phys. Rev. Lett.* **92**, 107901 (2004).

[433] A. S. Bracker, *et al.*, submitted to *Science* (2004).

[434] P. Chen, C. Piermarocchi, L. J. Sham, D. Gammon, D. G. Steel, "Theory of quantum optical control of a single spin in a quantum dot", *Phys. Rev. B* **69**, 075320 (2004).

[435] J. Cheng, "private communications", (2004).

[436] S. E. Economou, R. Liu, L. J. Sham, *in preparation* (2004).

[437] J. M. Elzerman, R. Hanson, L. H. W. van Beveren, B. Witkamp, L. M. K. Vandersypen, L. P. Kouwenhoven, "Single-shot read-out of an individual electron spin in a quantum dot", *Nature* **430**, 431 (2004).

[438] D. Fattal, E. Diamanti, K. Inoue, Y. Yamamoto, "Quantum Teleportation with a Quantum Dot Single Photon Source", *Phys. Rev. Lett.* **92**, 037904 (2004).

[439] D. Fattal, K. Inoue, J. Vučković, C. Santori, G. S. Solomon, Y. Yamamoto, "Entanglement Formation and Violation of Bell's Inequality with a Semiconductor Single Photon Source", *Phys. Rev. Lett.* **92**, 037903 (2004).

[440] M. Friesen, C. Tahan, R. Joynt, M. A. Eriksson, "Spin Readout and Initialization in a Semiconductor Quantum Dot", *Phys. Rev. Lett.* **92**, 037901, si - SiGe quantum dots (2004).

[441] X. M. Hu, J. P. Zheng, "Coherent population trapping via quantum interference of incoherent pump processes in three-level Λ systems", *J. of Physics B* **37**, 345 (2004).

[442] A. K. Hüttel, J. Weber, A. W. Holleitner, D. Weinmann, K. Eberl, R. H. Blick, "Nuclear spin relaxation probed by a single quantum dot", *Phys. Rev. B* **69**, 073302 (2004).

[443] K. Karrai, R. J. Warburton, C. Schulhauser, A. Högele, B. Urbaszek, E. J. McGhee, A. O. Govorov, J. M. Garcia, B. D. Gerardot, P. M. Petroff, "Hybridization of electronic states in quantum dots through photon emission", *Nature* **427**, 135 (2004).

[444] D. Leibfried, M. D. Barrett, T. Schaetz, J. Britton, J. Chiaverini, W. M. Itano, J. D. Jost, C. Langer, D. J. Wineland, "Towards Heisenberg-Limited Spectroscopy with Multiparticle Entangled States", *Science* **304**, 1476 (2004).

[445] D. Leibfried, B. DeMarco, V. Meyer, D. Lucas, M. Barrett, J. Britton, W. M. Itano, B. Jelenković, C. Langer, T. Rosenband, D. J. Wineland, "Experimental demonstration of a robust, high-fidelity geometric two ion-qubit phase gate", *Nature* **422**, 412 (2004).

[446] X. Li, *et al.*, "Raman quantum beats of interacting excitons in a single quantum dot", *Submitted to Phys. Rev. B.* (2004).

[447] J. McKeever, A. Boca, A. D. Boozer, R. Miller, J. R. Buck, A. Kuzmich, H. J. Kimble, "Deterministic Generation of Single Photons from One Atom Trapped in a Cavity", *Science Express* **10**, 1126, URL `http://www.scienceexpress.org/10.1126/science.1095232` (2004).

[448] M. Riebe, H. Häffner, C. F. Roos, W. Hänsel, J. Benhelm, G. P. T. Lancaster, T. W. Körber, C. Becher, F. Schmidt-Kaler, D. F. V. James, R. Blatt, "Deterministic quantum teleportation with atoms", *Nature* **429**, 734 (2004).

[449] C. F. Roos, M. Riebe, H. Häffner, W. Hänsel, J. benhelm, G. P. T. Lancaster, C. Becher, F. Schmidt-Kaler, R. Blatt, "Control and Measurement of Three-Qubit Entangled States", *Science* **304**, 1478 (2004).

[450] R. M. Slayton, K. A. Nelson, "Picosecond acoustic transmission measurements. I. Transient grating generation and detection of acoustic responses in thin metal films", *J. Chem. Phys.* **120**, 3908 (2004).

[451] T. Unold, K. Mueller, C. Lienau, T. Elsaesser, A. D. Wieck, "Optical Stark Effect in a Quantum Dot: Ultrafast Control of Single Exciton Polarizations", *Phys. Rev. Lett.* **92**, 157401 (2004).

[452] L. M. Woods, T. L. Reinecke, R. Kotlyar, "Hole spin relaxation in quantum dots", *Phys. Rev. B* **69**, 125330 (2004).

[453] Y. Wu, X. Li, D. Steel, D. Gammon, L. J. Sham, "Coherent optical control of semiconductor quantum dots for quantum information processing", *Physica E (in press)* (2004).

[454] M. Xiao, I. Martin, E. Yablonovitch, H. W. Jiang, "Electrical detection of the spin resonance of a single electron in a field-effect transistor", *Nature* **430**, 435 (2004).

[455] Z. Zhao, Y.-A. Chen, A.-N. Zhang, T. Yang, H. J. Briegel, J.-W. Pan, "Experimental demonstration of five-photon entanglement and open-destination teleportation", *Nature* **430**, 54 (2004).

[456] I. Žutić, J. Fabian, S. D. Sarma, "Spintronics: Fundamentals and applications", *Rev. Mod. Phys.* **76**, 323 (2004).